

HYDROGEN ABSORPTION AND EMBRITTLMENT OF CANDIDATE CONTAINER MATERIALS

Prepared for

**Nuclear Regulatory Commission
Contract NRC-02-88-005**

Prepared by

N. Sridhar

**Center for Nuclear Waste Regulatory Analyses
Southwest Research Institute
San Antonio, Texas**

**B. E. Wilde, C. Manfredi, S. Kesavan, C. Miller
Fontana Corrosion Center
Department of Materials Science and Engineering
The Ohio State University
Columbus, Ohio**

Center for Nuclear Waste Regulatory Analyses

JUNE 1991

HYDROGEN ABSORPTION AND EMBRITTLEMENT OF CANDIDATE CONTAINER MATERIALS

Prepared for

**Nuclear Regulatory Commission
Contract No. NRC-02-88-005**

Prepared by

**N. Sridhar
Center for Nuclear Waste Regulatory Analyses
Southwest Research Institute
San Antonio, Texas**

**B. E. Wilde, C. Manfredi, S. Kesavan, C. Miller
Fontana Corrosion Center
Department of Materials Science and Engineering
The Ohio State University
Columbus, Ohio**

Center for Nuclear Waste Regulatory Analyses

JUNE 1991

426.1

TABLE OF CONTENTS

ABSTRACT	ii
LIST OF FIGURES	iv
EXECUTIVE SUMMARY	1
1. INTRODUCTION	2
2. ANTICIPATED SOURCES OF HYDROGEN	3
2.1 Galvanic Coupling	3
2.2 Crevice Corrosion Induced Hydrogen Evolution	5
2.3 Microbiologically Influenced Hydrogen Evolution	8
2.4 Radiolysis Products	8
3. HYDROGEN EMBRITTLEMENT OF CANDIDATE CONTAINER ALLOYS	13
3.1 Hydrogen Embrittlement of Stainless Steels and Ni-base Alloys	13
3.1.1 Role of Environmental Variables	13
3.1.2 Role of Microstructure	22
3.2 Copper Based Alloys	24
4. A REVIEW OF HYDROGEN PERMEATION DATA	27
4.1 Austenitic Stainless Steels and Ni-base Alloys	27
4.2 Copper Based Alloys	28
5. SUMMARY AND RECOMMENDATIONS	32
REFERENCES	33
APPENDIX A: Analysis of Permeation Transients	36
APPENDIX B: Hydrogen Absorption and Potential Embrittlement of Candidate High-Level Waste Package Containers in the Proposed Tuff Repository Environment - Final Report Under SwRI Contract No. 20020698, 1991	40

LIST OF FIGURES

<u>Figure</u>	<u>Page</u>
1. Schematic illustration of galvanically generated cathodic current on the higher alloy when it is coupled to carbon steel.	4
2. Effect of external potential on the hydrogen permeations in an artificial crevice. (Cottis, 1986)	6
3. Steady-state permeation current-potential relationships for type 304 stainless steel membrane in 0.5 M Na ₂ SO ₄ solutions of different pH at 95°C (potentiostatic experiments). (Ohnaka, 1990)	7
4. Hydrogen permeation current and culture parameters of a hydrogen-producing bacterium, clostridium acetobutylicum. (Walch, 1989)	9
5. Effect of pH on the primary products of water irradiation. Yields are for γ or fast-electron radiation with energies of the order of 0.1 to 20 MeV, and assume that OH and H ₂ O ₂ achieve acid-base equilibrium. (Spinks, 1990)	10
6. Hydrogen take-up by annealed Grade 12 Ti in brine vs. immersion time (month) calculated on the basis of metal surface area (γ signifies gamma radiation). (Kim, 1987a)	11
7. Effect of additions of H ₂ , O ₂ , and H ₂ O ₂ together on the hydrogen take-up by as-received Grade 12 Ti in brine at 108°C. (Kim, 1987b)	11
8. Fracture behavior of cathodically-charged nickel, containing Fe or Cu. (Smith, 1974)	14
9. Sustained load crack growth rate in Inconel 718 TDCB specimens as a function of stress intensity at various hydrogen pressures. Temperature: Room temperature. (Walter, 1973)	15
10. Stage II (stress-intensity independent) crack velocity as a function of charging current density. Temperature: Room temperature. (Sridhar, 1980)	17
11. Effect of text environment and charging current density on the failure time of stressed C-ring specimens of Inconel 625 [59% CR + 932 F (500 C)/50 hours] and Hastelloy G [59% CR + 500 F (260 C)/250 hours]. Temperature: Room temperature. Stress: 100Y. Yield. (Kane, 1978)	18
12. Temperature dependence of the slow-crack-growth rate of 4130 steel. (Williams, 1969)	19

LIST OF FIGURES (cont'd.)

<u>Figures</u>	<u>Page</u>
13. Effect of environmental temperature on HE of Hastelloy alloy C-276. Environment: 4% NaCl + 0.5% CH ₃ COOH + H ₂ S (1 atm), coupled to carbon steel. Stressed to 90% yield. Alloy aged: 500 C/100 hours.	20
14. The reduction in area at fracture of Monel 400 tested in the presence of hydrogen. (Price, 1985)	21
15. Illustration of a pile-up of dislocation (represented by \perp) at a grain boundary causing a stress concentration.	23
16. Correlation of RA loss in gaseous hydrogen (69 MPa) with SFE, using data from several sources. Filled points are for nitrogen-containing steels.	25
17. v-K curves of C-276 as a function of aging time at 500°C. (Sridhar, 1980)	26
18. Effect of Fe addition to binary Ni-Fe alloys on permeability, diffusivity, and solubility of hydrogen. (Beck, 1971)	29
19. Variation of diffusivity D with T ⁻¹ for Hastelloy Alloy C-276. (Mezzanotte, 1980)	30
20. Correlation of quantity of tritium absorbed vs. oxygen content of copper. (Caskey, 1976)	31
A-1. Theoretical rise transient superimposed on typical experimental data. This figure also illustrates the method of fitting experimental data to the theoretical curves.	38

EXECUTIVE SUMMARY

This report presents a compendium of the results of a recent research activity conducted at the Fontana Corrosion Center (FCC) of The Ohio State University and additional analyses of the literature performed at the Center for Nuclear Waste Regulatory Analyses (CNWRA). This research activity is part of the research project, Integrated Waste Package Experiments (IWPE), being conducted at the CNWRA under the sponsorship of the Nuclear Regulatory Commission. The aim of the research program at the Fontana Corrosion Center was to develop techniques for the study of hydrogen permeation in some of the candidate container materials. Such techniques can be used eventually at the CNWRA to study hydrogen absorption under repository thermal and radiation conditions.

An analysis of the potential sources of hydrogen in the engineered barrier system indicated that four sources can exist: hydrogen from galvanic coupling of the container material with carbon steel borehole liner, hydrogen evolved in crevices as a result of acidic conditions prevailing there, hydrogen from microbiological sources, and hydrogen radicals generated by radiolysis of water or water vapor. Of these, the last is the least likely, given the current state of knowledge, because of the formation of oxidizing products from radiolysis of water vapor — air mixtures (nitric acid, hydrogen peroxide, etc.) and the existing environment (i.e. slightly alkaline pH, consumption of hydrogen by oxygen present in the Yucca Mountain site). However, radiolytic generation of hydrogen radicals may be a possibility in crevices (due to acidic and anoxic conditions) if aqueous conditions prevail. Not enough is known about the survivability of microorganisms, such as *C.Acetobutylicum*, known to generate hydrogen under repository conditions, although this source cannot be ruled out with the present state of knowledge. The first two sources are viable if aqueous conditions prevail.

Literature data on hydrogen embrittlement susceptibility of candidate container materials were assessed. Copper based alloys have not been shown to embrittle in hydrogen even at relatively high hydrogen pressures. The austenitic alloys have a decreasing tendency to embrittle with increasing temperature, the maximum susceptibility being around 25°C. The preliminary embrittlement data developed at the FCC support this conclusion. Since high temperatures reduce the possibility of hydrogen embrittlement of all the current, candidate container materials, hydrogen embrittlement may be considered to be a low-priority degradation process for container performance. However, all the literature data are based on short term tests. Assessment of the long-term embrittlement due to hydrogen can be performed only by a combination of experimental data with suitable models. The hydrogen embrittlement models currently available are discussed briefly.

The permeability techniques developed by Wilde et al. at the FCC are shown to be applicable to the study of hydrogen absorption kinetics of candidate container materials under repository thermal conditions. The tests performed at the FCC have yielded values of hydrogen diffusivity for the austenitic alloys and Cu-based alloys which are consistent with those found in the literature, given the various factors affecting the measured values. Additionally, the data generated by the FCC has been analyzed to yield values for the fractional surface coverage of adsorbed hydrogen that will be absorbed into the metal. Preliminary data on the hydrogen embrittlement of the austenitic alloys in the annealed condition show that the higher Fe-containing alloys are less prone to cracking than the low-Fe containing Ni-base alloy, alloy C-22. This is in agreement with the literature. Additionally, an increase in temperature from 25° to 95°C eliminated embrittlement for all the austenitic alloys tested in the short-term test, again in agreement with the literature.

1. INTRODUCTION

The NRC regulation 10 CFR 60.113 requires the waste package to provide substantially complete containment of radionuclides for a minimum period of 300 to 1000 years. Arising from this requirement is the need for the license applicant (DOE) to demonstrate, through proper material selection, design, and testing, successful long-term performance of the waste package system. This entails resolution of technical issues pertaining to assessment of all viable degradation modes and the uncertainties in the data bases. The NRC must develop an understanding of the important types of degradation processes that the waste package can undergo in the repository and the parameters that affect the occurrence and rate of these processes. The Integrated Waste Package Experiments (IWPE) research project is aimed at assisting the NRC in developing this understanding, not only for the license review process but also for providing timely guidance to DOE in their design of the engineered barrier system. Since the current DOE waste package design places great reliance on the outer container, the bulk of the experimental program has been oriented towards the investigation of various degradation modes of the candidate container materials.

The IWPE project plan consists of five tasks:

- Task 1 - Corrosion
- Task 2 - Stress Corrosion Cracking
- Task 3 - Materials Stability
- Task 4 - Microbiologically Influenced Corrosion
- Task 5 - Other Degradation Modes

One of the activities within Task 5 is the investigation of hydrogen absorption and embrittlement of candidate container materials. The development of suitable techniques for the measurement of hydrogen absorption in candidate container materials was carried out at the Fontana Corrosion Center (FCC). It is the objective of this report to review the results of the investigations carried out at the FCC and the literature on hydrogen embrittlement of candidate container materials in order to recommend further research to be carried out at the CNWRA. From the point of view of future research on hydrogen absorption and embrittlement, two essential questions must be answered:

1. What are the sources of hydrogen in the repository and how much hydrogen are these sources expected to generate and deliver to the surface of the containers?
2. Assuming that hydrogen will be present and absorbed into the containers, will the container material embrittle under repository thermal conditions?

The answer to the second question will depend not only on the concentration of hydrogen absorbed but also on the characteristics of the container material (composition, microstructure, etc.). The first part of this report attempts to answer the above questions. A review of the various possible sources of hydrogen in the repository along with an assessment of their importance is made. Following this, a review of the literature on hydrogen embrittlement of candidate materials, the CNWRA's reference alloy, alloy C-22, and other alternate metallic materials listed by DOE (LLNL) is provided. Finally, the literature on hydrogen absorption and transport kinetics in candidate materials is reviewed and compared to the results from the FCC. Based on these evaluations, recommendations for future effort are made. The report from the FCC to the CNWRA is attached as Appendix B.

2. ANTICIPATED SOURCES OF HYDROGEN

Hydrogen embrittlement, as an important degradation mode for the containers in the proposed Yucca Mountain repository, has not been investigated experimentally thus far by DOE. However, the effects of hydrogen in the candidate materials have been reviewed as part of an extensive survey of degradation modes by Gdowski and Bullen (Gdowski, 1988). A main limitation of their report is that the sources of hydrogen in the proposed repository site at Yucca Mountain and the waste package design are not analyzed. Four sources of hydrogen in the repository may be identified:

1. **Galvanic Coupling**: The higher alloy container material may come into contact with the carbon steel borehole liner rendering the container material cathodic. This effect can be ignored if the same material is used for both the container and liner.
2. **Crevice Corrosion**: It is well established that the pH inside a crevice is quite acidic (approximately 2 or lower for some stainless steels). Hence, depending upon the potential drop within the crevice, hydrogen evolution within the crevice is possible and has been observed in some cases.
3. **Microbiologically Influenced Effects**: It has been shown that some microbiological organisms can evolve hydrogen at metal surfaces independent of corrosion reactions.
4. **Radiolysis Products of the Surrounding Environment**: It has been argued that radiolysis of water and water vapor can form hydrogen free radicals which may then diffuse to the metal surface to be absorbed.

Note that sources 1 and 2 require the presence of an aqueous phase. Source 3 depends on the characteristics of the microorganism. The microorganism investigated so far, *Clostridium Acetobutylicum*, has been grown in aqueous, anaerobic conditions. Source 4 can function in both aqueous and gaseous media, but the products of radiolysis are different.

2.1 Galvanic Coupling

Galvanic coupling of higher alloys with carbon steel has been shown to cause hydrogen embrittlement in many applications, particularly in the oil and gas field. The results of these galvanically coupled tests are discussed in Section 3. Most of these environments are more severe than the projected environmental conditions at the Yucca Mountain repository site. For example, the cracking of Monel K-500 bolts in off-shore applications has been established to be due to hydrogen generated by galvanic coupling of this Ni-Cu alloy with aluminum components (Efird, 1985). In this case, the galvanic potential was estimated to be -1.0 V vs. SCE, and the hydrogen concentrations in the failed bolts were as high as 18 ppm. Galvanic coupling to steel components has been reported to be the cause of failure in down-hole oil and gas components (Erlings, 1986), and hydrogen concentrations as high as 200 ppm have been reported in failed components.

In the latter case, the presence of sulfur compounds, such as H₂S, enhances the entry of hydrogen into the metal by limiting (poisoning) the recombination of adsorbed hydrogen atoms. The rate of hydrogen generation due to galvanic coupling under repository conditions can be estimated if the anodic and cathodic polarization curves of the candidate container material and carbon steel under identical environmental conditions are known. This is illustrated schematically in Figure 1, where all the currents are plotted as logarithms of their absolute values. Since galvanic coupling involves short-circuiting the

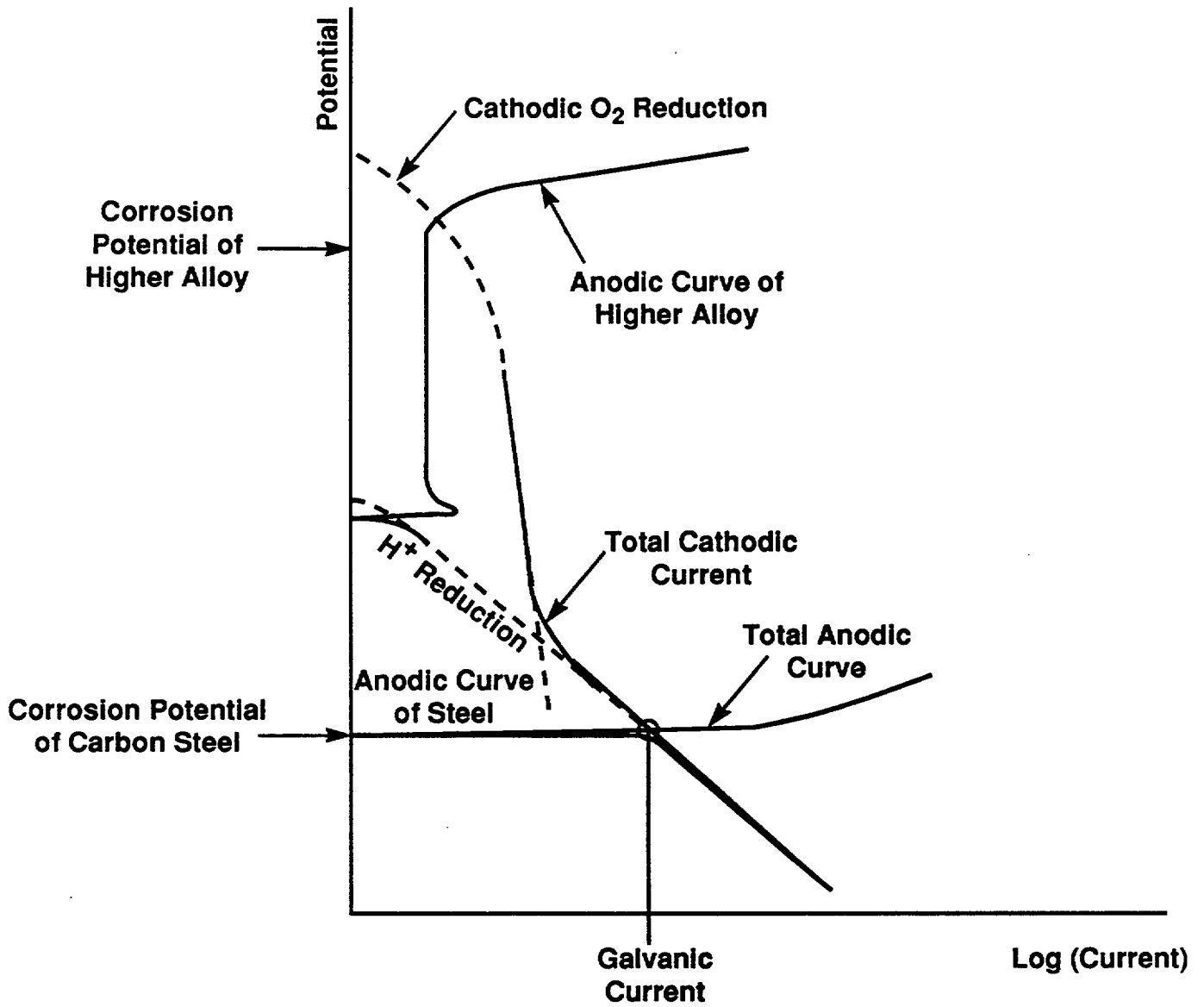


Figure 1. Schematic illustration of galvanically generated cathodic current on the higher alloy when it is coupled to carbon steel.

two metals, the total anodic and cathodic curves of the two metals can be superimposed to determine the galvanic potential. Assuming no solution resistive losses and equal areas of the two materials, the potential at which the total anodic and cathodic currents are equal is the galvanic potential, and the cathodic current density at this potential can then be assumed to be the maximum rate at which hydrogen evolves at the cathode. This is usually an overestimation, however, since resistive losses and other cathodic reactions (oxygen reduction) tend to reduce the hydrogen evolution current. In addition, only a fraction of the adsorbed hydrogen is absorbed into the metal.

Unfortunately, polarization curves for carbon steel and candidate container materials under identical environmental conditions simulating those of the Yucca Mountain repository are not available. Galvanic corrosion in sea water at low temperatures has been examined in detail by Hack and Scully (Hack, 1984). For a HY80 steel - alloy 625 (Ni-22Cr-9Mo) galvanic couple, the predicted galvanic current density was $4\mu\text{A}/\text{cm}^2$ while the measured value was $9\mu\text{A}/\text{cm}^2$. Mansfeld and Kenkel (Mansfeld, 1975) measured the galvanic current density between various couples in 3.5% NaCl at 21°C. For a 304L stainless steel - 4130 steel couple, the galvanic current density was $9.53\mu\text{A}/\text{cm}^2$. Rhodes (Rhodes, 1986) estimated the galvanic current density of carbon steel coupled to many Ni-base alloys in a 4% NaCl + H₂S (1 atm.) environment to be 10 - 100 $\mu\text{A}/\text{cm}^2$. Since the repository environment is not expected to be as severe, the galvanic current density and hence, the rate of hydrogen evolution may be assumed to be of the order of $10\mu\text{A}/\text{cm}^2$. Though this is low (by an order of magnitude) compared to the typical current densities used for short-term tests, long-term embrittlement has been observed at these low-charging current densities. However, these embrittlement phenomena have been mainly confined to low temperatures (about 25 - 30°C). This will be examined later.

2.2 Crevice Corrosion Induced Hydrogen Evolution

It is well recognized that the environmental conditions inside a crevice or an occluded area in electrolytic contact with the bulk environment tend towards the more acidic. Because of deoxygenation, acidic conditions, and the potential drop along the crevice, reducing conditions prevail in the crevice, promoting hydrogen ion reduction as the cathodic process. This has been shown to be the case for plain carbon steel by performing permeation studies on a creviced sample (Cottis, 1986). As shown in Figure 2, hydrogen permeation inside a crevice in a bulk solution of 3.5% NaCl solution increases when the external potential is either anodic (more corrosion) or cathodic (more hydrogen evolution externally).

Although similar experiments have not been tried for stainless steels or Ni-base alloys, Ohnaka and Furutani (Ohnaka, 1990) have attempted to establish the conditions where hydrogen evolution inside a crevice is possible in stainless steels. Figure 3 shows the hydrogen permeation rate as a function of applied potential for type 304 stainless steel in Na₂SO₄ solution at various pH values. They established that detectable permeation occurred only at applied potentials lower than the equilibrium potentials for hydrogen evolution for the calculated pH at temperature. They noted that for a solution of pH = 3.8, permeation of hydrogen did not occur above a potential of -0.2 V (SCE). Turnbull (Turnbull, 1983) has shown that the measured potential inside crevices for stainless steels is only slightly below the external potential.

The measured potential of 304L stainless steel in a aerated, tuff-conditioned J-13 solution augmented with a NaCl concentration of 1000 ppm at 95°C is -0.15 V (SCE) (Glass, 1984). If the solution is deaerated, the corrosion potential drops to about -0.5 V (SCE). Hence, hydrogen evolution inside crevices cannot be ruled out for 304L stainless steel under repository environmental conditions. Since similar potential and crevice solution compositions are expected for the other Ni-Fe-Cr-Mo alloys, hydrogen evolution in crevices is a viable mechanism. The conditions for hydrogen evolution on Cu-based alloys have not been so well established.

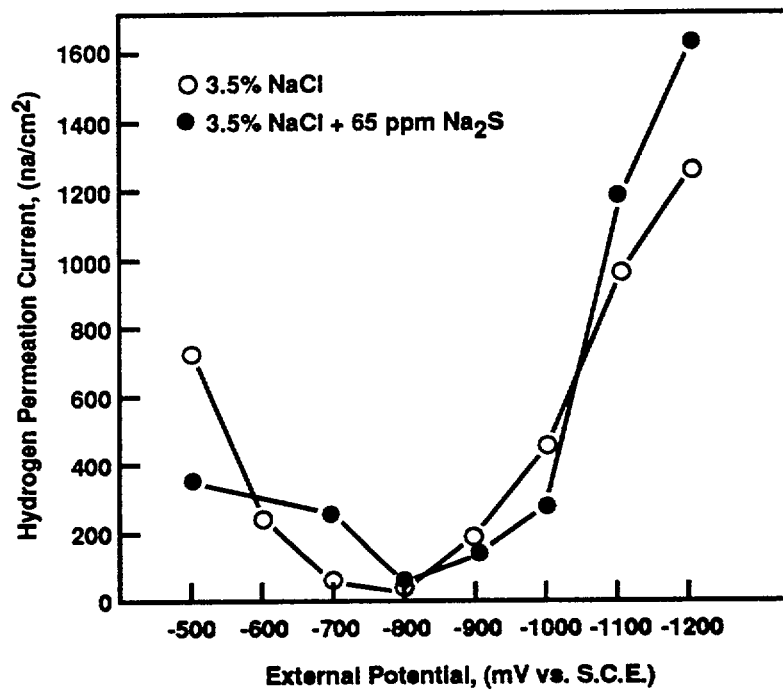


Figure 2. Effect of external potential on the hydrogen permeation in an artificial crevice. (Cottis, 1986)

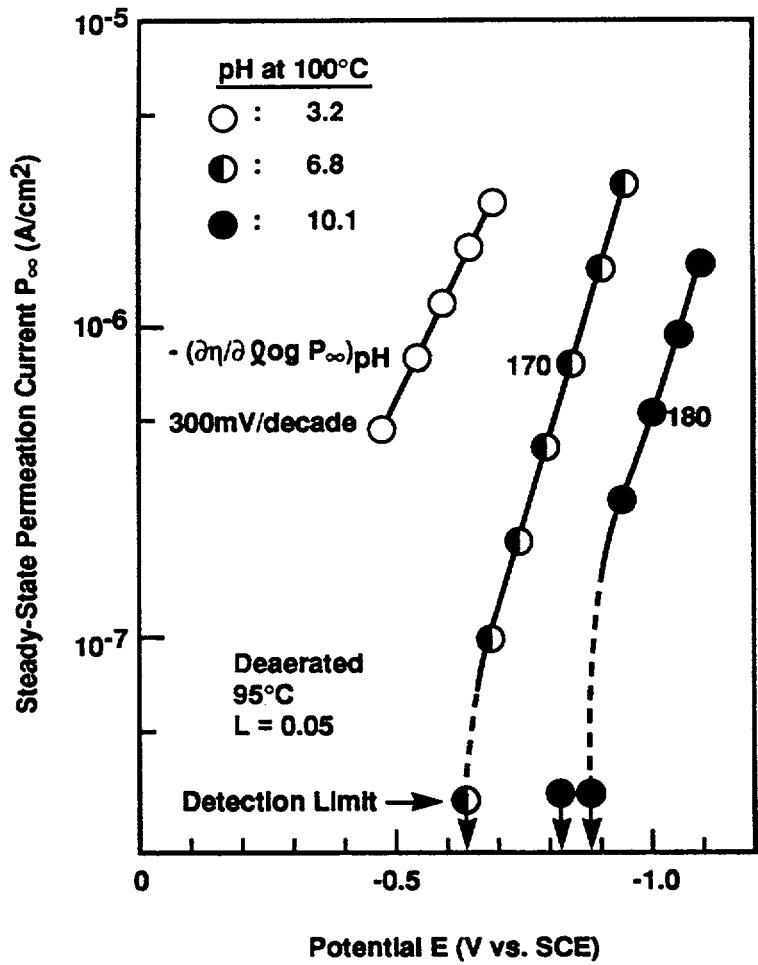


Figure 3. Steady-state permeation current-potential relationships for type 304 stainless steel membrane in 0.05 M Na₂SO₄ solutions of different pH at 95°C (potentiostatic experiments). (Ohnaka, 1990)

2.3 Microbiologically Influenced Hydrogen Evolution

Some microorganisms have been shown to generate hydrogen (Walch, 1989; Ford, 1990). As shown in Figure 4, growth of the organism, *Clostridium Acetobutylicum*, on one surface of a steel sample (top solid line with circular points) corresponds with an increase in permeation current (bottom line) measured on the other surface of the steel sample. This increase in permeation current did not occur in the presence of a non-hydrogen producing bacterium, *Clostridium Limosum*, or with *Desulfovibrio Desulfuricans ssp. Astuarii*. The permeation current densities, about $10 \mu\text{A}/\text{cm}^2$, can be considered significant, although the data shown by Walch et al. exhibits high background current densities. The hydrogen producing bacterium has to be maintained in an anoxic medium, whereas the environmental conditions in the repository are aerobic. However, anoxic conditions can exist underneath biofilms which themselves may survive in aerobic conditions. An additional factor that needs to be evaluated is the survivability of this or other hydrogen producing strains in the radiation and thermal field. Hence, further information is needed before considering microorganisms to be important sources of hydrogen.

2.4 Radiolysis Products

Ionizing radiations produce activated neutral species as well as ions and free radicals. In aqueous systems, such species include, among others, $\text{H}\cdot$, $\text{OH}\cdot$, H^+ , OH^- , e_{aq}^- , and H_2O_2 . The steady state concentrations of various species depend among many factors on pH, aeration, temperature, and concentration of solute species such as Cl^- , Fe^{2+} , etc. The effect of pH on the yield of radiolytic products in water a short time after radiation (10^{-7} sec) is shown in Figure 5 (Spinks, 1990). This figure (approximate dose rate of 3.6×10^5 rads/hr or 1 Gy/sec) indicates that in near neutral solutions, e_{aq}^- (solvated electrons), $\text{OH}\cdot$ (hydroxyl radical), and H_2O_2 dominate. In the presence of aeration, both solvated electrons and hydrogen radicals will be converted to hydrogen peroxide which will be the predominant species (Spinks, 1990). A further confirmation of this analysis is the measurement of open-circuit potential (Glass, 1986) of type 316L stainless steel in J-13 water while it was exposed to gamma irradiation (dose rate: 3.3×10^6 rad/hr or 9.2 Gy/sec), which showed that potential increased by about 200 mV. This increase in potential is due to the presence of an oxidizing species and was simulated in separate experiments without irradiation by the addition of H_2O_2 . Kim and Oriani (Kim, 1987b) examined the open-circuit behavior of Grade-12 Ti in a deaerated brine solution and found a similar increase in open-circuit potential that could be simulated by the addition of H_2O_2 . Increase in redox potential of brine environments by gamma irradiation has also been documented by Gray (Gray, 1988). The formation of chlorine from chloride has been indicated by Spinks and Wood (Spinks, 1990) but has not been reported by the foregoing investigations in brine environments.

The effect of gamma radiation on hydrogen uptake by Grade-12 Ti was also investigated by Kim and Oriani (Kim, 1987a, b), and their results are reproduced in Figures 6 and 7. In Figure 6, it can be seen that gamma irradiation (dose rate: 0.42 Gy/sec) reduced the absorbed hydrogen concentration. Similar reduction was also noted in an unirradiated environment when H_2O_2 was added to the solution or when the solution was purged with H_2 or O_2 (Figure 7). The authors hypothesized that the reduction in hydrogen absorption due to irradiation was due to the reduction in concentration of $\text{H}\cdot$ (hydrogen radical) by conversion to H_2 , and H_2O_2 . The presence of H_2O_2 also acted to reduce the electrolytic generation of hydrogen by increasing the corrosion potential.

Radiolysis of water vapor plus air mixtures have been reviewed by Reed et al. (Reed, 1988). In the presence of both nitrogen and oxygen, nitric acid is the predominant species. While these authors did not indicate the yield of hydrogen radical in these systems, it can be assumed to be negligible. In any case, presence of nitric acid can be expected to increase the redox potential, and thus preclude electrolytic

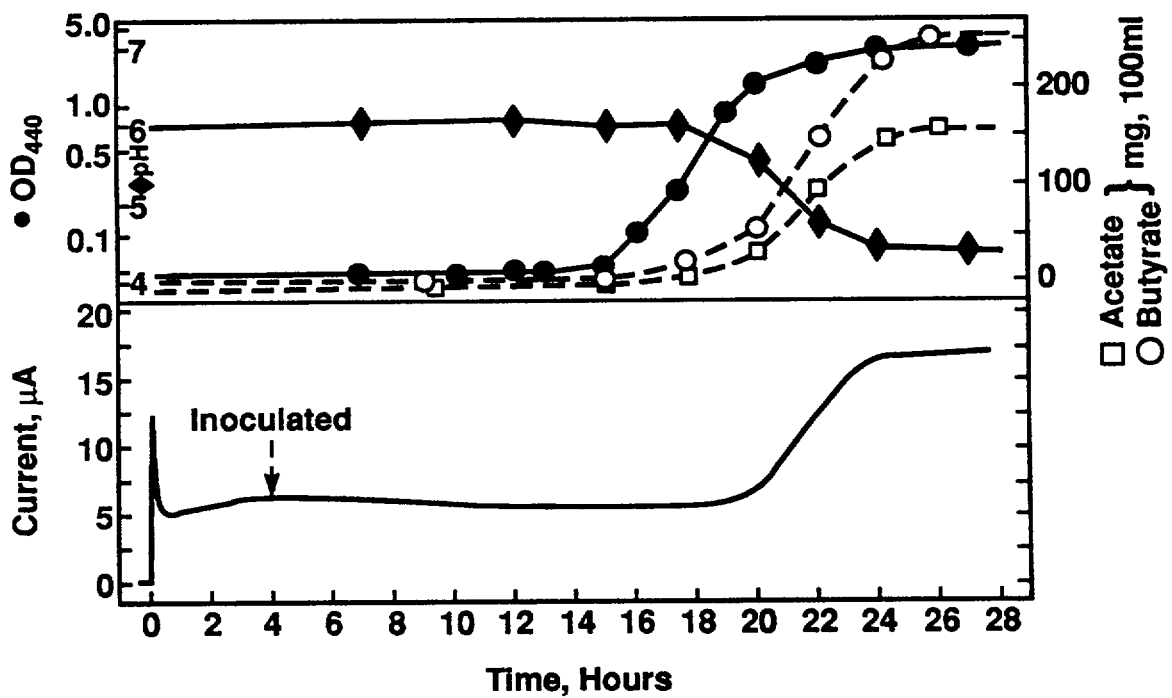


Figure 4. Hydrogen permeation current and culture parameters of a hydrogen-producing bacterium, *Clostridium acetobutylicum*. (Walch, 1989)

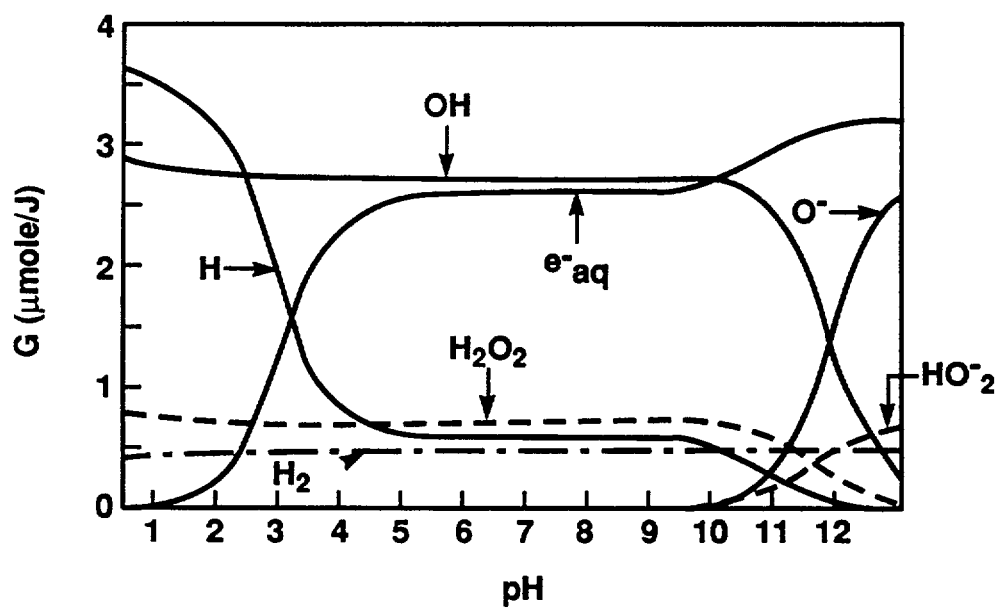


Figure 5. Effect of pH on the primary products of water irradiation. Yields are for γ or fast-electron radiation with energies of the order of 0.1 to 20 MeV, and assume that OH and H₂O₂ achieve acid-base equilibrium. (Spinks, 1990)

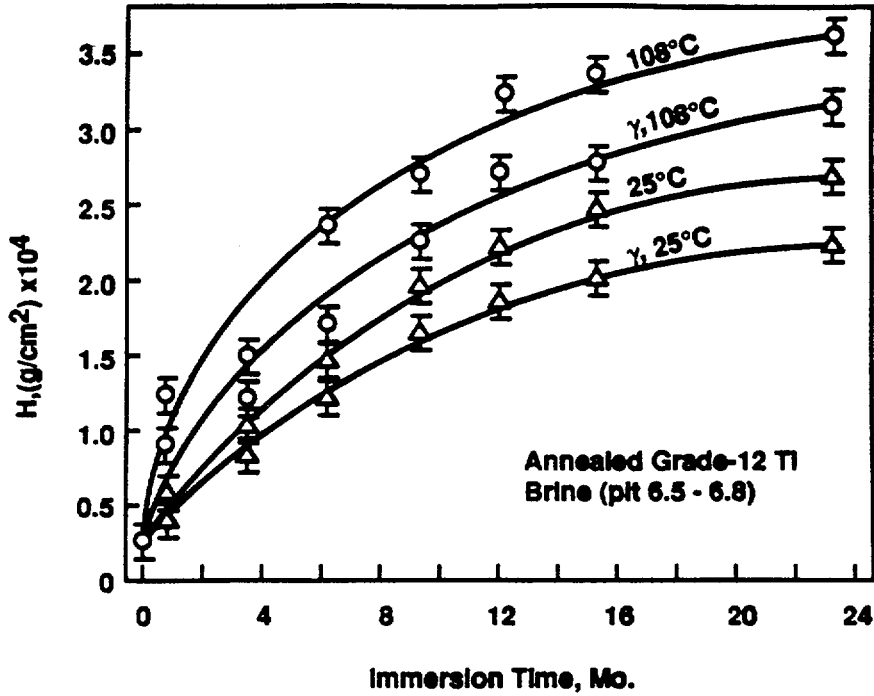


Figure 6. Hydrogen take-up by annealed Grade 12 Ti in brine vs. immersion time (month) calculated on the basis of metal surface area (γ signifies gamma radiation). (Kim, 1987a)

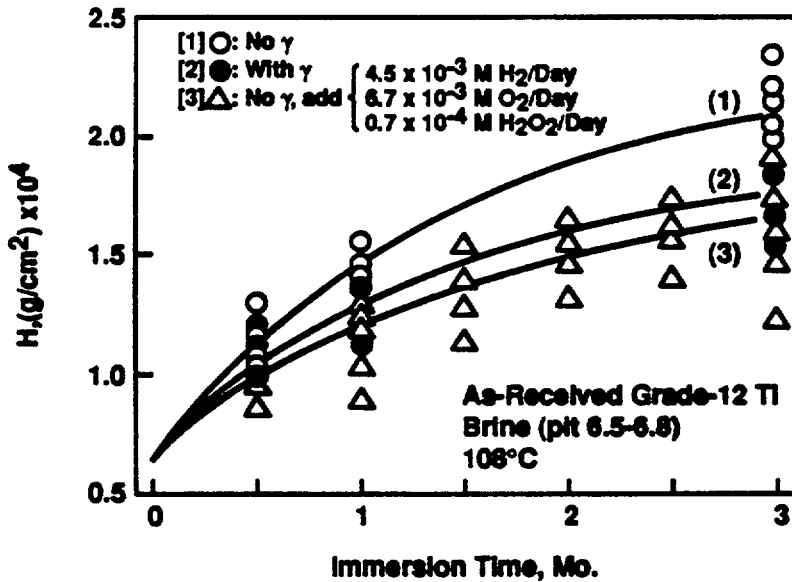


Figure 7. Effect of additions of H_2 , O_2 , and H_2O_2 together on the hydrogen take-up by as-received Grade 12 Ti in brine at 108°C . (Kim, 1987b)

evolution of hydrogen. Additionally, nitric acid may be expected to strengthen the passive film of stainless alloys, thus decreasing permeation of hydrogen further.

From the foregoing discussion, it is clear that radiolytic generation of hydrogen radical in aqueous solutions, water vapor, and two-phase mixtures will be minimal. However, in creviced areas, acidic conditions and lack of oxygen (which is consumed by corrosion reactions) may favor hydrogen radical generation and this needs to be examined further.

3. HYDROGEN EMBRITTLEMENT OF CANDIDATE CONTAINER ALLOYS

Embrittlement due to hydrogen can manifest itself in a variety of ways. These include embrittlement due to: absorbed atomic hydrogen (usually called hydrogen embrittlement), hydride formation in reactive materials such as Ti, Nb, Ta, and Zr, absorbed hydrogen which reacts with carbides or oxides to create internal methane or steam bubbles (called hydrogen attack or hydrogen sickness), and pressure build-up from formation of molecular hydrogen in internal cavities. Embrittlement due to absorbed atomic hydrogen, termed from here on as hydrogen embrittlement, is the focus of this report. While hydride formation has been claimed to be the cause of embrittlement in Ni-base alloys, it has not been established unequivocally nor is it necessary to consider it as a separate phenomenon for the current candidate materials. Hydrogen attack is more important in higher carbon materials than in the austenitic alloys currently being considered, at least in the temperatures that are anticipated to prevail in the repository. However, because of the long time periods involved, it cannot be ruled out as a possible embrittlement mechanism. It will be considered in future reports. "Hydrogen sickness" has been the subject of considerable research in tough-pitch copper which contains numerous oxide inclusions (Gdowski, 1988). It is not expected to be an important failure mode in oxygen-free copper such as CDA-102.

The extent of research activities on hydrogen embrittlement of stainless steels and Ni-base alloys in the past 40 years has been considerable, though much of this effort has been directed towards phenomenological understanding and design considerations rather than long-term prediction. Copper and its alloys, with the exception of some precipitation hardenable alloys, have not been examined as extensively, a testimony towards their greater resistance to hydrogen embrittlement. This is demonstrated in Figure 8 for a series of Ni-Fe and Ni-Cu alloys. Addition of Fe to Ni improves the resistance to embrittlement, but once the crystal structure changes from face centered cubic (fcc) to body centered cubic (bcc), hydrogen embrittlement resistance decreases dramatically. On the other hand, addition of copper increases the resistance to hydrogen embrittlement monotonically. The effect of environmental and microstructural variables on hydrogen embrittlement of these two classes of alloys is discussed in the following sections.

3.1 Hydrogen Embrittlement of Stainless Steels and Ni-base Alloys

3.1.1 Role of Environmental Variables

The three most important environmental variables affecting hydrogen embrittlement are the surface hydrogen fugacity (cathodic charging current density in the case of electrolytic source of hydrogen), presence of recombination "poisons" (e.g. S, P, As, Sb, Sn), and temperature. Other environmental variables that can affect embrittlement include presence of oxidizing species that can either reduce cathodic hydrogen current or increase resistance of passive film to entry of hydrogen. In this section, only the first three environmental factors are considered.

Hydrogen Fugacity: The effect of gaseous hydrogen pressure on embrittlement has been examined with respect to high-strength steels and Ni-base alloys. Generally, a steep dependence on pressure is noted at low pressures, followed by a region of cracking that is independent of pressure. This is illustrated for a Ni-base, precipitation hardenable alloy, alloy 718 (18% Cr-3% Mo-5% Nb), in Figure 9. In the case of embrittlement by electrolytic charging of hydrogen, a monotonic decrease in time to failure or increase in crack growth rate with charging current density has been noted. For example, in alloy C-276 (Ni-16Cr-16Mo-4W), the stage-II crack growth rate (stress-intensity independent

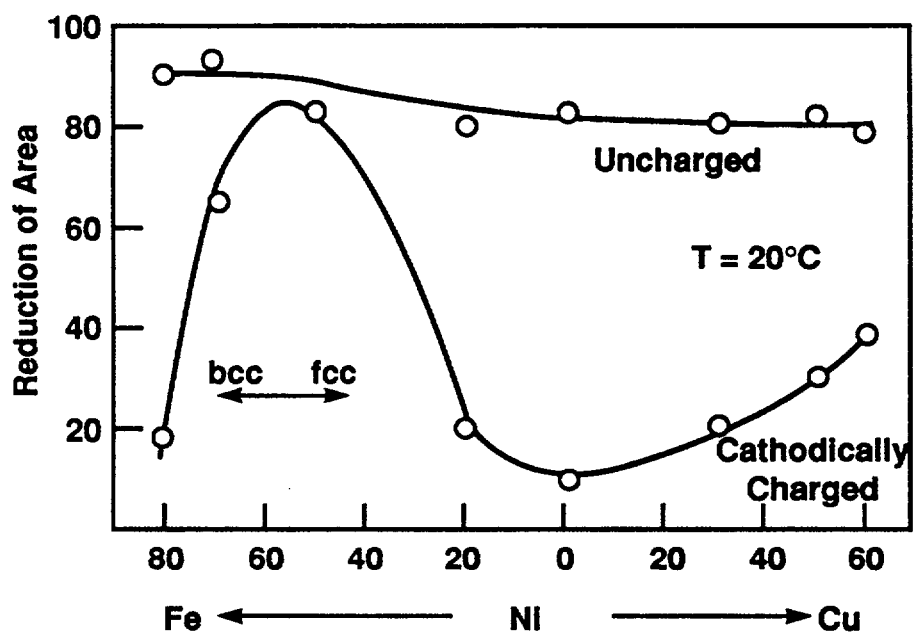


Figure 8. Fracture behavior of cathodically-charged nickel, containing Fe or Cu. (Smith, 1974)

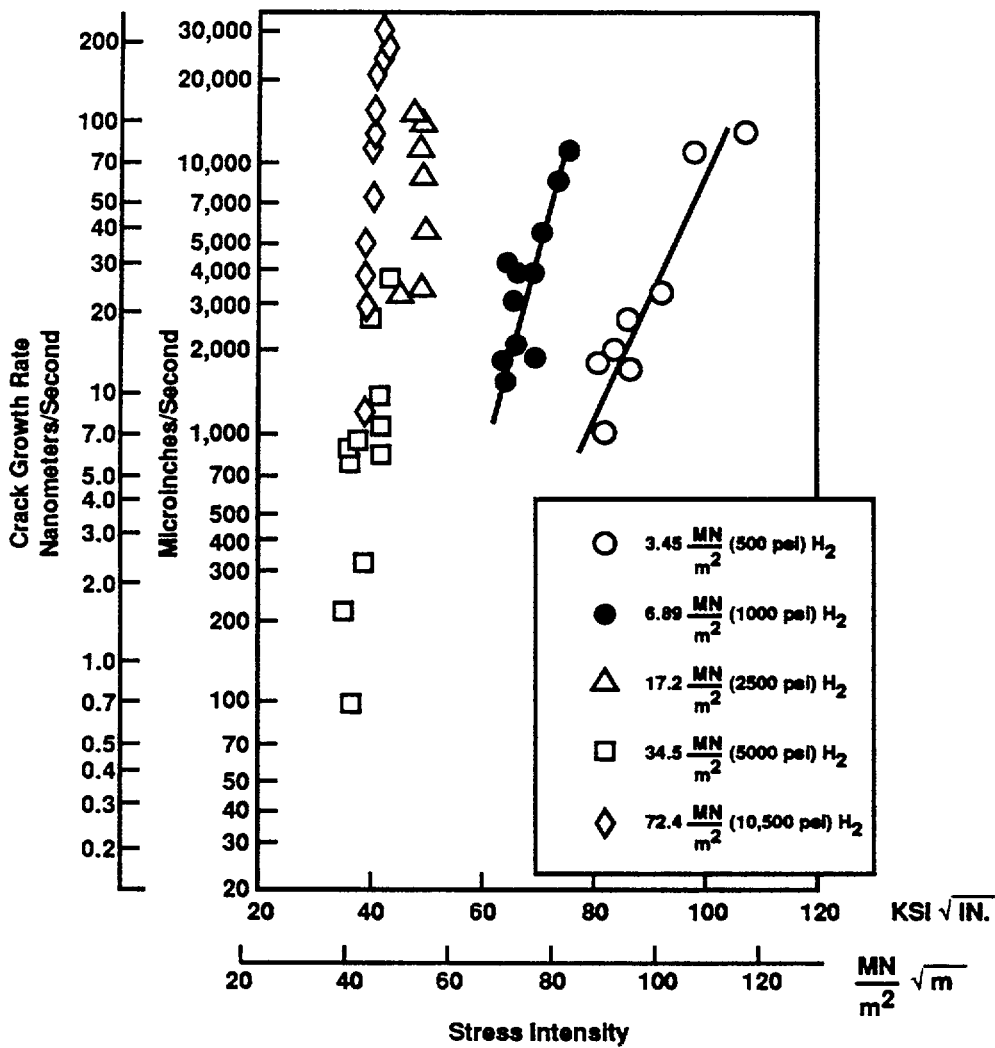


Figure 9. Sustained load crack growth rate in Inconel 718 TDCB specimens as a function of stress intensity at various hydrogen pressures. Temperature: Room temperature. (Walter, 1973)

cracking) increases with cathodic current density as shown in Figure 10. Longer times and lower current densities have been studied by Kane (Kane, 1978) for many Ni and Co-base alloys. Some of his data are shown in Figure 11. Two points are worthy of note in this figure: 1) alloy G which contains higher iron (20% Fe) is much more resistant to cracking than alloy 625 (3% Fe) and 2) at current densities typical of cathodic coupling with carbon steel, cracking can occur at room temperature within a relatively short time provided the applied stresses approach the 0.2% yield strength.

Recombination Poisons: It is by now well established that minor concentrations of impurities in the environment or alloy can greatly influence the entry of hydrogen into the metal. It is not the intent to review the rather extensive literature available in this area (for example, McCright, 1977). Typically, these poisons aid entry of adsorbed hydrogen into the metal by inhibiting the recombination of hydrogen adatoms to form hydrogen gas which can then escape. In sour gas environments, for example, hydrogen permeation has been shown to be increased by the presence of H₂S (Kane, 1985). Such recombination poisons are not known to be present in the repository environment. The effect of impurity elements present inside the alloy is much more debatable. Many investigators have shown that presence of alloying impurities such as P (Berkowitz, 1980), Sb and Sn (Latanision, 1973), and S (Jones, 1980) cause increased embrittlement of austenitic stainless steels and Ni-base alloys. The cause of the increased embrittlement has been hypothesized to be either due to the direct action of these impurities on grain-boundary cohesion or indirectly due to their enhancement of hydrogen entry in the metal. From the high-level waste container point of view, the interest in these impurities is in their segregation to grain boundaries due to prolonged exposure to temperatures in the range of 200 - 300°C (Berkowitz, 1980).

Effect of Temperature: Hydrogen embrittlement has been known to decrease with an increase in temperature from the earliest investigations of this phenomenon. In high-strength steels, embrittlement has been shown to have a three stage behavior: at low temperatures below about 0°C, embrittlement increases with temperature; at intermediate temperatures around 0°C, there is a plateau region followed by a decrease in embrittlement with an increase in temperature (Williams, 1969; Wei, 1985). A classic example of this type of behavior is illustrated in Figure 12 (Williams, 1969). The temperature at which maximum embrittlement is observed depends on the composition and microstructure of the alloy. Though Williams and Nelson rationalized this three stage behavior in terms of hydrogen adsorption kinetics, other explanations based on a multiplicity of rate controlling processes have been advanced (Wei, 1985). For example, in the low temperature regime, the embrittlement can be transport controlled, and hence increasing the temperature results in greater availability of hydrogen to the critical stress region (e.g. plastic zone/elastic region transition area). In the higher temperature regime, the rate of accumulation of incoming hydrogen at these sites may be offset by the rate of diffusion away from these sites. In austenitic materials with a face centered cubic crystal structure, the diffusivity of hydrogen is low, and hence diffusion enhanced by the movement of dislocations has been proposed. In this case, increasing the temperature can be shown to result in less accumulation of hydrogen at the dislocation site, and hence less embrittlement. In the case of Ni-base alloys, the three-stage behavior has not been observed, perhaps because sufficiently low temperatures have not been explored. However, the decrease in cracking tendency with an increase in temperature has been reported in many alloy systems. This is illustrated for a Ni-Cr-Mo-W alloy in an H₂S-containing environment (Figure 13) and for Ni-30%Cu alloy under cathodic hydrogen charging conditions in a sulfuric acid solution (Figure 14). In contrast, stress corrosion cracking in chloride and Cl + H₂S environments, which is thought to occur by localized, stress-assisted anodic dissolution mechanisms, increases with an increase in temperature (e.g. Vaughn, 1980).

From the above discussion, the degree of hydrogen embrittlement may be reduced significantly by the high temperatures expected to prevail in the repository. It must be emphasized,

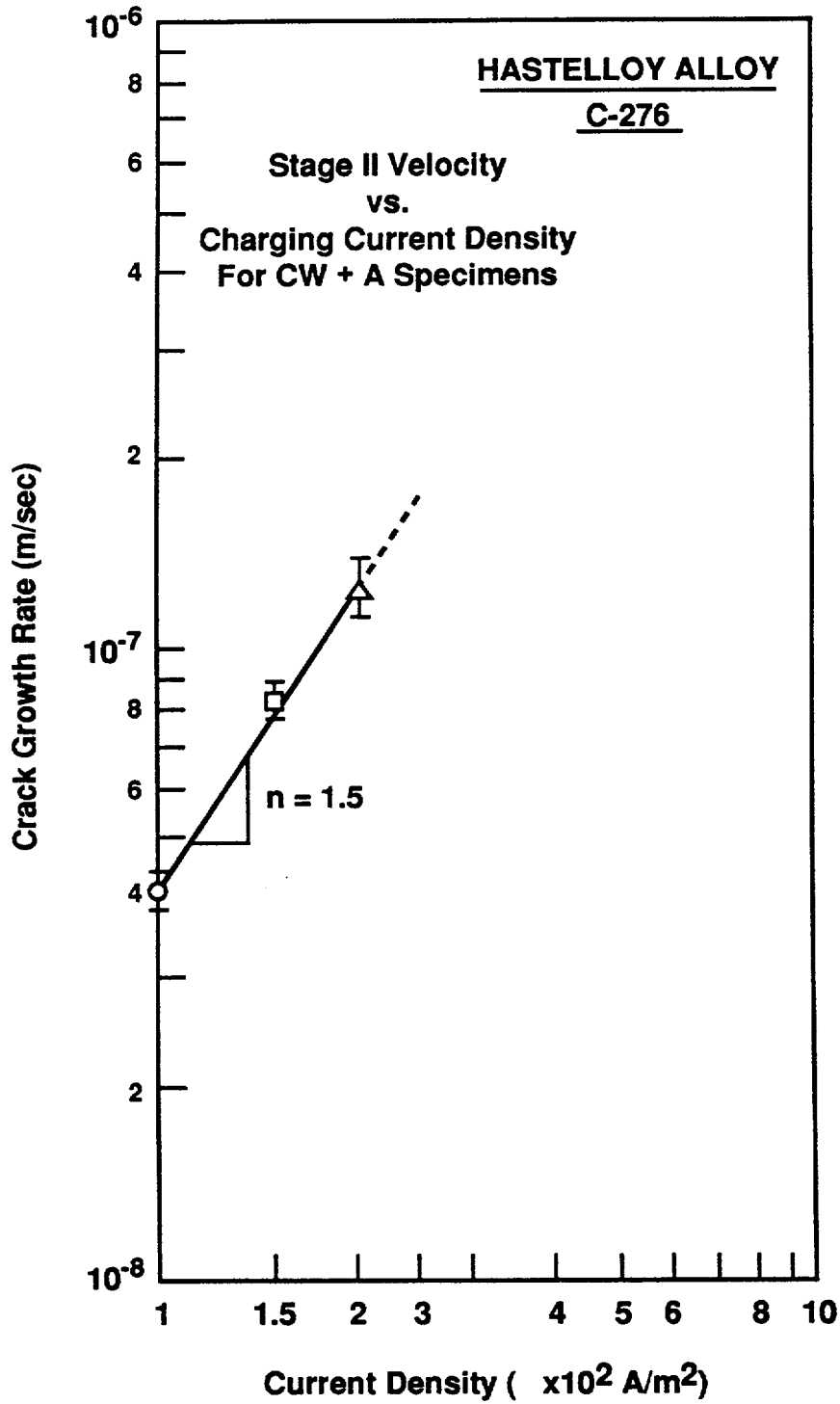


Figure 10. Stage II (stress-intensity independent) crack velocity as a function of charging current density. Temperature: Room temperature. (Sridhar, 1980)

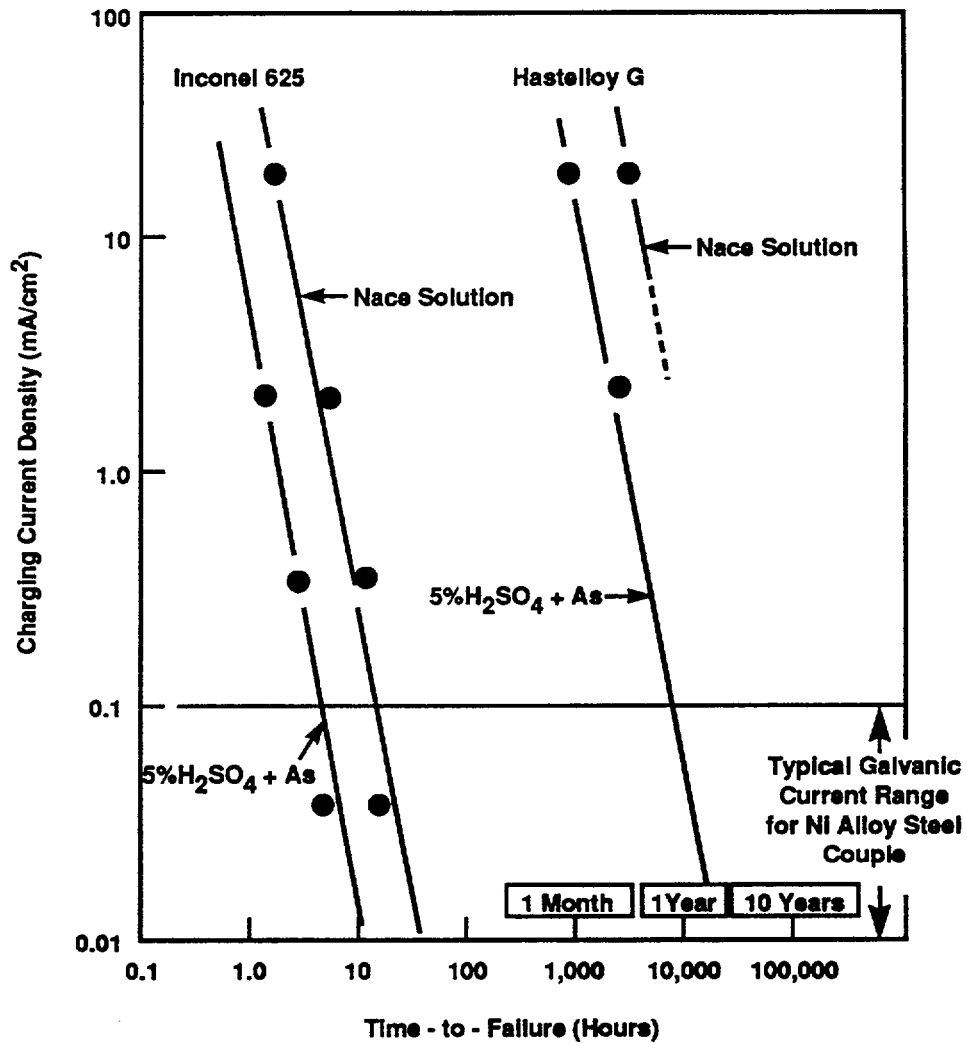


Figure 11. Effect of test environment and charging current density on the failure time of stressed C-ring specimens of Inconel 625 [59% CR + 932 F (500 C)/50 hours] and Hastelloy G [59% CR + 500 F (260 C)/250 hours]. Temperature: Room temperature. Stress: 100Y. Yield. (Kane, 1978)

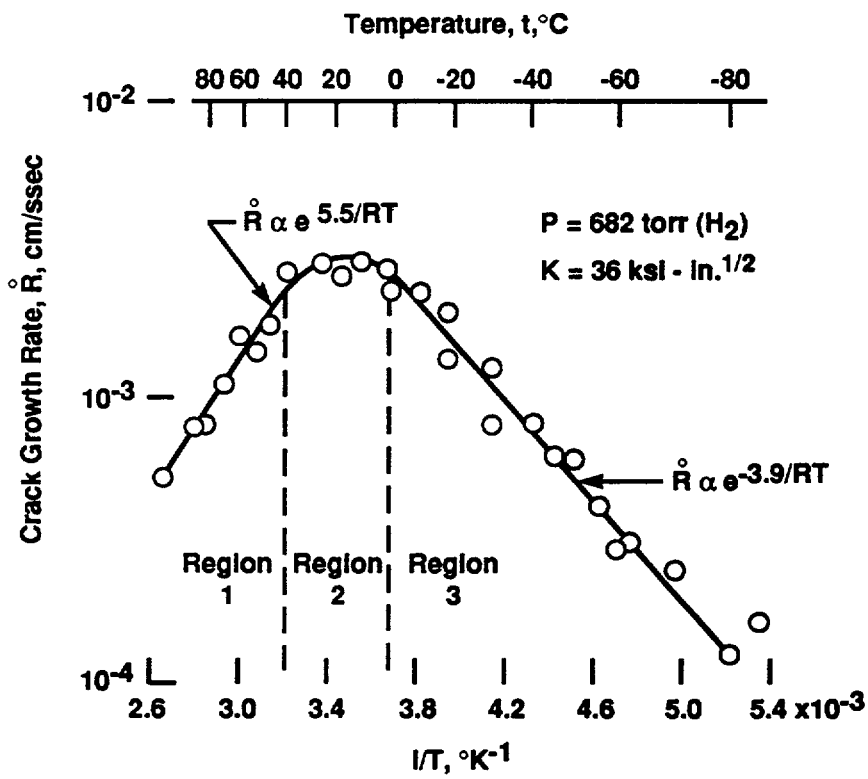


Figure 12. Temperature dependence of the slow-crack-growth rate of 4130 steel. (Williams, 1969)

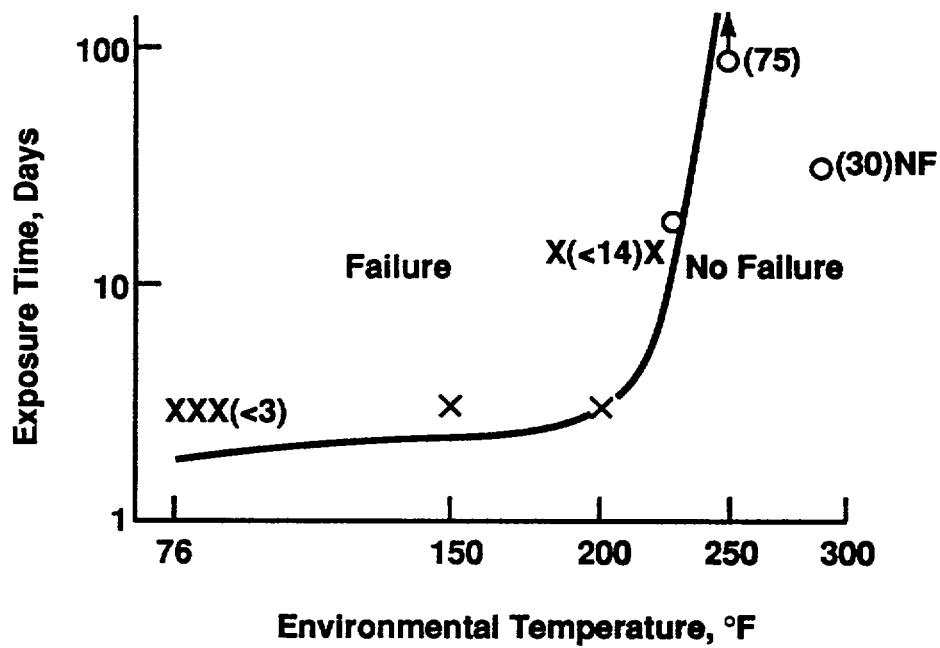


Figure 13. Effect of environmental temperature on HE of Hastelloy alloy C-276. Environment: 4% NaCl + 0.5% CH₃COOH + H₂S (1 atm), coupled to carbon steel. Stressed to 90% yield. Alloy aged: 500 C/100 hours.

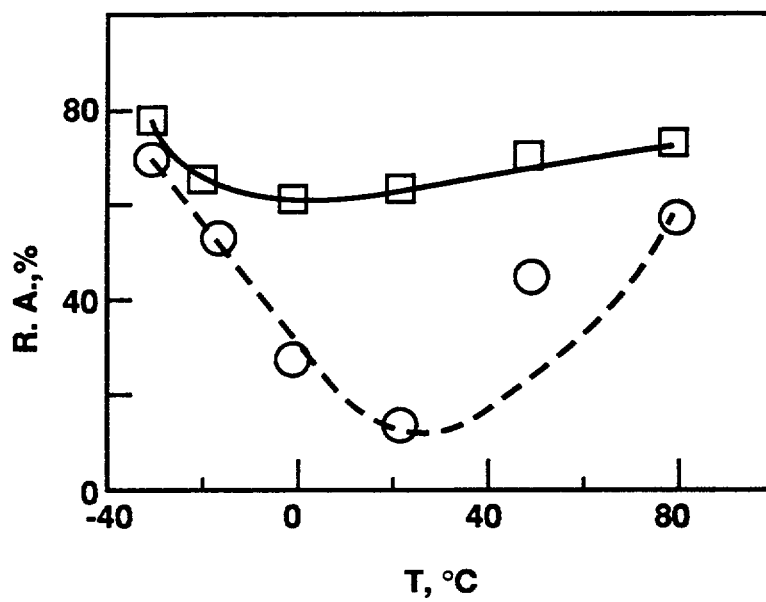


Figure 14. The reduction in area at fracture of Monel 400 tested in the presence of hydrogen. (Price, 1985)

- - $1.6 \times 10^3 \text{ sec}^{-1}$
- - $1.6 \times 10^5 \text{ sec}^{-1}$

however, just as in other degradation processes, that the data suggesting lack of embrittlement at higher temperatures are relatively short term in nature. Modeling of the rate controlling processes of hydrogen embrittlement in combination with experimental data may be needed to predict the long term behavior. Such models have been advanced for steels (e.g. Wei, 1985, Wei, 1990), and for metastable austenitic alloys (Singh, 1982). A critical review of the available models of hydrogen embrittlement and their limitations will be provided in a future report.

3.1.2 Role of Microstructure

The most important microstructural feature governing the hydrogen embrittlement susceptibility in austenitic alloys and Ni-base alloys is the deformation mode. Other microstructural factors affecting embrittlement include grain size, segregation of impurities, inclusions and second phase particles, and grain boundary precipitation of carbides or intermetallic phases. The last factor, while important for stress corrosion cracking and intergranular corrosion, is less significant for hydrogen embrittlement.

Deformation mode is controlled by alloy composition and precipitation of coherent phases and, in turn, controls formation of secondary phases during plastic deformation. Plastic deformation can occur either in a planar mode in which the dislocation motion occurs along certain preferred combinations of crystallographic planes (slip planes) and directions or by extensive cross-slip in which dislocations can "circumvent" obstacles in a given slip plane by moving on to another slip plane which intersects the original slip plane on which the dislocation was moving. It is not the intent here to describe the dislocation dynamics in a detailed manner, and the interested reader is referred to other sources (e.g. Hirth, 1982). One consequence of planar deformation mode is the pile-up of dislocations at an obstacle, such as a grain boundary, resulting in the build-up of stress concentrations. This is shown in a rather simplistic manner in Figure 15. If cross-slip were to occur, the stress concentration will be relieved by the movement of dislocations onto another slip plane. Another consequence of planar deformation mode in the case of hydrogen embrittlement is the dislocation assisted transport of hydrogen. Tensile triaxial stresses associated with dislocations can result in the segregation of hydrogen at dislocations. This has been verified visually by autoradiographic images of tritium segregation to triaxially stressed regions at crack tips and, indirectly, by observations of hydrogen trapping in heavily cold-worked metals containing numerous dislocations. Motion of dislocations upon plastic deformation causes migration of the associated hydrogen cloud which can result in greater penetration than by diffusion alone. While this mechanism has not been universally accepted, dislocation drag of hydrogen can explain many of the observations related to the effects of strain rate, temperature and deformation mode on embrittlement. For example, if dislocation motion enhances the penetration of hydrogen to critically strained regions, then planar deformation would tend to enhance the accumulation of hydrogen at these regions compared to cross-slip deformation which would tend to carry away hydrogen as much as bring hydrogen to these locations. This mechanism of dislocation assisted/enhanced transport of hydrogen is not universally accepted, however (Zakrocymski, 1985). As indicated in Appendix B, Part 3, Figure 36, plastic straining of alloy C-22 did not increase the permeability of hydrogen. The effect of test techniques on observation of dislocation transport must be examined since observations favoring dislocation transport have come from a variety of techniques including electrochemical permeation studies, whereas the only observations disfavoring dislocation transport have come from electrochemical permeation tests. Whether one accepts this mechanism or not, it has been shown rather conclusively that materials within the same class suffer greater hydrogen embrittlement (and stress corrosion cracking) if they deform by planar slip (Thompson, 1976).

Planar slip can be brought about by a number of factors such as low stacking fault energy (SFE), precipitation of coherent phases, short and long-range ordering, clustering, and low temperature.

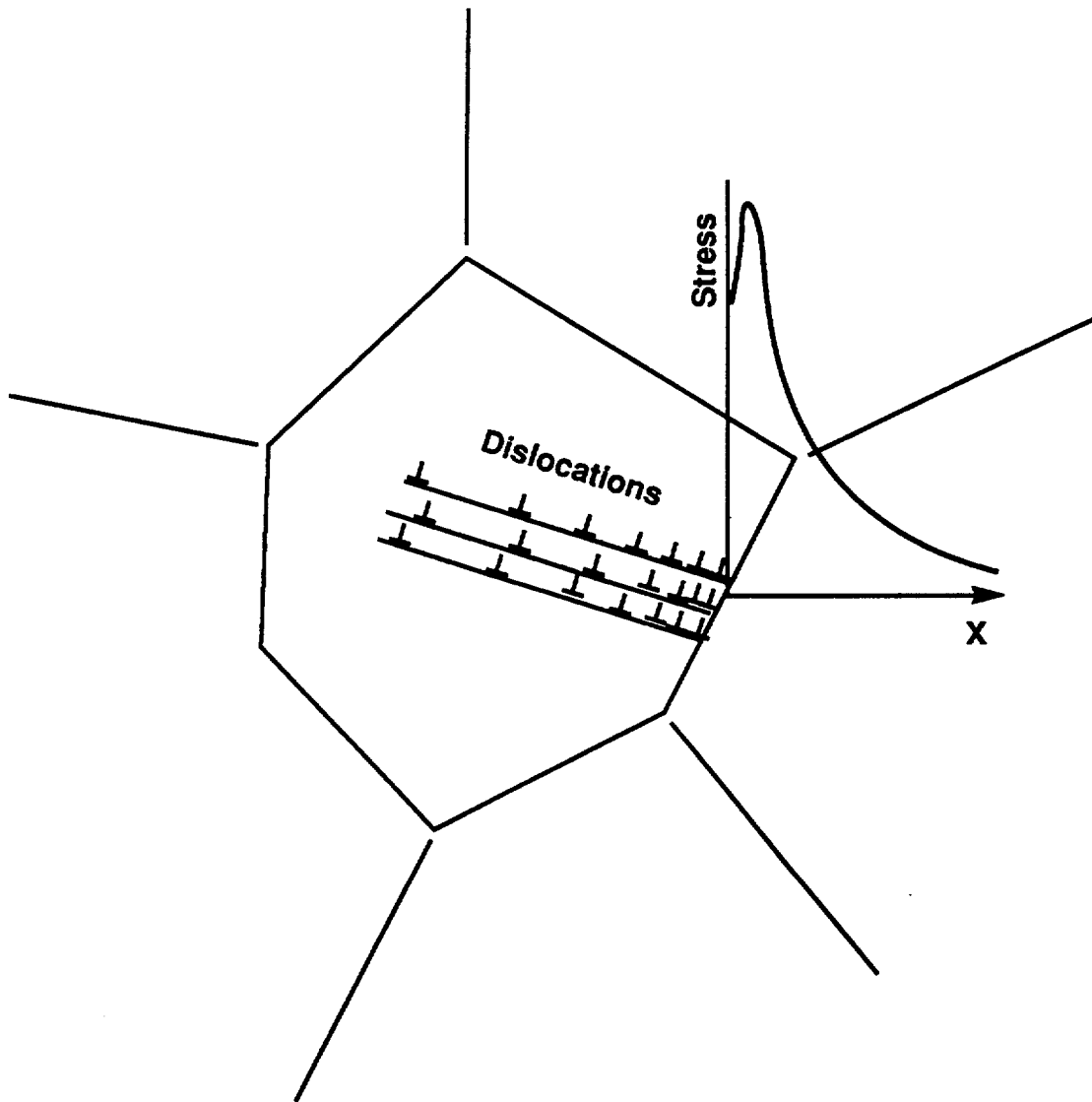


Figure 15. Illustration of a pile-up of dislocation (represented by \perp) at a grain boundary causing a stress concentration.

Stacking faults, which are planar defects contained by two dislocations, force planar deformation mode because cross-slip would entail creation of new interfaces on other slip planes, thus requiring greater energy. Decreasing stacking fault energy results in greater planarity of deformation. The effect of decreasing fault energy on embrittlement in gaseous hydrogen is shown in Figure 16 for a number of austenitic stainless steels of varying Ni and Cr content. Similar relationships have also been reported for Ni-Co alloys and Cu-Al alloys. Precipitation of coherent precipitates (i.e. precipitates whose crystal plane spacing matches that of the parent crystal) also tends to force planar deformation. This occurs because once deformation initiates on a plane, the precipitate is cut, creating surfaces with other orientations which may not match up with the parent crystal planes. Creating new surfaces entails expenditure of energy, hence favoring continued deformation on the same plane rather than new planes. Thus, age-hardening in Ni-base alloys or Cu-base alloys causes coherent precipitation and planar deformation and leads to an increase in embrittlement. Similarly, precipitation of short- and long-range ordered domains can cause planarity of slip. This occurs in the Ni-base alloys containing low Fe upon prolonged exposure to low temperatures in the 200 - 500°C range. One such case is shown in Figure 17 for alloy C-276. The behavior of alloy C-22 is similar to alloy C-276 in hydrogen. Addition of Fe to Ni-base alloy beyond about 10% suppresses ordering reactions considerably, and hence low-temperature aging has much less effect on hydrogen embrittlement in alloys such as alloy G (Kargol, 1982) and alloy 825. Since segregation of deleterious impurities such as phosphorus also occurs in this temperature range, the effects of ordering and segregation cannot be separated in the low-Fe alloys. However, the available data indicates that segregation has less deleterious effects than ordering. From a repository point of view, the higher Fe containing Ni-base alloys (e.g. 825, G, G-3, etc.) are less susceptible to hydrogen embrittlement and low-temperature aging than the low-Fe containing alloys (e.g. C-276, C-22, 625). This is further demonstrated by the data shown in Appendix B, Part 3, Table 8.

In the case of the austenitic stainless steels, it is well established that the stainless steels that are marginally stable are the ones that are more susceptible to hydrogen embrittlement (e.g. Singh, 1982). In these stainless steels, plastic deformation induces formation of martensite, with the low stacking fault energy alloys having a greater tendency to form martensite. While the role of the martensite has not been clarified, steels with deformation-induced martensite have been shown to exhibit greater susceptibility to hydrogen embrittlement. Thus, type 304 stainless steel is more susceptible to hydrogen embrittlement than type 310 or 316 stainless steels.

3.2 Copper Based Alloys

It has been mentioned that the addition of copper to nickel increases the resistance to hydrogen embrittlement (Figure 8). Hydrogen embrittlement of commercially pure copper has not been investigated extensively, with the exception of the hydrogen reaction with oxide inclusions. This is further confirmed by tests in 34.5 MPa (5000 psi) hydrogen gas where oxygen-free copper did not exhibit any loss of ductility in comparison to the test in an inert environment (He) while alloy 625 (Ni-21Cr-9Mo) which exhibited a 64% reduction in ductility (Walter, 1973). Similar resistance of copper and Cu-Al alloy in 69 MPa (10,000 psi) hydrogen gas has been indicated by others (Louthan, 1976). However, high pressures of 69 MPa (10,000 psi) of hydrogen have been shown to induce a change in fracture morphology of oxygen-free copper alloys (Vennett, 1969). Similar data is not available for the Cu-Ni alloys (Gdowski, 1988). However, one area of concern that has not been addressed is the effect of iron-rich particles that are present in commercial Cu-Ni alloy (e.g. CDA 715) and their potential growth during thermal exposure on hydrogen embrittlement. It is also surprising to encounter lack of hydrogen embrittlement in Cu-Al alloys because addition of Al to copper has been shown to decrease the stacking fault energy drastically (Gallagher, 1970). The high resistance to embrittlement by the Cu-based alloys may be partly related to their low permeability to hydrogen, which is discussed in the next section.

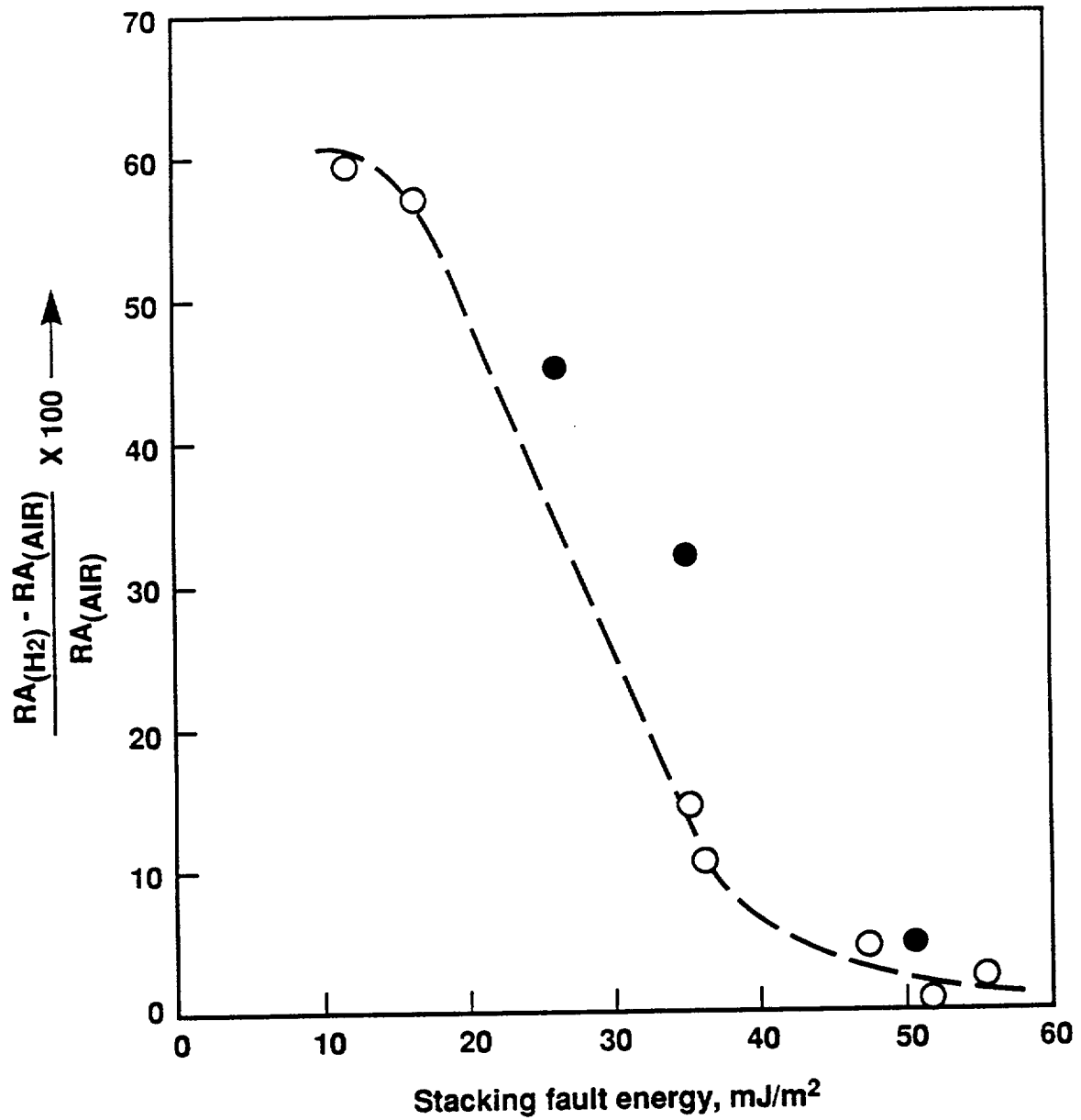


Figure 16. Correlation of RA loss in gaseous hydrogen (69 MPa) with SFE, using data from several sources. Filled points are for nitrogen-containing steels.

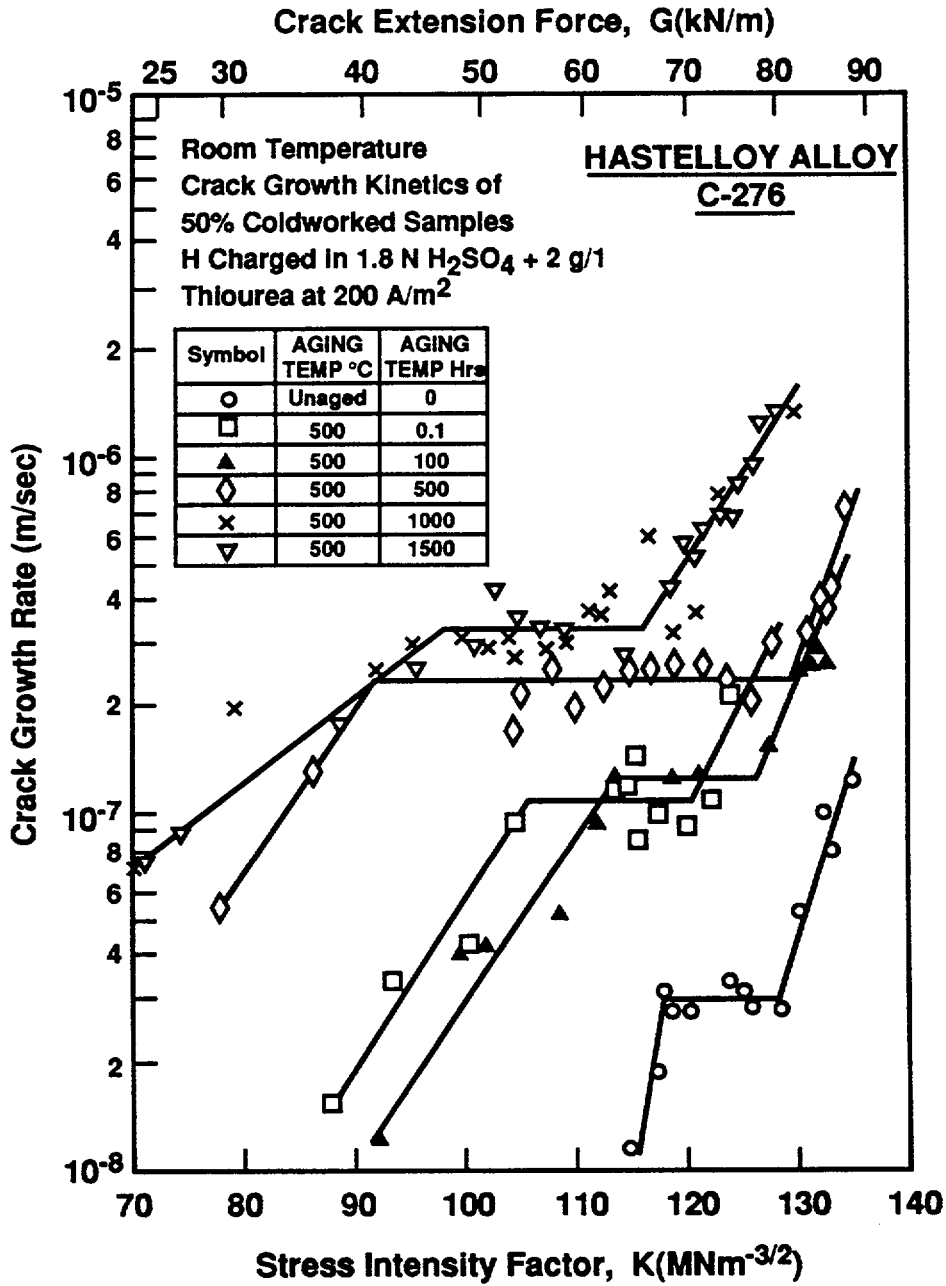


Figure 17. v - K curves of C-276 as a function of aging time at 500°C. (Sridhar, 1980)

4. A REVIEW OF HYDROGEN PERMEATION DATA

The focus of the research program at the FCC was establishing test techniques and generating some initial data on the kinetics of hydrogen permeation at various temperatures. Description of the electrochemical permeation technique and the permeation data on some of the candidate alloys are given in the final report from the FCC (Appendix B). The emphasis on the FCC investigations has been on measuring Θ , the fractional of surface covered by hydrogen that will be absorbed. Diffusivities of hydrogen for various alloys have been calculated, but the technique for obtaining these values has not been described. Appendix A describes methods to obtain diffusivities and solubilities of hydrogen from permeation transients. The following sections provide further information from the literature that support and amplify the findings of research performed at the FCC.

4.1 Austenitic Stainless Steels and Ni-base Alloys

The diffusion coefficients for hydrogen in pure metals Fe and Ni have been assembled and evaluated by Völkl and Alefeld (Völkl, 1978). The lattice diffusivity of hydrogen in Ni is remarkably reproducible over a wide temperature range spanning from about 0°C to 1400°C. This is particularly noteworthy considering the multitude of test techniques used to measure diffusivity. The diffusivity for hydrogen in Ni follows the Arrhenius relationship given below:

$$D(\text{cm}^2/\text{sec}) = 4.8 \cdot 10^{-3} e^{-\frac{9690 \text{ cal/mole}}{RT}} \quad (1)$$

The diffusivity in Fe, however, has varied considerably (sometimes over 3 orders of magnitude) among investigators. This has been attributed to surface controlled processes which can affect the measurements (Völkl, 1985). Based on the number of data that agree with each other, the diffusivity up to about 600°C may be given as:

$$D(\text{cm}^2/\text{sec}) = 7.5 \cdot 10^{-4} e^{-\frac{2490 \text{ cal/mole}}{RT}} \quad (2)$$

Equations 1 and 2 indicate that diffusivity of hydrogen in the body centered cubic iron is considerably higher than that in the face centered cubic Ni. However, when Fe is added to Ni while maintaining a face centered cubic crystal structure (up to about 60% wt.), the diffusivity is lowered while the solubility is only slightly affected. The permeability, which is a product of diffusivity and solubility, is also lowered by the addition of Fe. This is shown for a number of binary Ni-Fe alloys (Beck, 1971) in Figure 18. Once the solubility limit for Fe in nickel is exceeded, body centered cubic phase starts precipitating and the diffusivity increases. This type of behavior has been verified by others in Ni-Fe alloys as well as Ni-Fe-Cr-Mo alloys (Thompson, 1976). The findings of the research at the FCC are in agreement with this since the diffusivity of alloy 825 calculated from the permeation rise transient (Appendix B, Part 1, Figure 22) at 95°C ($1.79 \times 10^{-10} \text{ cm}^2/\text{sec}$) is lower than that of alloy C-22 (Appendix B, Part 1, Figure 23) at the same temperature ($4.66 \times 10^{-10} \text{ cm}^2/\text{sec}$). The diffusivity of type 316L stainless steel from the permeation rise transient (Appendix B, Part 1, Figure 17) is found to be $1.94 \times 10^{-10} \text{ cm}^2/\text{sec}$. It must be noted that these values are somewhat lower than the values given in Table 5 of Appendix B, Part 3. In any case, the values from these measurements are in reasonable agreement with values reported for similar alloys in the literature. For example, Ohnaka and Furutani

(Ohnaka, 1990) measured a value of diffusivity for 304 stainless steel at 95°C to be 1.4×10^{-10} cm²/sec. Mezzanotte et al. (Mezzanotte, 1980) measured the value of diffusivity at 90°C for alloy C-276 (an alloy similar to alloy C-22) to be 7×10^{-10} cm²/sec.

From the perspective of hydrogen embrittlement, it may be tempting to conclude that the greater resistance of the higher-Fe containing Ni-base alloys is due to their lower diffusivity for hydrogen. Indeed, Coyle et al. (Coyle, 1977) constructed an index which they termed Hydrogen Affinity Index which was proportional to the solubility divided by the diffusivity. They showed that a Ni-base alloy containing 20% Fe (alloy G) had a higher affinity index (lower diffusivity, higher solubility) and concomitantly lower susceptibility to embrittlement to hydrogen than a 5%-Fe alloy (alloy C-276). However, this correlation should be used with care since the diffusivity and embrittlement are affected by many microstructural features. For example, in alloy C-276, long-term aging at 500°C results in lower diffusivity (Figure 19) but increased embrittlement (Figure 17).

4.2 Copper Based Alloys

Permeability data for copper and Cu-Al alloys were reported by Louthan (Louthan, 1976) in gaseous hydrogen system in the temperature range of room temperature to 730°C. Völkl and Alefeld (Völkl, 1978) report diffusivity data for copper for temperatures 400°C and above. From these data, the diffusivity of hydrogen in copper appears to be similar to that of Ni, while the permeability of hydrogen in copper is an order of magnitude lower than that of the austenitic materials. This indicates that the solubility of the copper base alloys for hydrogen is lower than the austenitic stainless steels and Ni-base alloys. This is confirmed by the data generated by B. Wilde et al. (Appendix B, Part 2). Caskey (Caskey, 1976) studied the effect of trapping and oxygen concentration on the measured diffusivity of hydrogen in copper. He showed that the measured permeation transient, even in oxygen free copper (O₂ content of 10 ppm) is critically dependant on the repetition of the test, i.e. the initial permeation transients or initial anneal in hydrogen fill the traps and reduce the surface oxides, thus yielding a larger diffusivity. On the other hand, decay transients are quite reproducible because the traps have already been filled. The extent of tritium dissolved as a function of oxygen concentration is shown in Figure 20. This may explain some of the problems encountered by Wilde et al. (Appendix B, Part 2) in generating permeation transients in copper. Nevertheless, the solubility of hydrogen in copper is quite low compared to that of Ni-base alloys and probably accounts for part of its resistance to embrittlement by hydrogen.

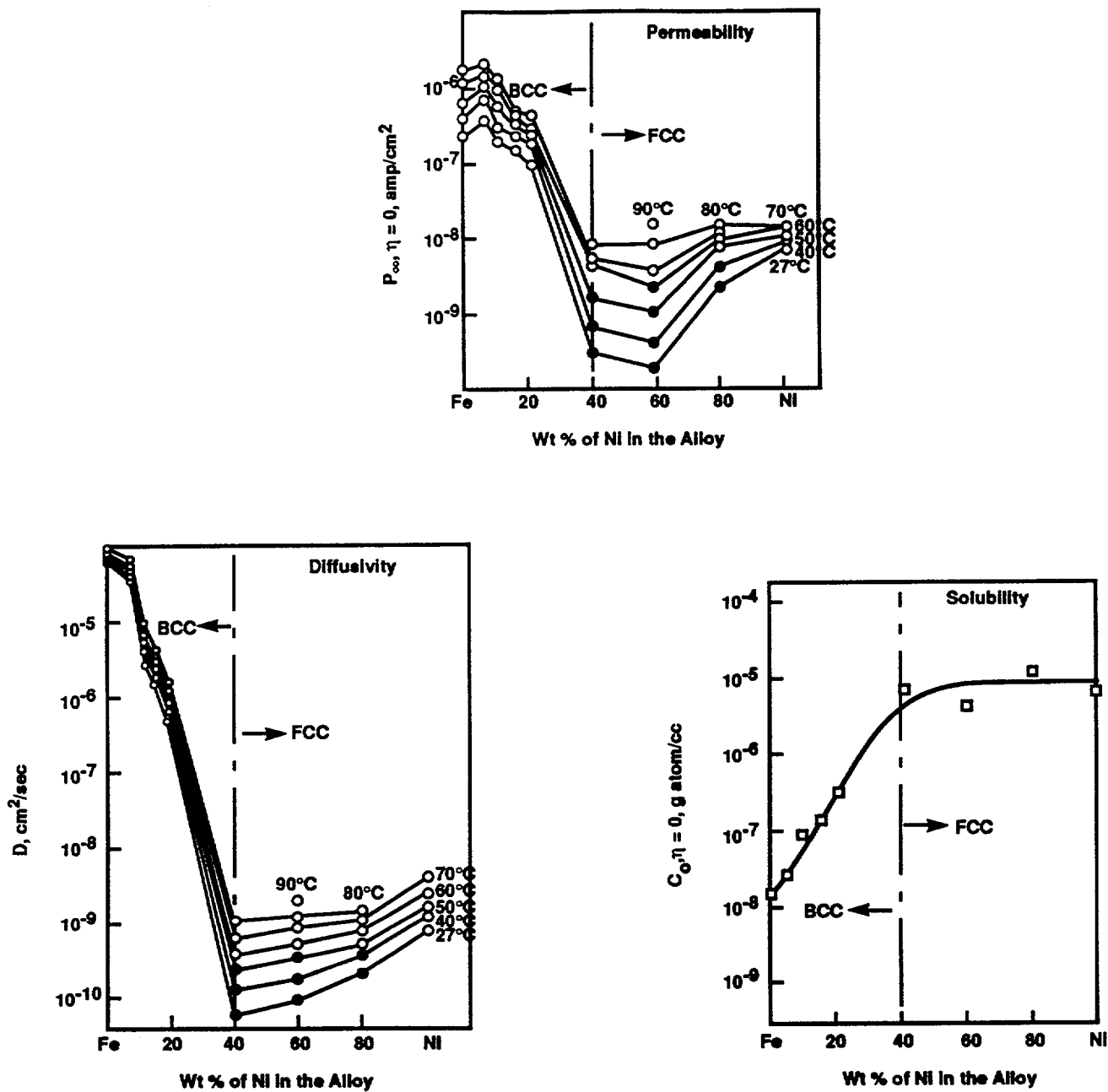


Figure 18. Effect of Fe addition to binary Ni-Fe alloys on permeability, diffusivity, and solubility of hydrogen. (Beck, 1971)

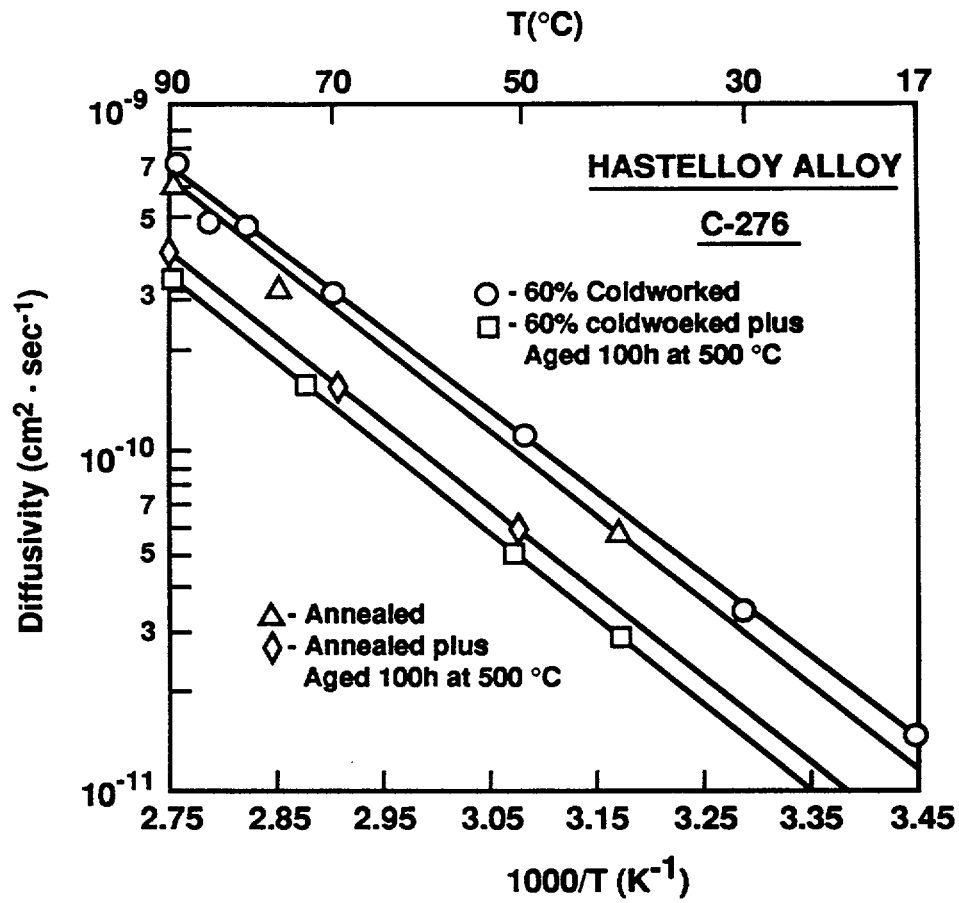


Figure 19. Variation of diffusivity D with T^{-1} for Hastelloy Alloy C-276. (Mezzanotte, 1980)

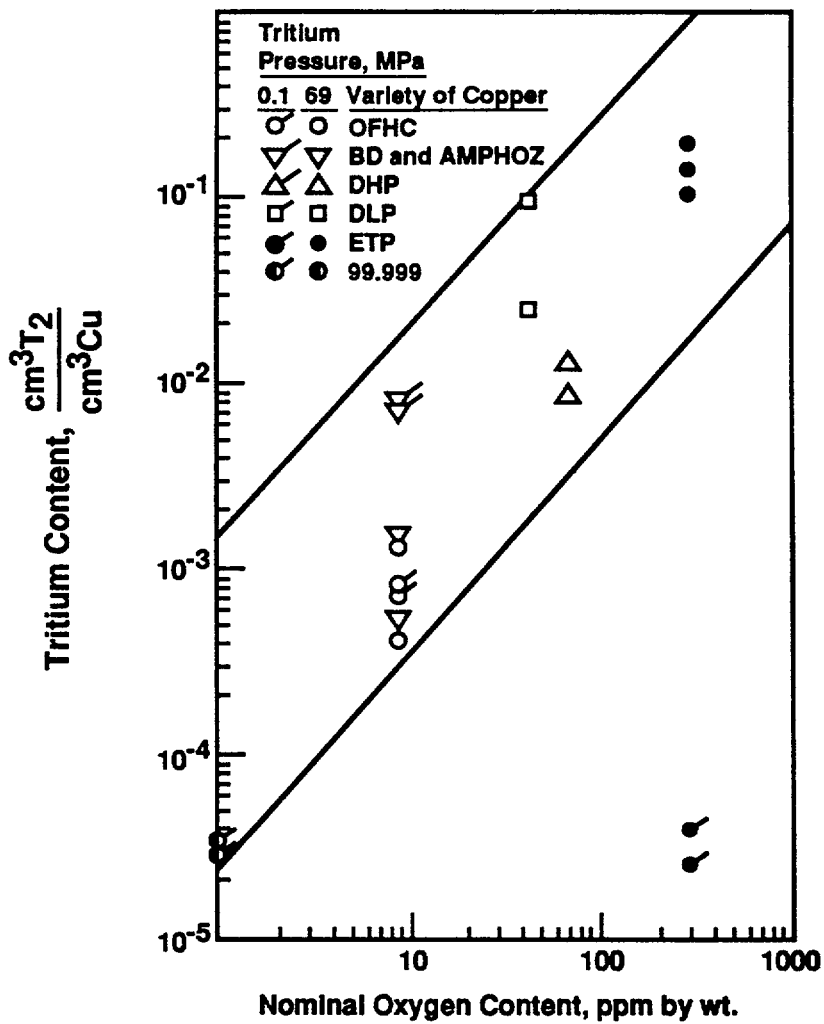


Figure 20. Correlation of quantity of tritium absorbed vs. oxygen content of copper. (Caskey, 1976)

5. SUMMARY AND RECOMMENDATIONS

The anticipated sources of hydrogen in the repository were examined. The most likely sources of hydrogen include crevice environments and galvanic coupling with carbon steel borehole liner. Microbiologically influenced generation of hydrogen cannot be precluded, but the survivability, in the repository environment, of organisms known to generate hydrogen on steels or other organisms with similar capabilities is yet to be demonstrated. Radiolytic generation of hydrogen from vapor sources is unlikely because of the predominance of the oxidizing species so generated, as well as the reactions of hydrogen radical with oxygen present in the unsaturated zone of the Yucca Mountain site. Radiolytic generation of hydrogen from aqueous environments inside crevices is a possibility because of the acidic and anoxic conditions prevailing in these regions.

Assuming hydrogen is generated in sufficient concentrations, the susceptibility to embrittlement of candidate container materials under repository thermal conditions was examined. The copper based alloys are the most resistant to embrittlement by hydrogen. There is a lack of extensive data on the effect of thermal exposure to embrittlement characteristics of Cu-alloys, especially those that contain Fe as an alloying element. The hydrogen embrittlement characteristics of the austenitic alloys are much better understood, at least, phenomenologically. Among the austenitic stainless steels and Ni-base alloys, 304/304L is the least resistant, followed by the high-Ni alloys such as alloy C-276, C-22, or 625. The higher Fe-containing Ni-base alloys such as alloy 825 are the most resistant of this class. All these alloys show a decreasing tendency to embrittle as the temperature is raised above room temperature. Long-term exposure to repository thermal conditions can be deleterious to the room temperature embrittlement susceptibility of the low-Fe, Ni-base alloys such as alloy C-22 because of ordering reactions. No embrittlement has been observed at the anticipated repository temperatures.

The hydrogen permeability techniques investigated at the Fontana Corrosion Center (FCC) enable measurement of hydrogen permeability in aqueous solutions up to boiling point and can be adapted for measurement at higher temperatures. Comparison of the initial data to data from the literature at the same temperatures indicates quite good agreement for all the alloys except oxygen-free copper (CDA-102). In CDA-102, a permeation transient could be generated only by the use of recombination poison, and the measured value of diffusivity agreed quite closely with the literature value. One possible reason for the difficulty in obtaining permeation transient in oxygen-free copper may be the trapping of hydrogen by residual oxygen.

Based on the evaluation of relatively short term data, hydrogen embrittlement of all the candidate materials appears to be negligible at the temperatures anticipated in the repository. Hence, hydrogen embrittlement may be considered to be less important than other degradation processes such as crevice corrosion, stress corrosion cracking, etc. However, it is prudent to examine the potential for embrittlement at long time periods. For this purpose, the existing models for hydrogen embrittlement should be evaluated. Since two of the potential sources of hydrogen in the repository involve crevices, the chemistry and electrochemical potential inside crevices must be investigated both experimentally and by modelling.

REFERENCES

- Berkowitz, B. J. and R. D. Kane, 1980, The effect of impurity segregation on the hydrogen embrittlement of a high strength Ni-base alloy in H₂S environment, *Corrosion*, V. 36, p. 24.
- Caskey, G. R., A. H. Dexter, M. L. Holzworth, M. R. Louthan, and R. G. Derrick, 1976, The effect of oxygen on hydrogen transport in copper, *Corrosion*, V. 32, p. 370.
- Cottis, R. A., K. R. Gowers, M. Haji-Ghassemi, and E. A. Taqi, 1986, The application of hydrogen permeation measurements to the study of corrosion fatigue crack growth in steels, *Electrochemical Methods in Corrosion Research*, M. Duprat (ed.), Materials Science Forum, V. 8, p. 243, Trans Tech Publications Ltd., Switzerland.
- Coyle, R. J., A. Atrens, N. F. Fiore, J. J. Bellina, and M. Jolles, 1977, Effect of metallurgical variables on hydrogen solubility in high alloys, *Environment Sensitive Fracture of Engineering Materials*, Z. A. Foroulis (ed.), TMS-AIME, Pittsburgh, Pennsylvania.
- Efird, K. D., 1985, Failure of Monel Ni-Cu-Al Alloy K-500 bolts in sea water, *Materials Performance*, V. 25, p. 37.
- Erlings, J. G., H. W. deGroot, and J. F. M. van Roy, 1986, Stress corrosion cracking and hydrogen embrittlement of high-strength nonmagnetic alloys in brines, *Materials Performance*, V. 26, p. 28.
- Gallagher, P. C. J., 1970, The influence of alloying, temperature, and related effects on the stacking fault energy, *Metallurgical Transactions*, V. 1A, p. 2429.
- Gdowski, G. E. and D. B. Bullen, August 1988, Survey of degradation modes of candidate materials for high-level radioactive waste disposal containers, V. 6, *Effects of Hydrogen in austenitic and copper-based materials*, UCID-21362, Vol. 6, Lawrence Livermore National Laboratory, Livermore, California.
- Glass, R. S., G. E. Overturf, R. E. Garrison, and R. D. McCright, 1984, Electrochemical determination of the corrosion behavior of candidate alloys proposed for containment of high-level nuclear waste in tuff, UCID-20174, Lawrence Livermore National Laboratory, Livermore, California.
- Glass, R. S., G. E. Overturf, R. A. Van Konynenburg, and R. D. McCright, 1986, Gamma radiation effects on corrosion - I, *Corrosion Science*, V. 26, p. 577.
- Gray, W. J., 1988, Effects of radiation on the oxidation potential of salt brine, *Materials Research Symposium*, V. 112, M. J. Apter and R. E. Westerman (eds.), p. 405, Materials Research Society, Pittsburgh, Pennsylvania.
- Hack, H. P. and J. R. Scully, 1986, Galvanic corrosion prediction using long-term potentiostatic polarization curves, *Corrosion*, V. 42, p. 79.
- Hirth, J. P. and J. Lothe, 1982, *Theory of Dislocations*, 2nd Edition, Wiley-Interscience.

- Jones, R. H., S. M. Bruemmer, M. T. Thomas, and R. D. Baer, 1980, Grain-boundary chemistry, fracture mode and ductility comparisons for iron, nickel tested at cathodic potentials, p. 369, *Hydrogen Effects in Metals*, I. M. Bernstein and A. W. Thompson (eds.), The Materials Society, Pittsburgh, Pennsylvania.
- Kane, R. D., 1978, Accelerated Hydrogen Charging of Ni-base and Co-base alloys, *Corrosion*, V. 34, p. 442, NACE.
- Kane, R. D., 1985, Role of H₂S in behavior of engineering alloys, *International Metals Reviews*, V. 30, p. 291.
- Kargol, J. A. and B. Ladna, 1982, The roles of ordering and impurity segregation on the hydrogen assisted propagation in Ni-base stainless alloys, *Scripta Metallurgica*, V. 16, p. 191.
- Kim, Y. J. and R. A. Oriani, 1987a, Corrosion properties of the oxide film formed on grade 12 titanium in brine under gamma radiation, *Corrosion*, V. 43, p. 85.
- Kim, Y. J. and R. A. Oriani, 1987b, Brine radiolysis and its effect on the corrosion of grade 12 titanium, *Corrosion*, V. 43, p. 92.
- Latanision, R. M. and H. Opperhauser, 1975, The intergranular embrittlement of Ni by hydrogen: Effect of grain boundary segregation, *Metallurgical Transactions*, V. 5A, p. 483.
- Louthan, M. R. and G. R. Caskey, 1976, Hydrogen transport and embrittlement of structural metals, *International J. of Energy*, V. 1, p. 291.
- Mansfeld, F. and J. V. Kenkel, 1975, Laboratory studies of galvanic corrosion - I. Two-metal couples, *Corrosion*, V. 31, p. 298.
- McBreen, J., L. Nanis, and W. Beck, 1966, A method for determination of the permeation rate of hydrogen through metal membranes, *J. Electrochem. Soc.*, V. 113, p. 1218.
- McCright, R. D., 1977, Effects of environmental species and metallurgical structure on the hydrogen entry into steel, *Stress Corrosion Cracking and Hydrogen Embrittlement of Iron-base Alloys*, R. W. Staehle et al. (eds.), NACE, Houston, Texas.
- Mezzanotte, D. A., J. A. Kargol, and N. F. Fiore, 1980, Hydrogen transport in a Ni-base superalloy, *Scripta Metallurgica*, V. 14, p. 219.
- Ohnaka, N. and Y. Furutani, 1990, Electrochemical investigation of hydrogen absorption of type 304 stainless steel in 0.05 M Na₂SO₄ solutions of different pH at 95°C, *Corrosion*, V. 46, p. 129.
- Price, C. E. and R. N. King, 1985, The embrittlement of Monel 400 by hydrogen and mercury as a function of temperature, p. 81, in *Corrosion Cracking*, V. S. Goel (ed.), ASM International, Materials Park, Ohio.
- Reed, D. T. and R. A. Van Konynenburg, 1987, Effect of ionizing radiation on moist air systems, *Materials Research Symposium*, V. 112, M. J. Apted and R. E. Westerman (eds.), p. 405, Materials Research Society, Pittsburgh, Pennsylvania.

- Rhodes, P. R., 1986, Stress cracking risks in corrosive oil and gas wells, Paper No. 322, CORROSION/86, NACE, Houston, Texas.
- Singh, S. and C. Alstetter, 1982, Effects of hydrogen concentration on slow crack growth in stainless steels, Metallurgical Transactions, V. 13A, p. 1799.
- Smith, G. C., 1974, Hydrogen in Metals, I. M. Bernstein and A. W. Thompson (eds.), p. 485, American Society for Materials, Materials Park, Ohio.
- Spinks, J. W. T. and R. J. Woods, 1990, Introduction to Radiation Chemistry, 3rd Edition, John Wiley & Sons, Inc., New York, New York.
- Sridhar, N., J. A. Kargol, and N. F. Fiore, 1980a, Hydrogen-induced crack growth in a Ni-base superalloy, Scripta Metallurgica, V. 14, p. 225.
- Sridhar, N., J. A. Kargol, and N. F. Fiore, 1980b, Effect of low-temperature aging on H-induced crack growth in a Ni-base superalloy, Scripta Metallurgica, V. 14, p. 1257.
- Thompson, A. W. and I. M. Bernstein, The role of metallurgical variables in hydrogen-assisted environmental fracture, Report No. SC-PP-75-63, Science Center, Rockwell International, Thousand Oaks, California.
- Turnbull, A., 1983, The solution composition and electrode potential in pits, crevices, and cracks, Corrosion Science, V. 23, p. 833.
- Vaughn, G. A. and J. B. Greer, 1980, High-strength Ni-alloy tubulars for deep sour gas well application, Paper SPE 9240, 55th Annual Fall Technical Conference of the Society of Petroleum Engineers of AIME, Dallas, SPE - AIME, Dallas, Texas.
- Vennett, R. M. and G. S. Ansell, 1969, A study of gaseous hydrogen damage in certain FCC metals, Transactions of ASM, V. 62, p. 1007.
- Völkl, J., G. Alefeld, 1978, Diffusion of hydrogen in metals, Hydrogen in Metals - I, G. Alefeld and J. Völkl (eds.), Springer-Verlag, Berlin.
- Walter, R. J. and W. T. Chandler, 1973, Influence of gaseous hydrogen on metals - Final Report, NASA CR-124410, National Aeronautics and Space Administration, Marshall Space Flight Center, Alabama.
- Wei, R. P. and M. Gao, 1985, Chemistry, Microstructure, and Crack Growth Response, p. 579, Hydrogen Degradation of Ferrous Alloys, R. A. Oriani, J. P. Hirth, and M. Smailowski (eds.), Noyes Publications, Park Ridge, New Jersey.
- Williams, D. P. and H. G. Nelson, 1969, Embrittlement of 4130 steel by low-pressure gaseous hydrogen, Metallurgical Transactions, V. 1A, p. 63.
- Zakrozcymski, T., 1985, The effect of straining on the transport of hydrogen in iron, nickel, and stainless steel, Corrosion, V. 41, p. 485.

APPENDIX A

APPENDIX A

ANALYSIS OF PERMEATION TRANSIENTS

Methods for analyzing electrochemical hydrogen permeation transients have been described by McBreen et al. (McBreen, 1966). A brief description is provided below.

Considering the diffusion of hydrogen through a thin membrane of a metal to be a one dimensional problem, the following diffusion equation may be written:

$$\frac{d^2C}{dx^2} - \frac{1}{D} \frac{dC}{dt} = 0; \quad 0 < x < L \quad (\text{A-1})$$

In electrochemical permeation studies, the hydrogen is charged at a constant cathodic current density and is oxidized completely on the anodic side of the membrane. Additionally, it is assumed that the concentration is negligible at the beginning of the test. Hence, the boundary conditions may be written as:

$$\begin{aligned} C &= C_0; & @ & \quad x = 0; & @ & \quad t = 0 \\ C &= 0; & @ & \quad x = L; & & \quad \text{at all times} \\ C &= 0; & \text{for} & \quad 0 < x < L; & \text{for} & \quad t < 0 \end{aligned}$$

If the boundary conditions defined above are carefully maintained, the permeation of hydrogen through the membrane follows the transient shown in Figure A-1. Somewhat analogous results will be obtained for decay transient where the initial concentration is maintained at a steady state value and the charging current turned off. However, this will not be analyzed here.

Fick's first law gives the steady state permeation to be:

$$J_{\infty} = \frac{DzF(C_0 - C_L)}{L} \quad (\text{A-2})$$

Where D is the diffusivity, z the charge (+1 for H^+), F the Faraday constant, L the thickness of the membrane, and C_0 the input concentration of hydrogen (solubility of hydrogen). The output concentration, C_L , is maintained to be zero, experimentally. Note that from the steady state permeability, one cannot obtain diffusivity without knowing the value of the surface concentration. However, diffusivity can be obtained independently from the transient permeation as shown below.

Application of Laplace transformation to Eq. A-1 with the boundary conditions above and solving for the resulting equation yields the concentration of hydrogen in the membrane at any position and time:

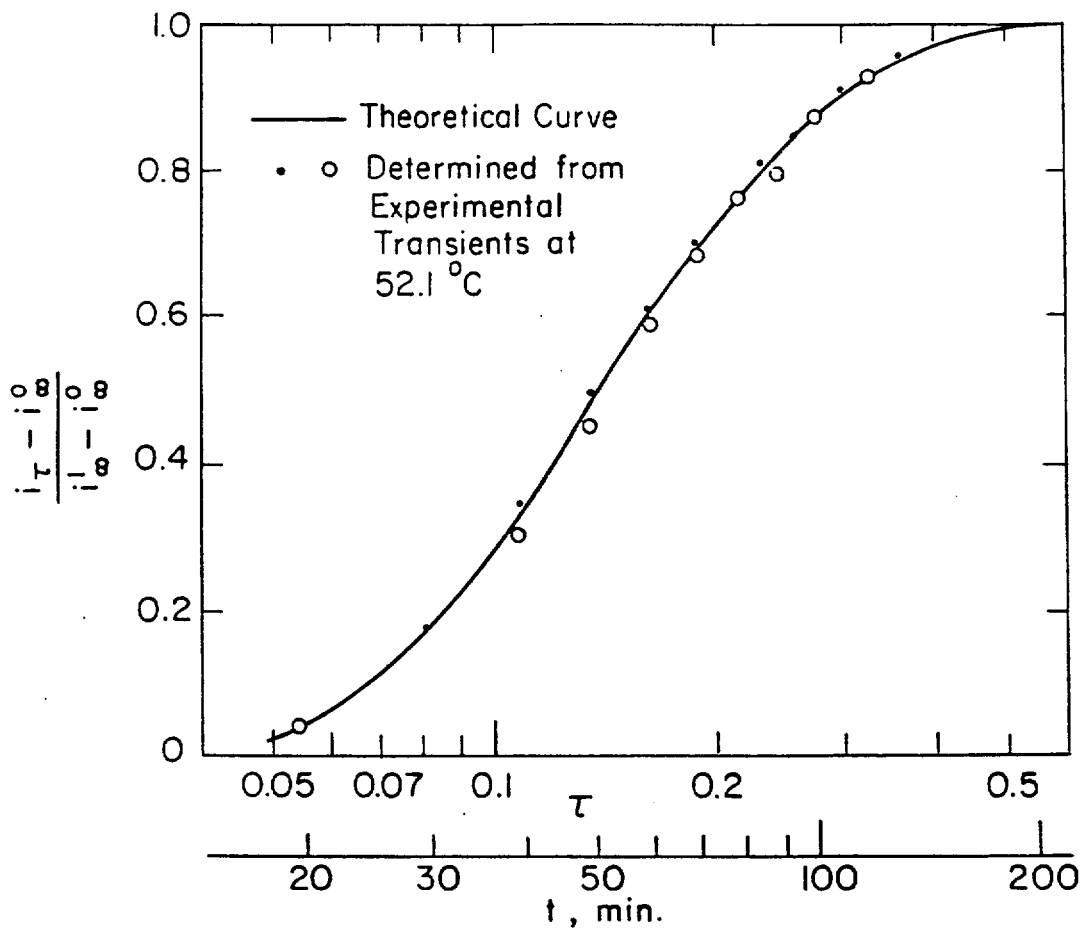


Figure A-1. Theoretical rise transient superimposed on typical experimental data. This figure also illustrates the method of fitting experimental data to the theoretical curves.

$$\frac{C(x,t)}{C_0} = \sum_{n=0}^{\infty} (-1)^n \operatorname{erfc} \frac{x+2nL}{2\sqrt{Dt}} - \sum_{n=0}^{\infty} (-1)^n \operatorname{erfc} \frac{2L(n+1)-x}{2\sqrt{Dt}} \quad (\text{A-3})$$

Since the measured anodic current (permeation transient at any time) is given by:

$$J_t = -DzF \left(\frac{dC}{dx} \right)_{x=L} \quad (\text{A-4})$$

Equations A-2 through A-4 can be combined, time t can be transformed to the dimensionless variable, $\tau = Dt/L^2$, and terms with n higher than 0 can be neglected to give:

$$\frac{J_t}{J_{\infty}} = \frac{2e^{-\frac{1}{4\tau}}}{\pi^{0.5}\tau^{0.5}} \quad (\text{A-5})$$

Thus, for various values of J_t/J_{∞} , the value of τ has been calculated as shown below:

τ	J_t/J_{∞}
0.1	0.2924
0.2	0.7227
0.25	0.8303
0.5	0.9677
0.8	0.9178

For example, for $J_t/J_{\infty} = 0.83$, $\tau = 0.25$ and $D = 0.25 L^2/t$. However, the approximation given by Eq. A-5 is valid only up to $J_t/J_{\infty} = 0.965$. Since the flux, J , is related to the measured current density, i , by Faraday's law, the same analysis can be used as above for the permeation current density replacing J with i .

APPENDIX B

The hydrogen absorption and potential embrittlement of candidate High Level Waste Package Containers in the proposed Tuff repository environment.

By:

B.E. Wilde, Principal Investigator,
C. Manfredi, Post-Doctoral Researcher,
S. Kesavan, Graduate Research Associate,
C. Miller, Graduate Research Associate.

The Fontana Corrosion Center,
Dept., of Materials Science and Engineering,
The Ohio State University,
Columbus, Ohio, 43210.

Final Report prepared under SwRI Contract No. 20020698 for Dr. Prasad K. Nair, Mgr., Engineered Barrier Systems, CNWRA , PO Drawer 28510, Culebra Road, San Antonio, Texas, 78284.

Executive Summary

As part of the responsibility to the US Congress to ensure that the public interests are safeguarded during the licensing of a repository in which to bury nuclear waste, the Nuclear Regulatory Commission (NRC), has developed a program of research to provide a basis for the licensing process.

To aid in these endeavors the NRC has commissioned a Center for Nuclear Waste Regulatory Analyses (CNWRA), to provide sustained high quality technical assistance and research in support of NRC's responsibilities. CNWRA is required to establish research activities to aid in identifying and resolving technical and scientific issues not necessarily being addressed by the Department of Energy (DOE). As part of this overall effort CNWRA has formulated a research program to develop an understanding of the various mechanisms which may cause failure of proposed waste package container materials of construction as a result of interaction between the container and the Tuff repository environment.

A potential failure mode that does not appear to have been addressed adequately by the DOE to date is that of container fracture by hydrogen embrittlement (HE), as a result of the absorption of hydrogen from non-corrosion processes into the proposed container in regions of high tensile stresses such as those located adjacent to welds, etc.

This final report describes work conducted in a program initiated by CNWRA on the question of hydrogen absorption/embrittlement of several candidate container materials. The program was divided into three parts; 1) development of new

investigative techniques suitable for use at estimated repository temperatures, 2) evaluation of the hydrogen absorption/cracking properties of several of the current DOE copper based candidate materials and 3) evaluation of stainless alloys including Incolloy 825, Hastelloy C22.

This final report describes the findings of the above program as follows:

Part 1. Technique development.

1) Acceptable hydrogen permeation measurement procedures have been developed for use at 95°C for type 316L stainless steel, Incolloy 825 and Hastelloy C22.

2) The use of Na_3PO_4 and Na_2SO_4 as inhibitors have allowed the determination of the hydrogen absorption kinetics into the above candidate materials at 95°C.

3) These procedures will allow the systematic determination of the influence of mechanical and metallurgical variables on the propensity of the candidate alloys to hydrogen induced cracking.

4) The procedures developed will allow the exact effects of gamma radiolysis in producing hydrogen or hydrogen containing species that could be active in absorption and hence HE.

Part 2. Hydrogen absorption characteristics of some copper based alloys.

1) CDA alloy 102 was found to be impervious to hydrogen absorption even under conditions of profuse hydrogen generation on the alloy surface. These characteristics suggest that this material by definition, will not be susceptible to failure by HE.

2) In the presence of a surface poison such as traces of arsenic however, CDA alloy 102 did evidence a small but measurable

amount of hydrogen absorption. These data indicate the great sensitivity of the material responses to the repository environment and the need to characterize it before any failsafe materials selection can be made.

3) CDA alloy 715 was found to absorb hydrogen in the absence of any surface poisons.

Part 3. Hydrogen absorption/HE of high nickel stainless alloys.

1) Incolloy 825 and Hastelloy C22 both absorb hydrogen. The amount absorbed was less with Incolloy 825 than Hastelloy C22.

2) The amount of hydrogen absorbed decreased for both alloys as the temperature was raised from 25°C to 95°C.

3) In accelerated HE tests using a slow-strain rate procedure, both alloys evidenced fracture by HE at 25 and 95°C.

4) Although not quantitative, the severity of the cracking noted at both temperatures was markedly less for the Incolloy 825 alloy than for the Hastelloy C22.

5) On the basis of the above results it is recommended that a longer term environmental cracking evaluation of these two alloys be conducted, including tests in a gamma radiation environment.

Background preamble.

The 1987 amendment to the Nuclear Waste Policy Act (NWPA), established the responsibilities of the Department of Energy (DOE), the Nuclear Regulatory Commission (NRC) and the Environmental Protection Agency (EPA) for the development of standards for the long term storage of nuclear waste in a repository.

To assist in these endeavors the NRC has established the Center For Nuclear Waste Regulatory Analyses (CNWRA), to provide sustained high quality technical assistance and research in support of NRC's responsibilities. CNWRA is required to establish research activities to aid in identifying and resolving technical and scientific issues not necessarily being addressed by the DOE.

The current NRC standard 10 CFR Part 60 requires the high level waste package to contain radionuclides for a period of 300 -1000 years. To achieve this requirement the waste package materials must be able to withstand environmentally induced degradation over this period when exposed to the conditions prevalent in the repository; currently the Yucca Mountain Tuff site in Nevada as proposed by the DOE.

As part of this overall effort CNWRA has formulated a research program to develop an understanding of the various mechanisms which may cause failure of proposed waste package container materials of construction as a result of interaction between the container and the Tuff repository environment.

A potential failure mode that does not appear to have been addressed adequately by the DOE to date is that of container

* see references.

fracture by hydrogen embrittlement (HE), as a result of the

absorption of hydrogen from non-corrosion processes into the proposed container in regions of high tensile stresses ¹⁾.

This final report describes work conducted in a program initiated by CNWRA on the question of hydrogen absorption/embrittlement of candidate container materials. The program scope of work is presented in detail in appendix 1 and can be briefly summarized as follows:

Phase 1. Modify current electrochemical hydrogen permeation procedures to allow their use at elevated temperatures, and if need be elevated pressures, for the detection of hydrogen absorption into candidate materials under simulated repository conditions. Because the anticipated waste package container surface will be in excess of the site water boiling point (95°C), modified methods will cover a temperature interval of ambient to 95°C with the capability to extend to 150°C in hyperbaric facilities.

Phase 2. Use the procedures and equipment developed in Phase 1 to determine the extent and rate of hydrogen absorption into copper based and nickel based candidate container alloys exposed to simulated repository environments. The effects of such variables as a) state of stress/strain etc), and b) material chemical composition.

Phase 3. Develop a CNWRA in-house capability with which to investigate the effects of gamma radiation on the absorption of hydrogen into candidate alloys to duplicate the anticipated repository conditions (e.g., substituting the generation of hydrogen on the metal surface by gamma radiolysis of the steam/water adjacent to the metal.

This report presents the results of Phases 1 and 2 of the

above program in three (3) distinct and complete parts:

Part 1. Development of high temperature techniques for the precise measurement of hydrogen absorption into iron based and nickel based alloys.

Part 2. Procedures for the study of copper based materials along with preliminary results and discussion of the data.

Part 3. Results and discussion of studies conducted on Incolloy 825 and Hastelloy C22

In order to make each part more assimilatable because of the large volume of data, each has been written as a complete entity in itself and contains it's own bibliography and figure sequencing, etc. Although this format may inadvertently lead to some repetition, we believe it to be easier for the reader to say for example, study technique development and methods in a part so dedicated, than to have to delve through a part dedicated to copper or nickel alloy behavior.

Because of time constraints in the program, no effort was expended on the Phase 3 work described above.

Historic and technical background.

In order for the technically astute but non-specialist reader to appreciate the basis for the work to be described it is necessary to briefly review the factors known regarding the environment to be engineered to in a repository.

Extensive work has been conducted on the nature of the repository environment the details of which have been reviewed

elsewhere ²⁾. Because the reference horizon of the proposed repository lies at least 200m above the known static water table, the containers will not be expected to be submerged in water. However there is reason to believe that they will be subject to a constant contact with a mixture of steam and water over the design life of 1000 years. Heat is generated by radioactive decay of the waste ³⁾, and the best estimate of the surface temperature/time profile is shown in Figure 1.

It is clear from the figure that the container surface will not cool to below the boiling point (95°C) for about 200 - 300 years; thus, the container will see an environment of steam and air along with the gamma radiolysis products of steam and air for up to 200 - 300 years.

The composition of the ground water is not known but the water chemistry is considered ⁴⁾ to be similar to that found in a well drilled in an adjacent site and known as the J-13 well. The composition of J-13 well water is summarized in table 1.

In addition to the chemical aspects of the ground or infiltrate water reaction with the container, there is the additional and probably dominating effect of the gamma radiolysis, which produces a gamut of transient radicals ⁵⁻¹¹⁾. Among the species known to be formed are the following:

H·	Hydrogen radical
OH·	Hydroxide radical
e _{aq} ⁻	solvated electron
H ₃ O ⁺	Hydronium ion
OH ⁻	Hydroxide ion
H ₂	Hydrogen molecule
H ₂ O ₂	Hydrogen peroxide
O ₂	Oxygen molecule
O ₂ ⁻	Peroxide ion
Cl ⁻	Chloride ion

Workers to date have regarded the above population from the point of view of the corrosion damage they may cause ¹⁾. However, the purpose of the present investigations are focussed on the possibility of the hydrogen containing species above not formed by container corrosion, causing a container failure by hydrogen embrittlement as a result of hydrogen absorption.

Table 1. Chemical analysis of water sample taken from well J-13.⁴⁾.

pH approx. 7.1.

<u>Species</u>	<u>Concentration, mg/L</u>
Na ⁺	51.0
K ⁺	4.9
Ca ²⁺	14.0
Mg ²⁺	2.1
Ba ²⁺	0.003
Sr ²⁺	0.05
HCO ₃ ⁻	120.0

Table 1 continued:

SO_4^{2-}	22.0
Cl^-	7.5
NO_3^-	5.6
F^-	2.2
PO_4^{3-}	0.12
SiO_2	66.4
Fe^{2+}	0.04
V^{2+}	0.002
Li^+	0.05
Al^{3+}	0.03

References.

- 1) P.S. Maiya, "A review of degradation behavior of container material for high-level nuclear waste in Tuff and alternative repository environments". Argonne National Laboratory Report ANL-89/14, June, 1989, USDOE Contract W-31-109-Eng-38, p 11-16.
- 2) R.V. Guzowski, F.B. Nimick, M.D. Siegel and N.C. Finley, "Repository site data report for Tuff: Yucca Mountain, Nevada,"NUREG/CR-2937 SAND82-2105, Sandia National Laboratories, Albuquerque, NM, (October, 1983).
- 3) R.D. McCright, "FY 1985 status report on feasibility assessment of copper-base waste package container materials in a Tuff repository", UCID-29509 DE86003960, Lawrence Livermore National Laboratory, CA, (September 30, 1985) .09-Eng-38,
- 4) Ref 1), p 4.
- 5) R.S. Glass, "Effects of radiation on the chemical environment surrounding waste canisters in proposed repository site and possible effects on corrosion processes", SAND-81-1677, Sandia National Laboratories, Albuquerque, NM, (December 1981).
- 6) R.S. Glass, G.E. Overturf, R.A. Van Konynenburg and R.D. McCright, Corrosion Science, 26, 577, (1986).
- 7) W.H. Yunker and R. Glass, "Long-term corrosion behavior of copper base materials in gamma-irradiated environments", Mat. Res. Soc. Symp. Proc., 84, 579, (1987).
- 8) M.A. Lewis and D.T. Reed, "Effects of gamma radiolysis on waste package components", Mat. Res. Soc. Symp. Proc., 84, 623, (1987).

- 9) W.H. Smyrl, B.T. Bell, R.T. Atanososki and R.S. Glass, "Copper corrosion in irradiated environments: the influence of H₂O₂ on the electrochemistry of copper dissolution in HCl electrolyte", UCRL-95961 Dec88 000419, Lawrence Livermore National Laboratory, Livermore, CA, (December 1988).
- 10) T. Abraham, H. Jain and P. Soo, "Stress-corrosion cracking tests on high-level waste container materials in simulated Tuff repository environments", NUREG/CR-4619 T186 013148, Brookhaven National Laboratory, Upton, NY, (June 1986).
- 11) Y.J. Kim and R.A. Oriani, Corrosion, 43, 85, (1987).

Part 1. Modification of ambient temperature and pressure hydrogen
absorption measurement procedures.

C. Manfredi.

B.E. Wilde.

1.0 Introduction.

To aid the reader in understanding the purpose of this part, a brief review of some essential technical background will be presented.

1.1 The physical chemistry of hydrogen deposition, absorption and diffusion.

With the exception of hydrogen occluded during material production and fabrication, all performance problems associated with hydrogen are a result of the interactions at the material interphase boundary between the material and the environment and subsequent interaction of absorbed hydrogen in the metal.

The elementary step can be represented as follows:



where H_{ads} represents the steady-state concentration or coverage of hydrogen atoms adsorbed on the surface commonly referred to as (θ_{H}) and H_{abs} is the concentration of hydrogen dissolved in the metal surface and k_{abs} and k_{des} are the rate constants associated with the elementary absorption and desorption processes respectively.

In the case of aqueous environments, the source of H_{ads} is the electrochemical reduction of solvated protons (hydronium ions) and/or water molecules as described recently by Wilde and Shimada ¹²⁾:





Typical processes in which the above occur are among the following: electroplating, corrosion, and cathodic protection.

Hydrogen absorption can also occur from other sources of hydrogen including hydrogen gas and gamma radiolysis processes, e.g.



The reaction represented by equation (5) is, at the moment, hypothetical and the basis for the current study.

The absorption rate of hydrogen into any material is controlled by the surface concentration of hydrogen "adatoms" and the rate constant for the absorption reaction. The absolute determination of both (θ_{H}) and k_{abs} , although possible, is difficult on materials that corrode in the environment¹³⁻¹⁵. In the present study, we have chosen to "bypass" the latter difficulty (at least for screening purposes) by using a simple electrochemical method of measuring the absolute flux of hydrogen across the surface of a metallic membrane resulting from a given combination of (θ) and k_{abs} which, although unknown, is invariant for the boundary conditions employed.

Suppose a metallic membrane is exposed to a source of hydrogen on one side (for the sake of simplicity, make the source of hydrogen be the electrochemical reduction of hydronium ion on the membrane surface), as shown schematically in Figure 1. At the same time, let the other side of the membrane be exposed to a system where the activity (fugacity) of hydrogen is maintained at

zero at all times (this is readily accomplished by controlling the potential of the membrane at values positive to the reversible hydrogen potential in an electrolytic solution that does not corrode the membrane material).

Any hydrogen absorbed at the generating surface (input surface) will diffuse through the membrane to the oxidation side because of the fugacity gradient where it will immediately be electrochemically oxidized. Under these conditions, the fraction of the evolving hydrogen that is absorbed will cause a flux through the membrane that can be expressed as:

$$J = D.C_0/L \quad (6)$$

where J is the hydrogen flux, D is the apparent diffusivity of hydrogen in the membrane material, L is the membrane thickness, and C_0 is the concentration of hydrogen absorbed just beneath the input surface. The boundary conditions for this experiment are presented in Figure 2.

Using the well known room temperature procedure developed by Devanathan and Stackurski ¹⁶⁾, a typical hydrogen permeation trace can be obtained, as shown in Figure 3, with extreme sensitivity and accuracy. In the figure, the height of the plateau J_∞ represents the absolute rate of hydrogen absorption into the input surface for the fixed input fugacity concerned. Further, the ratio of J_∞ /[hydrogen generation rate] represents the fraction of hydrogen absorbed for a given input surface condition; in the case of electrochemically generated hydrogen, the ratio becomes J_∞/i_c where i_c represents the cathodic current density used to generate

hydrogen. Division of i_c by the number of electrons involved in the charge transfer process and the Faraday constant converts the hydrogen generation rate to moles/cm².second.

In addition to the data mentioned above, Figure 3 can be analyzed to give a value of the apparent hydrogen diffusivity in the membrane material of study along with the parameter (t_b) which is related to the number of hydrogen traps inherent in the material.

Although the above electrochemical procedures have been used successfully by the writer and others ¹⁷⁻²⁰, even under hyperbaric conditions, there is no information on their use at elevated temperatures in the literature. The major hurdle to be overcome in adapting these procedures for use at elevated temperatures is the avoidance of accelerated corrosion occurring on the oxidation side of the membrane due to the increase in temperature.

Since the sensitivity of the technique relies on the ability of the oxidation circuit to oxidize diffusing hydrogen, any increase in the rate of another anodic process (such as membrane corrosion) will cause a loss in sensitivity.

The purpose of Part 1 of the study is to develop methods to allow the detection and measurement of absorbed hydrogen at elevated temperatures at which the anodic dissolution of the test material is maintained at a suitably low rate.

1.2 Materials and Experimental Procedures.

The simulation of radiation generated hydrogen was accomplished by the electrolysis of 1N NaOH at various cathodic current densities to simulate various input surface fugacities.

The basic electronic equipment employed was as follows:

Potentiostats, (Model Wenking TS3 Brinkman Inst., Westbury, NY)

Kiethley electrometers, (Model 602, Kiethley Inst., Cleveland, OH)

Digital picoammeters, (Model 8010A, Fluke Inst., Everett, WA)

Electronic strip-chart recorders, (Model Speed Serve 2, Esterline Angus Inst., Inc.)

All the above equipment was calibrated prior to use on each experiment to see if it met the makers published specifications and was not used until it did.

Because of the need for experiments to be conducted at temperatures up to 100°C, and the propensity for electrical interference when using electrical hot-plates, two large air thermostats were built in which up to three separate experiments could be conducted in each. Each employed a low voltage heating system with an external fan to ensure rapid temperature homogenization with a minimum of electrical interference. A schematic of the set-up is shown in Figure 4. The accuracy of the temperature control was monitored visually and automatically using a thermometer and a calibrated thermocouple/strip chart recorder for the duration of the experiments (usually one to two weeks) and was +/- 0.5°C.

The experimental cell was custom manufactured in borosilicate glass based on a design published by Wilde and Kim ¹⁹⁾, a schematic representation of which is shown in Figure 5. Because of the need to control condensation at temperatures at or near the boiling point of the J-13 simulate, additional ports were added in which a

water cooled Liebig-type condenser was located on each side of the cell; thus, even during the longest experiment no liquid was lost. To facilitate the transfer of electrolyte at temperature to the input side of the cell, the input environment was contained in a glass vessel in the air thermostat during the attainment of a steady-state background current density on the oxidation side. The environment used on the latter side of the cell was added and deoxygenated with nitrogen during heat-up only.

An in-situ silver/silver chloride reference electrode (model number 13-620-45) was employed in each side of the cell. These were obtained from Fisher Scientific Co., and were certified for use up to 110°C.

The experimental start-up procedure employed was as follows:

- 1) Prepare the membrane of choice and degrease in an ultrasonic bath containing acetone followed by a hot air dry.

- 2) Mount the specimen in the cell using neoprene o-rings and adjust for leak tightness.

- 3) Fill the oxidation side of the cell with the appropriate electrolyte and the input side holding flask with the test environment.

- 4) Insert the platinum auxiliary and reference electrodes in each side of the cell and place in the air thermostat. Connect the water cooled condensers and degas the oxidation side with purified nitrogen, (less than 10 ppm O₂).

- 5) Heat thermostat to the desired operating temperature and discontinue the nitrogen degassing.

- 6) Activate the control potentiostat to maintain an applied potential of +0.100V_{Ag/AgCl}. Record the anodic current density on a

high impedance system shown schematically in Figure 4 (either a strip chart recorder in conjunction with a cathode follower device or a data acquisition system described in Appendix Part 1.1).

7) When the background current density reaches a steady-state (usually after 24 to 48 hours), the test environment is gravity fed into the input side of the cell and this surface of the specimen is immediately cathodized at the appropriate current density value.

8) The hydrogen permeation flux is recorded continuously until a time independent value of J_{∞} is achieved.

9) Number 8) can be repeated without shutdown at various values of cathodic current density to simulate the absorption kinetics resulting from various input fugacities of hydrogen.

10) At the termination of an experiment, the system is shutdown and the components of the cell are cleaned.

The materials used in Part 1 were i) AISI 1018 carbon steel, ii) AISI Type 316L stainless steel, iii) an iron/nickel alloy (Incolloy 825), and iv) a nickel based high performance alloy (Hastelloy C22). The chemical composition of these materials is given in table 2.

Table 2. Chemical composition of materials investigated.

<u>Alloy</u>	<u>Composition (percent by weight)</u>											
	<u>C</u>	<u>Cr</u>	<u>Ni</u>	<u>Fe</u>	<u>Mo</u>	<u>W</u>	<u>Cu</u>	<u>Ti</u>	<u>Mn</u>	<u>Si</u>	<u>P</u>	<u>S</u>
1018	.17	ND	ND	Bal	ND	ND	ND	ND	.83	.46	.023	.021
304L	.029	18.6	10.2	Bal	2.7	ND	.08	ND	1.6	.40	.003	.006

I825 .014 20.6 40.6 28.7 5.9 ND 2.12 .72 .76 .31 ND .008

C22 .004 22.0 bal 4.3 13.6 3.1 ND ND .30 .02 .009 .002

0.8 Co.

* ND denotes not detected.

Because of the extremely low hydrogen diffusivity of the 316L, I825, and the C22 alloy, the original 0.0625-inch thick sheet stock was rolled to a thickness more suitable to experimentation. The material was cold-rolled according to the schedule shown below:

<u>Cold Rolling</u>	<u>Degrease</u>	<u>Anneal</u>	<u>Pickle</u>
Total reduction	Hot NaOH	970-990C	HNO ₃ +HF for I825
50% after each annealing	solution	W&Q	HCl + HNO ₃ for C22.

The final heat treatment of each alloy used in this study was as follows:

AISI 1018	As received hot rolled strip; final thickness 25 mils (thousandths of an inch).
AISI 316L	As received solution annealed foil; 1000°C followed by a water quench, 5.5 mil foil.
Incolloy 825	Cold reduction followed by annealing at 980°C in an argon atmosphere; hold time 40 minutes followed by air cooling; final thickness 4 mils.
Hastelloy C22	Anneal at 1120°C under argon for 20 minutes followed by air cooling; final foil

thickness 2,3 4 and 5 mils.

Representative metallurgical microstructures on each of the materials tested are presented in Figure 6 and appear to be normal for these types of materials. Note that no anomalous grain growth was observed on any material even though several had received extensive thermomechanical working.

Specimens for hydrogen permeation tests were cut from the foil stock to a 2-inch by 2-inch shape that was abraded using 600 grit silicon carbide paper followed by ultrasonic cleaning in acetone immediately before an experiment.

Various methods of coating one side of the foil specimens with the noble metal palladium (Pd), were evaluated in the initial experiments including i) electroplating, ii) electroless deposition, and iii) plasma sputter deposition. The precise details of these techniques are given in appendices 3, 4, and 5. Subsequent studies indicated that inhibition of anodic dissolution was more effective than noble Pd coating which was abandoned.

The environments utilized on the input side of the specimens was 1N NaOH. All solutions were manufactured using double deionized water having a resistance of greater than 10 megohm.cm at 25°C.

A computerized data acquisition program was written for the collection of the permeation data the details of which are summarized in Appendix Part 1.1. The purpose of this system was to avoid the occasional loss of ink and/or running out of chart paper that sometimes happened on the 10- to 20-day test runs.

1.3 Results and Discussion.

In the interest of clarity, the results will be developed in three sections: 1) noble metal deposition studies, 2) iron based alloys, and 3) iron based high nickel alloys and nickel based high performance alloys.

1.3.1 Noble metal deposition studies.

As discussed previously, the major factor to be controlled in the successful extension of the ambient temperature to high temperature applications is the relative magnitude of the partial anodic dissolution current density for metal dissolution, $i_{OX(M)}$, compared with that for hydrogen oxidation $i_{OX(H)}$. The relationship of these parameters to the overall transmembrane scenario is depicted in Figure 7; e.g. for maximum sensitivity, the value of $i_{OX(M)}$ should be small compared with the magnitude of $i_{OX(H)}$.

In traditional experiments, this has been satisfactorily achieved by coating the reactive metal surface on the oxidation side of the membrane with a noble metal such as Pd. The Pd layer readily allows the passage of diffusing hydrogen whilst maintaining a low value of $i_{OX(M)}$.

Initial experiments were conducted in which Pd coatings were deposited on steel, copper, and Hastelloy C22 (C22), using:

- a) electrodeposition
- b) electroless deposition
- c) plasma sputter deposition

The details of the various Pd deposition procedures are given in Appendices Part 1.2-4.

Examples of typical deposits are shown in Figures 8 and 9 for steel and C22, respectively. It is seen that the coating obtained

by electroless deposition appeared to be pore free in both the optical and scanning electron microscope (SEM) at a magnification of 2000X, e.g. no evidence of Fe X-ray fluorescence was observed, for example, even at scratch marks on the original surface prior to plating.

The Pd coated specimens were exposed to 1 N NaOH solution at 95°C for 15 hours to evaluate the coatings for long-term deterioration. In all cases investigated, the deposits produced by all methods were found to be porous which led to severe galvanic corrosion. Typical examples of galvanic attack are presented in Figures 10 and 11 for each generic type of material.

Because the coating deterioration was so severe in only 15 hours and the hydrogen permeation studies were anticipated to have a 1 to 2 week duration, another method of controlling $i_{ox(M)}$ was sought.

An obvious method of controlling the anodic dissolution of the membrane was the use of a passivating-type inhibitor. Initial experiments were conducted on steel specimens in a 1 N Na_3PO_4 solution having a room temperature pH of 9.6. Corrosion tests were conducted on AISI type 316L stainless steel in 1N NaOH at 95°C for 2 weeks. No measurable weight change was recorded over the test duration which prompted the evaluation of the hydrogen permeation performance of this electrolyte described in the following section.

1.3.2 Iron based materials.

Electrochemical hydrogen permeation experiments were conducted on 25 mil thick carbon steel membranes using the split-cell apparatus shown in Figure 5. Carbon steel was employed as the test membrane in the screening phase of the experiments,

rather than type 316L stainless steel, because the diffusivity of hydrogen in the body centered cubic carbon steel was approximately 10^6 times that in the austenitic stainless alloy which translated into a 24-hour test versus a 10- to 14-day test at room temperature.

Figure 12 shows the background anodic dissolution current density/time, i_b , plot for a carbon steel membrane polarized at $+0.100 V_{Ag/AgCl}$ in 1N Na_3PO_4 solution at $95^\circ C$. It is clear from the data that i) the steel passivated readily down to a background $i_{ox(M)}$ of $0.4 \mu A/cm^2$, and ii) the i_b maintained a constant value of $0.4 \mu A/cm^2$ for 300 hours. The repeatability in triplicate experiments was $\pm 15\%$.

After the membrane used in obtaining the data in Figure 12 had maintained an i_b for 300 hours, hydrogen was impregnated into the charging side of the membrane by cathodic polarization at various current densities. The results of these tests are shown in Figures 13 and 14. In Figure 13, a classical hydrogen permeation transient can be seen with a breakthrough time (t_b) of 1.1 minutes and a steady state hydrogen permeation flux (J_∞) of $11.3 \mu A/cm^2$ for a cathodic current of $600 \mu A/cm^2$. These data show that at $95^\circ C$ in 1N NaOH, 1.88% of the hydrogen being evolved on the input surface is being absorbed into the steel.

Future measurements will allow the steady state atomic hydrogen coverage at each cathodic current to be evaluated, thereby allowing the relationship between θ_H and J_∞ to be determined exactly for each candidate material, anticipating the day when a relationship between radiation flux and θ_H on the canister is determined.

Figure 14 shows the relationship between J_{∞} and $i_c^{0.5}$ for carbon steel under the chosen experimental conditions. It is of interest to note that the graph is a straight line as predicted by theory for a coupled discharge/hydrogen recombination mechanism ²⁰⁾

These data show clearly that permeation data can be obtained on carbon steel at elevated temperatures that are simple and consistent with that predicted from theory. That this situation is correct over the temperature range of 25 to 95°C the Arrhenius plot in Figure 15 is presented where the expected straight line relationship between $\log J_{\infty}$ and $1/T$ is observed.

Identical experiments were conducted on a 5.5 mil thick membrane of type 316L stainless steel, the results of which are shown in Figures 16 through 19. In Figure 16, a value of i_p of $0.05 \mu\text{A}/\text{cm}^2$ was obtained which is slightly lower than that observed on carbon steel but which attained a steady state value in 40 hours that remained constant for 300 hours. Figure 17 shows the hydrogen permeation transient for type 316L stainless steel at a cathodic current density of $2.2 \mu\text{A}/\text{cm}^2$ in 1 N NaOH solution at 95°C. It is of interest to note that a smaller fraction of the surface hydrogen was absorbed into the austenitic matrix at steady state than that observed with carbon steel even at a higher charging current density. Figures 18 and 19 show the relationships between J_{∞} and $i_c^{0.5}$ and $\log J_{\infty}$ and $1/T$ respectively.

It is clear that although the absolute values of the parameters differ from carbon steel, nevertheless, the experimental procedure employed is capable of determining the hydrogen absorption behavior of type 316L stainless steel at 95°C in aqueous media.

1.3.3 Iron based high nickel alloys and nickel based high performance alloys.

Equivalent experiments were conducted on 5 mil membranes of both the Incolloy 825 (I825) and Hastelloy C22 (C22) in 1 Normal Na_3PO_4 solution at 95°C on the oxidation side of the membrane and 1 Normal NaOH solution on the input side.

The extended time stability of i_b observed on both the carbon and stainless steel was not noted on I825 and C22. On visual inspection of the membrane specimens after a test run, it was noted that a white deposit had occurred on the oxidation side due to the precipitation of $\text{Ni}_3(\text{PO}_4)_2$ on the membrane surface. Review of the literature revealed that phosphates of nickel are insoluble as shown in table 3 taken from the Chemical Rubber Handbook.

Table 3. Solubilities of orthophosphates in water.

	<u>Solubility, g/100cc</u>	
	<u>cold water</u>	<u>hot water</u>
$\text{Ni}_3(\text{PO}_4)_2 \cdot 8\text{H}_2\text{O}$	insoluble	insoluble
$\text{Cr}(\text{PO}_4)_2 \cdot 2\text{H}_2\text{O}$	slightly sol.	slightly sol.
$\text{Cr}_2(\text{PO}_4)_2$	soluble	soluble
$\text{Fe}_3(\text{PO}_4)_2 \cdot 8\text{H}_2\text{O}$	insoluble	insoluble
$\text{FePO}_4 \cdot 2\text{H}_2\text{O}$	slightly soluble	0.67

Previous studies by one of the authors ²¹⁾ had indicated that high nickel alloy readily passivated in solutions of Na_2SO_4 .

Accordingly, experiments were conducted using a solution of 0.1 N Na_2SO_4 on the oxidation side at 95°C. The results of i_b /time

stability studies are shown in Figures 20 and 21 for I825 and C22, respectively. It is clear from both figures that excellent time stability was observed along with a very low i_b , on the order of 0.05 and 0.02 $\mu\text{A}/\text{cm}^2$, to be compared with the equivalent value of 0.05 $\mu\text{A}/\text{cm}^2$ observed for the stainless steel.

Typical hydrogen permeation curves for both alloys are shown in Figures 22 and 23. In both cases, simple J_{∞} transients were obtained with steady state J_{∞} values of 1.51 $\mu\text{A}/\text{cm}^2$ for I825 (Figure 25) to be compared with 1.0 $\mu\text{A}/\text{cm}^2$ for the C22 at a cathodic charging current density of 400 $\mu\text{A}/\text{cm}^2$. It is clear from these simple experiments that C22 absorbs a smaller fraction of the hydrogen evolving on its surface than does I825, at least in 1 N NaOH solution at 95°C.

Figures 24 and 25 show the simple relationship between hydrogen permeation flux and cathodic charging current density for I825 and C22, respectively. As in the case of the steels, the hydrogen evolution reaction was one of discharge/coupled recombination.

1.4 Conclusions.

The following conclusions can be drawn from the data presented:

- 1) Acceptable hydrogen permeation data on iron and nickel based alloys cannot be obtained at 95°C using the traditional method of palladium plating of the oxidation side of the membrane. Palladium electroplate, electroless deposits, and plasma deposits all appeared to produce a coating that is porous and lead to severe galvanic corrosion of the substrate material in sodium hydroxide

solutions.

2) The use of chemical inhibitors to decrease the metal oxidation partial current density to a low stable value, even at 95°C, was found to be an effective method of developing meaningful hydrogen permeation data.

3) A 1N solution of Na_3PO_4 was found to be satisfactory for the development of hydrogen permeation curves on both carbon steel and AISI type 316 stainless steel at 95°C. Background current densities of $0.4 \pm 0.05 \mu\text{A}/\text{cm}^2$ were measured for carbon steel and were stable within the above error limits over 300 hours. Equivalent values for stainless steel were $0.05 \pm 0.01 \mu\text{A}/\text{cm}^2$ stable over a period of 300 hours.

4) Using the above procedure, traditional permeation flux/time transients can readily be obtained for both steels with clearly defined steady state fluxes at each value of cathodic charging current density. As would be expected, the time taken to achieve steady state flux was markedly less for the carbon steel than the stainless alloy due to the difference in hydrogen diffusivity. Also, the amount of hydrogen absorbed by the carbon steel at the same cathodic charging current density was approximately twice that observed with stainless steel.

5) Well defined straight line functions of J_{∞} versus $i_c^{0.5}$ and $\log J_{\infty}$ versus $1/T$ were measured for both steels, indicating that the cathodic hydrogen charge transfer mechanism is that of the coupled discharge/recombination type which did not change over the hydrogen input fugacities and temperatures studied.

6) Equivalent well defined and repeatable hydrogen permeation data can be obtained on the Incolloy 825 and the

Hastelloy C22 materials using 0.1N Na₂SO₄ inhibited solution at 95°C. Background current densities of 0.05 +/-0.005 μA/cm² and 0.02 +/- 0.005 μA/cm², respectively.

7) Using the above described methods, it is concluded that meaningful hydrogen absorption data can be obtained in Parts 2 and 3 in which the influence of mechanical and metallurgical variables on the hydrogen absorption and possible embrittlement of copper and nickel based candidate materials will be evaluated.

1.5 References.

- 1) P.S.Maiya,"A review of degradation behavior of container material for high-level nuclear waste in Tuff and alternative repository environments".Argonne National Laboratory Report ANL-89/14,June,1989, USDOE Contract W-31-109-Eng-38,p11-16.
- 2) R.V.Guzowski,F.B.Nimick,M.D.Siegel and N.C.Finley,"Repository site data report for Tuff: Yucca mountain,Nevada,"NUREG/CR-2937 SAND82-2105,Sandia National Laboratories,Albuquerque,NM,(October,(1983).
- 3) R.D.McCright,"FY 1985 status report on feasibility assessment of copper-base waste package container materials in a Tuff repository",UCID-29509 DE86003960,Lawrence Livermore National Laboratory,CA,(September 30,1985).09-Eng-38,
- 4) Ref 1),p4.
- 5) R.S.Glass,"Effects of radiation on the chemical environment

- surrounding waste canisters in proposed repository site and possible effects on corrosion processes", SAND-81-1677, Sandia National Laboratories, Albuquerque, NM, (December 1981).
- 6) R.S.Glass, G.E.Overturf, R.A.Van Konynenburg and R.D.McCright, Corrosion Science, 26, 577, (1986).
 - 7) W.H.Yunker and R.Glass, "Long-term corrosion behavior of copper base materials in gamma-irradiated environments", Mat.Res.Soc. Symp.Proc., 84, 579, (1987).
 - 8) M.A.Lewis and D.T.Reed, "Effects of gamma radiolysis on waste package components", Mat.Res.Soc>Symp.Proc., 84, 623, (1987).

 - 9) W.H.Smyrl, B.T.Bell, R.T.Atanososki and R.S.Glass, "Copper corrosion in irradiated environments: the influence of H₂O₂ on the electrochemistry of copper dissolution in HCl electrolyte", UCRL-95961 Dec88 000419, Lawrence Livermore National Laboratory, Livermore, CA, (December 1988).
 - 10) T.Abraham, H.Jain and P.Soo, "Stress-corrosion cracking tests on high-level waste container materials in simulated Tuff repository environments", NUREG/CR-4619 T186 013148, Brookhaven National Laboratory, Upton, NY, (June 1986).
 - 11) Y.J.Kim and R.A.Oriani, Corrosion, 43, 85, (1987).
 - 12) B.E.Wilde and T.Shimada, Scripta.Met., 22, 551, (1988).
 - 13) J.O'M.Bockris and H.Kita, J.Electrochem.Soc., 108, 676, (1961).
 - 14) C.D.Kim and B.E.Wilde, J.Electrochem.Soc., 118, 202, (1986).
 - 15) B.E.Wilde and C.D.Kim, Corrosion, 42, 243, (1986).
 - 16) M.A.V.Devanathan and Z.Stachurski, Proc.Roy.Soc.A, 270, 90, (1962).
 - 17) B.E.Wilde and D.C.Deegan, Corrosion, 29, 310, (1973).

- 18) B. E. Conway, Proc. Roy. Soc. 247A, 400, (1958).
- 19) B. E. Wilde and C. D. Kim, Corrosion, 37, 449, (1981).
- 20) J. O' M. Bockris and M. A. V. Devanathan, Office of Naval Research
Report No. ONR551, August, 1957.
- 21) B. E. Wilde, Unpublished results US. Steel Corporation, Monroeville,
Pennsylvania, 15146, (1981).

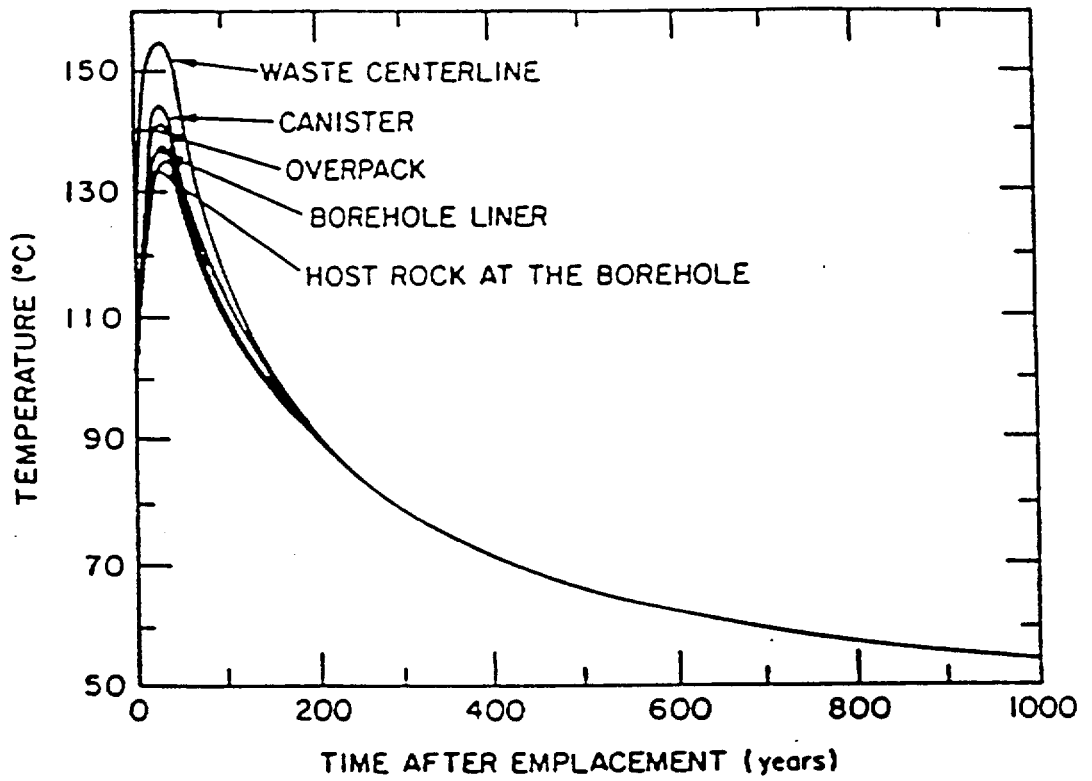


Figure 1. Calculated Decay heat/Time profile for the proposed Tuff repository.

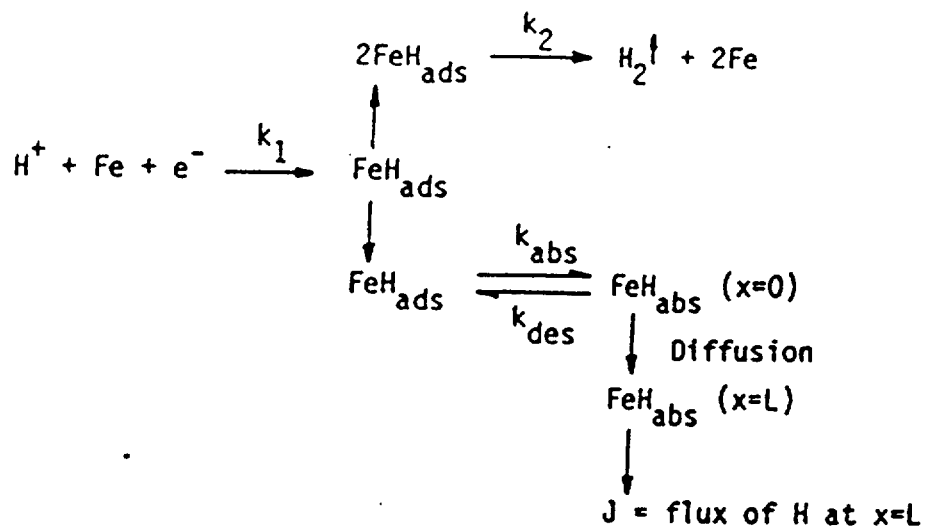


Figure 1. Schematic of hydronium ion discharge and hydrogen absorption reactions at a metal surface.

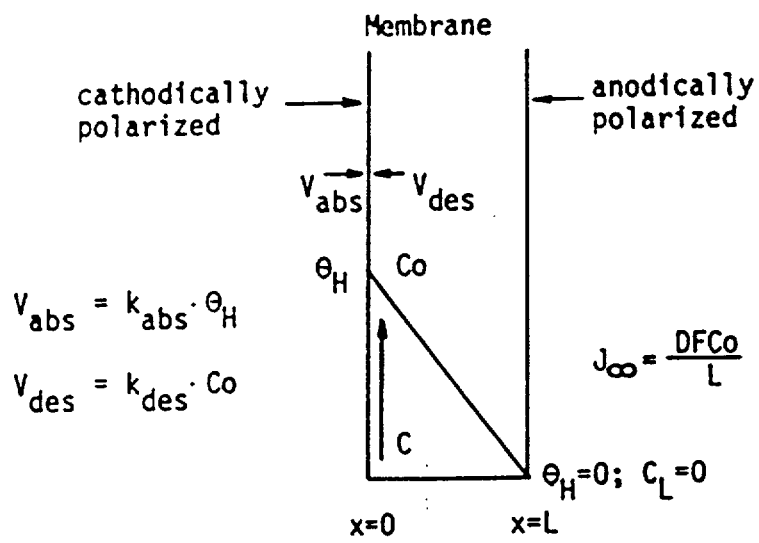


Figure 2. Schematic diagram of membrane cell boundary conditions for the hydrogen permeation measurement.

Appendix 1.

SCOPE OF WORK

For

"The Hydrogen Absorption and Potential Embrittlement of
Candidate High-Level Nuclear Waste Package Containers
in the Proposed Tuff Repository Environment"

In support of the CNWRA Research Project on the Integrated Waste Package Experiments, a 28-month research program, extending from September 1988 through December 1990, is planned. The end product of the research program is to experimentally verify conditions under which proposed waste package container materials absorb hydrogen and the extent to which the materials are embrittled. The program will consist of three phases, as detailed below.

Phase 1. Modification of Experimental Procedures. Modify existing measurement procedures and experimental equipment to permit the conduct of hydrogen permeation studies at temperatures expected at container surfaces in both liquid and vaporous tuff repository environments. (It is anticipated that several hundred years will be required for the temperature at the surface of a waste package container to decrease from an initial value of about 230°C to the boiling point of water under repository conditions, approximately 95°C during this period, it is anticipated that a vaporous environment will be in contact with waste package containers. After the temperature has decayed to approximately 95°C, it will be possible for a liquid environment to be in contact with the containers.)

In this research effort, a simple electrochemical method of measuring the absolute flux of hydrogen through a membrane resulting from a given combination of hydrogen atoms concentration (O) and absorption rate constant k_{abs} will be used.

The basic effort in Phase 1 will be to modify ambient temperature techniques to operate at temperatures in the range of 75°C to 150°C (i.e., the range where the effect of hydrogen can be studied without the complicating factors of high corrosion rates and oxide formation at temperatures >150°C), with sufficient sensitivity to allow the parametric study proposed in Phase 2.

Investigations will be conducted in autoclaves using tubular specimens. Exploratory tests will be conducted in J13 well-water simulate and/or environment identified by CNWRA, producing hydrogen evolution on the outside of the tube by cathodic polarization. The conditions to be used on the inside detection surface of the tube will be defined by investigation, along with the final design of the membrane specimen to be used.

Phase 2. Experimental Studies. The procedures and equipment developed in Phase 1 will be used to define the extent and rate of hydrogen absorption in the candidate container alloys exposed in liquid and vaporous environments as functions of factors such as temperature, environmental composition (e.g., water chemistry and gaseous composition), metallurgical condition (e.g., welded vs base metal, sensitized vs solution annealed, etc.), and state of stress.

Phase 2 investigations will be used to evaluate hydrogen absorption, if any, as a systematic fraction of temperature, environment composition, state of stress and alloy composition. The influence of stress (such as may result adjacent to a weld) will be evaluated using a hollow tensile sample, the gage section of which is the permeation membrane.

For conditions under which hydrogen is absorbed by an alloy tests will be conducted to define the degree, if any, of hydrogen embrittlement, (HE). Two test procedures are currently contemplated:

- 1) Slow-strain rate tests under conditions of cathodic polarization followed by fractographic examination.
- 2) Constant load tests conducted under cathodic polarization.

The results of these test will provide the basis for long-term tests.

Phase 3. Evaluation of Radiation Effects. The contractor will assist the CNWRA in this phase to evaluate the combined effects of gamma radiation and repository environments on absorption of hydrogen by candidate container alloys in liquid and vaporous environments as a function of radiation intensity and other factors show to be important in Phase 2, e.g., temperature, environmental composition, metallurgical condition, state of stress, etc. If effects of radiation are expected to be significant, test in Phase 3 will be conducted by the Center and Southwest Research Institute (SwRI) staff, with support from the contractor, in radiation test cells located at SwRI. To minimize uncertainty in the program results, test equipment developed in Phase 1 and employed in Phase 2 would be transported to SwRI and used in Phase 3.

Test Materials

The experimental program includes the evaluation of the following six candidate alloys that presently are included in the consultation draft of the NNWSI site characterization plan:

Type 304L stainless steel;

Type 316L stainless steel;

Iron-nickel Alloy 825;

CDA 102 (oxygen-free, high conductivity copper);

CDA 613 (8% aluminum bronze); and

CDA 715 (70Cu-30Ni).

It is anticipated, however, that Type 304L stainless steel may be replaced by another material, such as Hastelloy C22, and it is possible that other changes in candidate alloys may occur as a result of ongoing DOE studies. Therefore, the proposed program will be sufficiently flexible to permit substitution for one or more of the alloys currently included in the NNWSI site characterization plan.

When one of the candidate alloys is designated by DOE as the reference material, (indicating that DOE currently believes it is the material most likely to be recommended for use in waste package containers), a greater portion of the program effort will be devoted to the study of the reference material than to the other five alloys.

Candidate alloys will be tested in the heat-treatment conditions in which they are expected to be used (e.g., annealed in the case of types 304L and 316L stainless steel and Alloy 825) and in additional conditions which may be produced as a result of welding or other fabrication procedures, or long-term exposure in the repository (e.g., sensitized for welded types 304L and 316L stainless steel and Alloy 825).

Environments

Data will be developed for the three general environmental cases described below:

Case 1. This case is intended to simulate conditions expected in the repository after the surface temperature of containers has decreased below the boiling point of water. A liquid with a composition that is believed to be representative of ambient water in the tuff formation should be used. Critical aspects of the chemistry (e.g., pH and fugacities of H_2) will be controlled. This may require a circulating (open) system apparatus. Tests will be conducted to examine the effects on hydrogen absorption of variation in these critical parameters. Specimens will be exposed in the liquid phase and in the vapor above the liquid at a temperature of approximately $90^{\circ}C$.

Since concentration of dissolved salts is most likely to occur at the liquid-vapor interface, consideration will also be given to exposing selected test specimens simultaneously to the liquid and the vapor phases.

Case 2. This case is intended to simulate compositional changes in water that may occur as a result of soluble species leached from the rock. Liquid compositions will be varied between experiments to simulate those that are anticipated to be present after long-term contact with tuff. Currently, such data do not exist, however, suitable data may become available as a result of studies to be conducted by the Center or DOE. As in the Case 1 tests, specimens will be evaluated in the liquid and vapor phases, and consideration will be given to exposing selected test specimens simultaneously to the liquid and the vapor phases.

Case 3. This case is intended to simulate conditions which may be present in the tuff repository during the initial period when no liquids are expected because of high container temperatures. Test exposures should be conducted in vaporous environments at several temperatures in the range of $100^{\circ}C$ to $230^{\circ}C$. Fugacities of all components in the gas phase will be controlled.

The vapor phases evaluated will include: dry air, to simulate conditions when no water is present in the environment; and a steam environment, to simulate vaporized repository water. In the latter case, it is proposed that the vapor phase be generated in the test apparatus by evaporation of the liquid to simulate natural concentration of dissolved salts on test specimen surfaces.

The detailed chemical compositions for the three cases will be developed by the Center and communicated to the Contractor prior to initiation of Phase 2 testing.

Key Personnel

Dr. B. E. Wilde will act as project manager and the principal investigator (PI) of the proposed program and will be responsible for all fiscal and technical aspects of the program. Dr. Wilde will be the key personnel for this program.

He will be assisted by a full-time Post Doctoral Research Fellow and two (2) Graduate Research Assistants. The program staff will be personally supervised by Dr. B. E. Wilde and will be selected so as to be free of conflicts of interest by CNWRA with respect to DOE high-level nuclear waste programs.

Quality Assurance

The proposed program will be part of, and subject to, the quality assurance (QA) requirements applicable to the Project Plan for Integrated Waste Package Project prepared by CNWRA for the NRC under contract No. NRC-02-88-005.

The PI will work with the Center QA Staff during the first 6 months (Phase 1) to develop a QA program. Such an approved program will be in place prior to the initiation of Phase 2 testing anticipated by September 1989.

Schedule

A scheduled time frame for the program is expected to be September 1988 - December 1990.

It is anticipated that Phase 1 will be initiated by September 1, 1988, and will continue through September 1, 1989.

Reports

Brief progress reports will be submitted every four weeks. These reports will include:

- o Technical progress during the period.
- o Technical problems identified during the period and corrective actions planned.
- o Activities planned for the next period.
- o Cost data.

More detailed summary reports will be submitted at periodic intervals to be decided upon. It is anticipated that the first such report will be due at the mid-point of calendar 1989 and that subsequent reports will be due at the ends of calendar 1989 and calendar 1990.

Appendix 3. Parameters for electrodeposition of palladium.

Bath Composition:

Palladium as Pd(NH ₃) ₄ Br ₂	30 g/liter
Ammonium Bromide	45 g/liter
pH	9.2
Temperature	50°C
Current Density	0.4 mA/cm ²
deposition rate	greater than 2.5 um/hr

References:

- 1) N.R. Rhoda, J. Electrochemical Soc., 108, 707, (1961).
- 2) S.D. Cramer and D. Schain, Plating, 22, 516, (1969).
- 3) F. Pealstein and R.F. Weightman, Plating, 22, 1158, (1969).
- 4) Modern Electroplating, Ed. F.A. Louenheim, J. Wiley and Sons, (1974).

Appendix 5. Palladium plasma deposition parameters.

Target	2 inch by 2 inch thickness
Source	2 inch diameter Pd disc
Sputter yield	2.4
Cathode voltage	0.6KEV
Target angle	90° to incident beam
Temperature	25°C

Target specimen was abraded on target surface using 600 grit silicon carbide paper followed by ultrasonic cleaning in acetone and warm air drying prior to insertion in the vacuum chamber.

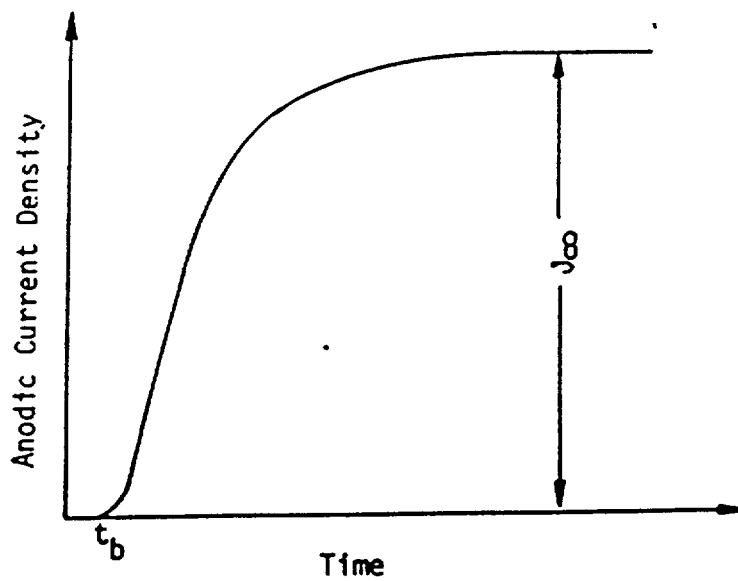
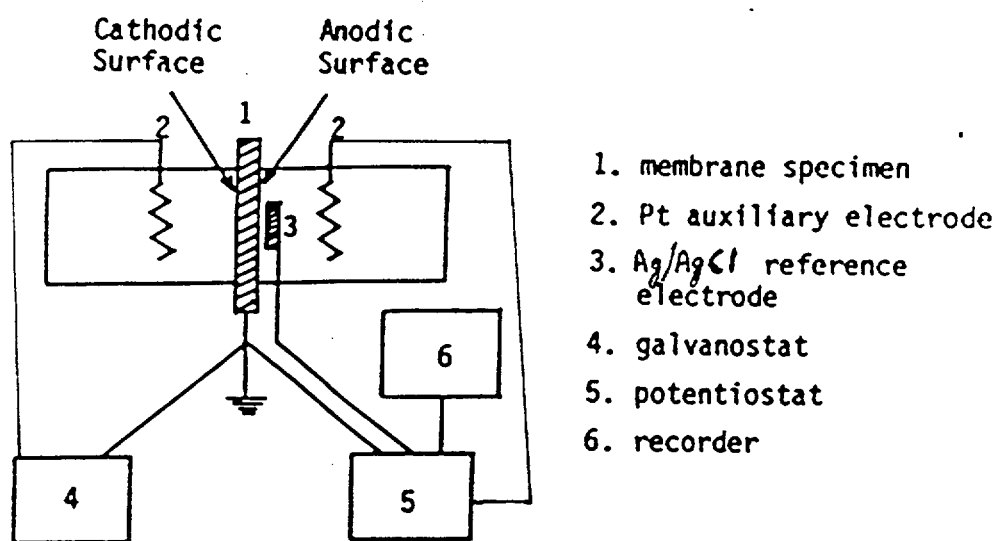
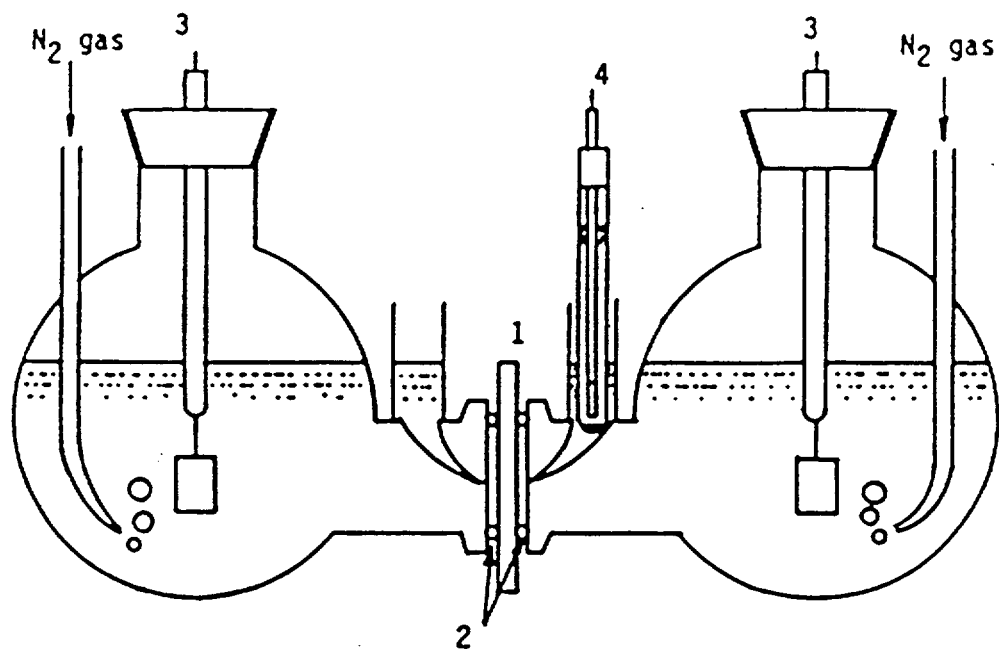


Figure 3. Schematic diagram of a typical hydrogen permeation trace.



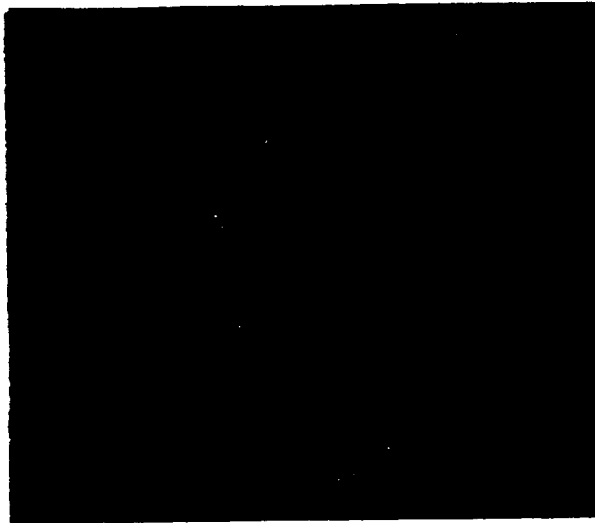
- 1. membrane specimen
- 2. Pt auxiliary electrode
- 3. Ag/AgCl reference electrode
- 4. galvanostat
- 5. potentiostat
- 6. recorder

Figure 4. Schematic diagram of the electrical circuits employed in the hydrogen permeation experiments.



- | | |
|---------------------------|--------------------------------|
| 1. Membrane specimen | 2. Rubber O-ring |
| 3. Pt auxiliary electrode | 4. Calomel reference electrode |

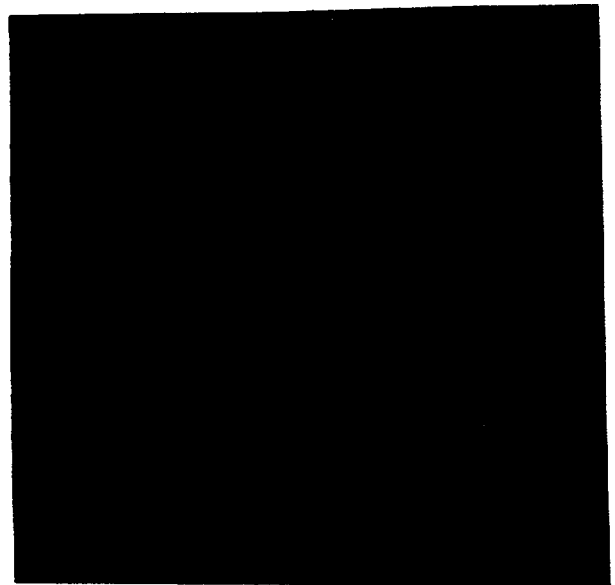
Figure 5. Schematic diagram of the glass cells used for the high temperature hydrogen permeation measurements.



Type 316L stainless steel



Incolloy 825



Hastelloy C22

Magnification 1000X

Figure 6. Typical metallographic microstructures of the materials used in this investigation.

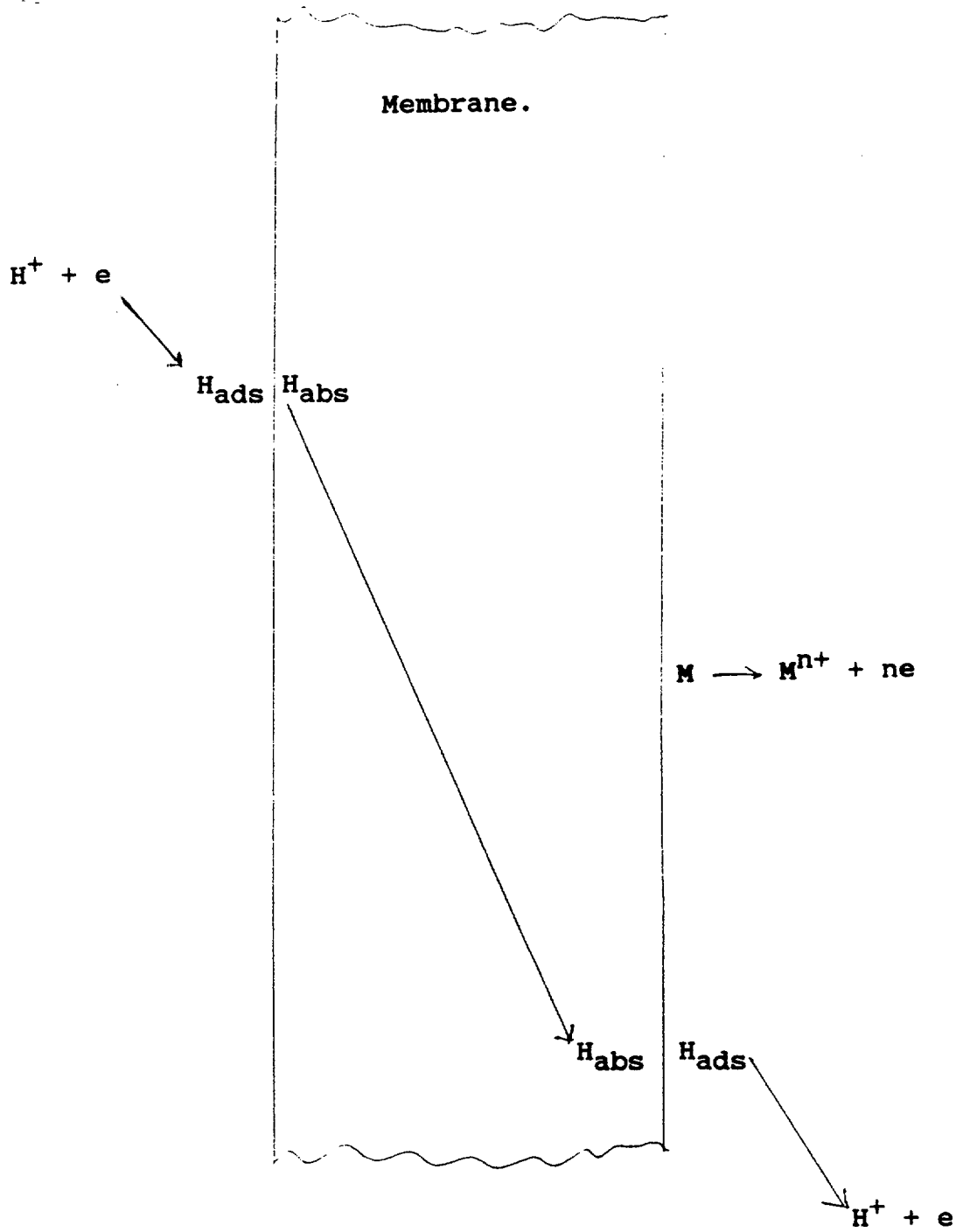


Figure 7. Membrane reaction scenarios occurring during a hydrogen permeation experiment.

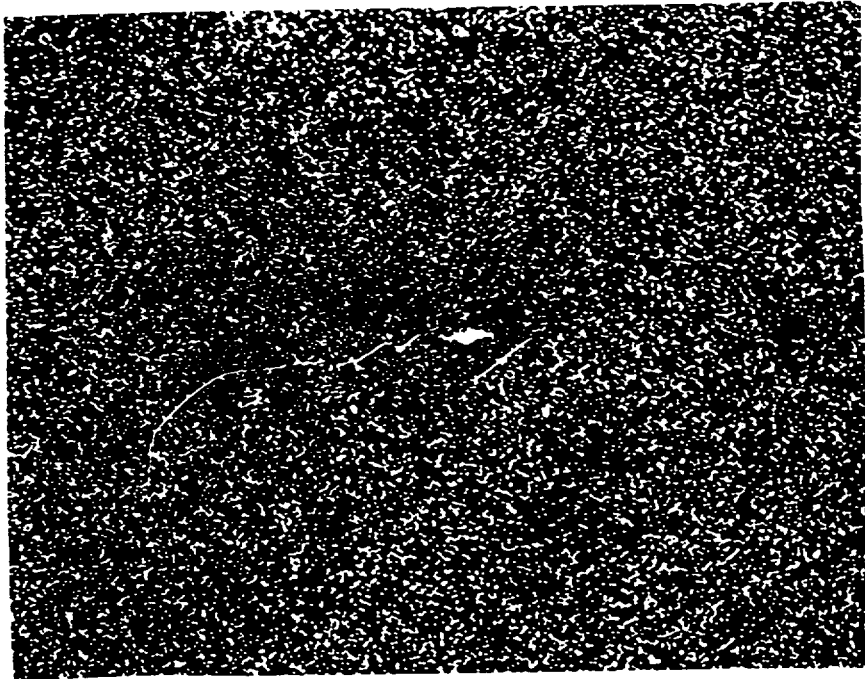
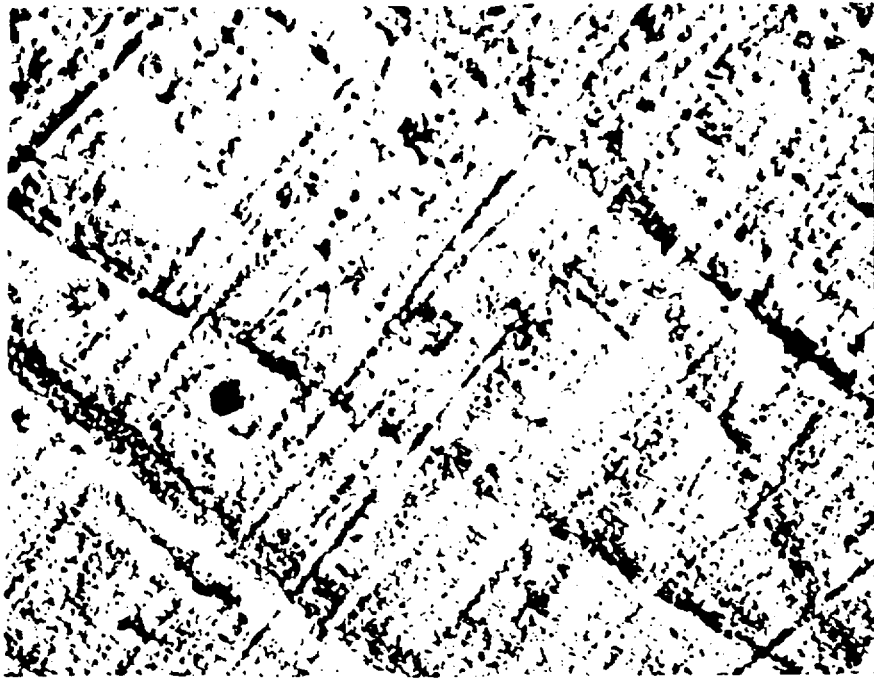


Figure 8. Typical electroless palladium deposit on carbon steel at 2000X magnification and SEM palladium EDAX dot mapping.

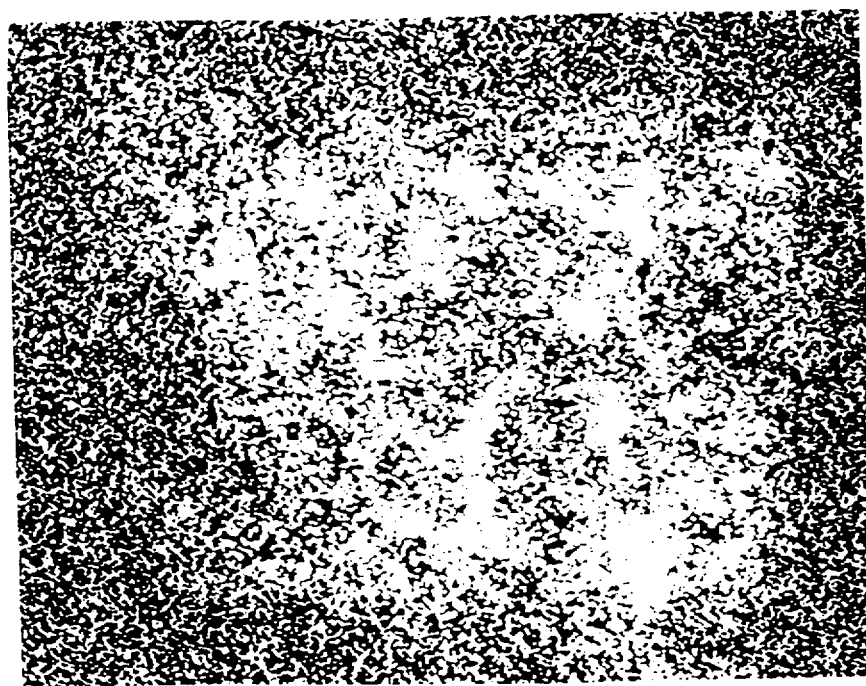
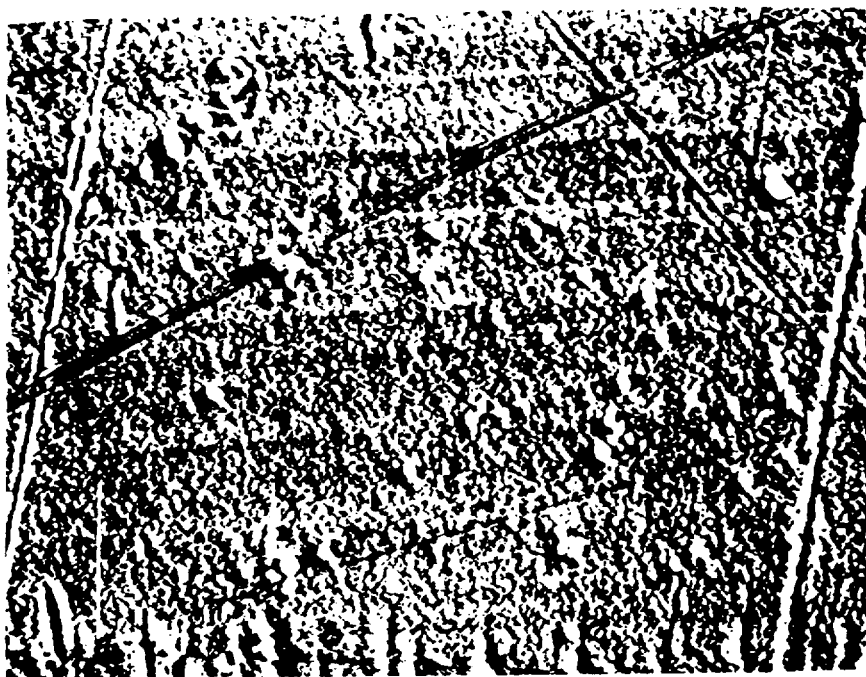


Figure 9. Typical plasma palladium deposit on C22 at 2000X magnification and SEM palladium EDAX dot mapping.

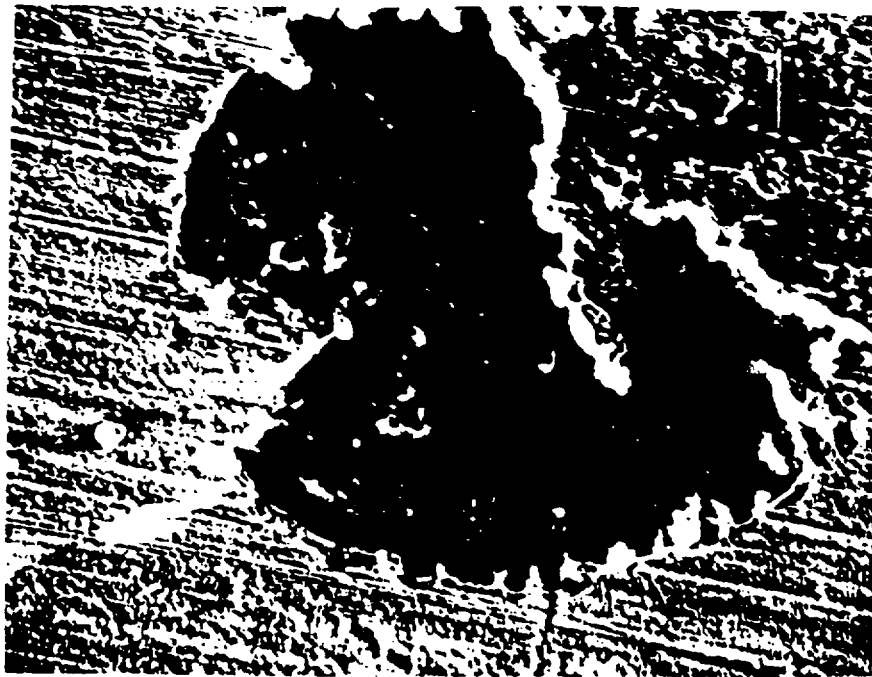


Figure 10. Example of the galvanic corrosive attack observed on palladium coated carbon steel at 1000X magnification .

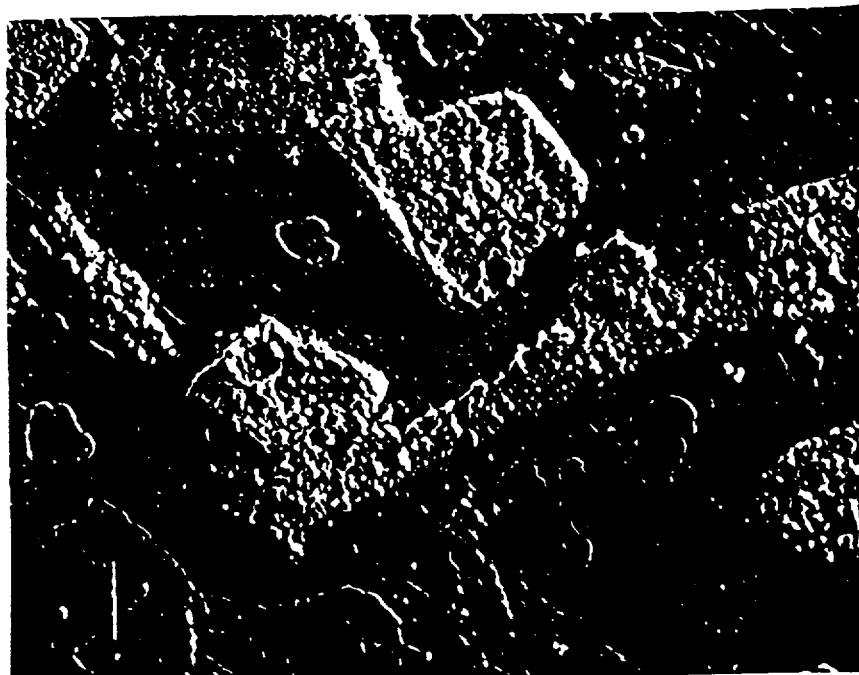


Figure 11. Example of the galvanic corrosive attack observed on palladium coated C22 at 1000X magnification.

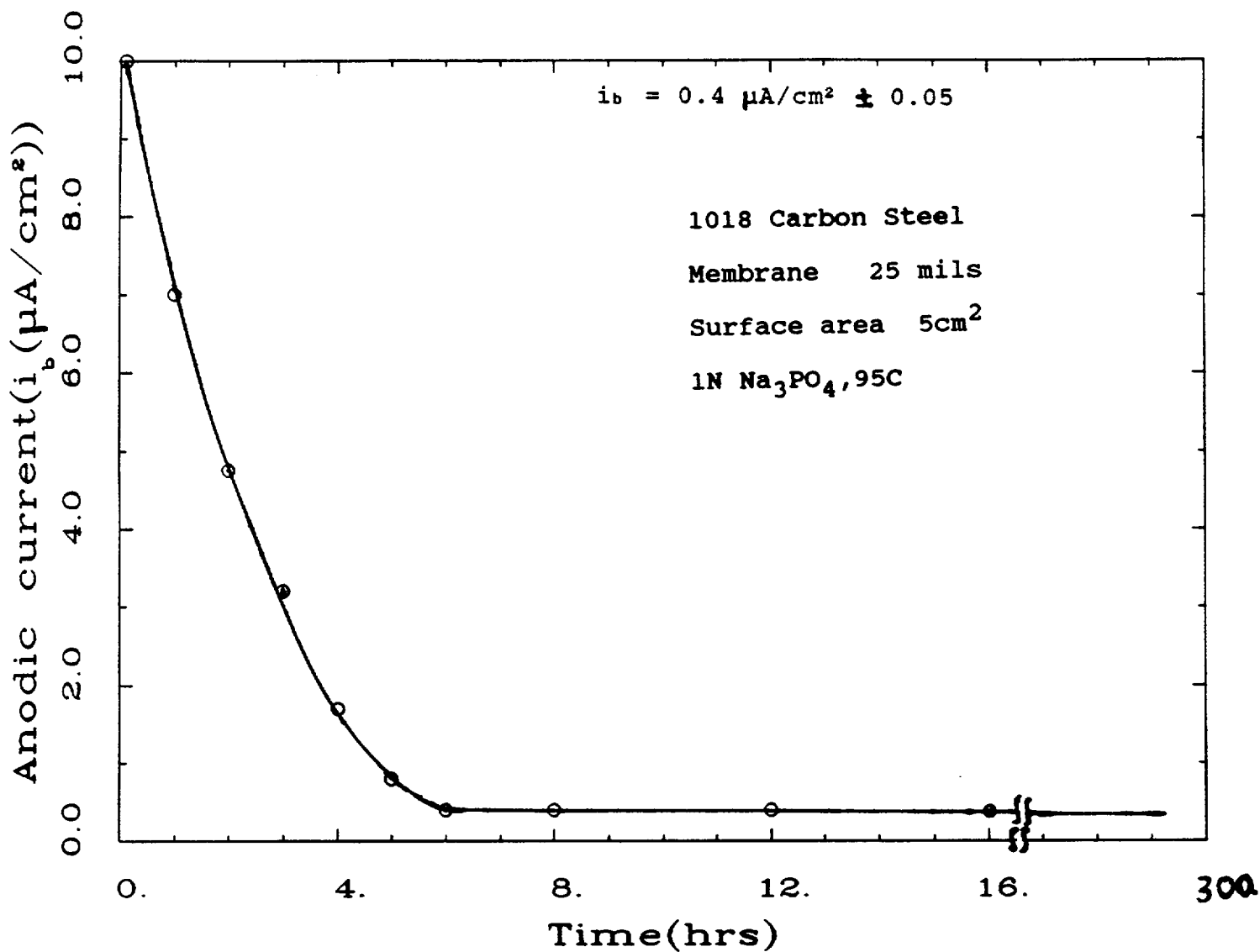


Figure 12. Background current density/time plot for carbon steel in 1N Na_3PO_4 solution at 95°C.

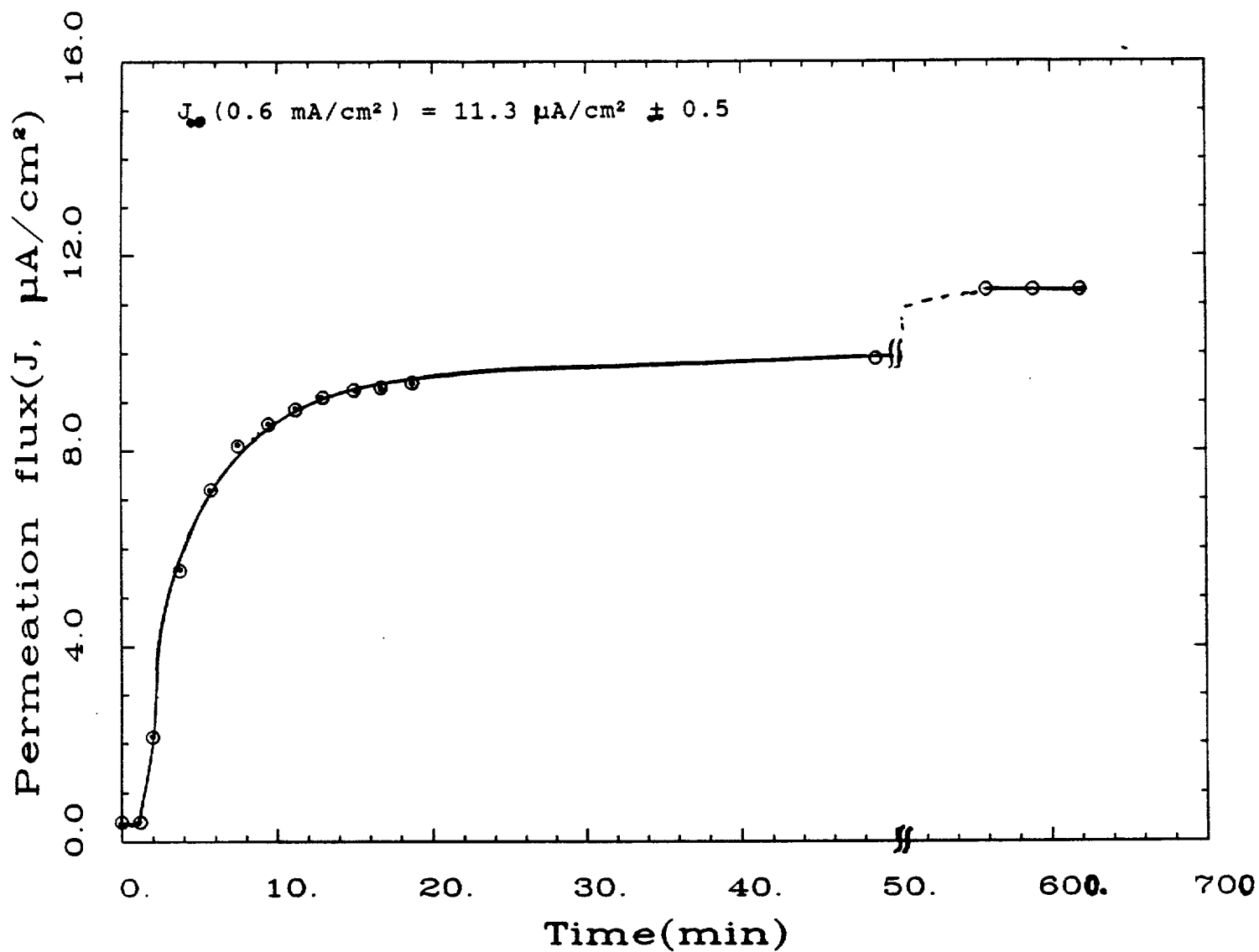


Figure 13. Hydrogen permeation/time curve obtained on carbon steel in 1N Na_3PO_4 solution at 95°C .

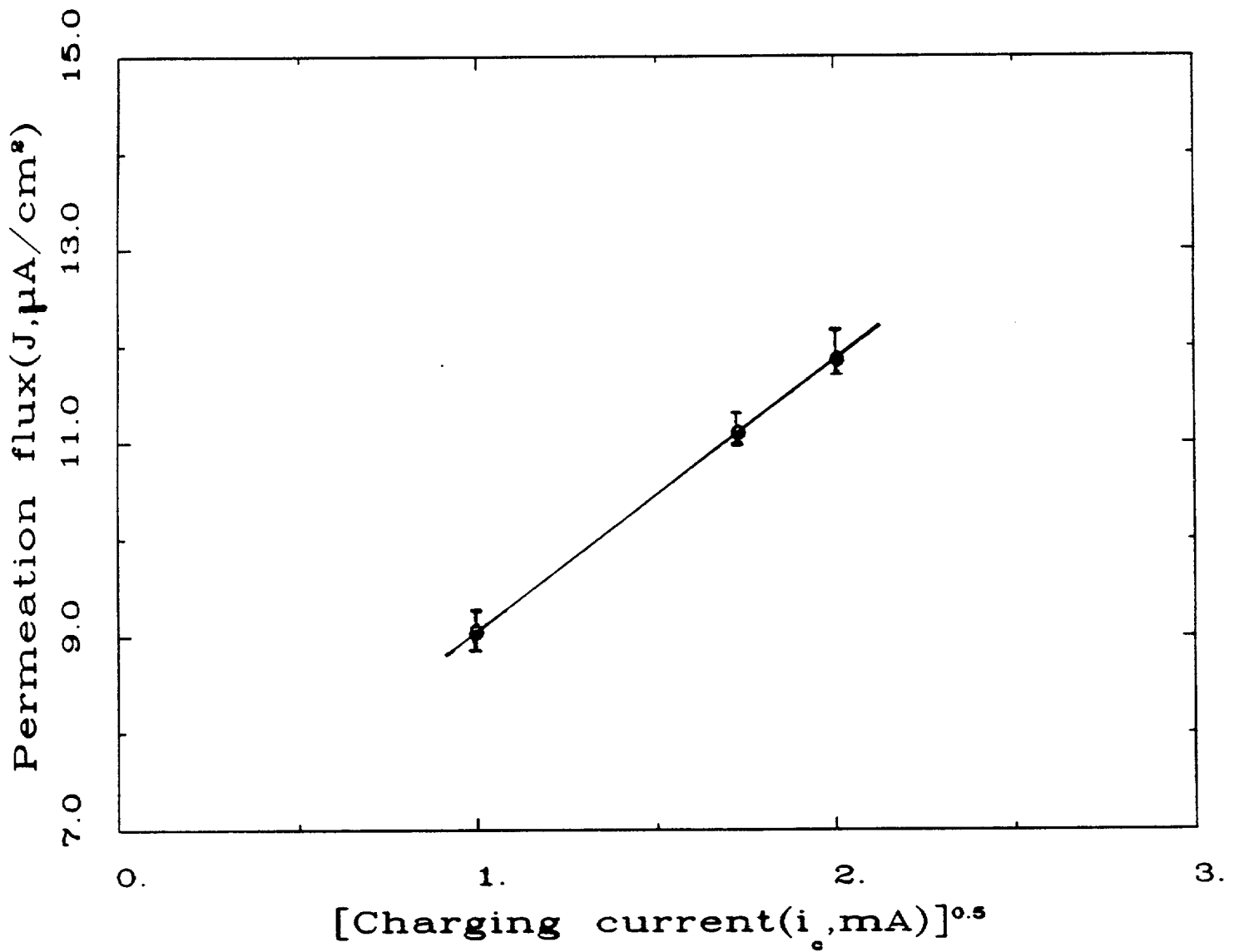


Figure 14. Relationship between steady state permeation flux and the cathodic charging current density for carbon steel.

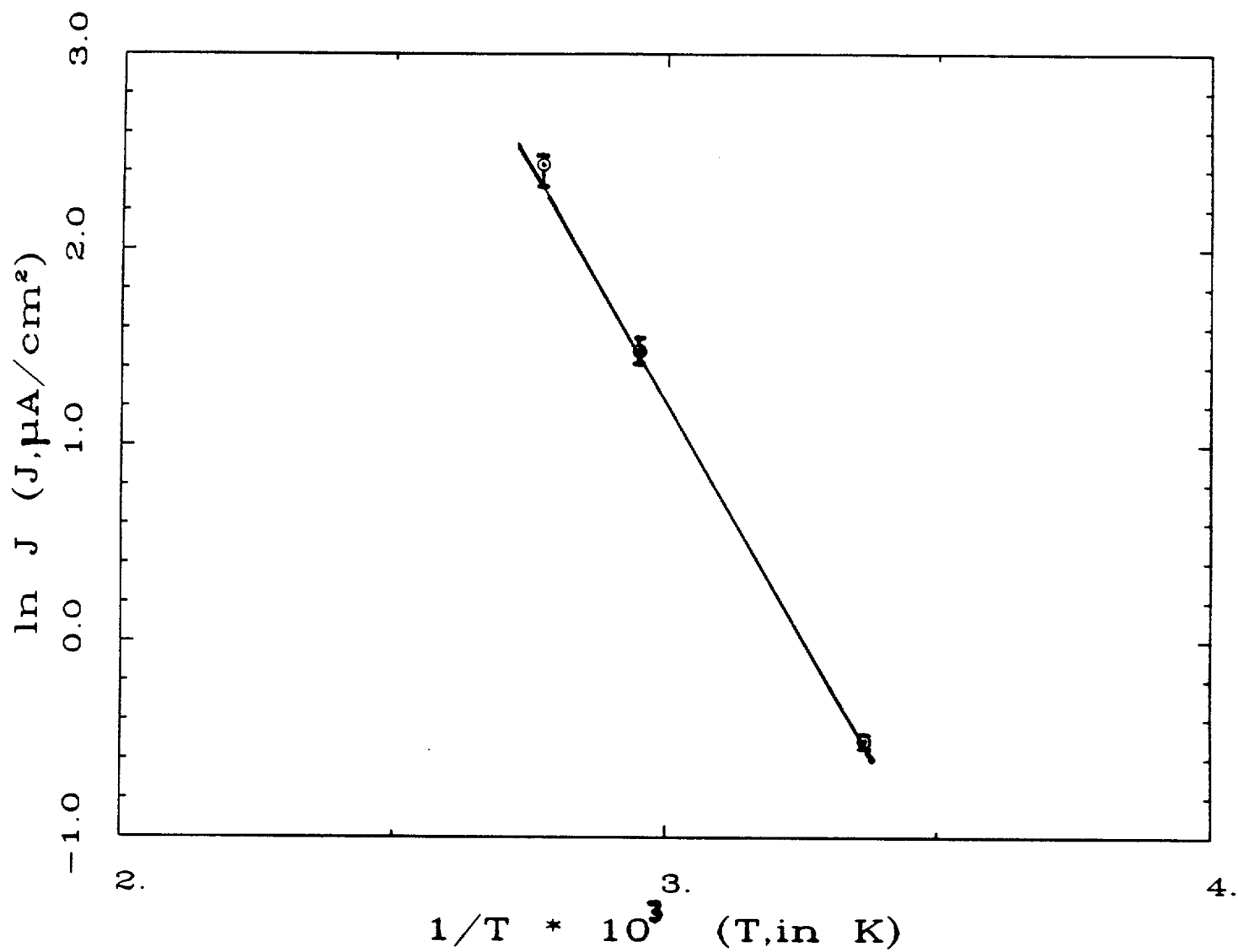


Figure 15. Relationship between the permeation flux and temperature for carbon steel in 1N Na_3PO_4 solution at 95°C .

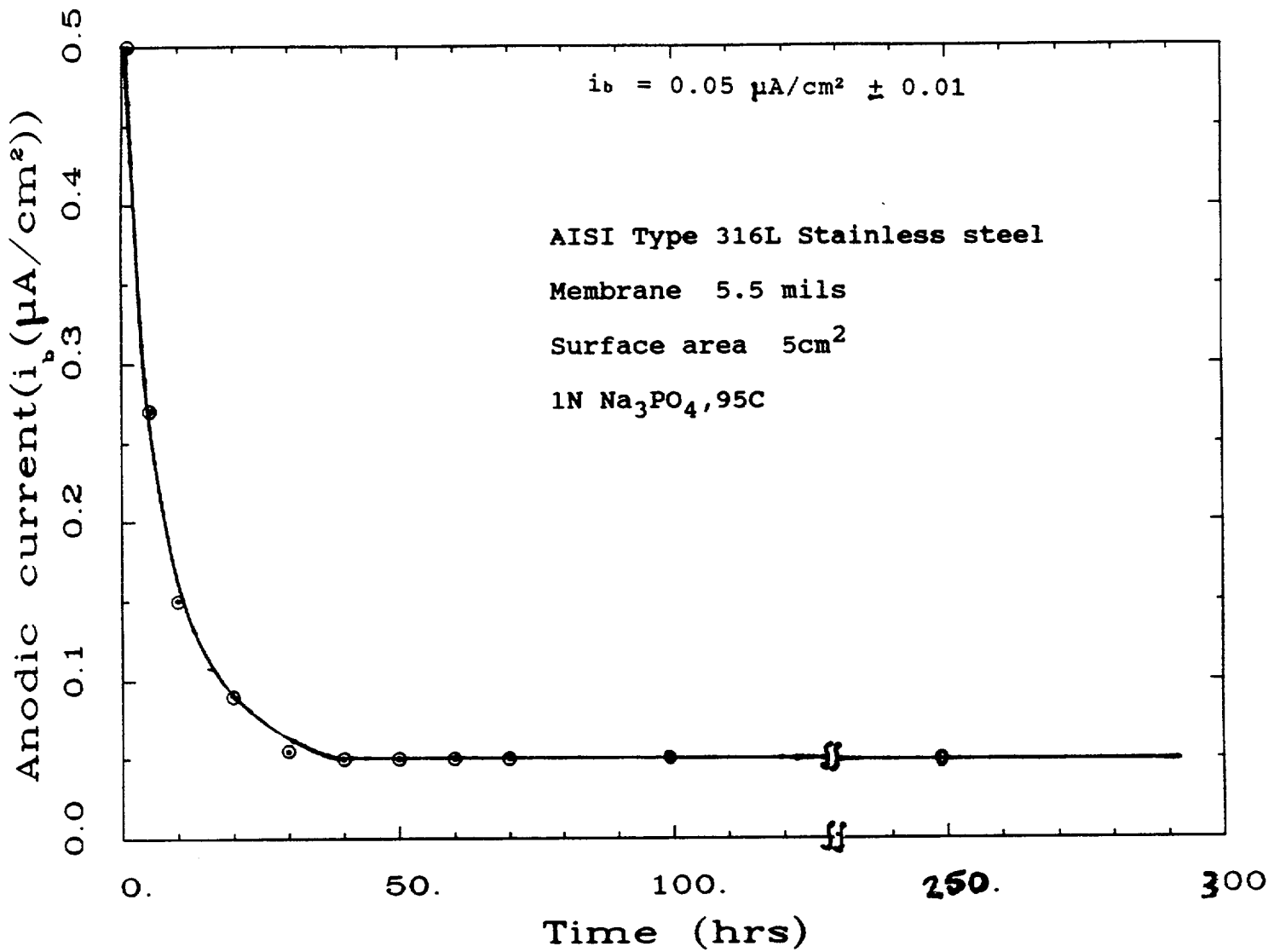


Figure 16. Background current density/time relation for type 316L stainless steel in 1N Na_3PO_4 solution at 95°C .

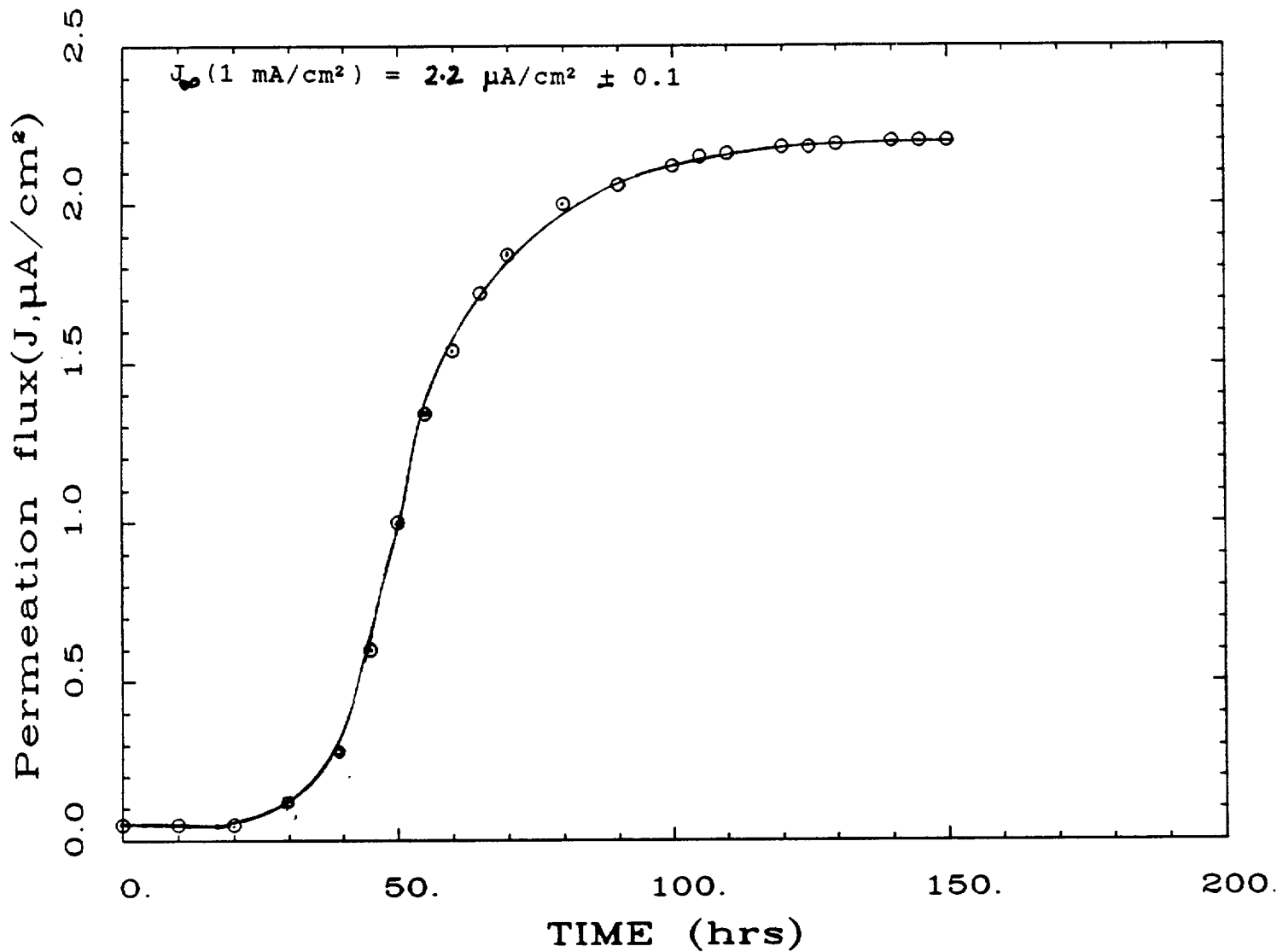


Figure 17. Experimental hydrogen permeation curve for type 316L stainless steel in 1 N Na_3PO_4 solution at 95°C.

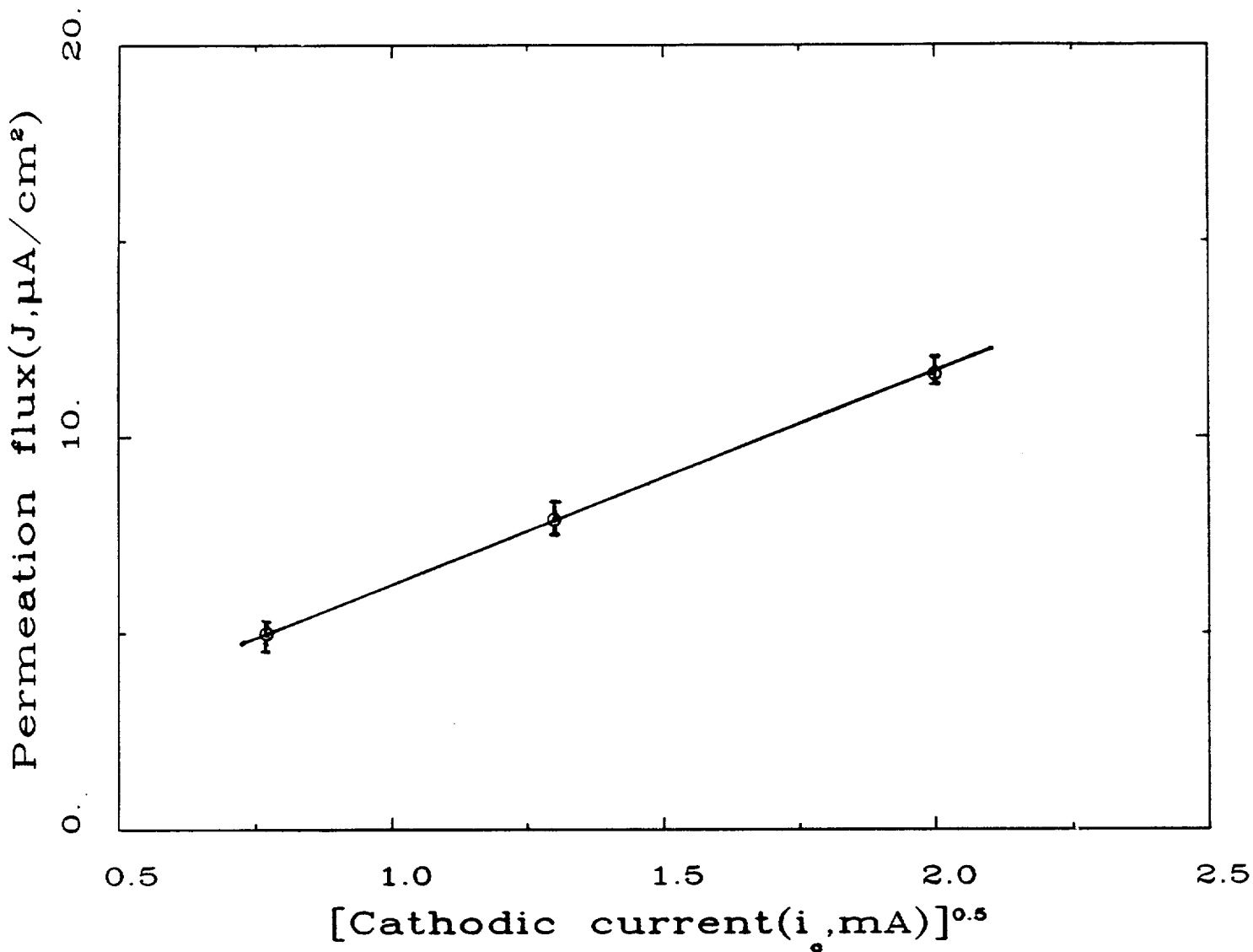


Figure 18. Relationship between the steady state hydrogen permeation flux and cathodic charging current for type 316L stainless steel observed in 1N Na₃PO₄ solution at 95°C.

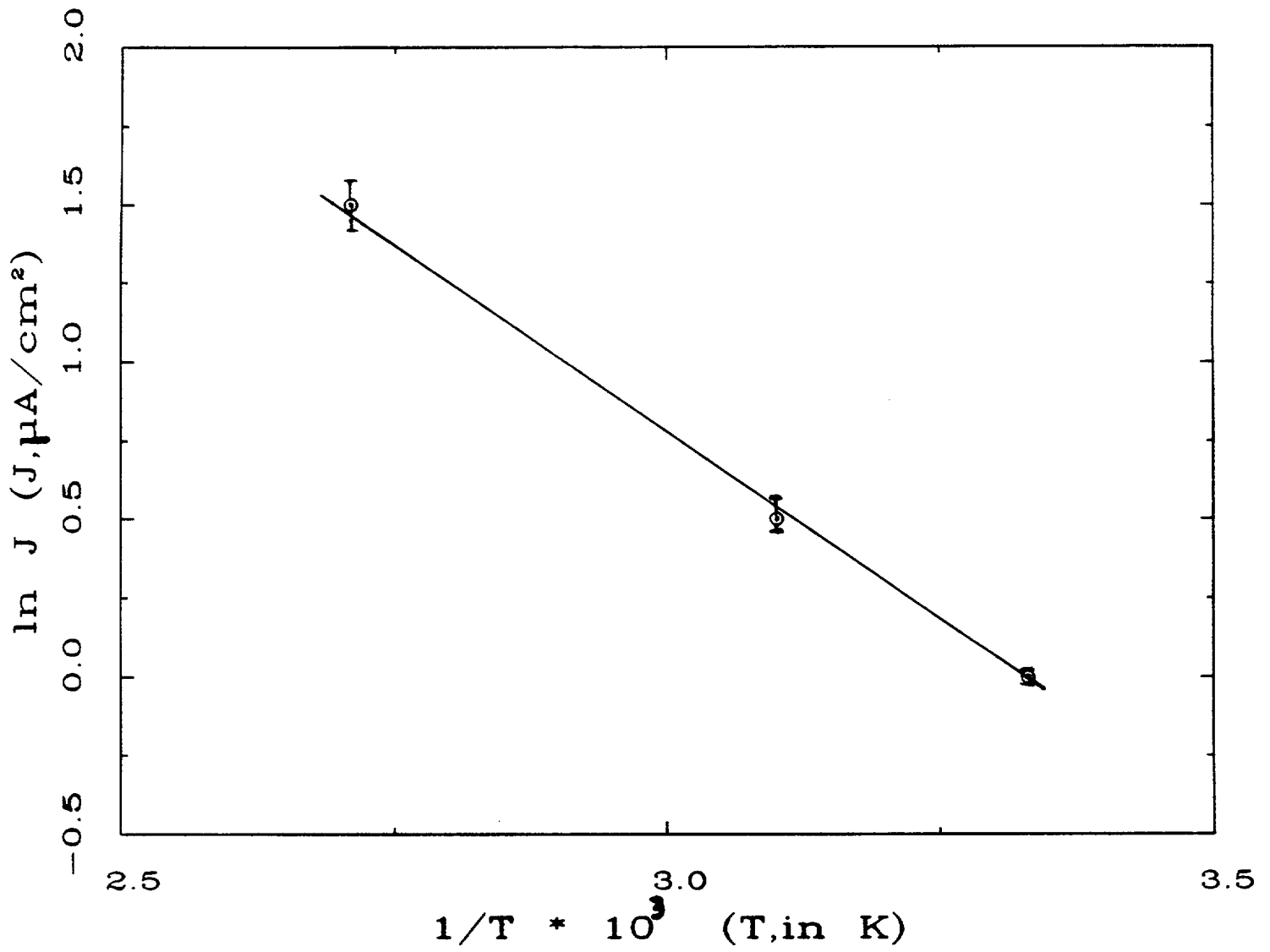


Figure 19. Relationship between steady state hydrogen permeation rate and temperature for type 316L stainless steel in 1N Na_3PO_4 solution.

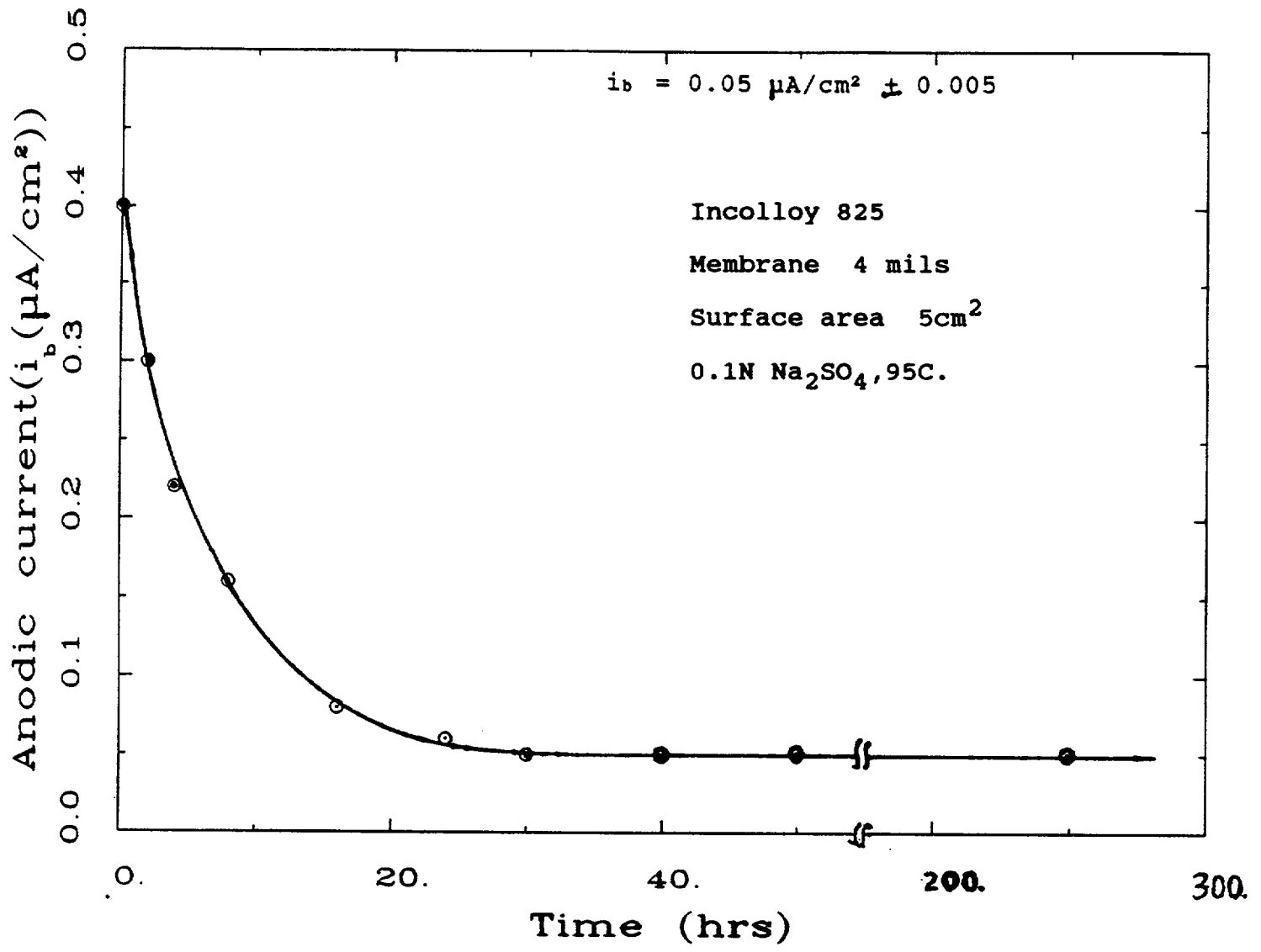


Figure 20. Background current density /time plot for the I825 alloy in 0.1N Na_2SO_4 solution at 95°C.

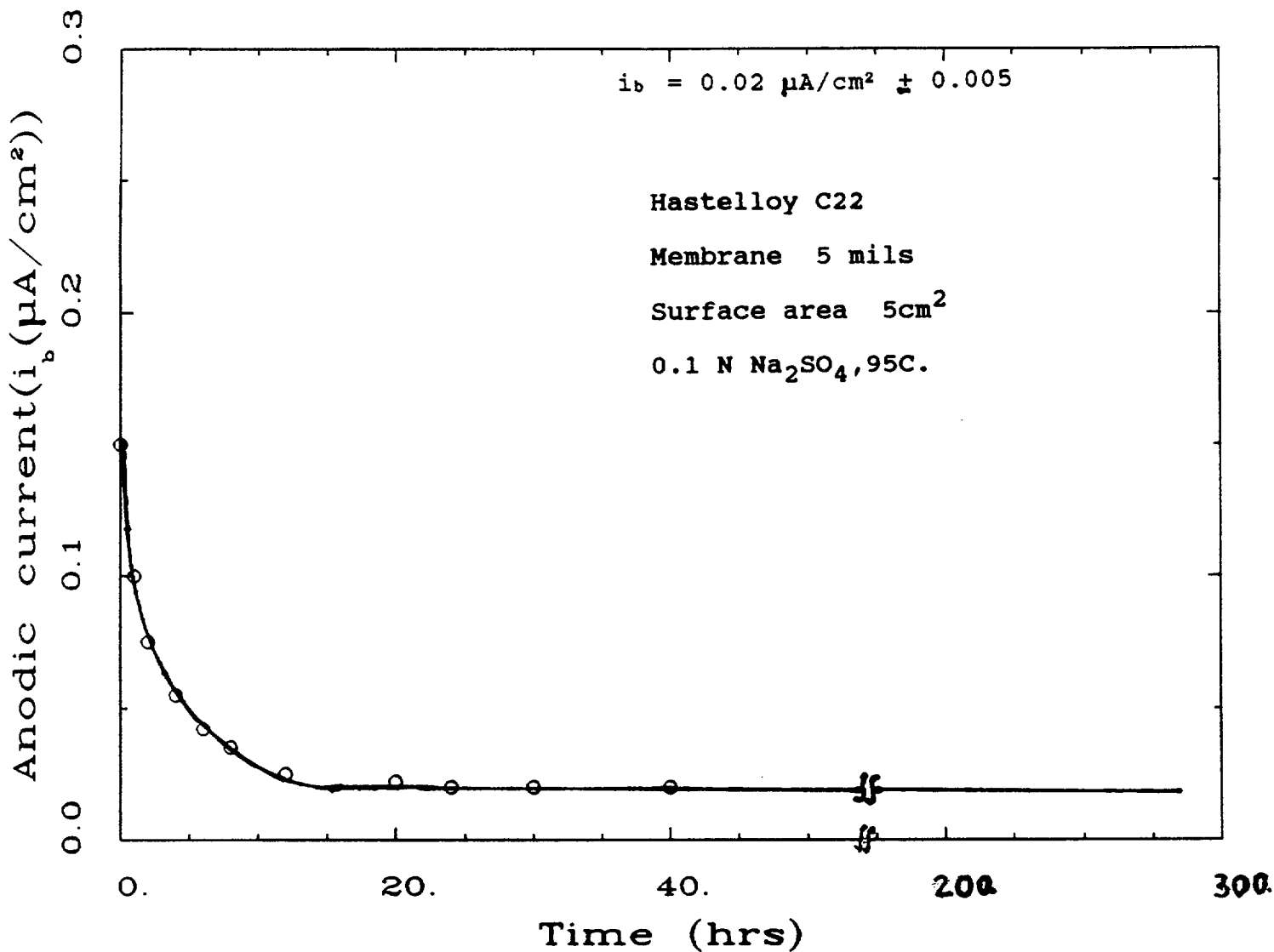


Figure 21. Background current density /time plot for the C22 alloy in 0.1N Na_2SO_4 solution at 95°C.

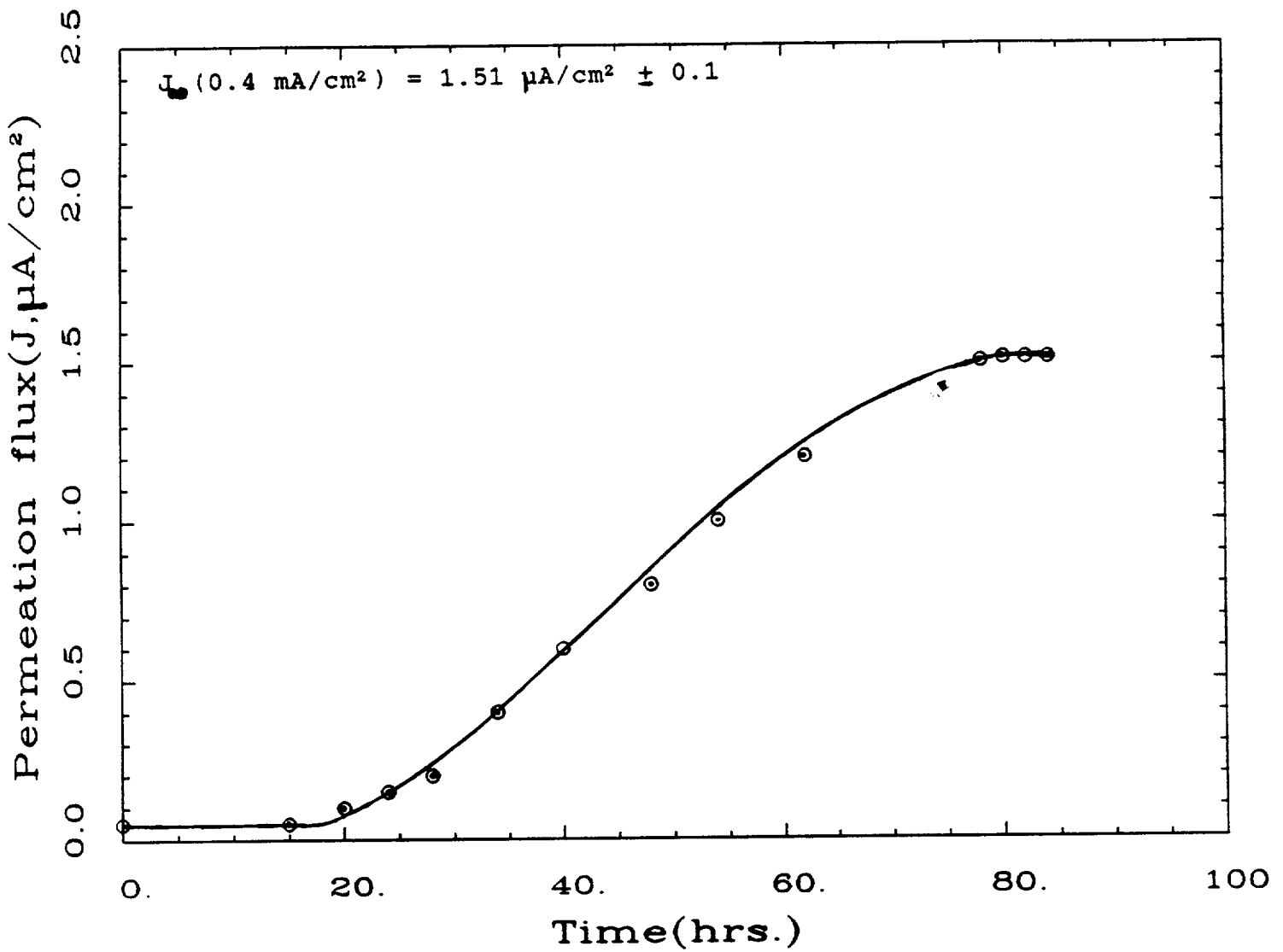


Figure 22. Hydrogen permeation curve obtained on I825 alloy in 0.1N Na₂SO₄ solution at 95°C.

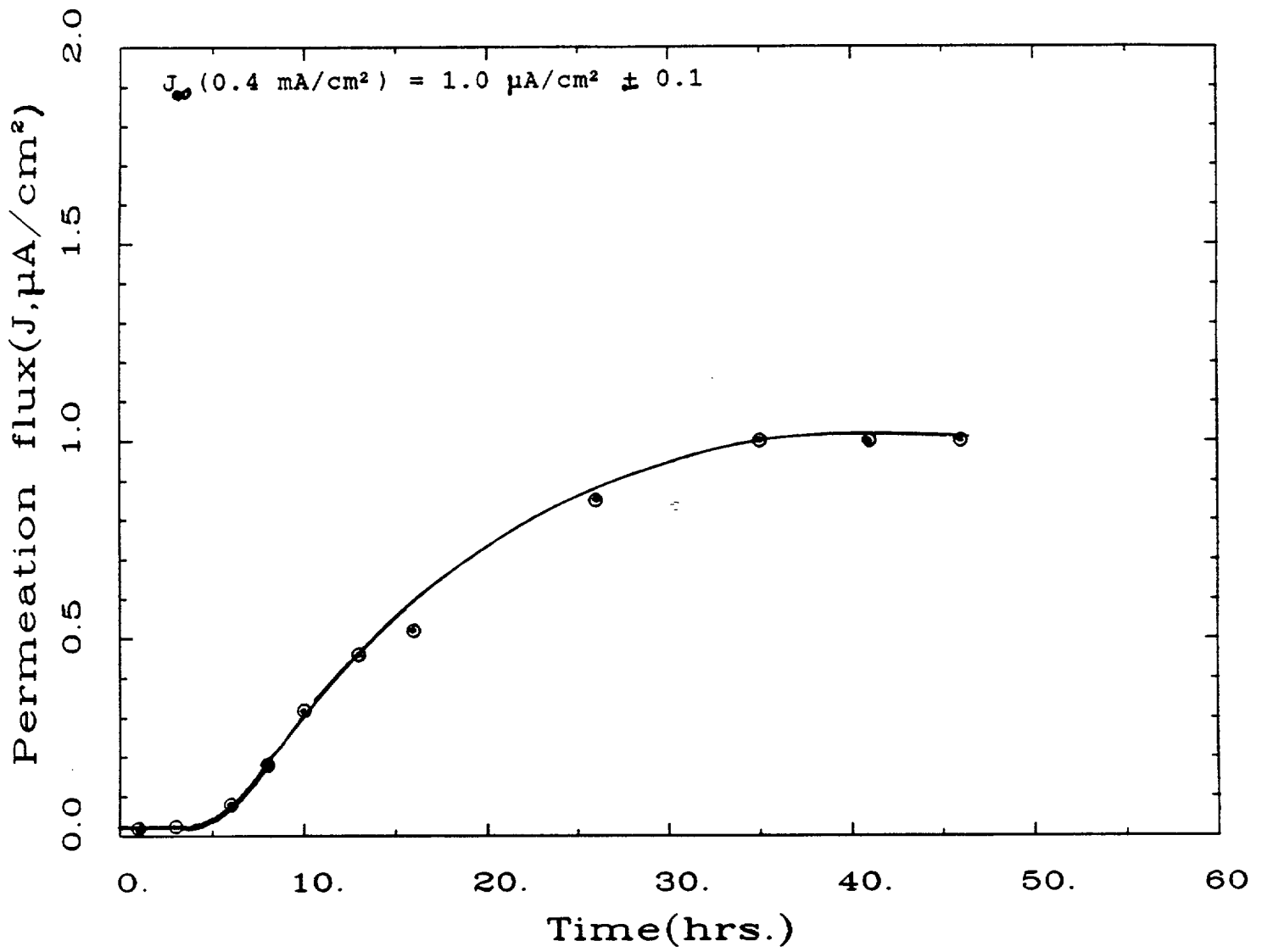


Figure 23. Hydrogen permeation curve obtained on C22 alloy in 0.1 N Na_2SO_4 solution at 95°C.

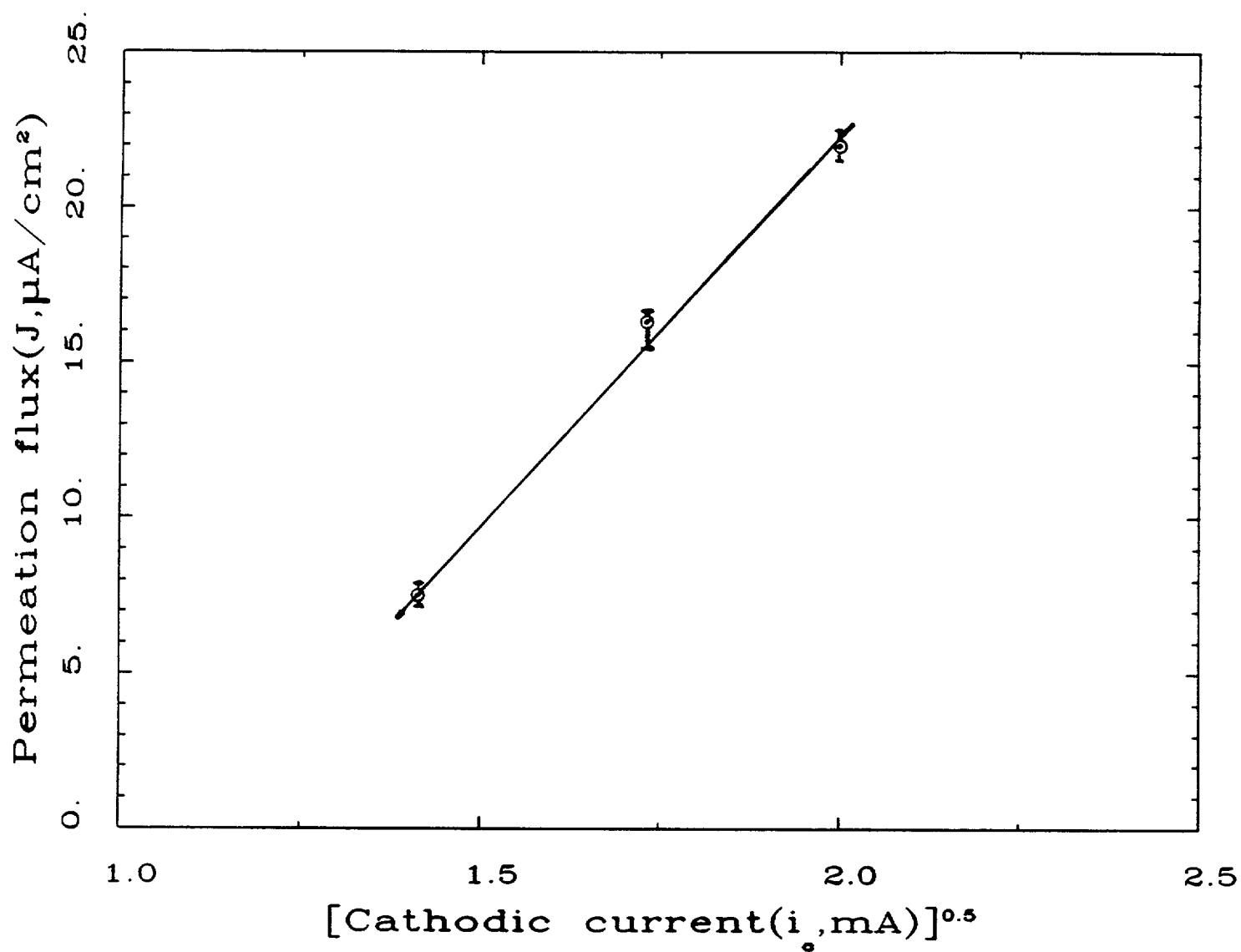


Figure 24. Relationship between permeation flux and cathodic charging current density for I825 alloy in 0.1N Na_2SO_4 solution at 95°C.

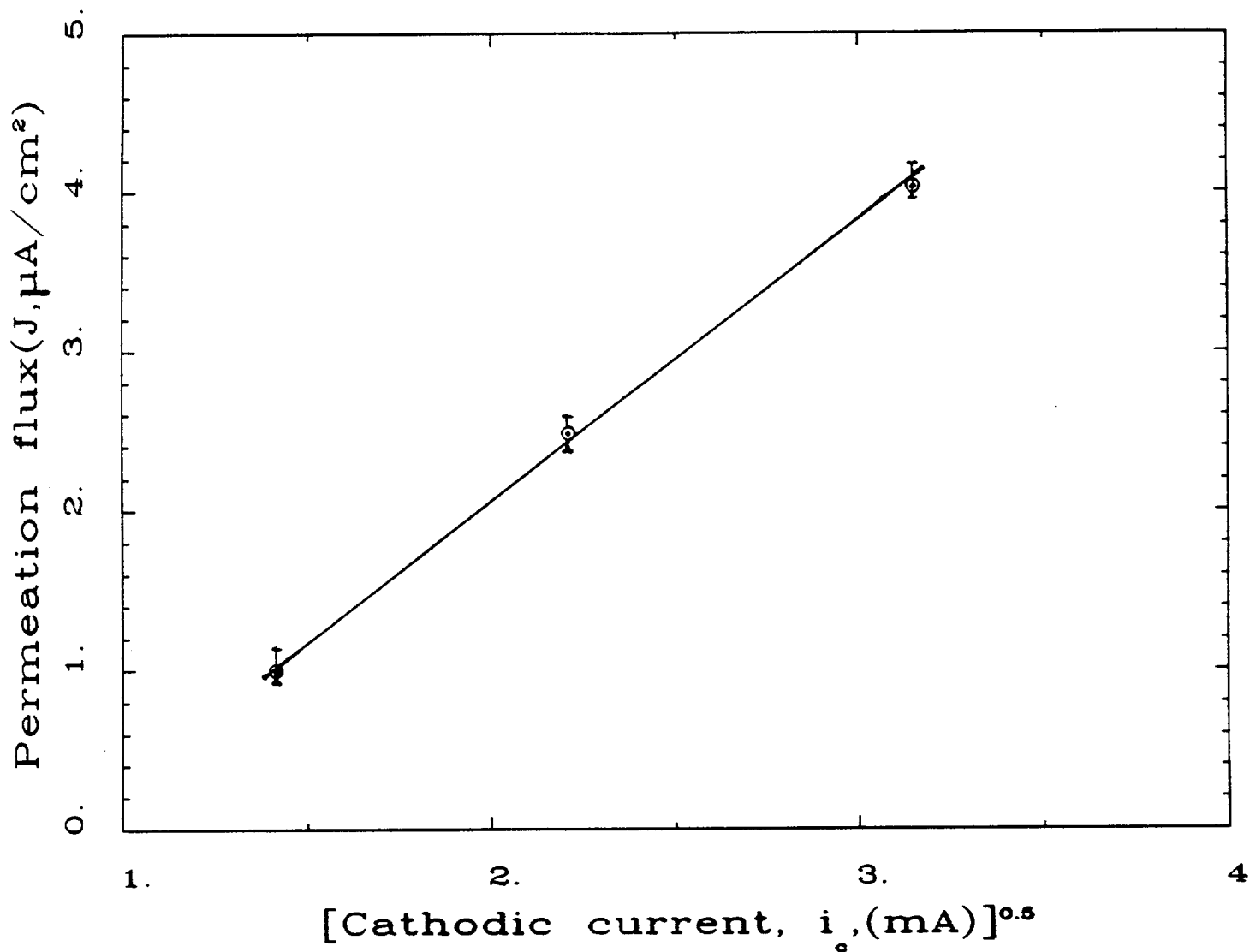


Figure 25. Relationship between permeation flux and cathodic charging current density for C22 alloy in 0.1N Na₂SO₄ solution at 95°C.

Appendix Part 1.1. Data acquisition program used in the study.

Load ISATEST 2

```
90  REM TO MEASURE POTENTIAL AND
    CURRENT AS A FUNCTION OF TIME
    USING ISAAC DATA ACQUISITION SYSTEM.
95  REM TO SAVE DATA IN A NEW DATA FILE
    STATEMENTS 107,108 AND 181 HAVE TO
    BE CHANGED.
    REPLACE DATA FILE NAME WITH THE
    NAME OF THE NEW FILE. BE CAREFULL
    WITH THE SYNTAX!
101 PRINT 'Z,Y,VOLTS,CUR'.
102 N=0
103 D$ =CHS$ (4)
106 PRINT D$;"MON I,C,O"
107 PRINT D$;"OPEN I VS T,D2"
108 PRINT D$;"WRITE I VS T"
110 Z=0
111 REM Z=0 TO 23 TAKES DATA OVER TWO
    DAYS AFTER WHICH Z IS REINITIALIZED
    TO 0 AND DATA LOGGING CONTINUES.
112 FOR Z=0 TO 23
113   Y=1
114   FOR N=0 TO 119
115     & ASSUM,(C#) = 6,(TV)=NUM,(RT)=3,
        (SW)=100
116     NUM=NUM/100
117     & ASUM,(C#)=2,(TV)=CUR,(RT)=3,(SW)=100
```

```

118  CUR=CUR/100
120  NUM=NUM/819.2-2.5
125  CUR=CUR/819.2-2.5
130  CUR=CUR/2
135  REM NUM=VOLTAGE(IN VOLTS)AND CUR=
      CURRENT(IN MILLIAMPS)
140  PRINT"Z","Y","NUM","CUR"
142  Y=Y+1
143  & PAUSE=59
145  NEXT N
150  NEXT Z
155  GO TO 110
160  REM 155 REINITIALITIZES Z TO 0.
      143 IS USED TO ACCOMODATE DATA FROM
      ONE TEST ON A SINGLE DISKET,THE LONGER
      THE TEST,GREATER THE & PAUSE(IN SECS)
181  PRINT D$;'CLOSE I VS T"
205  END.

```

Part 2. The kinetics of hydrogen evolution, absorption, and diffusion in candidate copper based alloys.

By:

C. Miller

B.E. Wilde

2.1 Introduction.

Increasing amounts of nuclear waste generated in the USA, has led to the search for methods of safe disposal to avoid the possibility of causing the public the and the environment serious harm. The current plan envisioned by the Department of Energy (DOE), proposes the burying of high level waste in containers (see Figure 1), that must remain intact for 300 - 1000 years.

One of the major difficulties in implementing this plan is the design of a containment vessel having a guaranteed 100% structural integrity for the above service lifetime. These difficulties are compounded by the need to clearly define the realistic potential modes of failure in the absence of specific environmental parameters. It is relatively easy to find metals which are sufficiently strong and ductile to be considered for this purpose (although this criterion does eliminate many non-metals) but the ability to predict suitability or failure by a corrosion mechanism is not currently available.

Corrosion mechanisms that have previously been considered are stress corrosion cracking and pitting susceptibility to cite a few ¹⁾. Failure by a hydrogen embrittlement mechanism (HE), has been dismissed because of the low corrosion rates of candidate materials in ground water and the fact that the repository environment will be above the dew point of water for the first 300 years. This latter point of view assumes however that corrosion and condensed phase water are necessary for the generation of hydrogen on the container wall.

* see references.

This assumption is, of course, not valid since the generation of hydrogen by gamma radiolysis of steam (and condensed water) will occur due to the radioactivity of the waste.

The candidate alloys currently being considered by the DOE as the principle material of construction are as follows:

- A) CDA 102 (oxygen free, high conductivity copper)
- B) CDA 613 (8% aluminum bronze)
- C) CDA 715 (70%Cu-30%Ni)
- D) Alloy 825 (Ni-Fe-Cr alloy)
- E) Type 304L stainless steel
- F) Type 316L stainless steel

The purpose of the Part 2 investigations is to evaluate the resistance of some of the copper based candidate container materials to generate a technical data base on hydrogen absorption and diffusion to allow estimates to be made regarding possible failure by HE.

The alloys evaluated in Part 2 were the alloys CDA 102 and CDA 715 having the composition and physical properties shown in Table 1.

Copper alloys were included in the DOE list of candidate container materials because (1) they have thermodynamic stability in aqueous environments, (2) they are easily fabricated, (3) they have a simpler metallurgical system than either the iron or nickel based alloys with less potential time-dependent phase changes to consider (see Figure 2), and (4) they are not susceptible to some of the failure mechanisms that stainless steels and high nickel alloys are well known to be ¹⁾.

The temperatures at which the Part 2 studies were conducted

are up to 95°C since the surface temperature of the canisters are estimated to be in this range after approximately 175 years (see Figure 3).

Very little HE work has been conducted on copper and its alloys in the literature. This is almost certainly because of the seemingly rare reported occurrence of HE in these materials. Hagi²⁾ investigated the diffusion of hydrogen at various temperatures through several cupronickels, and made the very interesting discovery that the diffusion coefficient of hydrogen through these alloys has a minimum for a 30%Ni-Cu alloy (CDA 715!). In fact, as seen in Figure 4, the value of the diffusion coefficient at 67°C for this alloy (about 10^{-10} cm².s⁻¹) is less than that for pure copper. A study by DeWulf and Bard³⁾ made the interesting discovery that unless a surface poison (which aids the absorption of hydrogen into a metal) is used as an additive to the catholyte, permeation of hydrogen through a pure copper membrane did not occur at room temperature. From this phenomenon it was postulated that the slow step of hydrogen permeation for copper at room temperature was the discharge process (no relationship between permeation and charging current is predicted by Table 2 for this mechanism). Hence, in the absence of a surface poison, they predict that copper is impervious to electrolytic hydrogen at room temperature. This would seem to make pure copper a material of choice for cladding a material that is needed for mechanical strength but is susceptible to hydrogen embrittlement. It should be noted here that Hagi's work²⁾ used As₂O₃ in the catholyte, so his data for pure copper should be interpreted as the permeation occurring after hydrogen has penetrated the surface of the metal, which according to DeWulf

and Bard does not occur in the absence of a poison. In industrial practice, Hagi's method may actually be quite relevant because of the fact that surface poisons such as phosphorus, sulfur, arsenic, and lead could quite possibly be present on the metal.

As mentioned previously, one possible failure mode which, to date, has not been sufficiently investigated is that of HE due to the absorption of hydrogen into the container material and its subsequent affinity for areas of high tensile stress ("hard" areas in the vicinity of welds, for example). The deleterious effect of hydrogen on metals has been investigated for many years ⁴⁾, although the exact mechanism(s) of embrittlement is still a matter of debate with some researchers ⁵⁻¹⁰⁾. The hydrogen is hypothesized to come from several possible sources. One possible source of hydrogen could be due to a reduction of hydronium ions in acidic solutions or water molecules in alkaline solutions if the container would be in contact with ground water ¹⁾. This is shown by:



Another more probable source is due to the gamma radiation being emitted by the high level waste which can, in the presence of water, produce a hydrogen radical according to:



The last potential source would be hydrogen gas adsorbing directly onto the container's surface:



It is hypothesized that with any of the container materials, and especially the thermodynamically inert copper and copper alloys, the amount of hydrogen from equations (1) and (2) would be quite small in water due to the low corrosion rate of these metals. However, the absorbed hydrogen formed due to gamma radiation could become quite substantial over the years. The product of gamma radiolysis is, in fact, identical to the hydrogen produced by water and hydronium reduction as far as the metal surface is concerned, but because it requires no anodic dissolution of the metal, it can be produced at a high rate independent of the corrosion rate of the container material in contact with steam or water.

Since the absorption and, hence, HE of a material is uniquely controlled by the percent surface covered by adsorbed atoms of hydrogen and by the rate constant of absorption, k_{abs} , the preliminary objectives of Part 2 were as follows:

1. Determine the apparent diffusivity of hydrogen through the two alloys mentioned above at 95°C.
2. Determine the mechanism of the hydrogen evolution reaction on each alloy at 95°C.
3. Determine the rate constants for the discharge, recombination, and the absorption-desorption reactions for each alloy at 95°C.

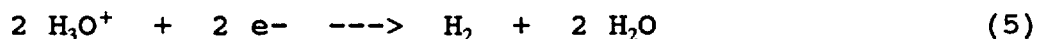
Once these objectives have been realized, other researchers can determine the susceptibility of the copper based alloys to HE at a value of surface coverage of hydrogen that will be found in the presence of gamma radiation.

2.2 Historical background.

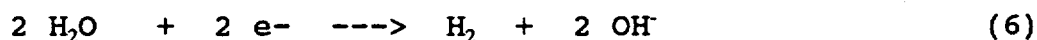
In order to provide the reader with a background necessary to understand the data analyses, a brief review of the electrode kinetic theory of hydrogen evolution and adsorption onto metal surfaces is presented along with the details of the analysis used to determine degree of coverage and the absorption rate constants.

2.2.1 Hydrogen evolution reaction (HER) kinetics.

The hydrogen evolution reaction is one of the most widely studied reactions. It has been shown to occur by a series of steps depicted in Figure 4, in this case, for an iron substrate. The overall reaction in acidic solutions is:



and in alkaline solutions;



The mechanism of the HER is thought to occur by two possible paths. The discharge step followed by either Tafel recombination or electrochemical desorption. The first step in the HER is the charge transfer reaction or the discharge step ; for acidic solutions:



for alkaline solutions:



Subsequent steps are common in both acidic and alkaline solutions. The adsorbed hydrogen atoms (adatoms) either recombine chemically and evolve as hydrogen gas (Tafel recombination):



or react with another proton also to form hydrogen gas (electrochemical desorption):



or the adatom can enter the metal lattice as absorbed interstitial hydrogen atoms:



It is the hydrogen absorption step (eq 11) that is responsible for hydrogen embrittlement leading to sudden structural failures.

A mechanism that does not involve the adsorbed state has been proposed by some Russian workers ^{11,12}. More recently, Ohnaka and Furutani ¹³ have postulated that in neutral and alkaline solutions Type 304 stainless steel absorbs hydrogen by a direct entry mechanism.



Considering the HER, either the discharge or the desorption step can be rate-determining. A total of six different mechanisms are possible, if the possibility of a coupled reaction is also taken into account. A reaction is termed coupled if the activated states of more than one step are within 1 to 2 kcal/mol with respect to their initial states.

The Tafel slope (β_c) and the permeation current (J_∞)/charging current (i_c) relations depend on the mechanism of the HER. The β_c is evaluated from the linear portion of the cathodic polarization plot, shown in Figure 5, which is commonly known as cathodic polarization curve. E_{revH^+/H_2} is the potential at which the hydrogen evolution reaction and hydrogen oxidation reactions are in equilibrium. The extrapolation of the linear portion of the cathodic polarization curve to E_{revH^+/H_2} gives the exchange current density for hydrogen evolution, $i_{o(H_2)}$. The cathodic polarization curve can also be plotted with overpotential on the ordinate as

opposed to the electrode potential; the overpotential for the hydrogen evolution reaction (η) is defined as:

$$\eta = E - E_{\text{revH}^+/\text{H}_2} \quad (13)$$

Table 2 illustrates the dependencies of η , J_∞/i_c on the HER mechanism.

Concurrent with the postulation of mechanisms of the HER, it was recognized that kinetics of the HER depends to a large extent on the rate constants of the constituent steps (viz. discharge, recombination, adsorption etc.,) and the degree of hydrogen surface coverage (θ_H).

Considering the hydrogen absorption reaction shown in eq 12, J_∞ can be written as:

$$J_\infty = k_{\text{abs}}\theta_H - k_{\text{des}}C_o. \quad (14)$$

The surface coverage (θ_H) can be defined as the ratio of the number of adsorption sites filled to the total number of adsorption sites available ^{14,15}. The surface concentration of hydrogen (C_o) is related to the surface coverage of hydrogen (θ_H) and the absorption constant (k_{abs}). Attempts have been made to estimate θ_H experimentally and theoretically. Pioneering work in the development of experimental techniques to measure θ_H was carried out by Bockris et al. ¹⁶. They developed a galvanostatic pulse technique to estimate θ_H on noble metals. In this method, hydrogen is evolved on a metal surface at a known rate. At steady state, an anodic pulse is superimposed for a very short time to oxidize the adsorbed hydrogen on the surface. θ_H is calculated from the potential transient response recorded on an oscilloscope. In b.c.c. metals and reactive metals, however, back-diffusion of hydrogen from bulk to surface and metal dissolution contributed to

the potential transient and therefore, this method could not be applied.

Kim and Wilde ¹⁷⁾ applied an analysis to take into account the above factors and, thus, expanded the scope of the technique to determine θ_H to be effective on bcc metals. Figure 6 is a schematic of the electrical circuit used for determination of θ_H . Two separate polarization circuits were superimposed on the test electrode; one to maintain a constant θ_H on the specimen surface and the other to apply the anodic pulse used to oxidize the adsorbed hydrogen. The potential transient varies in shape depending on the steady-state θ_H .

$$(dV/dt)_1 = [1/C_v] \cdot [i_a - i_H - i_{ox}(1 - \theta_H)] \quad (15)$$

where,

i_a is the applied anodic pulse

i_H is the partial current used to oxidize the adsorbed hydrogen

$i_{ox}(1 - \theta_H)$ is the partial current used for metal dissolution and C_v is the capacity of the electrical double layer at potential V .

When the metal surface is oxidized without the presence of adsorbed hydrogen, the potential transient is;

$$(dV/dt)_2 = (1/C_v) \cdot (i_a - i_{ox}) \quad (16)$$

Subtracting eq. 15 from eq. 16;

$$(i_H - i_{ox}\theta_H) = C_v \cdot [(dV/dt)_2 - (dV/dt)_1] \quad (17)$$

$(dV/dt)_1$ and $(dV/dt)_2$ were calculated from potential transients recorded on an oscilloscope (Figure 7). $(i_H - i_{ox}\theta_H)$ was calculated using equation 18. Area under a plot of $(i_H - i_{ox}\theta_H)$ vs. time (Figure

8) represents the charge required to oxidize all the adsorbed hydrogen. Corrections to account for hydrogen diffusing from the bulk to surface were applied.

Using this technique, Kim and Wilde ¹⁷⁾ obtained a hydrogen surface coverage (θ_H) of 5-12% on iron in a NaOH solution (pH 9.5). More recently, Bockris et al. ¹⁸⁾ estimated θ_H on iron in an alkaline solution (pH 8.4) by an indirect method, using FTIR spectroscopy. This method utilizes quantities calculated from quantum-mechanical considerations. Therefore, this method may, at most, be suitable for pure metals and will include errors due to simplifying assumptions when applied to alloys.

2.2.2 Analysis of electrochemical kinetic data

A mechanistic model has been proposed by Pickering et al. ¹⁹⁻²²⁾ to analyze the evolution of hydrogen and its entry into metals. The main advantage of this model is that it enables calculation of the reaction rate constants and surface coverage of hydrogen using only data from hydrogen permeation experiments and polarization data. Thus, it is possible to make a comparison of different hydrogen charging situations (viz. electrochemical, gaseous, radiolytic decomposition) to evaluate θ_H resulting from each. Because of the above simplifying advantage, this model has been used to analyze data from the hydrogen permeation experiments in Parts 2 and 3 of this investigation.

The mechanistic model developed by Pickering et al. has been referred to as the I-P-Z model after the surname initials of the three authors. In addition to determination of θ_H and k_{abs} , the I-P-Z model (in its modified form) is capable of analyzing the

effect of poisons and high hydrogen surface coverages quantitatively ²²⁾. The model is based on the following assumptions:

- 1) the HER occurs by a discharge-recombination mechanism involving single electron transfer,
- 2) Recombination step is not rate-limiting,
- 3) Langmuirian conditions for adatom adsorption are satisfied,
- 4) the adsorption-absorption reaction is at local equilibrium,
- 5) Permeation occurs by simple diffusion (no trapping),
- 6) Only steady-state conditions are considered.

The reader is referred to a Pickering et al. publication ¹⁹⁻²²⁾ for a detailed derivation of the I-P-Z model. A key result of the model which enables the calculation of θ_H and k_{abs} is the following equation:

$$i_c \cdot \exp(a \cdot \alpha \cdot \eta) = (-b \cdot i_o' / k'') (J_\infty - c_g) / b + i_o' \quad (18)$$

where $a = F/RT$,

$$i_o' = i_o / (1 - \theta_c),$$

c_g/b is the intercept in a plot of J_∞ versus $\sqrt{i_c}$,

k'' is the ratio of the absorption constant (k_{abs}) to the adsorption constant (k_{ads}).

A plot of the left hand side of eq. 18 vs. $(J_\infty - c_g/b)$ results in a straight line with a slope of $(-b \cdot i_o' / k'')$ and a y-intercept of i_o' (Figure 9). Since $b = L/FD_H$ is a constant, k'' can be evaluated from the slope.

Data from permeation and polarization experiments serve as input to the above mechanistic model. A plot based on eq. 18 requires a minimum of 4 data points, each data point representing

permeation of hydrogen (J_{∞}) at a given i_c and corresponding hydrogen overpotential (η). The transfer coefficient (α) is determined from an equation involving slopes of a plot of η vs $\log i_c$ (Figure 10) and η vs $\log J_{\infty}$ (Figure 11). The constant b is calculated from the permeation membrane thickness (L) and diffusivity of hydrogen (D_H).

Figure 9 is a representative plot of equation 18. From Fick's first law of diffusion, the surface coverage of hydrogen is given by, $\theta_H = bJ_{\infty}/k$. Further, k_{ab} can also be calculated from eqn 18.

In summary, this method enables the calculation of hydrogen surface coverage at different overpotentials and rate constants of HER steps.

2.3 Materials and experimental procedures

2.3.1 Preparation of Samples

The CD 102 alloy was available commercially from Aldrich Chemical Company in the thickness ranges needed to do an experiment in a reasonable time (1-4 mils uniform thickness). However, the CDA 715 alloy was not available commercially in these thicknesses, therefore, it was necessary to buy a thicker membrane ($\approx 1/4$ inch thick) and reduce it to the desired thickness (2-4 mils). This was done by first rolling the membrane down to about 10-20 mils in a small rolling mill followed by an anneal for 45 minutes at 1400°F to soften it and prevent the sample from tearing when it was next rolled down to 4-6 mil thickness. The sample was further annealed as before to produce a uniform microstructure for all the membranes.

The scale formed during the annealing treatments was quite thick and adherent and was removed with polishing paper which

further reduced the thickness by 1-2 mils. The final surface finish was a 600 grit finish. The thickness of the membranes were measured with pointed calipers in several locations to insure that the thickness was uniform across the cross-section of the sample.

Preparation for Pd Sputtering Deposition

The success of any sputtered coating depends most on the cleanliness of the substrate when it is inserted into the vacuum chamber. Therefore, the sample was cleaned as perfectly as possible in the following manner. First, the sample was wiped with a Kay-Dry towel to remove any solid particles and was rinsed briskly in tap water. The sample was immersed immediately in a beaker of trichloroethylene for approximately 15 seconds and allowed to air dry. Immediately prior to sputter deposition, the samples were rinsed with acetone followed by methanol and allowed to air dry.

2.3.2 Polarization procedures.

Cathodic Polarization.

The electrolyte consisted of a solution of 0.1N NaOH and was heated to 95°C while nitrogen was bubbled vigorously through the sealed cell (see Figure 12) which contained a small opening for the oxygen and nitrogen to escape. The sample was "masked" except for a known surface area by a silicone rubber compound that was found to be much more adherent at this temperature than any other masking technique.

The test was initiated by applying a potential of -1.5 volts and after a three minute interval, the potential was increased by

30 mV. This was repeated until the applied potential was near the reversible potential of the HER. Starting at this highly negative potential has the beneficial effect of suppressing any oxide formation until very small overpotential values are reached with respect to the HER reversible potential.

By plotting the data a linear region could be located on the plots from which β_c could be found along with i_0 .

2.3.3 Permeation Experiments

Pd Sputtered Deposition

The test membranes were inserted into the vacuum chamber of a Veeco Microtech glow-discharge type sputtering unit. The specimens were etched for one minute in order to further prepare a clean surface for the deposition process. Pd was deposited for ten minutes which resulted in a film thickness of 0.5μ (see table 3 for equipment parameters used during deposition).

Cell and Electrical Circuit

The cell employed was of the Devanathan-Stachurski type (see Figure 12). It was comprised of two identical halves which were joined together at the metal membrane. The cells were clamped tightly shut by a clamp, and leakage was prevented by using rubber O-rings. The O-rings were completely isolated from any solution by wrapping teflon tape around them. Both cells had platinum counter electrodes, a Luggin probe extending to the specimen surface, and a tube for introducing nitrogen gas into the center of the bottom of the cell to purge oxygen from the system. The cell pair was placed into an oven to allow high temperature tests to be conducted. The cells had condensers connected directly on top of

them in order to facilitate higher temperature use (95°C). The anodic cell of each pair had a long pyrex glass tube extending from the luggin probe reservoir straight up and out the top of the oven (see Figure 13). A porous zirconia plug was used to plug the bottom of the tube and to allow electrolytic conductance with no mass transport. The tube was filled with the same solution as was the cell, 0.1N NaOH. A Ag/AgCl reference electrode was inserted into the top of the tube and was in contact with the solution. Ag/AgCl electrodes are recommended as stable electrodes at these elevated temperatures; the more commonly used calomel is not ²³⁾. The air passage left between the tube and the electrode was sealed with clay in order to prevent evaporation of the tube solution over time. This was done to minimize reference electrode maintenance and to maximize stability of the measurements, for it was found that the temperature fluctuations inside the oven caused noisy current readings to be made when the reference electrode was inside the oven itself. Also, the reference electrode's internal solution tended to evaporate over time and could be refilled only by opening the oven and interrupting a test. There was a thermal junction potential ²³⁾ between the top and bottom of the tube of about 96mV.

The electrical circuit is shown in Figure 14. One side of the membrane (cathodic side) was connected to a galvanostat (left side on the figure). Hydrogen was produced on this side at a constant rate determined by the current. The other side of the membrane (anodic side) was connected to potentiostat maintained at a potential sufficiently positive that all hydrogen atoms arriving there are assumed instantly oxidized ($\theta_H = 0$). This creates a concentration gradient, allowing some of the hydrogen that is

produced galvanostatically to diffuse through the membrane and out the anodic side. The current on the anodic side of the membrane was measured on a chart recorder as a function of time. This allowed the recording of the arrival of the hydrogen from the other side of the membrane, and hence, from this, diffusion parameters (apparent diffusivity, etc.) were calculated.

Test Procedure

The first step was to achieve a low background current on the anodic side of the membrane. Due to its low corrosion rate in 0.1N NaOH, the Pd was plated onto the anodic side of the membrane. A potential of 0.0 mV versus a Ag/AgCl electrode was maintained on this side by a potentiostat. The current normally decayed quickly to a steady state value which did not change with time (a steady background current with time was verified experimentally). The decay transient is due to the current having two components--first, there is the corrosion current which occurs at a constant value, and the second is due to the oxidation of hydrogen which may have been dissolved in the matrix. When the anodic current reached a steady, constant value, this value was recorded as the background current.

Immediately after this, the cathodic test solution (catholyte), which had been in a flask inside the oven, was added to the cathodic cell half. A known cathodic current was instantly applied to that side of the membrane. In this way, the temperature of the catholyte was already the same as the membrane, and the possibility of oxidation of that surface was reduced.

A small fraction of the hydrogen galvanostatically produced on the cathodic side of the membrane was absorbed into the metal

matrix as hydrogen atoms which diffuse to the other side, where it was instantly oxidized and measured as a current by the potentiostat. The variation of this permeation current vs. time was recorded by a chart recorder (see Figure 15 for a typical current vs. time curve). J_{∞} designates the steady state permeation current for a single charging condition. The diffusivity was calculated by measuring the time at which $J = 0.5 \times J_{\infty}$. and inserting this value into the following relation:

$$D_{app} = 0.138 \times L^2 / t_{1/2} \quad (19)$$

where D_{app} is the apparent diffusivity of hydrogen in the alloy at 95°C in $\text{cm}^2 \cdot \text{s}^{-1}$,

L is the thickness of the membrane in cm,

$t_{1/2}$ is the time from the moment the cathodic current is on until $J = J_{\infty} \times \frac{1}{2}$.

Permeation vs. time curves were conducted in duplicate for both alloys to insure accuracy.

2.4 Results and Discussion.

In the interests of clarity, the results obtained in Part 2 will be presented in three sections: i) cathodic polarization characteristics, ii) hydrogen absorption behavior, and iii) hydrogen surface coverage factors and HER mechanisms on copper alloys.

2.4.1 Cathodic polarization characteristics.

Cathodic polarization experiments were conducted using the procedure outlined in 2.3. Initial tests were conducted on the CDA 102 alloy at 25°C to compare the data with that already published

in the literature ²⁴⁾. The results are shown in Figure 16 in which approximately two decades of charge transfer controlled Tafel region were noted. The value of β_c obtained from the graph was -130 mV/decade which is in close agreement with the value of -120 mV/decade obtained by Potter ²⁴⁾ on pure copper in 0.15 N NaOH.

These data allow two conclusions to be drawn:

1) the experimental procedure adopted in his work is comparable to that reported in the literature in that almost identical data are obtained on similar materials.

2) the value of -130 mV/decade obtained indicates that the HER mechanism is possibly that of slow discharge/fast recombination as suggested previously by Subramanyan et al. ²⁵⁾.

The results from cathodic polarization experiments conducted on CDA 102 and 715 alloys at 95°C are shown in Figures 17 and 18. For the 102 alloy (Figure 17), the increase in temperature is seen to have destroyed the well-defined Tafel region, resulting in a continuously curving relation suggestive of either mass transport limiting processes (such as oxide film formation) or resistive factors at the metal/solution interface. The value of β_c was estimated by a best-fit method and was found to be -170 mV/decade. The exchange of current density for hydrogen evolution on the 102 alloy was determined to be 3×10^{-6} A/cm² by extrapolation of the "Tafel" line to the reversible hydrogen potential (-857 mV_{Ag/AgCl}).

The CDA 715 alloy results shown in Figure 18 evidenced approximately two orders of magnitude of charge transfer controlled activity with a β_c of -170 mV/decade. This value is somewhat greater than that predicted by theory at 95°C of -148.2mV/decade on the assumption that α is 0.5 and that the reaction mechanism

corresponds to $2RT/F$ with Langmuirian adsorption. It is of interest to note that both the 102 and 715 alloy had the same value of β_c .

The value of the extrapolated exchange current density was $1 \times 10^{-5} \text{A/cm}^2$, which was approximately a factor of three higher than that obtained on the 102 alloy. The symmetry coefficient, α , was calculated from β_c to be 0.44 which agrees well with that required by the coupled discharge/recombination mechanism of the HER.

2.4.2 Hydrogen absorption kinetics.

Hydrogen permeation experiments were conducted on both alloys at 95°C . It should be noted that the electrolyte used on the oxidation side (Pd coated side) of the sample was 0.1 N Na_2SO_4 solution. This electrolyte was employed in order to decrease the background current to as low a value as possible to maximize the detection sensitivity to permeating hydrogen.

The results for the 102 alloy are presented in Figure 19 from which it is immediately obvious that, even after 200 + hours, no hydrogen was absorbed. This observation is all the more remarkable when one reflects that hydrogen was being evolved electrochemically on the alloy surface. Assuming that hydrogen was absorbing in the above experiment, calculation of D_{app} using 200 hours as $t_{1/2}$ (see Equation 19) yields a value of $10^{-12} \text{cm}^2 \cdot \text{s}^{-1}$, which is two orders of magnitude lower than that reported for this temperature by Hagi ²⁾. Therefore, we must conclude that alloy 102 is immune to hydrogen absorption under the conditions of the experiment; 1 N NaOH at 95°C at a cathodic charging current density of $2 \times 10^{-4} \text{A/cm}^2$.

DeWulf and Bard ³⁾ have reported previously that pure copper

membranes were impervious to hydrogen absorption in the absence of surface poisons. When their experiment was repeated in the presence of As_2O_3 in the catholyte, however, they observed readily detectable hydrogen absorption at 25°C .

The above experiments on the 102 alloy were repeated at 95°C with 0.5 g/l As_2O_3 dissolved in the catholyte. The results are shown in Figure 20 in which a "perfect" hydrogen permeation trace was obtained. This result indicates clearly that the 102 alloy surface in the absence of poisons is inherently resistant to hydrogen absorption--a property of considerable interest in a candidate material for nuclear waste disposal.

Using the permeation transient in Figure 20 and Equation 18, the D_{app} for the poisoned 102 alloy was $9.9 \times 10^{-10} \text{ cm}^2.\text{s}^{-1}$.

The resistance to hydrogen permeation of the 102 alloy makes it of obvious interest as a candidate material. It is, however, mechanically quite weak and may only find application in designs where it is used as a cladding over a structurally more attractive material. Because these results are only initial investigations, we feel that the hydrogen absorption characteristics of 102 alloy should be further investigated in natural ground waters and with radiolytically-generated hydrogen either from steam or water.

The permeation results obtained for the 715 alloy are shown in Figures 21-23 from which it can be seen that hydrogen absorption readily occurred. Values of D_{app} were $5 \times 10^{-10} \text{ cm}^2.\text{s}^{-1}$ which are in excellent agreement with the predictions made by Hagi.

The relation between J_∞ and cathodic charging current (hydrogen input fugacity), was found to be linear as shown in Figure 24, which along with the Tafel slope of -170 mV/decade

indicates that the HER is a coupled discharge/recombination mechanism.

2.4.3 Hydrogen surface coverage and absorption kinetics.

The specific details of the I-P-Z method for examining the HER was discussed in an earlier section (2.2.2) and basically involves using the hydrogen permeation data along with the cathodic polarization data to calculate the various kinetic constants for hydrogen absorption reaction.

The results of applying this analysis to i) zone refined Ni and iron and ii) to the data obtained on the 715 alloy are summarized in tables 4 and 5, respectively. Before proceeding with a discussion, however, the parameters presented in the tables require some definition:

D_{app} is the apparent diffusivity of hydrogen through the alloy,

L is the thickness of the membrane in cm,

b is a constant = L/FD where F is Faraday's constant,

i_0 is the exchange current density for the HER,

α is the transfer coefficient which is calculated from the Tafel slope of the cathodic polarization curve.

k'' is called the absorption-desorption constant, and is approximately equal to k_{abs}/k_{des} .

k'' is calculated by finding the slope of the $\ln i$ versus $J\infty$ curve (Figure 25) and using equation (18).

k_s is the recombination reaction rate constant and is calculated by using the value of k'' found previously in equation (18).

k_7 is the discharge rate coefficient and is calculated by equation (18).

θ_H is the value of fractional hydrogen surface coverage at various overpotentials,

θ_0 is the surface coverage at zero hydrogen overpotential, which is obtained by extrapolating the linear portion of Figure 26 to zero overpotential.

In examining the data in Tables 4 and 5, the following observations can be made:

i) the apparent diffusivity of CDA 715 is much lower than the iron-based alloys.

ii) the discharge rate constant is roughly one order of magnitude bigger, and the recombination rate constant is about two orders of magnitude smaller than the alloys in Table 4.

iii) the absorption-desorption constant is much higher than the ferrous based materials, but is quite comparable (within an order of magnitude) with the zone-refined Ni.

iv) the equilibrium surface coverage of hydrogen for CDA 715 is comparable with that found with the other alloys. Not unexpectedly, CDA 715 is much more comparable with zone-refined Ni than with ferrous materials in terms of the kinetics of the HER and permeation.

The significant findings in this research, however, is the relationship between cathodic overpotential and degree of surface coverage by hydrogen as shown in Figure 26. Once the surface coverage as a function of gamma flux is determined, this function will allow experiments to be conducted to investigate

the HE resistance of copper alloys at an electrochemically controlled surface coverage equal to that found in a gamma radiation field.

2.5 Conclusions.

On the basis of the research described in Part 2, the following conclusions may be drawn:

1) Under conditions of electrochemically generated hydrogen from a aqueous solution of sodium hydroxide, the CDA alloy 102 is impermeable to hydrogen.

2) Since hydrogen absorption is a necessary precursor to HE, this finding suggests that CDA alloy 102 should be a serious candidate material for the fabrication of nuclear waste disposal canisters.

3) The CDA alloy 102 under conditions where an HER recombination "poison" such as arsenic was incorporated in the sodium hydroxide electrolyte, evidenced hydrogen absorption that could in principle lead to HE. These findings indicate the absolute need to define the exact chemical nature of the repository environment before rational choices of materials can be made.

4) The CDA alloy 715 under poison-free conditions indicated a tendency to absorb a small amount of hydrogen. The apparent hydrogen diffusivity was $5 \times 10^{-10} \text{ cm}^2 \cdot \text{s}^{-1}$.

5) Using the permeation kinetics for CDA alloy 102 under poisoned conditions, the apparent hydrogen diffusivity was $9.9 \times 10^{-10} \text{ cm}^2 \cdot \text{s}^{-1}$.

6) Because of the very low hydrogen diffusivity, the CDA alloy 102 could possibly be considered as a cladding material over

a more mechanically stronger base alloy. The advantage to this concept is that this alloy is not only resistant to hydrogen absorption but is also resistant to corrosion.

7) The mechanism of HER on CDA alloy 102 is the slow discharge/fast recombination type. The mechanism found on the CDA alloy 715 was that of the coupled discharge/recombination type.

8) Using the procedures developed in this research, excellent long-term hydrogen diffusion/absorption experiments can be conducted on copper alloys with Pd sputter deposited anode coating and a solution of 0.1 N NaOH at 95°C.

2.6 References.

- 1) PEER Review, Report by the Center for Nuclear Regulatory Analyses, July, 1989.
- 2) H. Hagi, Trans.Japan.Inst. Met., 27, 233, (1986).
- 3) D.W. DeWulf, A.J. Bard, J. Electrochem. Soc., 132, 2965, (1985).
- 4) J.P. Hirth, Met. Trans. A, 11A, 861, (1980).
- 5) C.A. Zapfe, C.E. Sims, Trans. AIME, 145, 225, (1943).
- 6) N.J. Petch, Phil. Mag., 1, 331, (1956).
- 7) A.R. Troiano, Trans. ASM, 52, 54, (1960).
- 8) D.G. Westlake, Trans. ASM, 62, 1000, (1969).
- 9) P. Bastien, P. Azou, "Proc. 1st World Met. Congress", ASM, Cleveland, Ohio, p. 535, (1951).
- 10) C.D. Beachem, Met. Trans., p. 437, (1972).
- 11) I.A. Bagotskaya, Zhur. Fiz. Khim., 36, 2667, (1962).
- 12) A.N. Frumkin, "Advances in Electrical and Electrochemical Engineering", Volume III,, Interscience Publishers Inc., NY,

- (1963).
- 13) N. Ohnaka, Y. Furutani, Corrosion, 46, 129, (1990).
 - 14) J. McBreen, A. Genshaw, "Proc. Int. Symp. on SCC", NACE, Houston, Texas, (1967).
 - 15) J. McBreen, L. Nanis, W. Beck, J. Electrochem. Soc., 113, 1218, (1966).
 - 16) J.O'M. Bockris, J. McBreen, L. Nanis, J. Electrochem. Soc., 112, 1025, (1965).
 - 17) C.D. Kim, B.E. Wilde, J. Electrochem. Soc., 118, 202, (1971).
 - 18) J.O'M. Bockris, J.L. Carbajal, B.R. Scharifker, K. Chandrasekaran, J. Electrochem. Soc., 134, 1957, (1987).
 - 19) R.N. Iyer, I. Takeuchi, M. Zamanzadeh, H.W. Pickering, Corrosion, 46, 460, (1990).
 - 20) S.S. Chatterjee, B.G. Atoya, H.W. Pickering, Met. Trans. A, 9A, 389, (1978).
 - 21) R.N. Iyer, H.W. Pickering, M. Zamazadeh, J. Electrochem. Soc., 136, 2463, (1989).
 - 22) R.N. Iyer, H.W. Pickering, M. Zamazadeh, Scripta.Met., 22, 911, (1988).
 - 23) D.D. Macdonald, Corrosion, 34, 75, (1978).
 - 24) E.C. Potter, "Electrochemical Principles and Applications", Cleaver-Hume Press, London, (1961).
 - 25) P.K. Subramanayan, "Comprehensive Treatise of Electrochemistry", Volume IV, p. 411, (1981).

Alloy	Cu	Pb	Fe	Ni	Zn	Mn
715	69.5	0.5	0.4-0.7	29-33	1.0 max	1.0 max
102	99.95	-	-	-	-	-

Table 1. Chemical composition of membrane materials, in weight percent.

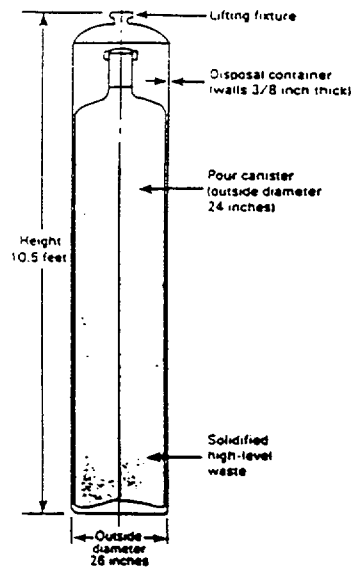


Figure 1. Disposal container for high-level nuclear waste.

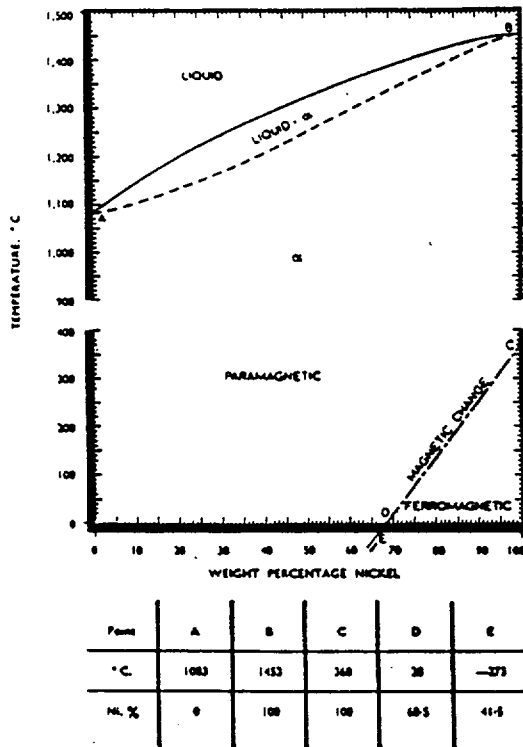


Figure 2. Copper - nickel phase diagram.

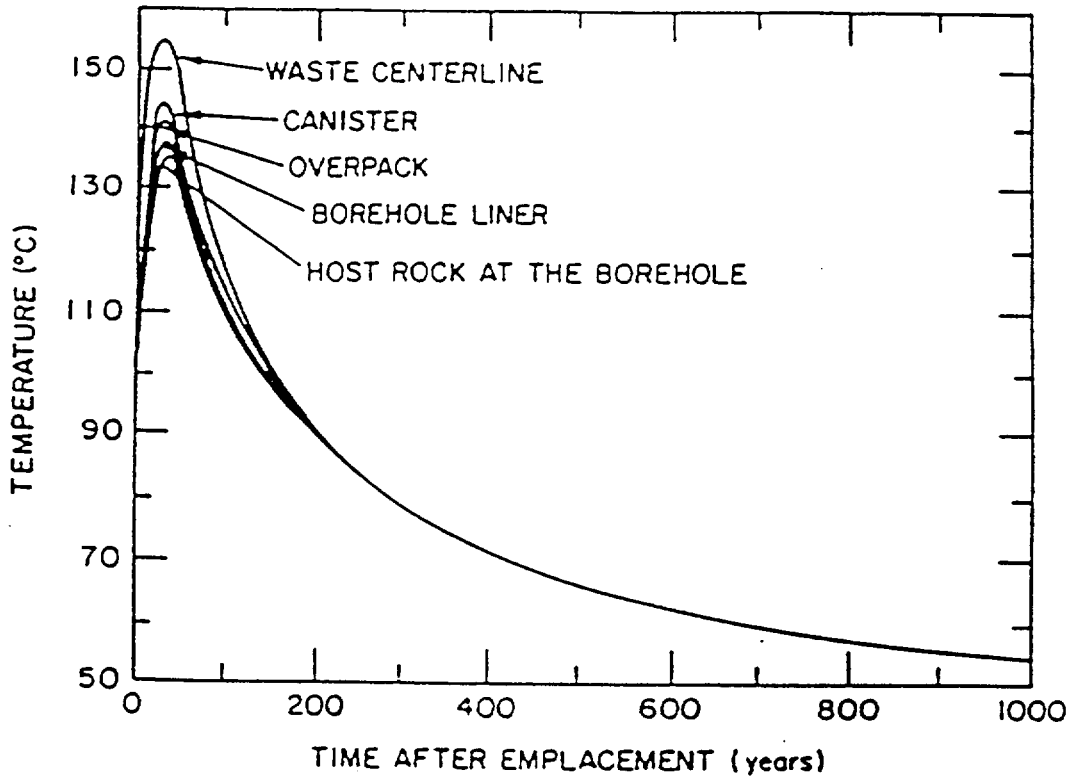


Figure 3. Calculated temperature versus time profile for the proposed Tuff repository, ¹⁾

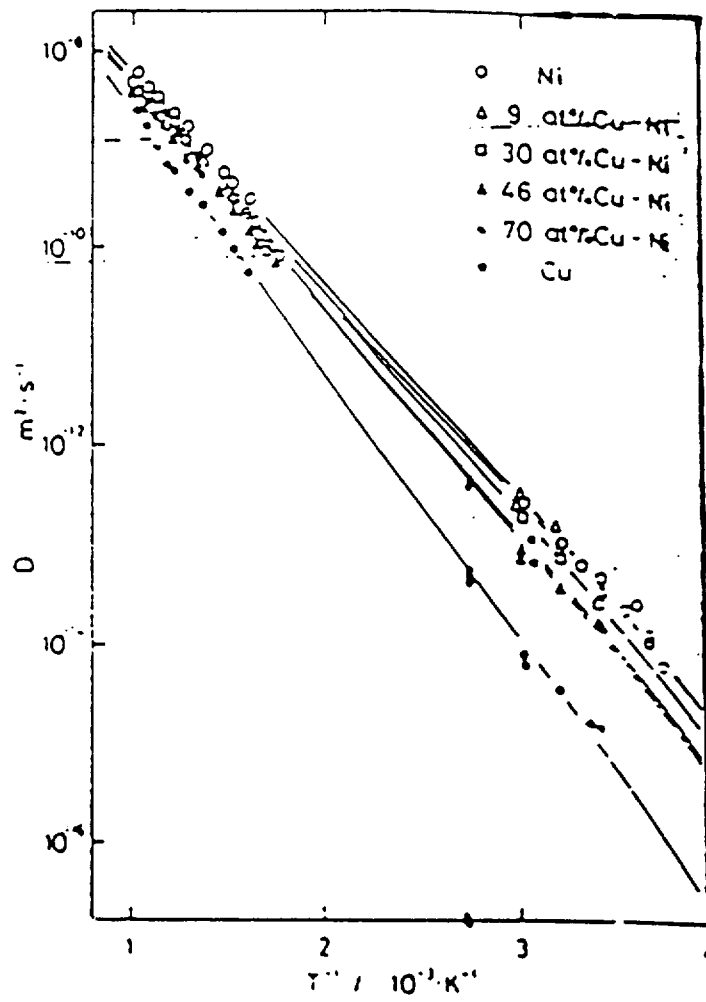
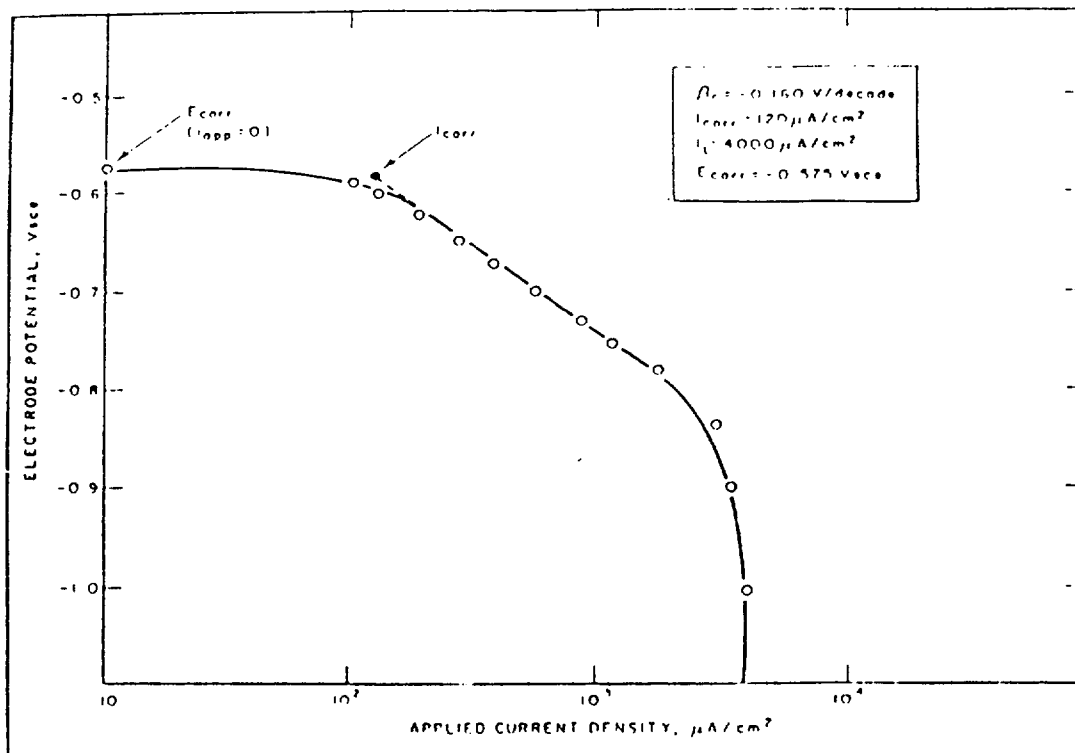


Figure 4. Arrhenius plot of the diffusion coefficient of hydrogen in nickel, copper and Ni/Cu alloys.

	$\frac{\partial V}{\partial \log i}$			$\frac{\partial V}{\partial \log J}$			$J = f(L)$		
	Langmuir Temkin			Langmuir Temkin			Langmuir Temkin		
	Non-Act.	Act.		Non-Act.	Act.		Non-Act.	Act.	
Slow Discharge-Fast Recombination	$\frac{2RT}{F}$	$\frac{2RT}{F}$	$\frac{2RT}{F}$	0	0	0	--	--	--
Slow Discharge-Fast Electrochemical	$\frac{2RT}{F}$	$\frac{RT}{F}$	$\frac{RT}{F}$	$\frac{RT}{F}$	$\frac{RT}{F}$	$\frac{RT}{F}$	i^{-2}	i	i
Fast Discharge-Slow Recombination	$\frac{RT}{2F}$	$\frac{RT}{2F}$	$\frac{RT}{F}$	$\frac{RT}{F}$	$\frac{RT}{F}$	$\frac{RT}{F}$	i	$i^{1/2}$	i
Fast Discharge-Slow Electrochemical	$\frac{2RT}{3F}$	$\frac{2RT}{3F}$	$\frac{RT}{F}$	$\frac{RT}{F}$	$\frac{RT}{F}$	$\frac{RT}{F}$	$i^{2/3}$	$i^{2/3}$	i
Coupled Discharge-Recombination	$\frac{2RT}{F}$	$\frac{5RT}{2F}$	$\frac{3RT}{F}$	$\frac{4RT}{F}$	$\frac{5RT}{2F}$	$\frac{3RT}{2F}$	$i^{1/2}$	i	i^2
Coupled Discharge-Electrochemical	$\frac{2RT}{F}$	$\frac{2RT}{F}$	$\frac{2RT}{F}$	0	0	0	--	--	--

Table 2. Values to aid in diagnosing the mechanism of the hydrogen evolution reaction.



Cathodic polarization curve of carbon steel in HCl (pH=2) [27]

Figure 5. A typical cathodic polarization curve.

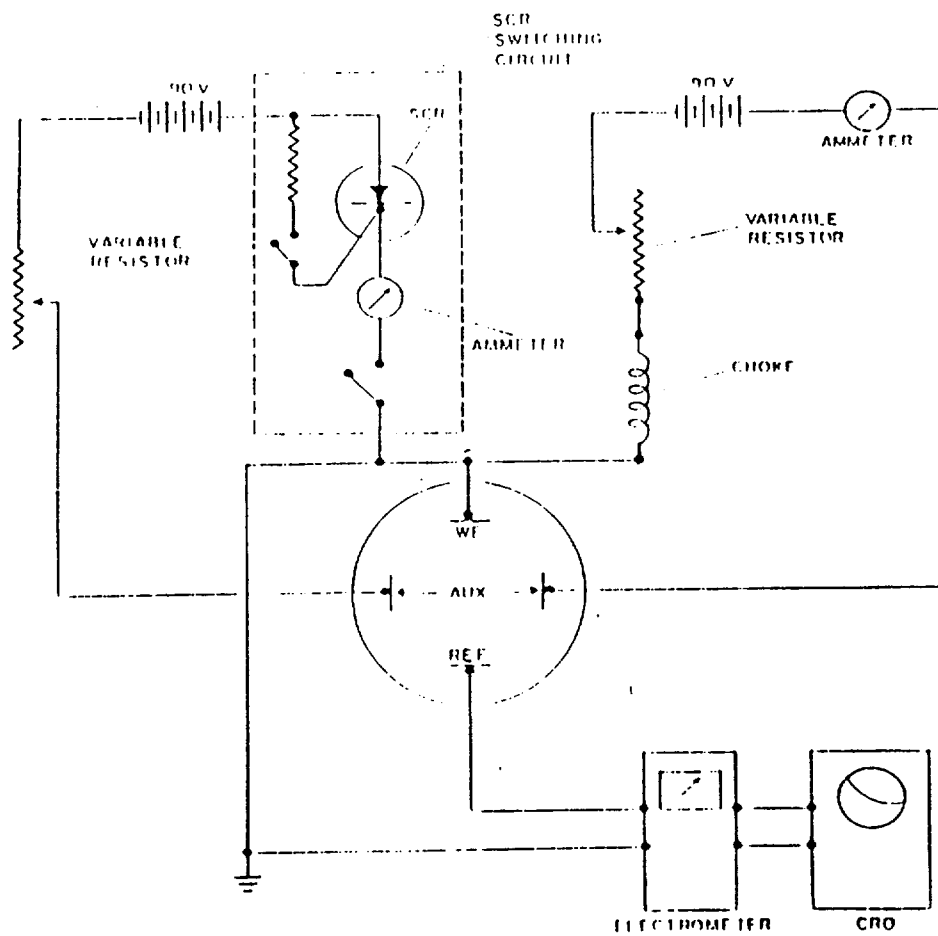


Figure 6. Electrical circuit used by Kim and Wilde¹⁷ for the determination of degree of hydrogen coverage on iron based materials.

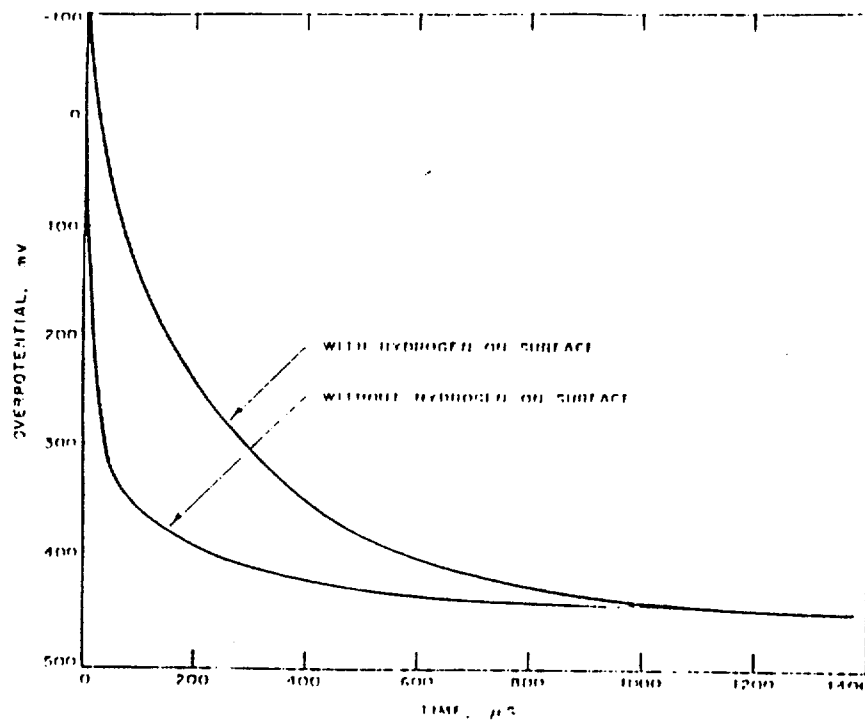


Figure 7. Typical oxidation potential transient obtained by Kim and Wilde ¹⁷.

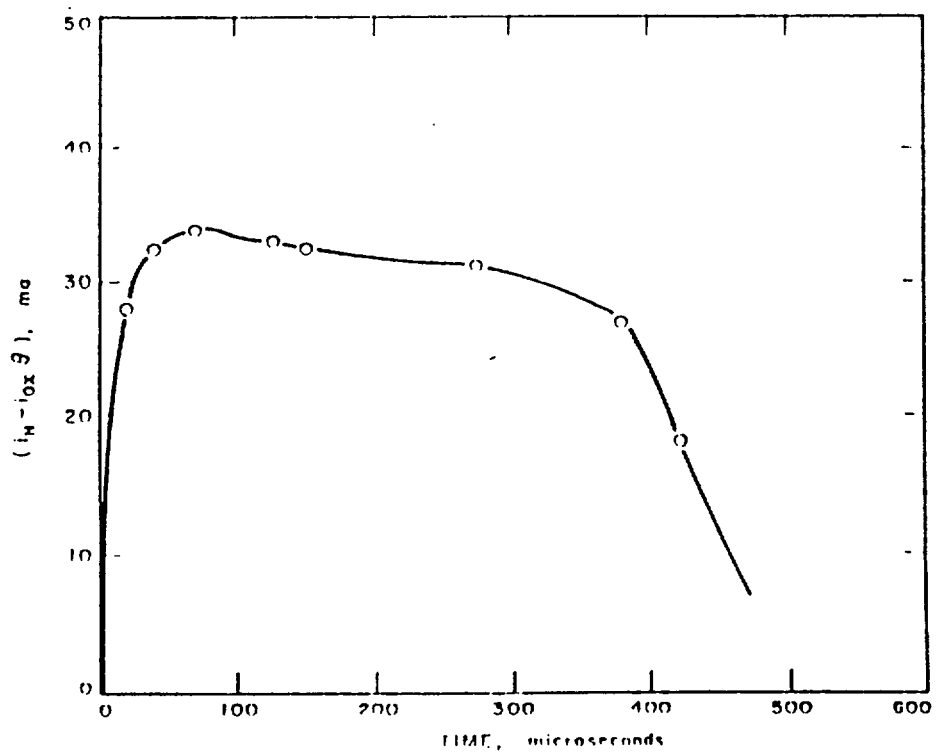


Figure 8. Method used by Kim and Wilde ¹⁷ to compensate for hydrogen absorbed into the test electrode.

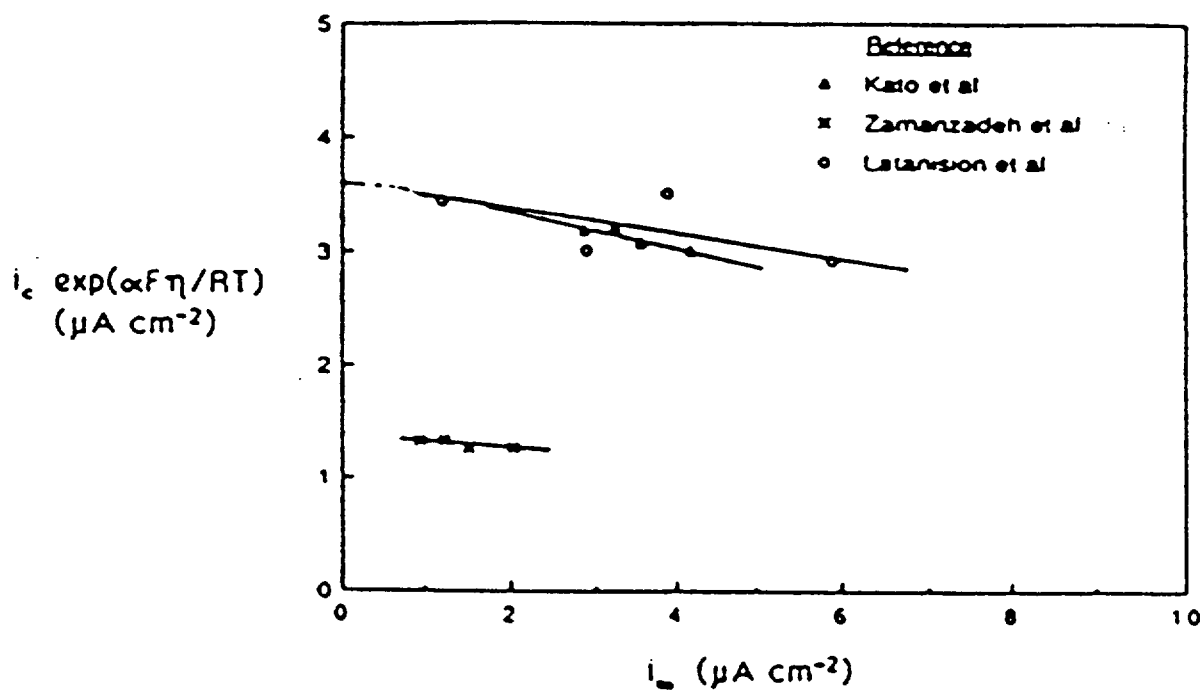


Figure 9. Typical plot of f_{in} versus J_a used in determining the absorption-desorption rate constant.

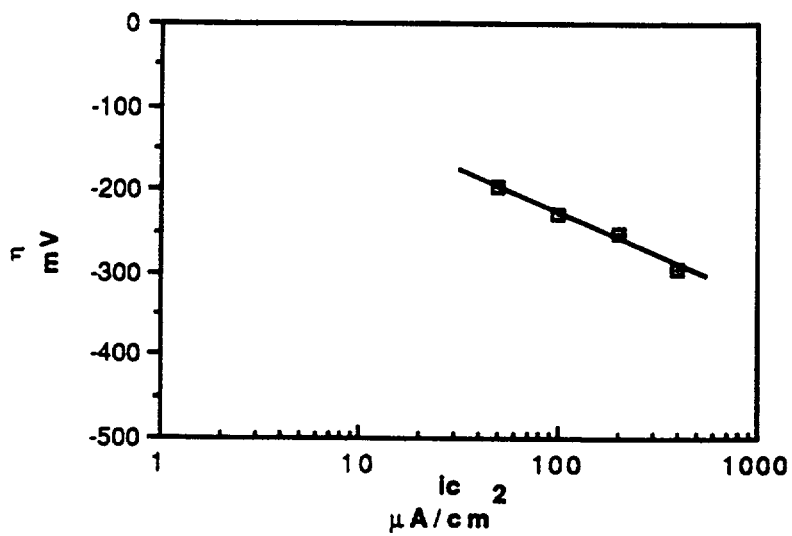


Figure 10. Typical hydrogen overpotential versus applied current density plot.

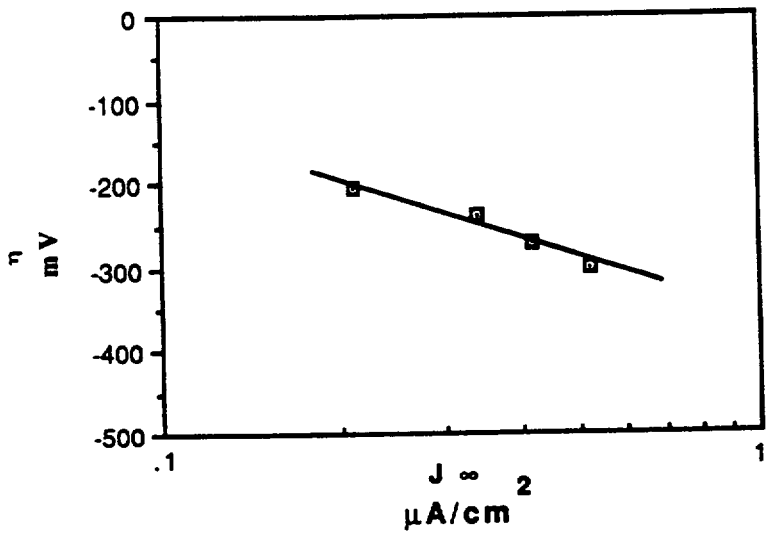


Figure 11. Typical hydrogen overpotential versus steady-state permeation plot.

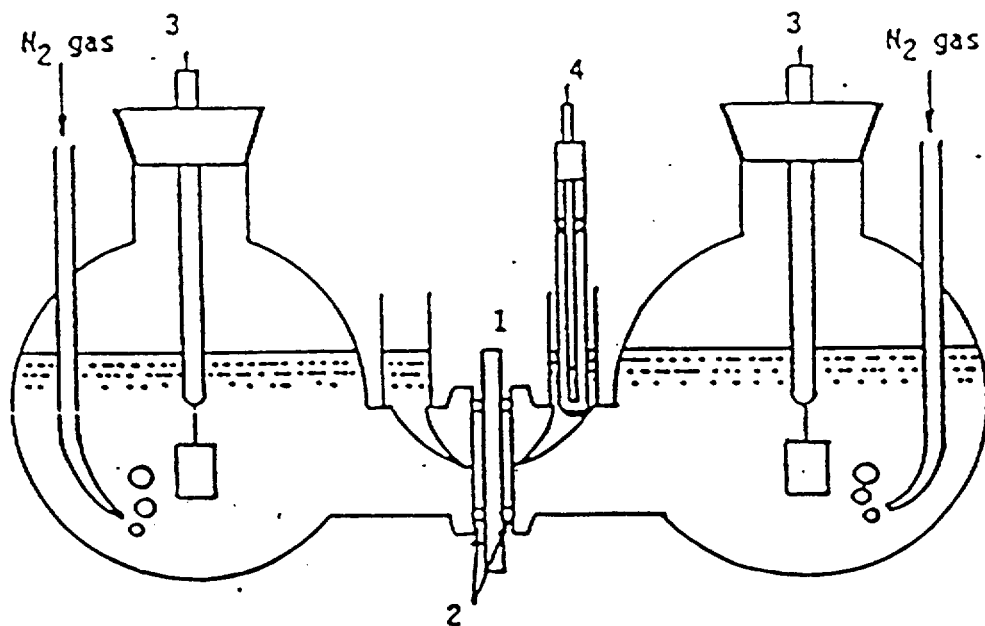
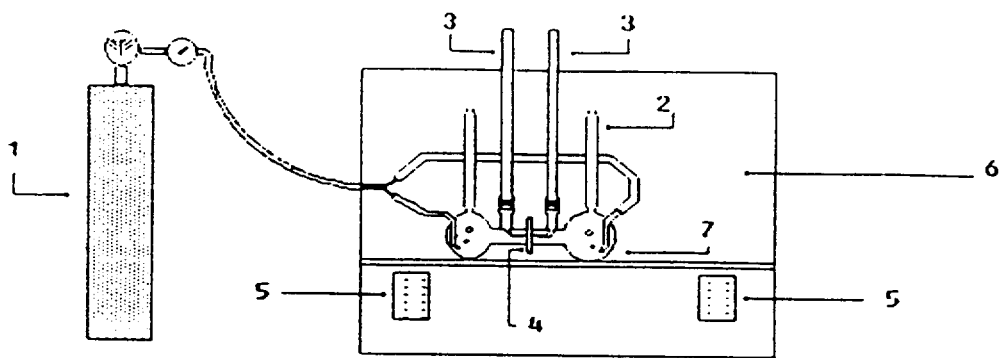


Figure 12. Devanathan-Stachurski type off cell used in the hydrogen permeation studies. Note: 1) membrane, 2) o-rings, 3) Pt electrode, 4) Ag/AgCl reference electrode.

Parameters	Value
Operating Pressure (torr)	$8 \cdot 10^{-5}$
Arc Discharge (A/V)	1/20
Cathode (A/V)	20/7.5
Magnet (A/V)	0.8/28
Suppressor (mA/V)	6/200
Acceleration (mA/kV)	60/1
Current Density (mA/cm ²)	1
Etch (min.)	1
Deposition (min.)	10

Table 3. Experimental parameters used for sputter depositing specimens with palladium.



- | | |
|-----------------------------|---------------------|
| 1. Nitrogen Gas | 2. Condenser |
| 3. Reference Solution Tubes | |
| 4. Metal Membrane | 5. Heating Elements |
| 6. Oven | 7. Test Cell |

Figure 13. Overall hydrogen permeation experimental setup showing modifications for use at 95°C.

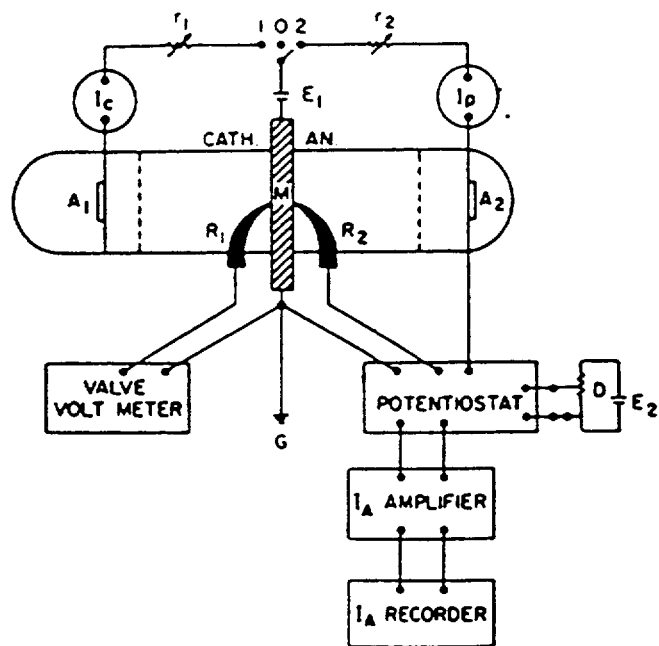


Figure 14. Schematic of the electrical circuit used in the hydrogen absorption studies.

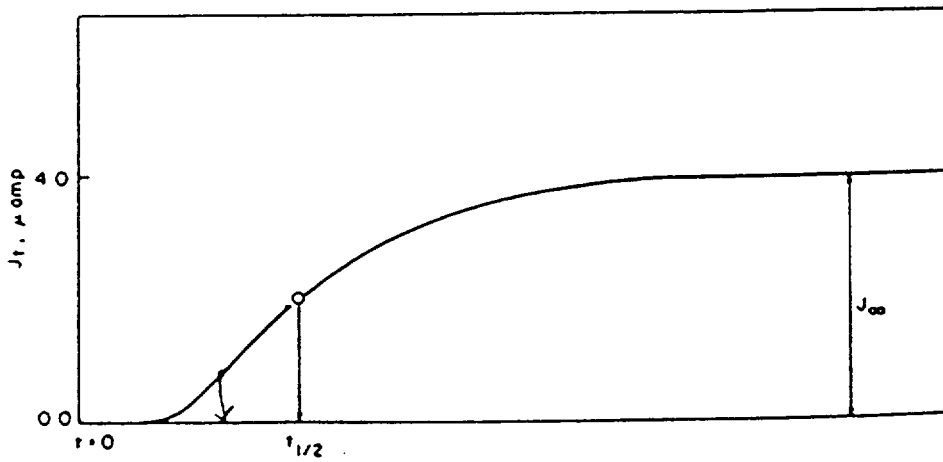


Figure 15. Typical hydrogen permeation flux versus time transient observed in this investigation.

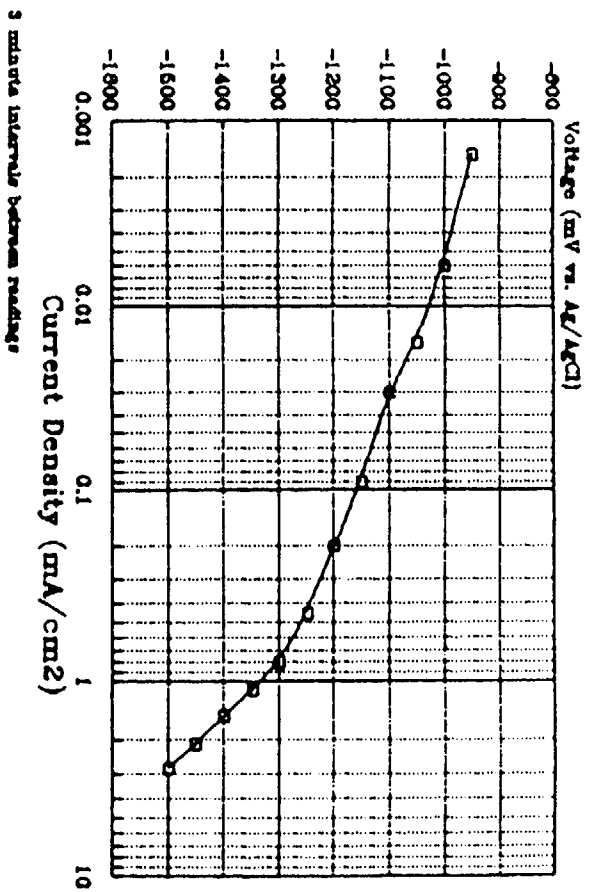


Figure 16. Cathodic polarization curve of CDA 102 alloy in 0.1 N NaOH at 25°C.

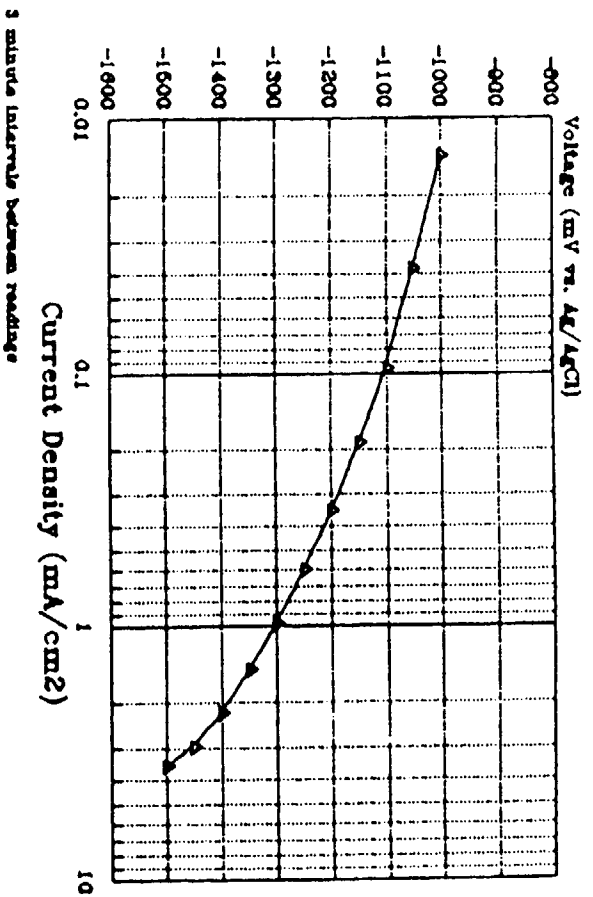


Figure 17. Cathodic polarization curve for CDA 102 in 0.1 N NaOH at 95°C.

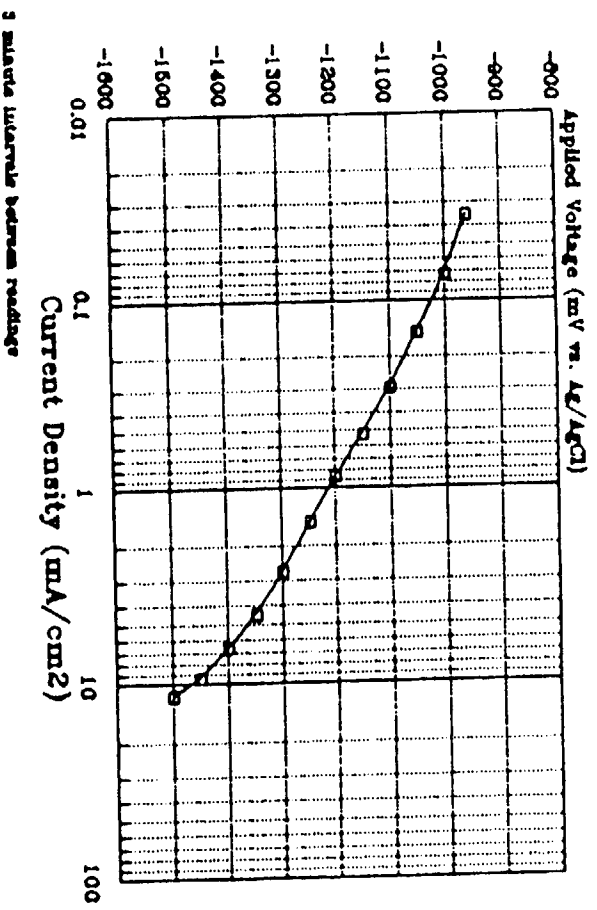


Figure 18. Cathodic polarization curve for CDA 715 in 0.1 N NaOH at 95°C.

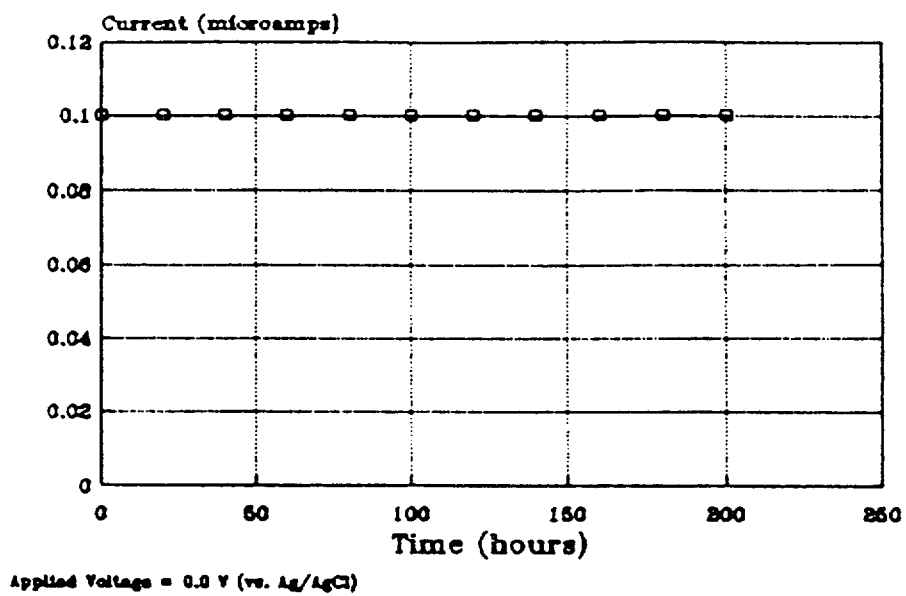


Figure 19. Experimental hydrogen permeation curve for CDA 102 at n 95°C. Charging current 0.2 mA/cm².

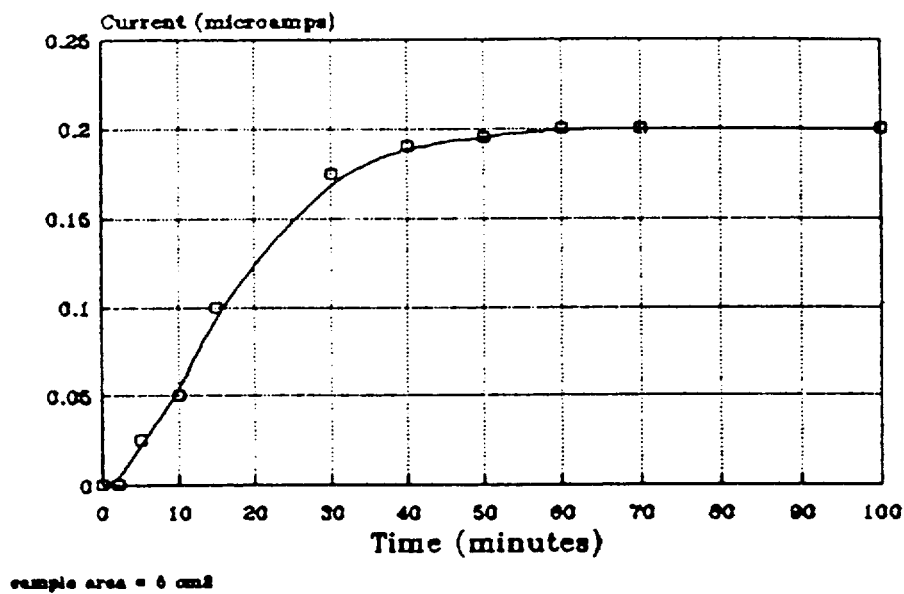
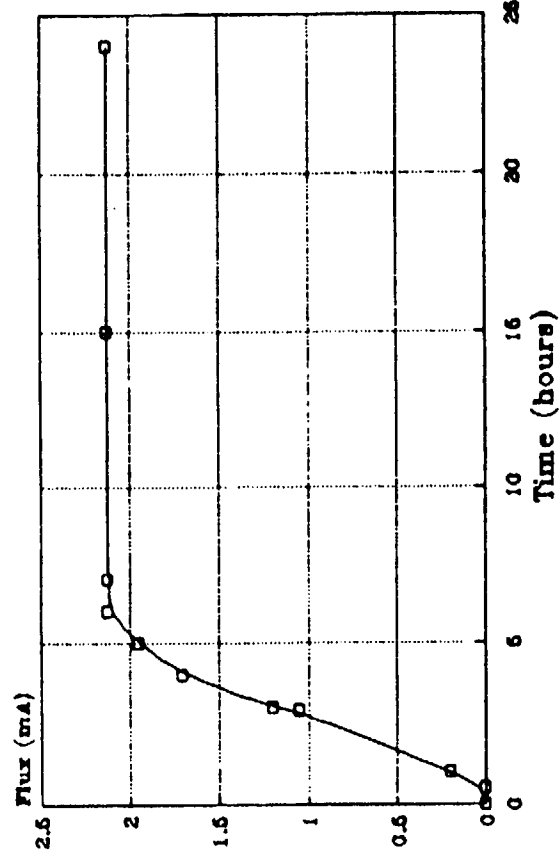


Figure 20. Experimental hydrogen permeation curve for CDA 102 at 95°C with 0.5 g/l arsenite added to the catholyte. Charging current 0.2 mA/cm².



Sample Size = 6 cm²

Figure 21. Experimental hydrogen permeation curve for CDA 715 at 95°C. Charging current 0.2 mA/cm².

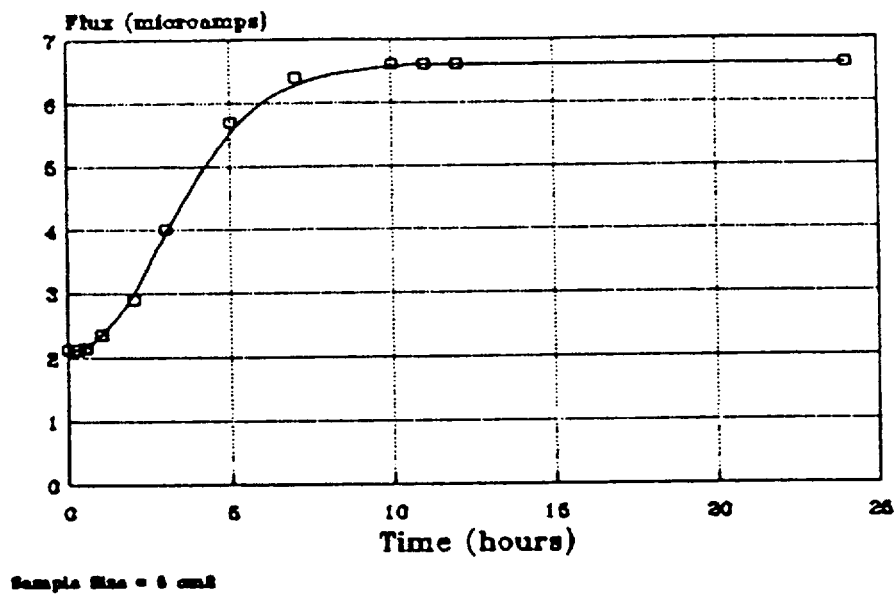
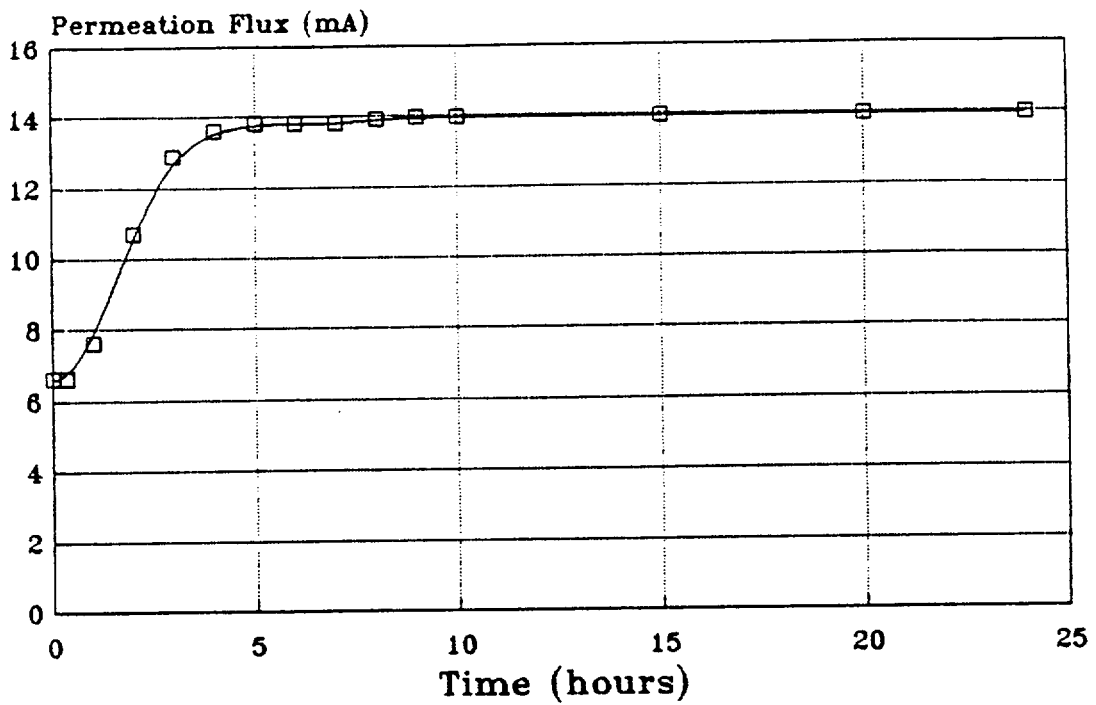


Figure 22. Experimental hydrogen permeation curve for CDA 715 at 95°C. Charging current 0.48mA/cm².



Sample Size = 5cm²

Figure 23. Experimental hydrogen permeation curve for CDA 715 at 95°C. Charging current 1 mA/cm².

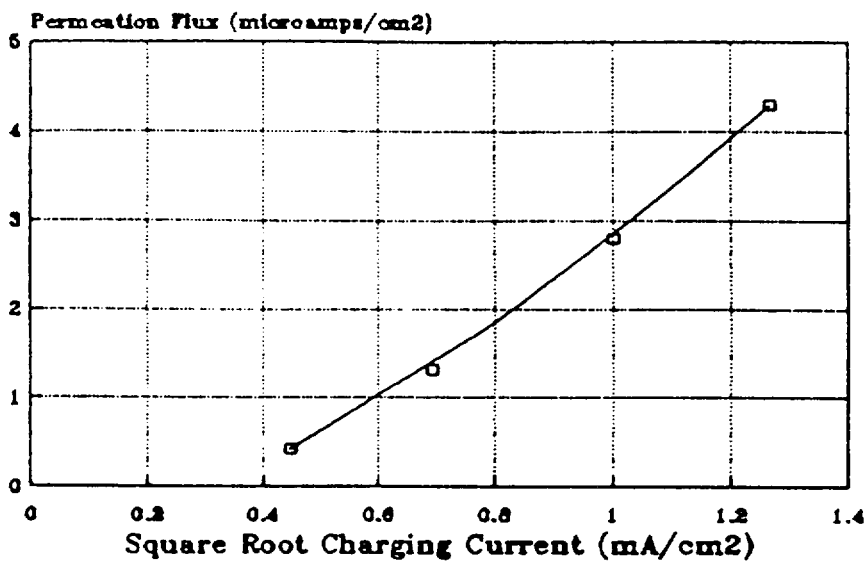


Figure 24. J_p versus $(i_c)^{0.5}$ curve used to assist in the diagnosis of the HER for CDA 715 at 95°C.

Parameter	Ref[3]	Value		Ref[2]
		Ref[6]	Ref[18]	
Material	Pure Fe	Ferrovac Fe	Zone-refined Ni	Armco Fe
D_1 ($\text{cm}^2 \text{s}^{-1}$)	5×10^{-5}	5×10^{-5}	4×10^{-10}	5×10^{-5}
L (mm)	2	0.37	0.08	0.77
b (mole(A·cm ⁻¹))	0.04	0.01	200	0.02
pH	1	13	1.3	1
α	0.38	0.45	0.56	0.56
$i_0 \equiv i_0'$ (A cm ⁻²)	3×10^{-6}	1×10^{-6}	4×10^{-6}	6×10^{-7}
k_1^0 (cm s ⁻¹)	1×10^{-7}	0.2	2×10^{-7}	2×10^{-8}
k_1 (mole (cm ² ·s) ⁻¹)	4×10^{-11}	1×10^{-11}	4×10^{-11}	6×10^{-12}
k_3 (mole (cm ² ·s) ⁻¹)	3×10^{-6}	1×10^{-7}	5×10^{-6}	7×10^{-11}
k'' (mole cm ⁻³)	2×10^{-6}	2×10^{-7}	8×10^{-3}	1×10^{-6}
c_g (mole cm ⁻³)				4×10^{-8}
θ_e	0.004	0.01	0.003	0.003
η_c^l (mV)	-610	-380	-440	-430
η_c^u (mV)	-920	-640	-650	-640

Table 4. Parameters calculated from past permeation data using the I-P-Z method.

Parameter	Value
D_{app} (cm ² /sec)	5.0×10^{-10}
L (cm)	.0061
b (mole/(A-cm))	126.4
pH	11.8
E_{rev} (mV vs. Ag/AgCl)	-857
α	0.44
i_0 (A/cm ²)	1.02×10^{-5}
k_7 (mole/(cm ² -sec))	1.06×10^{-10}
k_5 (mole/(cm ² -sec))	1.41×10^{-9}
k'' (mole/cm ³)	0.0014
c_g (μ A/cm ²)	-1.2
θ_e	0.002
η_c^1 (mV vs. Ag/AgCl)	-20
η_c^u (mV vs. Ag/AgCl)	-352

Table 5. Parameters calculated for CDA 715 at 95°C from the data obtained in this study using the I-P-Z method.

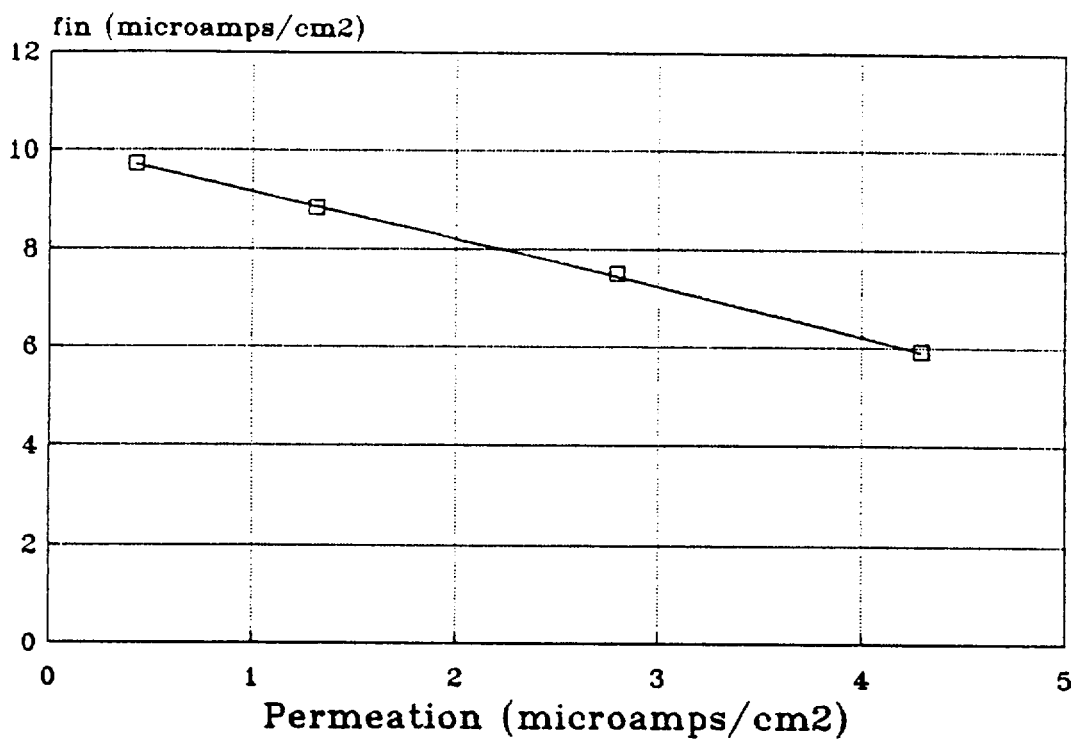


Figure 25. Experimental f_{in} versus J_e curve for CDA 715 at 95°C.

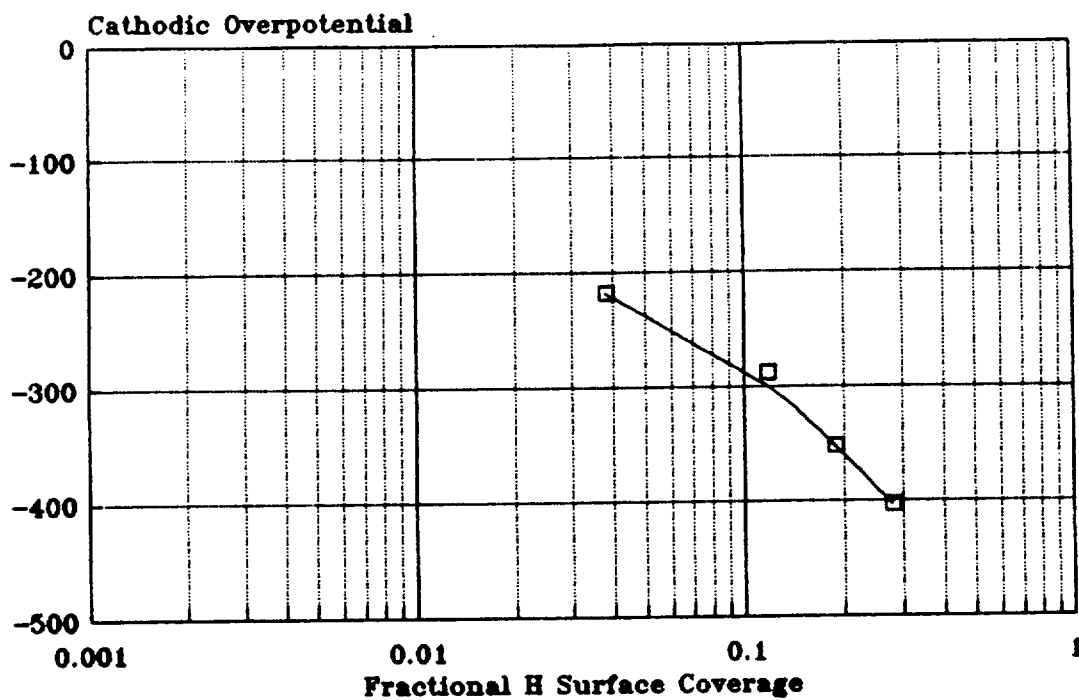


Figure 26. Plot of overpotential versus fractional hydrogen coverage, θ_H , obtained by application of the I-P-Z analysis to the present data.

Part 3. The kinetics of hydrogen evolution, absorption and
fracture of Incolloy 825 and Hastelloy C22.

S. Kesavan

B.E. Wilde

3.0 Introduction.

Corrosion of metallic alloys used in waste-package containers is one of the most likely causes of container failure. The forms of corrosion that may occur are uniform corrosion, galvanic corrosion or the traditional localized forms of corrosion such as pitting, crevice corrosion, intergranular corrosion, dealloying, stress corrosion cracking, and hydrogen induced damage ¹⁾*

Localized corrosion of candidate container materials has been investigated by many workers⁽²⁻⁷⁾. Lukezich and Wilde ²⁾ evaluated the susceptibility of candidate container materials (Type 316 L stainless steel (316L), Incolloy 825 (I825), and Hastelloy C-22 (C22)) to pitting and crevice corrosion in J-13 water utilizing exposure and electrochemical techniques. Type 316L stainless steel was found to be susceptible to pitting and crevice corrosion in J-13 water. Incoloy 825 exhibited no evidence of localized corrosion in J-13 water. However, I825 became susceptible to pitting when the chloride content was increased to 1000 times the natural concentration. Concentration of chlorides is predicted due to evaporation of the ground water on the hot surface of the container.

Hastelloy C-22 was found to be immune to localized corrosion in both J-13 water and concentrated chloride environment.

Juhas and Wilde ³⁾ investigated low temperature sensitization in 316L stainless steel with minor variations in carbon and nitrogen content and its influence on susceptibility to

* see references

intergranular corrosion.

Tests conducted at Southwest Research Institute ⁴⁾ have indicated that Type 304L stainless steel is susceptible to transgranular stress corrosion cracking in a repository vapor-phase environment.

Kassner et al. ⁵⁾ evaluated the susceptibility of candidate container materials to stress corrosion cracking by slow strain rate tests. These tests were conducted on specimens exposed to simulated J-13 water (Table 1) at 93°C and strain rates of 10^{-7} and 10^{-8} sec⁻¹ under crevice and non-crevice conditions. Crevice conditions were simulated by drilling holes through the tensile specimen and inserting a plug made of the same material. Susceptibility to cracking was evaluated (Figure 1) based on a stress ratio, which is defined as the ratio of the increase in stress following the initiation of local yielding for the material in the environment to the corresponding stress increase for an identical test in air at the same elongation ⁵⁾.

Based on the stress ratio, the ranking of the materials in order of increasing resistance to cracking is Type 304L stainless steel < Type 316L stainless steel < Alloy 825/Cu-30%Ni < Cu/Cu-7%Al.

The present investigations are motivated by the possibility of any of the hydrogen containing species referred to in Part 1 (not necessarily formed by container corrosion), causing a container failure by hydrogen embrittlement (HE) as a result of hydrogen absorption in a region such as the container welded cap.

It has been shown that high nickel and stainless steels can be susceptible to HE but no basic data exists on the hydrogen

absorption factors that control such attack.

HE was detected in Fe-Ni alloys in 1960 ⁶⁾ and the increased use of stainless steels in nuclear power plants and Ni-based superalloys in severe hydrogen generating aqueous environments ⁷⁾ resulted in a sharp increase in HE investigations.

Hydrogen permeation through austenitic stainless steels has been examined primarily by gaseous charging techniques at elevated temperatures (200-500°C) little or no information exists for hydrogen absorption from aqueous solutions at elevated temperatures. Surface condition has been shown to be an important factor, especially at low hydrogen pressures. Effects of hydrogen on mechanical properties of austenitic stainless steels differ widely depending upon the alloy and its metallurgical condition. The degree of hydrogen damage does not correlate uniquely with an alloying element. For example, tensile ductility correlates with Ni content in Fe-Cr-Ni alloys but not in Fe-Cr-Ni-Mn alloys. However, segregation ⁸⁾ of elements such as manganese, silicon, phosphorous and sulfur have been shown to augment the extent of hydrogen damage.

Entry of hydrogen into nickel and Ni-based alloys has been studied by Fiore et al. ⁹⁾. This latter study showed that hydrogen permeation in pure nickel was independent of the source of hydrogen (gaseous or electrochemical). Attempts were also made to identify the mechanism of the hydrogen evolution reaction. Hydrogen permeation as a function of temperature was studied using a cell immersed in an oil bath. Subsequently, an analytical technique to model hydrogen absorption by metals ¹⁰⁾ was developed. This model was based on measuring hydrogen released from a heated and melted

sample and computer modeling of hydrogen ingress and egress.

The question of hydrogen transport by mobile dislocations has been investigated by many scientists. Evidence for dislocation transport has been provided by observation of tritium release ¹¹⁾ during plastic deformation and in-situ TEM observations ¹²⁾. Tien et al. ¹³⁾ have developed a kinetic model for transport of hydrogen as Cottrell atmospheres and predicted strain rates at which such transport ceases. Hydrogen permeation experiments have also been carried out to investigate the role of strain in permeation.

Donovan ¹⁴⁾ observed a fifteen fold increase in the subsurface hydrogen concentration of annealed nickel tubes after straining plastically. He also observed a change in apparent diffusivity of tritium due to plastic deformation. The large increase in absorption was attributed to transport of hydrogen by dislocations.

Kurkela et al. ¹⁵⁾ observed that the diffusion coefficient of hydrogen in nickel increased by a factor of 10^5 on plastic straining. The experiments were carried out at room temperature and in a standard electrochemical permeation cell. Later, Otsuka et al. ¹⁶⁾ and Lin et al. ¹⁷⁾ showed that the effect attributed to plastic deformation was caused by Joule heating during hydrogen charging. du Plessis et al. ¹⁸⁾, using a gas phase permeation technique, observed no increase in hydrogen permeation with stress (up to 80% elastic limit) at 400-600°C.

Frankel and Latanision ¹⁹⁾ studied hydrogen permeation through nickel as a function of strain rate. They observed an increase in permeation flux at low strain rates and a decrease at higher strain rates. A dynamic trapping and lattice refilling model was proposed to explain the observed behavior. According to this

model, at high strain rates, trapping at newly created dislocations decreases the hydrogen concentration gradient at the exit surface, resulting in a lower permeation flux. At low strain rates, lattice sites are refilled by lattice diffusion and probable dislocation transport. This, coupled with an increased solubility (due to creation of active sites), leads to a higher permeation flux. They suggested a qualitative diffusion parameter (D/eL^2), where D is the diffusivity of hydrogen, e is the strain rate used and L the thickness of the permeation membrane) to be used to assess contribution due to trapping during plastic deformation. A high value (>10) indicates negligible effect due to trapping (in other words, adequate lattice refilling) and a lower value indicates effect of trapping on hydrogen permeation.

The effect of strain on permeation at elevated temperatures, however, has not been formally addressed in the literature. The increase in diffusivity at elevated temperatures coupled with possible strain-enhanced absorption could significantly affect hydrogen permeation.

A part of the present investigation addresses this point within the overall objectives of Part 3 of the program which are as follows:

1. Development of a high temperature hydrogen permeation database from which the kinetics of hydrogen absorption and diffusion can be measured on C 22, I825 and 316L,
2. Development of data on the HE resistance of C22 and I825 as a function of temperature under aggressive simulated conditions,
3. Development of a technique to evaluate the effect of

plastic deformation on hydrogen permeation at temperatures up to 150°C.

3.2 Technical background to embrittlement

The technical aspects of hydrogen evolution, absorption and diffusion in metals has been reviewed in detail in Parts 1 and 2 and will, therefore, not be repeated here. However, a comprehensive review of current theories on HE will be presented to assist the reader in understanding the discussion of the results.

3.2.1 Hydrogen embrittlement theories

Hydrogen embrittlement ²⁰⁾ is defined as the hydrogen caused reduction of the load-bearing and/or the mechanical energy absorption ability of a metallic alloy.

Over the years, several theories have been proposed to explain HE: i) the pressure expansion theory; ii) the surface energy theory; iii) the brittle crack tip theory; iv) the enhanced plastic flow theory; v) the hydride formation theory; and vi) the decohesion theory. There is not a single theory that can explain all HE phenomena. It has been proposed that not one but several of the specific mechanisms act in series culminating in HE with decohesion playing a major role.

Pressure expansion theory: This theory was suggested by Zappfe and Zims ²¹⁾. According to this theory, gaseous molecular hydrogen of very high fugacity precipitates at pre-existing microcracks and voids in the metal. The very high internal pressure enhances void growth and crack propagation. This is true in blister formation ²²⁾ but not relevant to cases of reduced ductility or increased rate of crack propagation induced by

exposure to low pressure hydrogen ²³⁾. It has also been suggested that dislocation transport could create large internal pressures in voids even when the source of hydrogen was at low fugacities ²⁴⁾.

Surface Energy theory: Petch and Stables ²⁵⁾ and others ²⁶⁾ proposed that the surface free energy (γ) is decreased by hydrogen adsorption. As per the Griffith fracture criterion, the fracture stress of a perfectly brittle material is proportional to $\gamma^{0.5}$. Hence, the work of fracture is reduced and cracking enhanced. More arguments have been made against the surface energy theory compared to those supporting it. One of the serious objections is the role of adsorbed oxygen. Oxygen, which has a greater heat of adsorption, not only fails to promote cracking but also stops the hydrogen effect. Vitek ²⁷⁾ has argued that the surface energy theory greatly underestimates the work of fracture. The objection that this theory cannot account for discontinuous cracking has been countered by Thompson ²⁸⁾. He has shown that the local crack propagation rate can be controlled by the Petch-Stables process, even though irreversible plastic deformation accompanies the cracking.

Decohesion theory: In 1926, Pfeil ²⁹⁾ proposed that hydrogen adsorbed on iron surfaces decreased the cohesion across cubic cleavage planes. Troiano ³⁰⁾ and Oriani ³¹⁾ supported and provided examples for this mechanism. In systems where fracture occurs transgranularly, failure is expected to be along the cleavage planes and to exhibit the fractography of cleavage while intergranular fracture should occur directly along the grain boundary surfaces. In situ TEM experiments ³²⁾ have shown that fracture occurs mostly along slip planes near the grain boundaries

often crossing the grain boundary to follow slip planes in adjacent grains. In systems which fracture transgranularly, evidence of significant local plasticity is observed as opposed to pure cleavage. The above examples seem to suggest that the phenomenon of interatomic bonds being weakened by hydrogen may be a cause of HE in many systems but not the sole reason for HE.

Enhanced plastic flow theory: Beachem ³³⁾ first suggested that HE of steels was associated with locally enhanced plasticity at the crack tip. Lynch ³⁴⁾ and Birnbaum's ³⁵⁾ work support this explanation. The enhanced plasticity phenomenon has been observed in pure metals, solid solution strengthened alloys and in fcc, hcp and bcc crystal structures. Lynch suggests, based on parallelism between HE and liquid metal embrittlement of high strength alloys, that the enhanced plasticity is due to a surface adsorption effect. Lynch further proposed that the major effect of hydrogen is the promotion of dislocation injection at the crack tip. Birnbaum considers the effect to occur in the volume of the material and near the surface. An extensive review ³⁶⁾ supporting the above statement has been published. On the other hand, hardening effects due to hydrogen ³⁷⁾ are also observed showing that softening is not general.

3.2.2 Slow Strain Rate Tests (SSRT)

The procedure used in this study to evaluate the resistance of I825 and C22 to HE was developed by Parkins ³⁸⁾ as a technique to evaluate stress corrosion cracking (SCC) of carbon steels in hot nitrate solutions. The main feature of this test method is the use

of dynamic strain to stress the specimen, in contrast to conventional SCC tests conducted under a static stress condition.

A SSRT-type test machine is shown in Figure 2 and applies a linear extension to a tensile specimen at a predetermined rate, usually in the range 10^{-4} to 10^{-7} cm/s. The principal components of a SSRT machine (Figure 2) are a power drive (a constant speed electric motor), speed reducers to achieve a low strain rate, worm gear to convert rotary motion to linear motion, load cell to monitor stress and a mechanically hard frame.

Such procedures are used widely ³⁹⁻⁴²⁾ to qualitatively detect stress corrosion cracking and hydrogen embrittlement. For a detailed description of the application of the SSRT technique to detect SCC in specific metals and alloys and in specific environments, the interested reader is referred to an ASTM publication ³⁹⁾ on SSRT technique. One of the features of this technique is that a fresh surface is created continuously and exposed to hydrogen evolved during the test. Hence, a material which does not exhibit hydrogen embrittlement in the mechanically severe but short duration SSRT is probably immune to embrittlement in practice.

The fracture surface of the specimen is usually examined to determine the presence/absence of embrittlement. In the absence of SCC or HE, the fracture exhibits a typical cup and cone character with no secondary cracking along the gage length (Figure 3). In the presence of SCC or HE, the ductility of the specimen is markedly reduced (Figure 4). Secondary cracks are usually observed along the gage length of the specimen. Propagation of secondary cracks, observed on a longitudinal section, reveals the

transgranular or intergranular mode of cracking (Figure 5). Time to failure, percent reduction in area of cross-section, maximum applied load, plastic strain to fracture and percent elongation are also used to quantify embrittlement. However, the parameters listed above must be used with caution. For example, comparison of ductility parameters (like percent reduction in area or time to failure) should be limited to materials with similar mechanical properties ⁴⁰. For such materials, reduction in area and time to failure scale linearly with increase in ductility (Figure 6).

The slow strain rate technique has also been used by Wilde and Kim ⁴⁰ to determine whether the failure mechanism in a given environment is stress corrosion cracking or hydrogen embrittlement. Stress corrosion cracking is observed over a specific range of strain rate (as it involves film-rupture), whereas severity of hydrogen embrittlement increases continuously with decrease in strain rate (Figure 7).

3.3 Materials and Experimental Procedures

Only the materials and special procedures used in Part 3 will be described in detail; the more generic procedures having been presented in Parts 1 and 2.

3.3 1 Materials

Hastelloy C22 (C22) and Incoloy 825 (I825) were the materials investigated in this study, although some comparative experiments were conducted on AISI 316L stainless steel (316L) since it is a reference container material. Hastelloy C22 and I825 are nickel base alloys, and Table 2 lists the chemical composition of the

alloys used in this investigation. Hastelloy C22 was obtained in foil form from Haynes International and I825 as 0.0625 in. thick sheet. Because of the extremely low hydrogen diffusivity of I825 and 316L, the original 0.0625 in. sheet stock was cold-rolled to a thickness more suitable to experimentation. The material was cold-rolled according to the schedule shown below:

<u>Cold rolling</u>	<u>Degrease</u>	<u>Anneal</u>	<u>Pickle</u>
Total reduction 50% after each annealing.	Hot NaOH solution	970-990°C water quench	HNO ₃ + HF for I825 HCl + HNO ₃ for C22

The final heat treatment of each alloy used in the study was as follows:

316L As received solution annealed foil.

I825 Cold reduction followed by annealing at 980°C in an argon atmosphere; hold time 40 minutes followed by air cooling; final thickness 6.4 mils.

C22 Cold reduction followed by annealing at 1120°C in an argon atmosphere; hold time 20 minutes followed by air cooling; final thickness 3, 4 and 5 mils.

The foil microstructure was observed before cold-reduction and after the final annealing treatment to ensure that no anomalous grain growth had occurred. Membrane specimens for hydrogen permeation experiments were polished on both surfaces to a 600 grit finish using SiC abrasive paper and were rinsed in double-distilled water and ultrasonically cleaned in acetone. The specimen preparation method was the same for all the alloys investigated.

Tensile samples for slow strain rate tests (C-22 and I825) were machined from a 0.5" plate in the mill-annealed condition. Samples (Figure 8) were machined such that their lengths were perpendicular to the rolling direction. Prior to testing, the samples were ultrasonically cleaned in acetone.

Tubular specimens (Figure 9) for straining permeation experiments were prepared from a 0.5" diameter tube (wall thickness

0.1"). The wall thickness was reduced to 0.015" by centerless grinding the inner surface of the tube. A surface roughness of less than 64 microns was achieved by the grinding procedure. The final surface preparation of straining permeation samples was identical to membrane permeation specimens. Both the surfaces were polished down to a 600 grit finish, rinsed in distilled water and ultrasonically cleaned in acetone. In the case of straining permeation samples, these steps were done before welding the connecting pieces to the ends of the tubular permeation specimens.

3.3.2 Experimental procedures

This section describes the procedures developed and adopted to conduct high temperature permeation experiment, polarization experiments, slow strain rate embrittlement tests and straining permeation experiments in Part 3.

High temperature permeation experiments

Figure 10 represents a schematic of the cell designed for high temperature permeation experiments that was custom manufactured in borosilicate glass. To minimize the loss of electrolyte at or near 100°C, a water-cooled Liebig-type condenser was located on each side of the cell. A sloping neck facilitates the escape of bubbles of hydrogen generated on the specimen surface. To allow the transfer of electrolyte at temperature to the input side of the cell, the input environment (0.1N NaOH) was contained in a pear-shaped glass flask in the air thermostat during the attainment of a steady background current density on the anodic side.

High temperature permeation experiments were conducted in an

air thermostat (Figure 11) large enough to accommodate three separate experiments. The temperature was controlled using a Fisher proportional controller, with an accuracy of $\pm 1^\circ\text{C}$. Although Ag/AgCl reference electrodes can be used at temperatures up to 110°C , they are not suitable for extended use at elevated temperatures. Therefore, an external Ag/AgCl reference electrode (maintained at room temperature) was used on both sides of the cell. A Luggin probe filled with 0.1N NaOH connected the reference electrode to the permeation cell.

The potentials measured using the external reference electrode were corrected for thermal diffusion potential errors, using a procedure developed by Macdonald⁴⁴⁾.

The sensitivity of the electrochemical permeation technique relies on the ability of the oxidation circuit (Figure 12) to oxidize diffusing hydrogen. As described in detail in Part 1, for maximum sensitivity the value of $i_{\text{ox(M)}}$ should be small compared to the magnitude of $i_{\text{ox(H)}}$. In room temperature experiments this has commonly been achieved by coating the reactive metal surface on the oxidation side of the membrane with a noble metal such as palladium. As described in Part 1, however, such an expedient could not be employed on basemetals at elevated temperature. Consequently, solutions of 1M Na_3PO_4 and 0.1 M Na_2SO_4 were employed.

The experimental start-up procedure employed for high temperature permeation experiments was as follows:

- 1) Prepare the membrane of choice and degrease in an ultrasonic bath containing acetone followed by a hot air dry.

- 2) Mount the specimen in the cell using teflon-coated neoprene O-rings and adjust for leak tightness. The teflon coating

prevents contamination of the electrolyte at elevated temperatures.

3) Fill the oxidation side of the cell with the appropriate electrolyte and the input side holding flask with the test environment.

4) Insert the platinum auxiliary and reference electrodes in each side of the cell and place in the air thermostat. Connect the water-cooled condensers and degas the oxidation side with purified nitrogen.

5) Heat thermostat to the desired operating temperature.

6) Activate the control potentiostat to maintain an applied anodic potential of $+0.100 V_{Ag/AgCl}$. Record the anodic current density on a high impedance system shown schematically in Figure 12 (either a strip chart recorder or a data acquisition system described in Part 1, Appendix 1).

7) When the background current density reaches a steady-state (usually after 24 to 48 hours), the test environment is gravity fed into the input side of the cell and the surface of the specimen is immediately cathodically polarized at the appropriate current density.

8) The hydrogen permeation flux is recorded continuously until a time independent value of J_{∞} is achieved.

9) Number 8 can be repeated without shutdown at various values of cathodic current densities to simulate the absorption kinetics resulting from various input fugacities of hydrogen.

Cathodic polarization experiments

Cathodic polarization experiments were conducted on C22, I825 and 316L at 25, 50 and 95°C. These experiments were conducted to calculate electrochemical parameters (β_c , i_0 , and α) required to

identify the mechanism of hydrogen evolution on the above alloys. Membrane specimens, identical to those used for permeation studies, were used for polarization experiments. In the potentiostatic experiments, the current response to applied potentials was recorded using a strip-chart recorder. An external Ag/AgCl electrode was used as the reference electrode. The applied potential was maintained for three minutes before recording the current response. This procedure was repeated over the potential range $-1.500 V_{Ag/AgCl}$ to $-0.900 V_{Ag/AgCl}$ in steps of 20 mv.

The reversible potential for hydrogen evolution (in 0.1N NaOH and at 25°C) was determined by measuring the potential between a platinized platinum electrode (saturated with hydrogen at 1 atmosphere pressure) and a Ag/AgCl electrode. The reversible potential for hydrogen evolution was utilized to evaluate hydrogen overpotential in subsequent cathodic polarization and high temperature permeation experiments.

Slow strain rate testing

Slow strain rate tests were conducted on smooth cylindrical test specimens (Figure 8) under cathodic polarization conditions. The diffusivity of hydrogen in high nickel austenitic alloys is very low over 25-100°C (of the order of $10^{-10} \text{ cm}^2.\text{s}^{-1}$). Hence, specimens were precharged with hydrogen for 24 hours prior to testing and hydrogen charging was continued throughout the test duration. The specimen was attached to a specimen support and mounted inside a 1 gallon titanium autoclave. The autoclave system enabled experiments to be conducted at elevated temperatures and high pressures. The threaded tensile specimen (Figure 13) was coupled to the pull rod on one end and to the specimen support on

the other end. The pull rod enters the autoclave through a Conax pressure fitting mounted on the autoclave head. The specimen support was coated with Teflon to electrically isolate the specimen from the autoclave and to limit hydrogen evolution to the gage length of the specimen (Figure 14). A constant crosshead displacement rate of 4×10^{-6} in.s⁻¹ was utilized in all the tests. Experiments were conducted at different temperatures to evaluate the effect of temperature on HE susceptibility. The load on the SSRT specimen was monitored during the test and recorded on a strip-chart recorder. After failure, the fracture surfaces were observed under an SEM. A longitudinal section (adjacent to the fractured region) of the specimen was prepared for metallographic examination, to identify the mode of cracking from the morphology of secondary cracks. From the above tests on C22 and I825 at three different temperatures, a relationship between HE susceptibility and relative hydrogen permeation fluxes was deduced.

3.4 Results and Discussion.

In the interests of clarity the results will be presented in several sections: 1) The kinetics of hydrogen evolution on, diffusion and absorption into C22, I825 and 316L, 2) the effect of temperature on the kinetics of hydrogen evolution and hydrogen absorption, 3) the effect of strain on hydrogen absorption and 4) the susceptibility of C22 and I825 to hydrogen embrittlement in the slow strain rate technique.

3.4.1 Hydrogen evolution, diffusion and absorption kinetics.

Gaseous hydrogen, electrochemical discharge of hydrogen ion and gamma radiolysis of steam are three potential sources of

hydrogen to enter a metal canister. A knowledge of the degree of surface coverage of hydrogen is essential to compare the rate of hydrogen absorption on various candidate metals. This parameter (θ_H) is determined by an evaluation of the kinetics of hydrogen permeation and the HER obtained from cathodic polarization curves.

Figures 15-17 present the cathodic polarization curves for C22, I825 and 316L in 0.1N NaOH at 95°C. The Tafel slope for C22 in 0.1 N NaOH at 95°C is -170 mv/dec and the exchange current density for the HER evaluated from the cathodic polarization curve was 60 mA/cm². The Tafel slope (β_c) is a function of electrons involved in the charge-transfer reaction (z), the transfer coefficient (α) and temperature. As mentioned earlier, the hydrogen evolution reaction mechanism cannot be uniquely identified on the basis of Tafel slope alone. For example, a Tafel slope of -120 mv/dec at 25°C corresponds to four different HER mechanisms. Nevertheless, the transfer coefficient (α) can be evaluated from the Tafel slope. An (α) of 0.5 limits the HER mechanisms from six to four possible rate determining steps; i) electron transfer (rds)/chemical desorption, ii) coupled discharge/chemical desorption, iii) charge transfer(rds)/electroodic desorption, and iv) coupled discharge/electroodic desorption.

For low surface coverages (which are expected at low hydrogen overpotentials), the electroodic desorption (ED) mechanism can be ruled out as the probability of protons discharging onto H atoms is quite low at small hydrogen surface coverages. Table 3 summarizes the parameters evaluated from the cathodic polarization curves. The transfer coefficients (α) are in the range 0.41-0.44, approaching 0.5 as required for a symmetrical potential energy

barrier. Therefore, any one of the four mechanisms corresponding to $\alpha = 0.5$ could be the HER mechanism on C22 and I825 in 0.1N NaOH at 95°C.

Because of a lack of published polarization data on C22 and I825 in an alkaline solution and at an elevated temperature, the results were compared with data in the literature for pure nickel⁴⁴; it is seen that the Tafel slopes agree well with reported data on pure nickel.

3.4.2 Hydrogen absorption kinetics.

High temperature permeation experiments were conducted in which successive permeation rise transients were recorded to obtain steady-state permeation current densities at a minimum of four different charging current densities. A typical experiment lasted 15 days. The reference electrodes were calibrated with respect to a new Ag/AgCl reference electrode after each experiment.

In Table 4, steady-state permeation current densities (J_{∞}) as a function of charging current densities have been compiled for C22, I825, and 316L. The samples used for the permeation experiments were of different thicknesses, hence all permeation currents were normalized to correspond to a sample thickness of 5 mils.

The steady-state permeation current density at 95°C was proportional to the square root of the charging current density in C22, I825, and 316L (Figures 18-20). The apparent diffusivities of hydrogen (D_H) were calculated from permeation rise and decay transients and were almost the same, indicating the absence of surface barriers to hydrogen permeation (Figures 21 and 22). Using

Fick's first law of diffusion, the subsurface concentration of hydrogen on the charging side (C_0) was calculated.

C22 and I825 were both investigated in their annealed state. The permeation flux in C22 is consistently higher than that observed in I825 at different charging current densities (Table 4). The lower permeation flux observed in I825 translates into a lower subsurface hydrogen concentration (C_0). The alloys (C22 and I825) are single phase and austenitic in nature and differ mainly in their chemical composition (wt%'s of iron and nickel). The above results give rise to the following questions; i) why is C_0 under identical charging conditions, lower for I825 when compared to C22 and ii) does it translate into superior HE resistance? Subsequent experimental results will address the above questions.

3.4.3 Determination of surface coverage

An analysis of the permeation and polarization data was carried out to obtain the rate constants of HER steps and the degree of surface coverage (θ_H). The parameters required to calculate the hydrogen surface coverage (θ_H) by the I-P-Z mechanistic model are obtained from polarization and permeation experiments and have been described in detail in Parts 1 and 2.

Figures 18-20 show plots of J_{∞} vs. $ic^{0.5}$ which are linear and confirm that the evolution of hydrogen on C22, I825 and 316L follows the discharge-recombination mechanism. In the plot, a small negative intercept for C22, I-825 and 316L was observed (Figures 18-20). The intercepts in these figures are used for a correction factor in Figures 23-25. Using the permeation data summarized in Table 4 and the polarization data in Figures 15-17,

the parameter $i_0 \cdot \exp(a\alpha\eta)$ was evaluated.

A plot of this parameter versus J_∞ resulted in a straight line which provides a check to determine whether the assumptions in the model have been violated. The y-intercept of Figure 23 equals i_0' . The parameter i_0' approaches the exchange current density (i_0) as θ_H tends to zero. From the slope of Figure 23, the absorption-adsorption constant (k'') can be calculated and a value of k'' equals $8.9 \times 10^{-3} \text{ mol/cm}^3$ was obtained for hydrogen evolution on C22 in 0.1N NaOH at 95°C. Hence, the surface coverage ($\theta_H = bJ_\infty/k''$) could be calculated.

The absorption rate constant k_{abs} , was calculated at different permeation current densities and the results are summarized in Table 5 and 6.

Review of θ_H values show that the surface hydrogen adsorption is Langmuirian. Also, i_0' (which approaches the exchange current density i_0 at low θ_H) calculated by the I-P-Z method compares well with i_0 estimated by Tafel extrapolation. The above observations show that assumptions in the model have not been violated and justify the application of I-P-Z model to the present investigation.

A comparison of calculated k'' values reveals that the order of magnitude is the same for C22 and I825, although numerically, k''_{C22} is twice k''_{I825} at 95°C. These values are comparable to k'' values for zone-refined nickel in the literature ⁴⁰. The specific absorption rate constant k_{abs} , was found to be very similar for C22, I825 and 316L as shown in table 5. In Table 6, it can be seen that for identical charging current densities, θ_H on C22 appears to be significantly lower than that observed for I825 inspite of the fact

that J_{∞} was higher in C22 than in I825 (see Table 5). This apparent inconsistency we believe, arises due to differences in apparent diffusivities of hydrogen in C22 and I825, see Table 5.

The above inconsistency emphasizes the importance of both diffusivity of hydrogen (D_H) and the sub-surface concentration of hydrogen, (C_0 , which is a function of θ_H) function of hydrogen surface coverage) in determining the absorption of hydrogen into a metallic surface.

3.4.4 The Effect of Temperature

Cathodic polarization and hydrogen permeation experiments were conducted at 25, 50 and 95°C on C22 and I825. The cathodic polarization characteristics of these two materials are presented in Figures 26-29. From the figure, it is observed that the Tafel slope (β_0) varies and increases with increasing temperature.

The value of the charge transfer coefficient (α) was calculated from the relation $\beta = 2.3RT/\alpha F$, and was found to be between 0.40-0.44.

The steady-state permeation current density was observed to be a linear function of square root of the charging current density see Figures 30-33, from which we can conclude that the HER follows a coupled-discharge/recombination mechanism over the temperature range 25 to 95°C.

The influence of temperature on the steady-state permeation current density for C22 and I825 is presented in Table 7 in which J_{∞} is seen to increase as expected with increase in temperature. It is of interest to note that the flux observed on I825 was

smaller at each temperature than that noted on C22.

Apparent diffusivities were calculated from permeation rise transients as a function of temperature and were found to obey a simple Arrhenius-type relationship as shown in Figure 34. Using Fick's first law of diffusion it was found that (C_0) decreased with increase in temperature. These observations are in agreement with previous published data for A-471 steel ⁴⁵⁾.

3.4.5 The influence of stress/strain on hydrogen absorption kinetics.

A schematic of the tubular straining permeation specimen used in this investigation is shown in Figure 35. In our investigation, hydrogen was evolved on the outer surface of the specimen and detected on the inside surface. Scully and Moran ⁴⁶⁾ charged hydrogen on the inner surface of a tubular specimen and experienced difficulty in maintaining a uniform current density throughout the length of the sample. In our experiments, a uniform current distribution on the length of the sample by the evolution of hydrogen on the outer diameter of the tubular specimen which diffuses through the wall of the tube to be oxidized on the inner surface. The inner surface was maintained at an anodic potential to oxidize the permeating hydrogen. An external, water-cooled Ag/AgCl reference electrode was used on the oxidation side which was found to be more stable with time compared to an internal reference electrode. A Luggin probe was provide to minimize IR drop and a platinum wire was wound over the Luggin probe (Teflon) served as the counter electrode.

The effects of static tensile stress on the rate of

absorption of hydrogen into C22 is summarized in Figure 36. When the tubular permeation specimen was stressed to 20 ksi and then charged with hydrogen, an increase in permeation current was noted when compared with that obtained in the absence of stress; e.g. the permeation current density increased from 1 mA/cm² ($\sigma=0$) to 1.35 mA/cm² ($\sigma=20$ ksi). It was not possible to achieve a greater elastic stress at 95°C.

When the C22 specimen was strained in dynamic tension at the rate of 4×10^{-7} s⁻¹ whilst being simultaneously charged with hydrogen, a decrease in hydrogen permeation ($J_{\infty} = 0.51$ mA/cm²) compared to the unstressed case was observed. When the straining was terminated and the specimen was left with a stress well into the plastic range, no change in the permeation current was observed for up to 48 hours after cessation of deformation.

These results suggests that dislocation enhanced transport of hydrogen does not occur in C22 under the conditions of test. It has been reported in the literature based on binding energy calculations ⁴⁷⁾, that concentration of hydrogen in defects is roughly equivalent to the lattice concentration in nickel. This suggests that, in nickel, hydrogen atoms in the lattice interstitial sites will not be attracted to dislocations which is in qualitative agreement with our observations.

Because of time constraints equivalent studies on I825 could not be conducted.

3.4.6 Hydrogen embrittlement studies using slow-strain rate procedures during hydrogen charging.

It has been reported previously that under similar hydrogen charging conditions, C22 absorbed more hydrogen than I825 as

evidenced by the higher J_{∞} . The purpose of SSRT was to determine if the noted differences in hydrogen absorption of these alloys would be reflected in their resistance to HE. In addition the effects of temperature on the HE characteristics were to be evaluated.

Solid tensile samples (1/8" dia) were subjected to a continuous tensile load at a strain rate of 4×10^{-6} in.s⁻¹. The results for C22 and I825 are summarized in Table 8 for various charging currents and temperatures. At 25°C in the absence of hydrogen charging, C22 exhibited a reduction in area of 75% with no cracks evident along the gage length when viewed under a 50X stereomicroscope. The fracture was of the cup and cone type; and was typical of a microvoid coalescence (MVC) when observed using a scanning electron microscope (SEM) (see Figures 37 and 38). In contrast, under hydrogen charging conditions the reduction in area observed on an equivalent C22 sample was 42.9% with numerous secondary cracks visible along the gage length; see Figure 39 and 40. SEM evaluation of the fracture surface indicated that the fracture was predominantly MVC in the core or central region of the round specimen, surrounded by a ring of quasi-cleavage (QC) region extending to the surface caused by HE; see Figure 41. A clear region of demarcation existed between the MVC and QC regions; see Figure 42.

These observations suggest that HE fracture originated on the surface of the specimen and is controlled by a diffusion process. Embrittlement of the near-surface region reduces the load-bearing cross section and results in a tensile overload fracture. Calculation of diffusion distance ($\sqrt{D_H t}$) agrees well with the

measured depth of embrittlement; see Figure 41. In other words, embrittlement features do not provide any evidence of enhanced transport of hydrogen by dislocations.

Under identical conditions, I825 exhibited a greater degree of ductility than C22 (67% RA compared with 42.9%RA respectively). The reduction in area value for I825 was not very different than observed with no hydrogen absorption (see Table 7). The fracture surface of the I825 sample was predominantly MVC and with a small number of secondary cracks; (see Figures 43 and 44).

Slow strain rate tests were conducted at 50 and 85°C to evaluate the effect of temperature on HE. At 85°C, a cathodically polarized C22 sample exhibited a ductility comparable to that observed at room temperature in the absence of hydrogen charging. SEM fractographic examination of the fracture indicated a predominance of MVC with cleavage features in a narrow region near the surface (see Figure 45). Further, time to failure and maximum load to fracture were almost identical in the two cases (see Table 7).

These observations indicate the embrittling HE process observed in C22 at 25°C disappears at a higher temperature (85°C). At 50°C, a hydrogen charged C22 sample exhibited reduced ductility, and secondary cracks along with a quasi-cleavage fracture surface, albeit to a lesser extent compared to the room temperature case (see Figure 46).

I825 when cathodically polarized at higher temperatures (85°C), exhibited ductility parameters that were identical to those obtained at room temperature (see Figure 47). These observations indicate that I825 appears to be more resistant to HE than C22 in

the temperature range 25-85°C.

In structurally similar materials, HE susceptibility has been shown to increase with increase in solubility ¹¹⁾. This correlation can probably explain the observed temperature dependence of HE susceptibility in C22. In a previous section, under identical hydrogen charging conditions, the hydrogen solubility was shown to be higher in C22 than in I825. Solubility, although a significant factor, cannot solely account for the observed differences in HE susceptibility of C22 and I825. The two alloys are structurally similar but differ markedly in chemical composition (Table 2). Both alloys contain the transition elements Cr, Ni, Fe, and Mo. I825 is richer in Fe (28%), whereas C22 is richer in Ni (56%) and Mo (14%).

One of the theories proposed to explain HE is the decohesion theory. Troiano ³⁰⁾ proposed that electrons of the hydrogen atoms, in solution in a transition metal, will enter the d-bands of the metallic cores. This increase of the electron concentration of these bands produces an increase in the repulsive forces between the metallic cores. The repulsive forces arise due to the overlapping of the d-bands and determine the interatomic distance of transition metals Fe, Ni, Co, etc. According to this theory, an increase in the repulsive forces (due to hydrogen in solution) manifests itself as a decrease in the cohesive strength of the lattice and hence embrittlement.

Our results on I825 and C22 are compatible with the decohesion theory of HE. Comparison of electronic structures of Ni and Fe (Figure 48) indicates that Ni has a higher concentration of electrons in the 3d band compared to Fe. I825 contains 29% Fe and

40% Ni, whereas C22 contains 56% Ni and 4% Fe. The difference in their HE characteristics is probably due to their different Fe/Ni contents.

In summary, the results of the HE studies indicate that I825 is more resistant to HE than C22 in the temperature range 25-85°C. From the high temperature permeation results presented in Table 11, the hydrogen absorption rate under identical charging conditions, is consistently higher in C22 compared with to I825. Although the SSRT is a very aggressive test, there is a good correlation between amount of hydrogen permeating a material and the observed embrittling tendency.

3.4.7 Conclusions

On the basis of the results obtained in Part 3, the following conclusions may be drawn:

1) Under conditions of identical rate of cathodic hydrogen evolution on the metal surface, I825 consistently absorbed less hydrogen than C22 over the temperature range 25 to 95°C.

2) Both I825 and C22 can fracture by HE in the SSRT under conditions of hydrogen evolution on the metal surface. In qualitative agreement with the observations made in conclusion 1 however, for the same rate of hydrogen generation on the metal surface, I825 evidenced a greater resistance to HE than C22.

3) Both materials evidenced markedly less HE tendencies as the test temperature was increased from 25 to 95°C, suggesting that both may be suitable for a material of construction for a repository canister.

4) Initial data indicate that elastic tensile stresses

increase the rate of hydrogen absorption on C22 at 95°C. Continuous plastic loading past the yield point, resulted in a marked drop in the hydrogen absorption rate on C22 at 95°C.

5) The mechanism of the hydrogen evolution reaction on 316L, I825 and C22 in 0.1N NaOH appears to be the coupled discharge/desorption reaction over the temperature range of 25 to 95°C.

6) Because of the HE noted albeit in the SSRT, it must be concluded that additional studies should be conducted including those in an atmosphere of hydrogen species generated by gamma radiolysis of both steam and water.

3.4.8 References.

- 1) P. Nair, "Project plan for integrated waste package experiments", Center for Nuclear Waste Regulatory Analyses, San Antonio, Texas, (1988).
- 2) S. J. Lukezich, B. E. Wilde, "Corrosion behavior of nickel-base high performance alloys in simulated repository environments", to be published; MS Thesis, The Ohio State University, (1989).
- 3) M.C. Juhas, B.E. Wilde, "The effect of low temperature isothermal heat treatments on the intergranular corrosion of AISI 316 stainless steel simulated weld heat affected zones", Corrosion, 46, 812, (1990).
- 4) C.T. Miller, B.E. Wilde, "Electrochemical studies of hydrogen diffusion and evolution on copper alloys at 95°C", to be published; MS Thesis, The Ohio State University, (1990).
- 5) P.S. Maiya, W.J. Shack and T.F. Kassner, Corrosion, 46, 954,

- (1990).
- 6) P. Blanchard, A.R. Troiano, Mem. Sci. Rev. Lett., 57, 409, (1960).
 - 7) J. P. Hirth and H. H. Johnson, Corrosion, 32, p. 3, (1976)
 - 8) C. L. Briant, Met. Trans. A, 10A, 181, (1979).
 - 9) D.A. Mezzanotte, J.A. Kargol, and N.F. Fiore, Scripta Met., 14, 219, (1980).
 - 10) J.A. Kargol, N.F. Fiore and R.J. Coyle, Jr., Met. Trans. A, 12A, 183, (1981).
 - 11) M.R. Louthan, Jr., G.R. Caskey, Jr., J.A. Donovan and D.E. Rawl, Jr., Materials Sci. Eng., 10, 289, (1972).
 - 12) T. Matsumoto, J. Eastman, and H.K. Birnbaum, Scripta Met., 15, 1033, (1981).
 - 13) J.K. Tien, A.W. Thompson, I.M. Bernstein and R.J. Richards, Met. Trans., 7A, 821, (1976).
 - 14) J.A. Donovan, Met. Trans. A., 7A, 1677, (1976).
 - 15) M. Kurkela and R.M. Latanision, Scripta Met., 13, 927, (1979).
 - 16) R. Otsuka and M. Isaji, Scripta Met., 15, 1157, (1981).
 - 17) R.W. Lin and H.H. Johnson, Scripta Met., 16, 1091, (1982).
 - 18) J.D. Plessis, E. Andrieu and J.P. Henon, Scripta Met., 20, 163, (1986).
 - 19) G.S. Frankel and R.M. Latanision, Met. Trans. A., 17A, 861, (1986).
 - 20) R.A. Oriani, Corrosion, 43, 390, (1987).
 - 21) C. Zappfe and C. Sims, Trans. AIME, 145, 225, (1941).
 - 22) M. Smialowski, "S.C.C. and H.E. of Iron base alloys", NACE, p. 405, (1977).

- 23) G.E. Kerns and R.W. Staehle, Scripta Met., 6, 631, (1972).
- 24) J.K. Tien, A.W. Thompson, I.M. Bernstein and R.J. Richards, Met. Trans., 7A, 821, (1976).
- 24) M.R. Louthan, "Hydrogen in Metals", ASM, p. 53, (1974).
- 25) N.J. Petch and P. Stables, Nature, 169, 842, (1952).
- 26) R. Thomson, J. Materials Science, 13, 128, (1978).
- 27) C.J. McMahon, Jr. and V. Vitek, Acta Met., 27, 507, (1979).
- 28) P. Blanchard, A.L. Troiano, Mem. Sci. Rev. Lett., 57, 409, (1960).
- 29) L.B. Pfeil, Proc. Royal Soc., London, 112A, 182, (1926).
- 30) A.R. Troiano, Transactions ASM, 52, 54, (1960).
- 31) R.A. Oriani and P.H. Josephic, Acta Met., 22, 1065, (1974).
- 32) I.M. Robertson, T. Tabata, W. Wei, F. Heubaum and H.K. Birnbaum, Scripta Met., 18, 841, (1984).
- 33) C. Beachem, "S.C.C. and H.E. of Iron base alloys", NACE, p. 376, (1977).
- 34) S.P. Lynch, Metals Forum, 2, 189, (1979).
- 35) T. Matsumoto and H.K. Birnbaum, Trans. Japan Inst. of Metals, 21, 493, (1980).
- 36) H.K. Birnbaum, ONR. Technical Report, May 1989.
- 37) J.P. Hirth, Met. Trans. A, 11A, 861, (1980).
- 38) R.N. Parkins, "Stress Corrosion Cracking- The Slow Strain Rate Technique, ASTM STP 665", eds. G.M. Ugiansky and J.H. Payer, p. 5, (1979).
- 39) Stress Corrosion Cracking - The Slow Strain Rate Technique, ASTM STP 665, eds. G. M. Ugiansky and J. H. Payer, (1979).
- 40) C.D. Kim and B.E. Wilde, "Stress Corrosion Cracking - The Slow Strain Rate Technique, ASTM STP 665", eds. G.M. Ugiansky

and J.H. Payer, p. 97, (1979).

- 41) J. Congleton, W. Zheng and H. Hua, Corrosion, 46, 621, (1990).
- 42) D.C. Deegan and B.E. Wilde, Corrosion, 29, 310, (1973).
- 43) D.D. Macdonald, Corrosion, 34, 75, (1978).
- 44) A. Atrens, D. Mezzanotte, N.F. Fiore, J.J. Bellina and M.A. Genshaw, NSF report, University of Notre Dame, (1979).
- 45) P.T. Wilson, Z. Szklarska-Smialowska and M. Smialowski, "Hydrogen Effects in Metals", eds. I.M. Bernstein and A.W. Thompson, AIME, p. 961, (1980).
- 46) J.R. Scully and P.J. Moran, J. Electrochem. Soc., 135, 1337, (1988).
- 47) M.I. Baskes, C.F. Melius and W.D. Wilson, "Hydrogen effects in Metals", eds. I.M. Bernstein and A.W. Thompson, AIME, p. 67, (1981).

THIS IS A BLANK PAGE ONLY

Species	Concentration mg/l.
Na ⁺	51.0
K ⁺	4.9
Ca ²⁺	14.0
Mg ²⁺	2.1
Ba ²⁺	0.003
Sr ²⁺	0.05
HCO ₃ ⁻	120.0
SO ₄ ²⁻	22.0
Cl ⁻	7.5
NO ₃ ⁻	5.6
F ⁻	2.2
PO ₄ ³⁻	0.12
SiO ₂	66.4
Fe ²⁺	0.04
V ²⁺	0.002
Li ²⁻	0.05
Al ³⁺	0.03
pH	7.1

Table 1:Chemical analysis of J-13 well water (1).

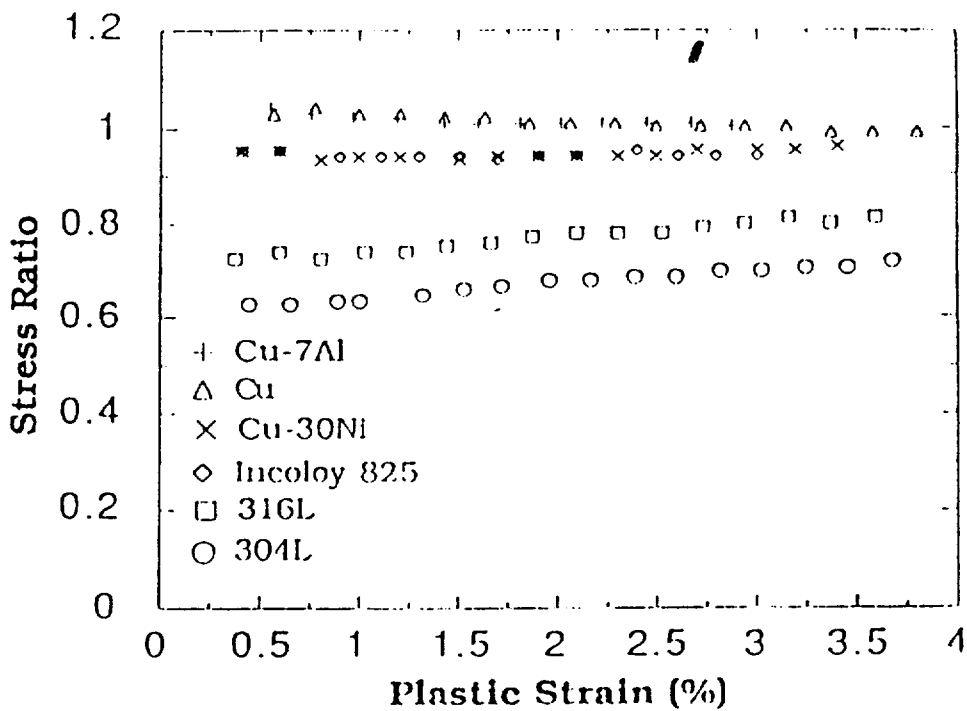


Figure 1: Relative susceptibilities of candidate container materials to stress corrosion cracking (5).

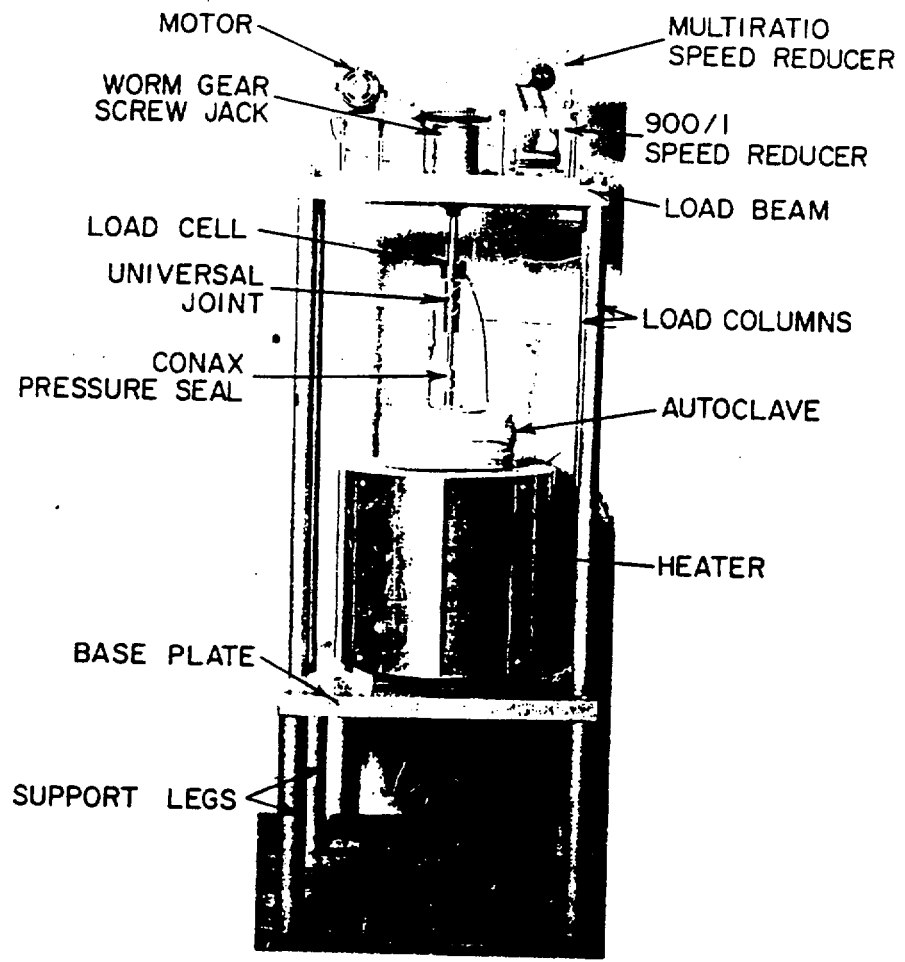


Figure 2: Schematic of a slow strain rate testing unit

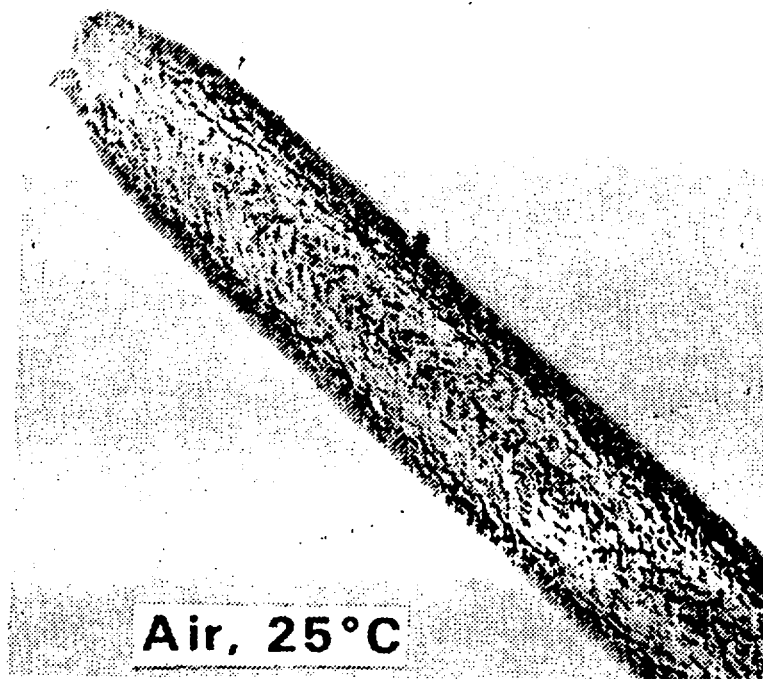


Figure 3: Typical ductile fracture of a SSRT specimen

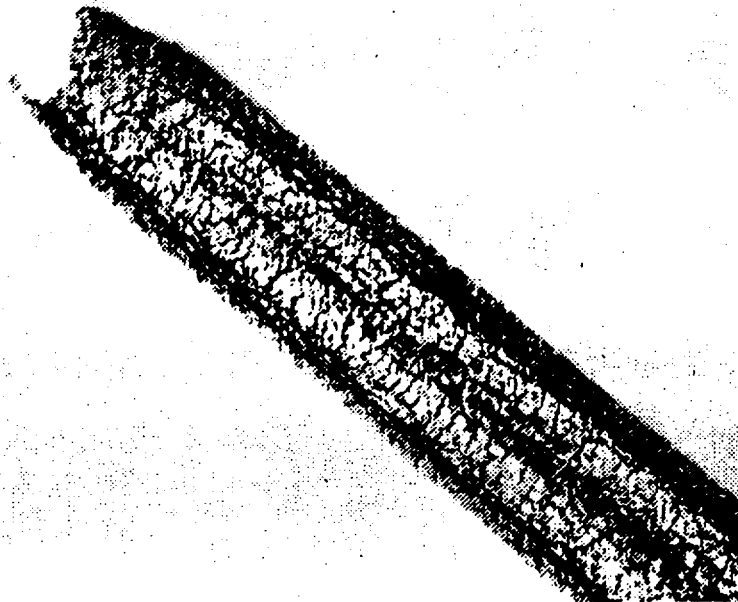


Figure 4: Example of a hydrogen embrittled SSRT specimen

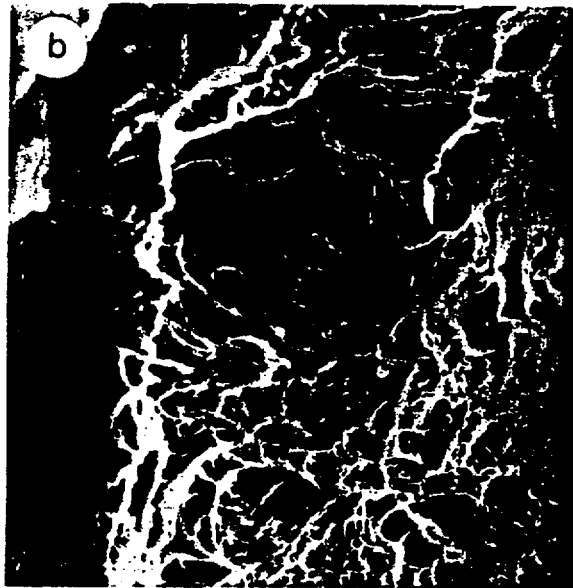


Figure 5: Typical fractographs of specimens investigated by the SSRT technique; a) quasi-cleavage (embrittled) b) dimple rupture (ductile)

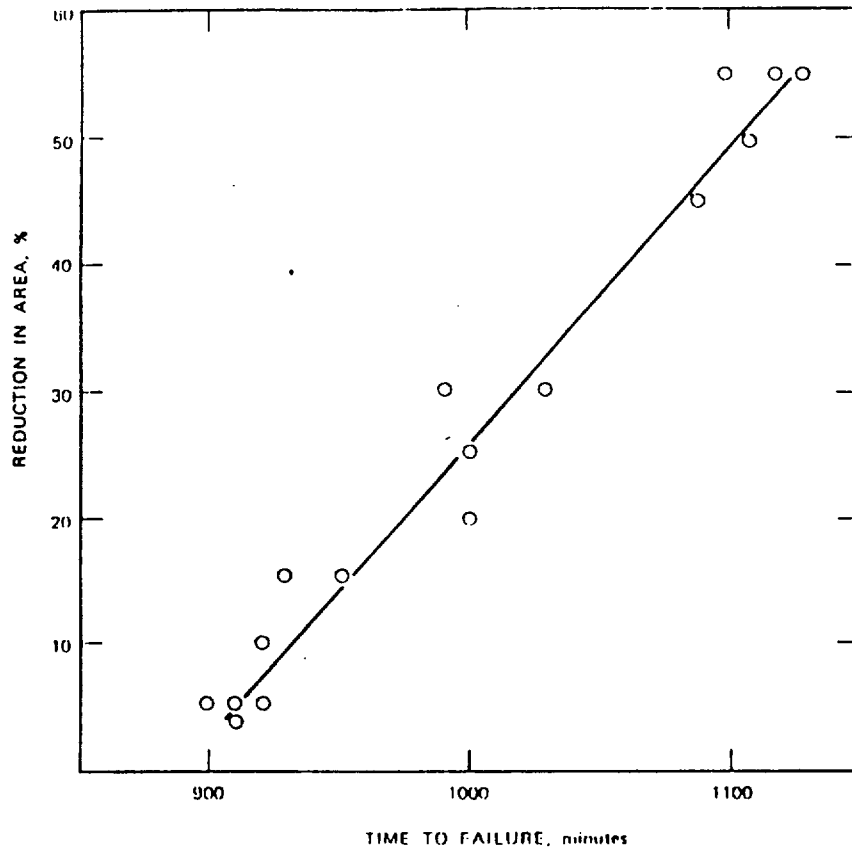


Figure 6: Correlation between ductility parameters (40).

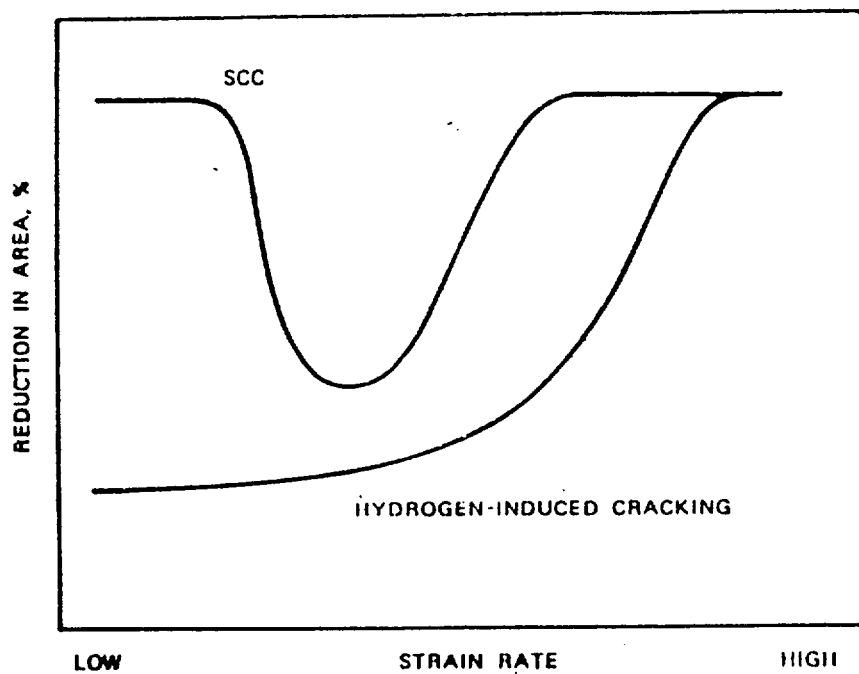


Figure 7: Effect of strain rate on SCC and HE (40).

	Hastelloy C-22	Incoloy 825
C	0.004	0.014
Cr	22.0	20.6
Ni	bal	40.6
Fe	4.3	28.7
Mo	13.6	5.9
W	3.1	ND
Cu	ND	2.12
Ti	ND	0.72
Mn	0.30	0.76
Si	0.02	0.31
P	0.009	ND
S	0.002	0.008
Co	0.80	ND

* ND not detected

Table 2: Chemical composition of alloys investigated

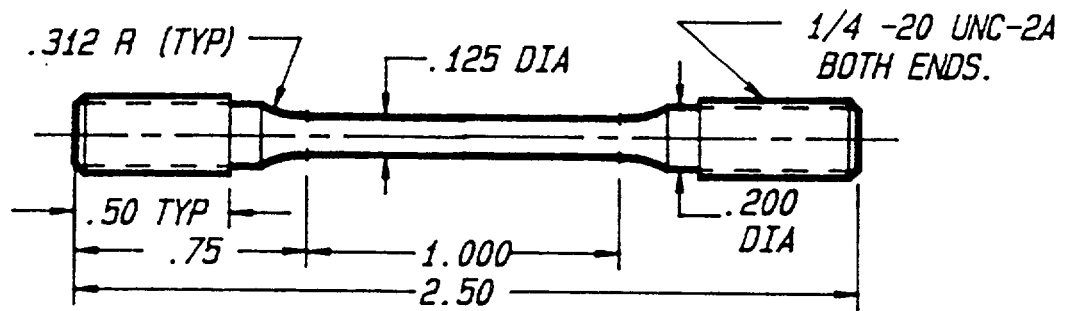


Figure 8: Schematic of cylindrical tensile specimen for SSRT

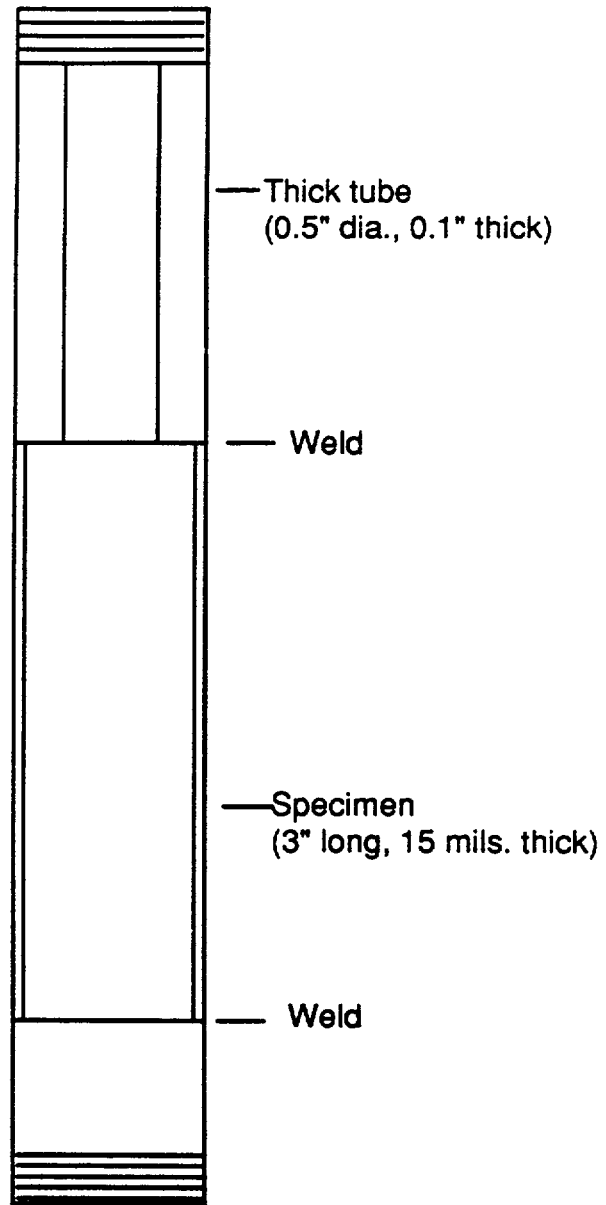
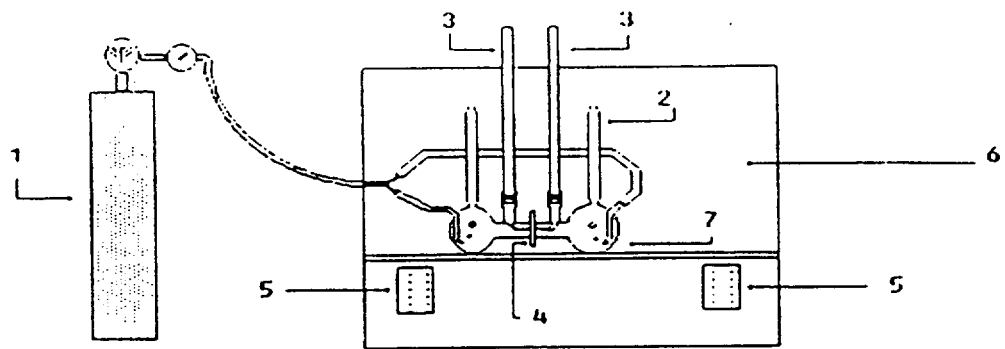
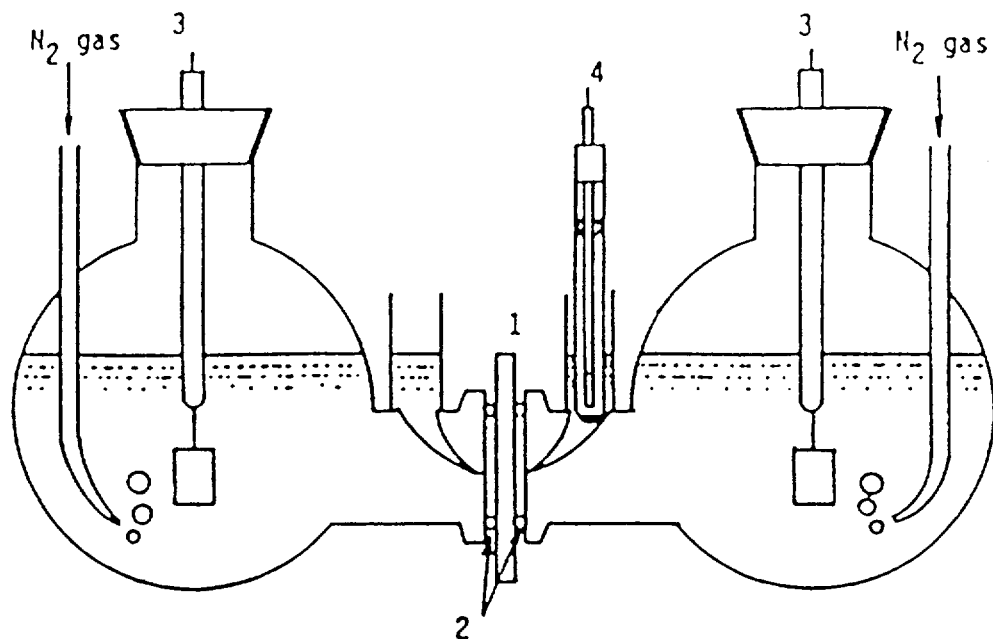


Figure 9: Schematic of a straining permeation specimen



- | | |
|---|---------------------|
| 1. Nitrogen | 2. Condenser |
| 3. Luggin probes for reference electrodes | |
| 4. Permeation membrane | 5. Heating elements |
| 6. Air thermostat | 7. Permeation cell |

Figure 11: layout of permeation cells in an air thermostat



- | | |
|---------------------------|--------------------------------|
| 1. Membrane specimen | 2. Rubber O-ring |
| 3. Pt auxiliary electrode | 4. Calomel reference electrode |

Figure 10: Schematic of the glass cells used for the high temperature hydrogen permeation measurements

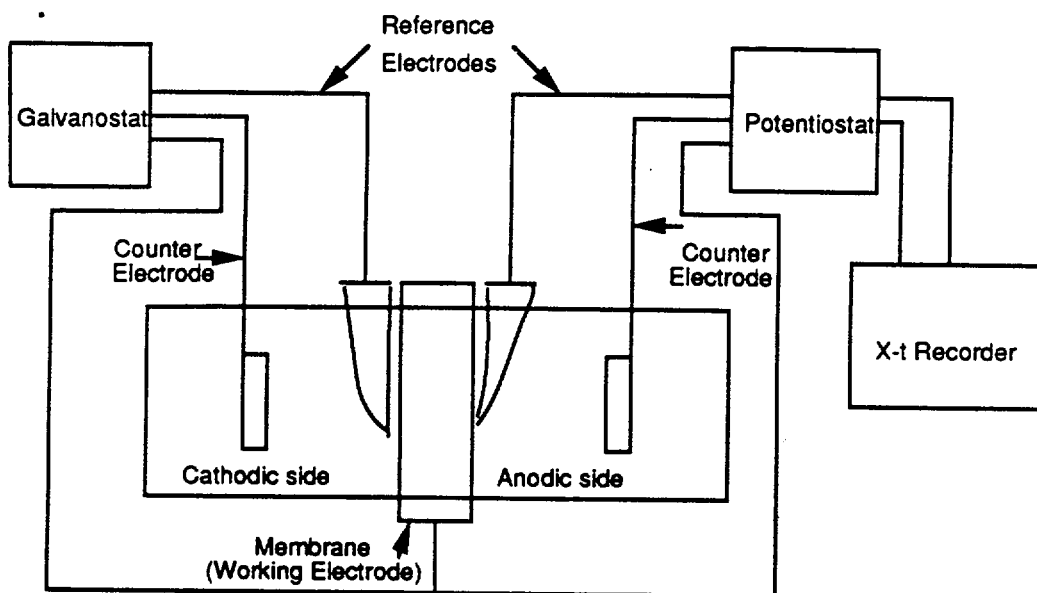


Figure 12: Schematic of the electrical circuit employed in the hydrogen permeation experiments

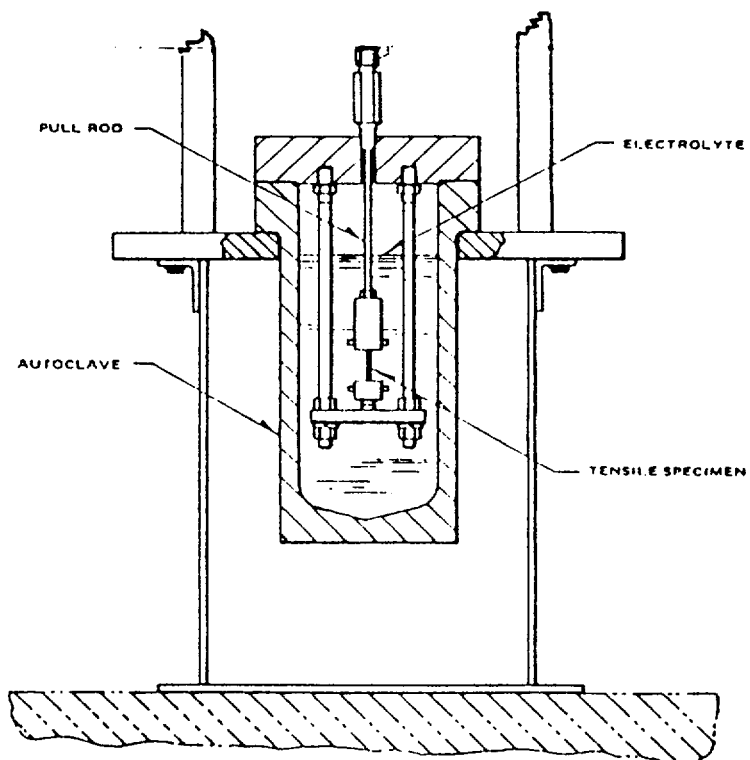


Figure 13: Tensile specimen assembly inside an autoclave

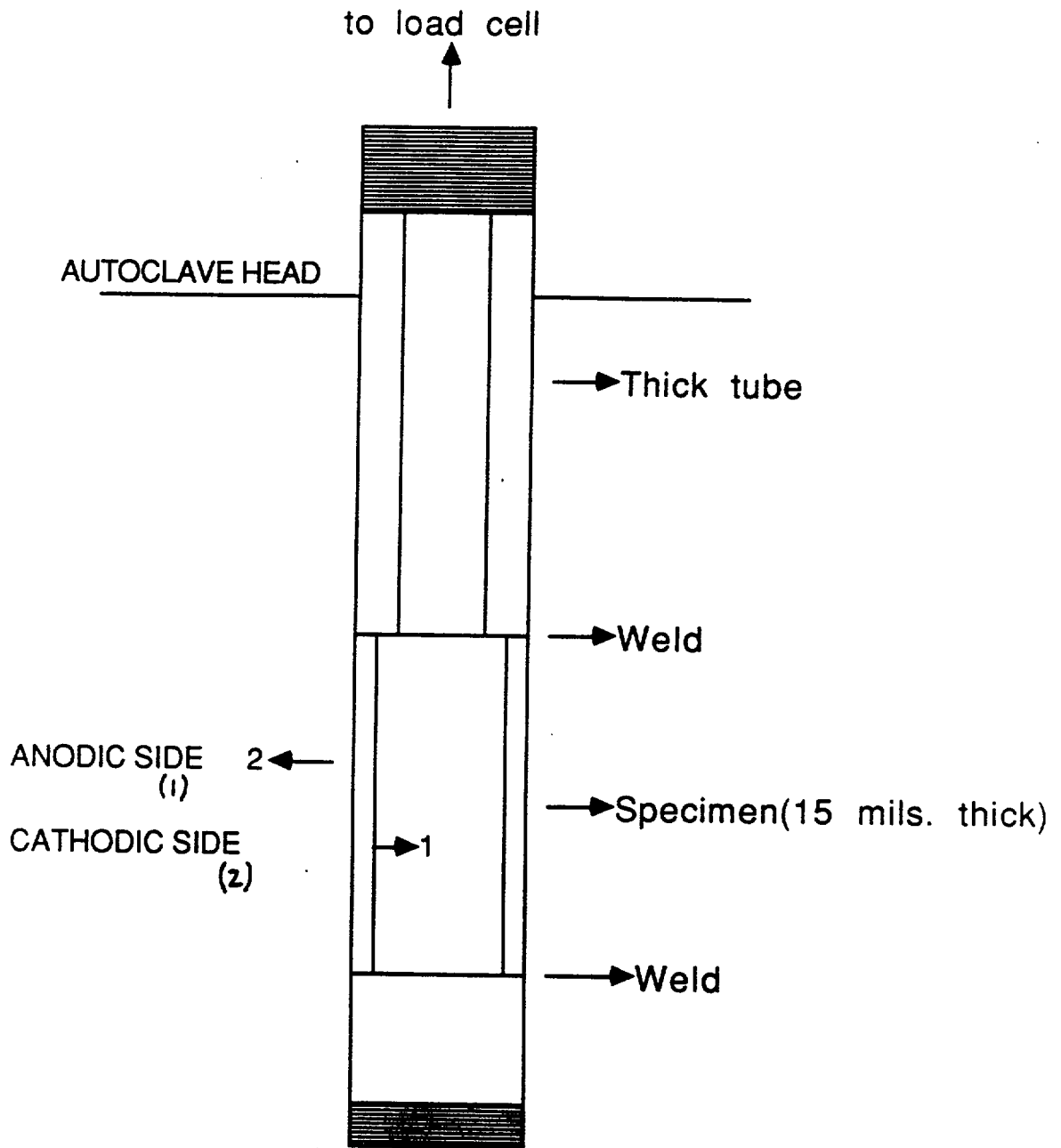


Figure 14: Schematic of a straining permeation specimen assembly

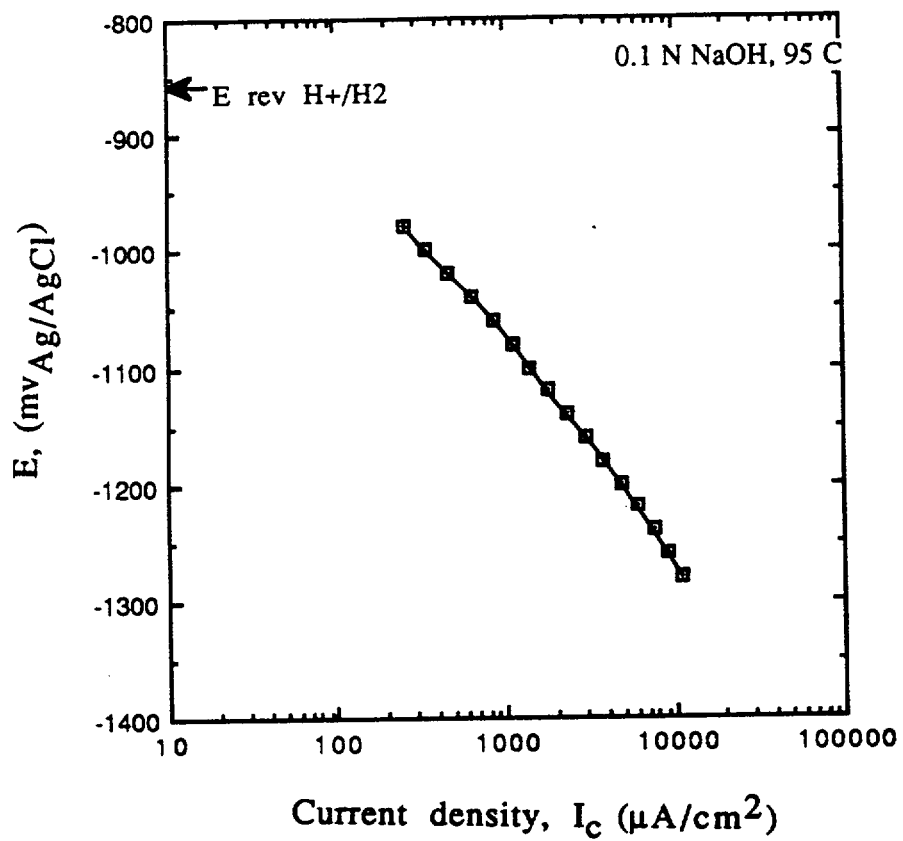


Figure 15: Cathodic polarization plot of C22 in 0.1N NaOH at 95°C

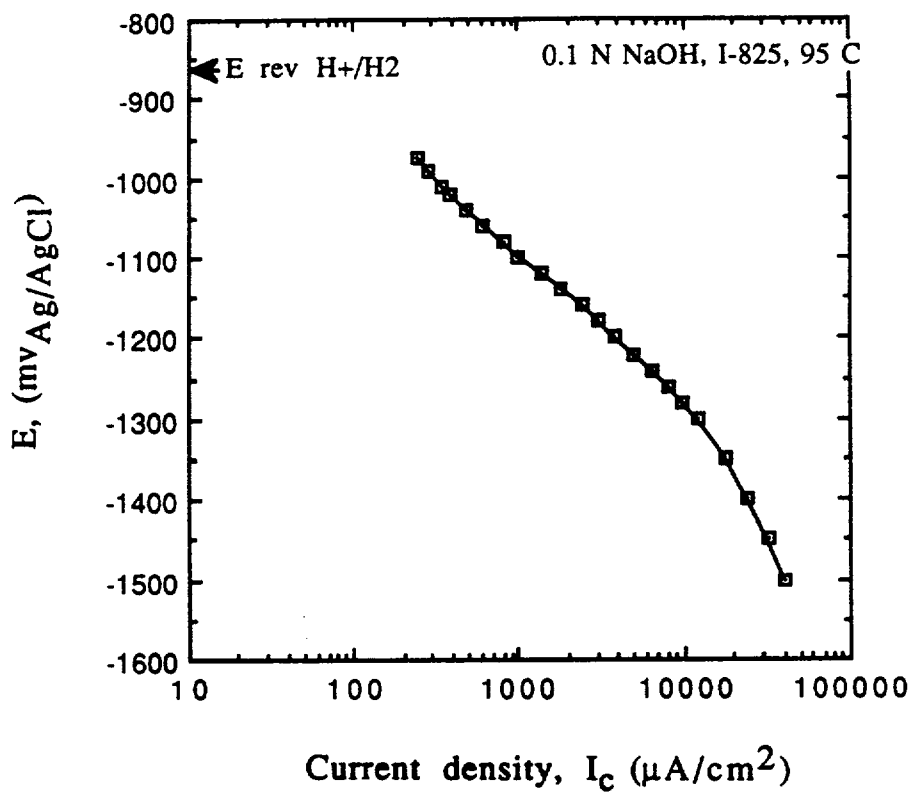


Figure 16: Cathodic polarization plot of I825 in 0.1N NaOH at 95°C

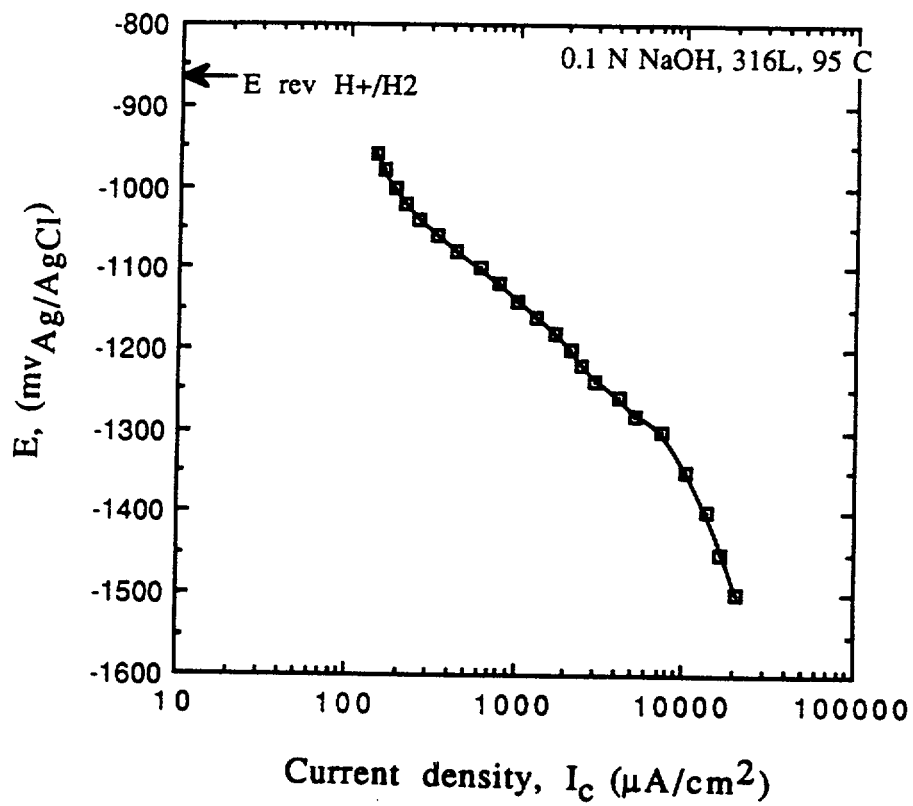


Figure 17: Cathodic polarization plot of 316L in 0.1N NaOH at 95°C

Material	Temp. °K	i_0, H_2 $\mu A/cm^2$	α	β_c mv/dec.
C-22	368	60	0.43	-170
I-825	368	50	0.41	-178
316L	368	30	0.41	-180
C-22	298	30	0.41	-145
C-22	323	40	0.43	-150
I-825	298	28	0.40	-146
I-825	323	38	0.43	-150

Table 3: Summary of parameters calculated from cathodic polarization curves

$i_c, \mu\text{A}/\text{cm}^2 \rightarrow$		200	400	600	1000
$J_\infty, \mu\text{A}/\text{cm}^2$	C22 (5 mils)	0.80	1.72	2.23	3.20
	I-825 (6.4 mils)	0.42	0.55	0.70	1.04
	I-825 (5 mils)	0.54	0.70	0.90	1.33
	316L (3 mils)	1.60	1.98	2.52	3.15
	316L (5 mils)	0.96	1.19	1.51	1.89

Table 4: Steady state permeation current density as a function of charging current density

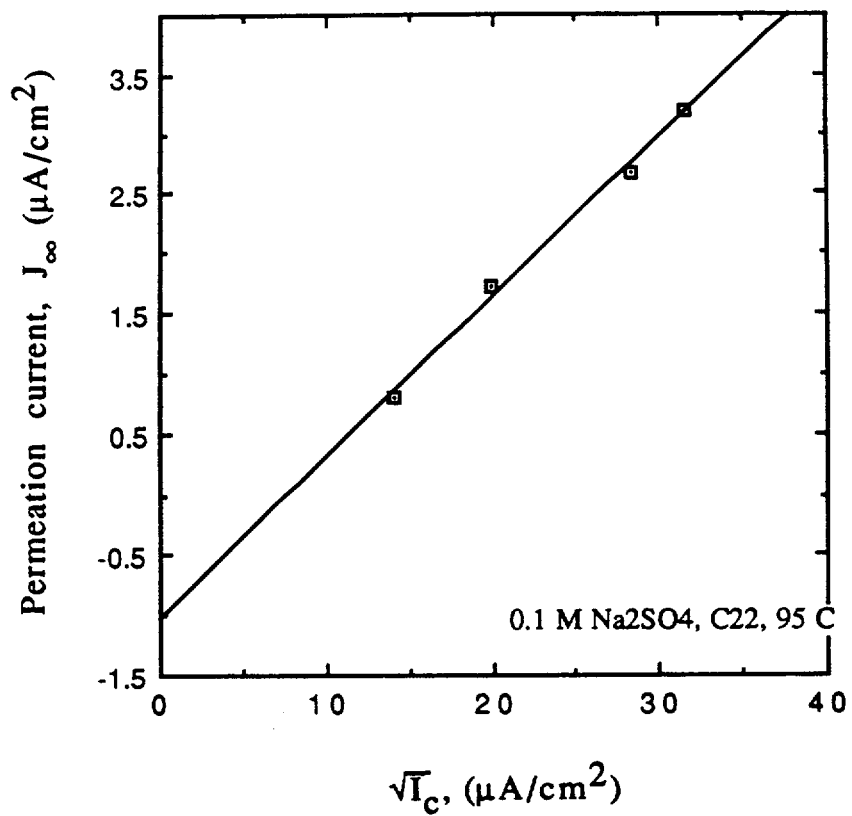


Figure 18: Permeation current-charging current relationship
C22 at 95°C

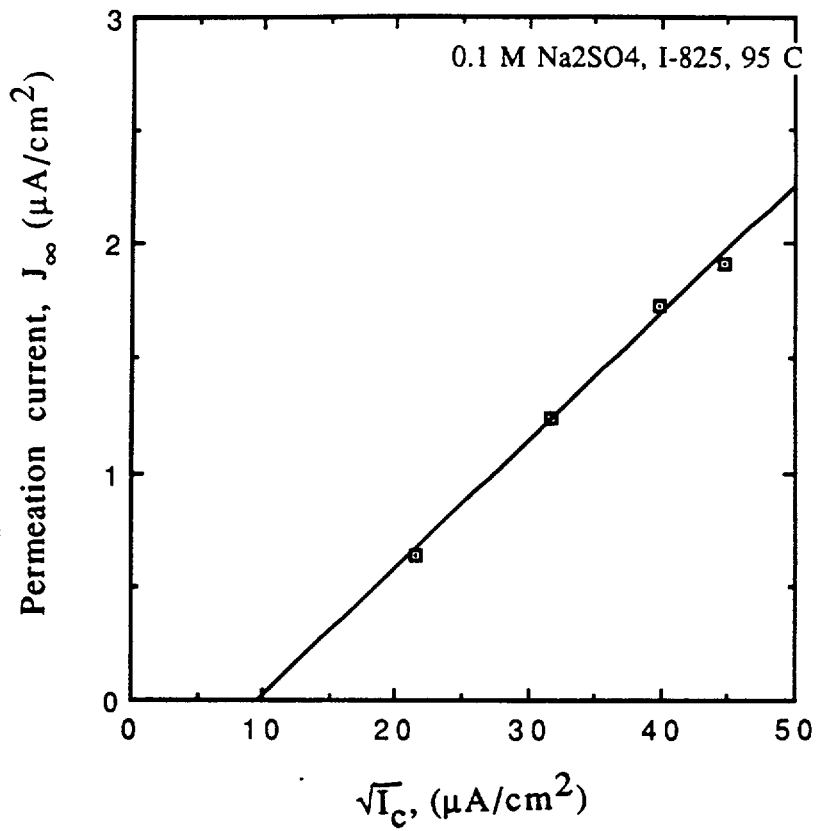


Figure 19: Permeation current-charging current relationship
I825 at 95°C

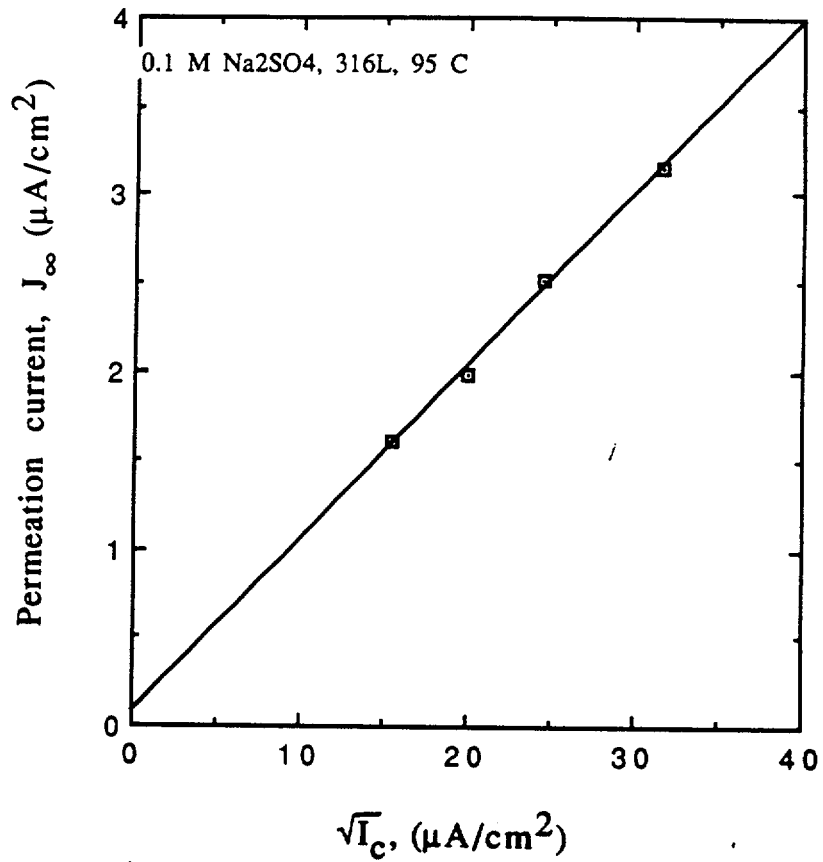


Figure 20: Permeation current-charging current relationship
316L at 95°C

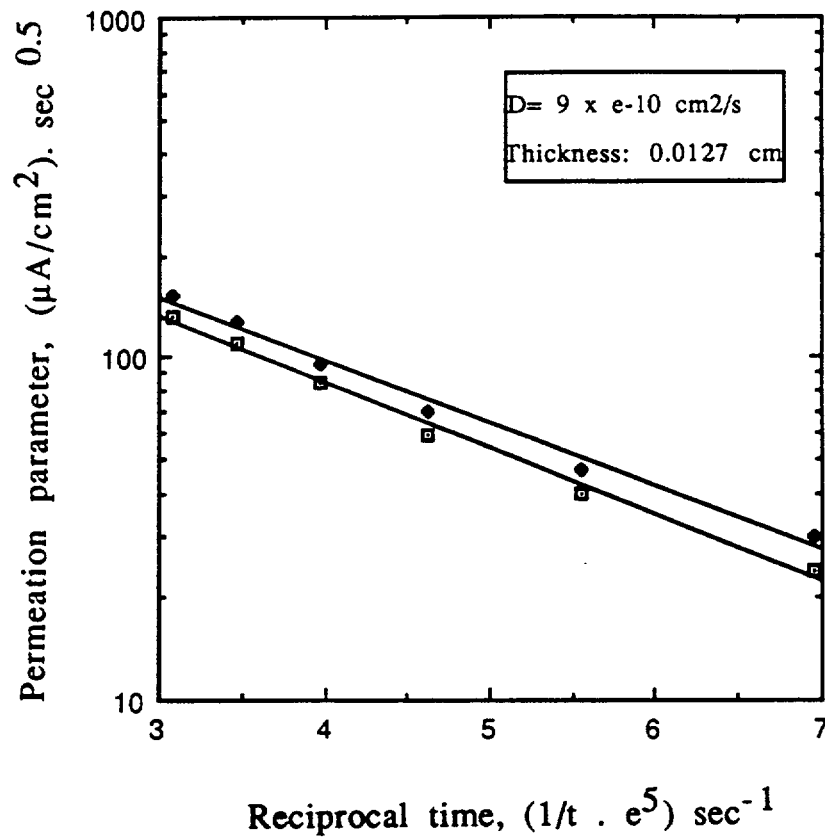


Figure 21: Diffusivity of hydrogen from rise and decay transients (in C22 at 95°C)

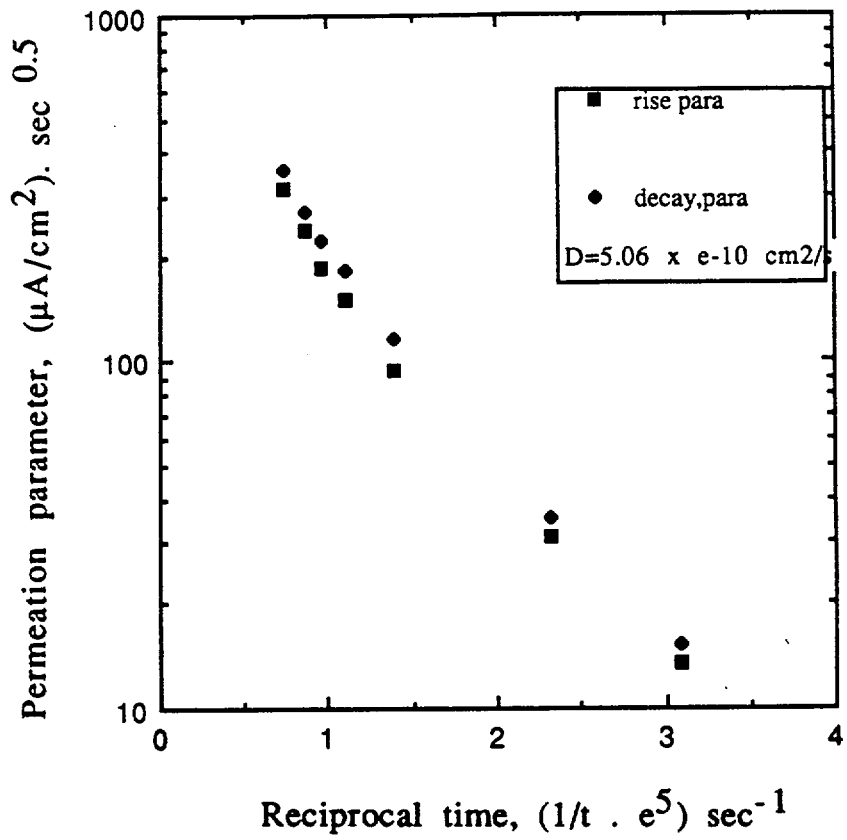


Figure 22: Diffusivity of hydrogen from rise and decay transients (in I825 at 95°C)

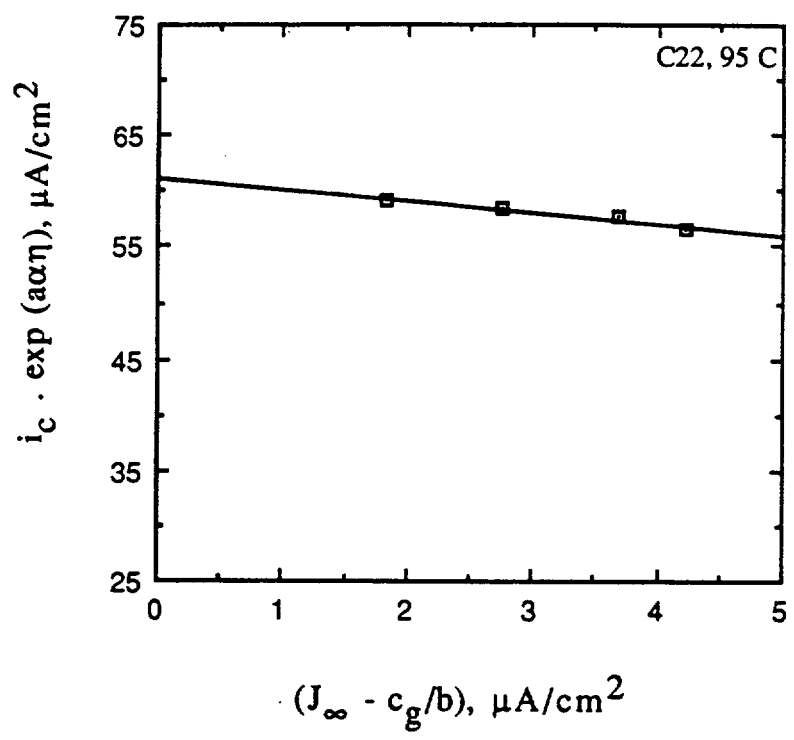


Figure 23: IPZ plot to evaluate surface coverage (C22 at 95°C)

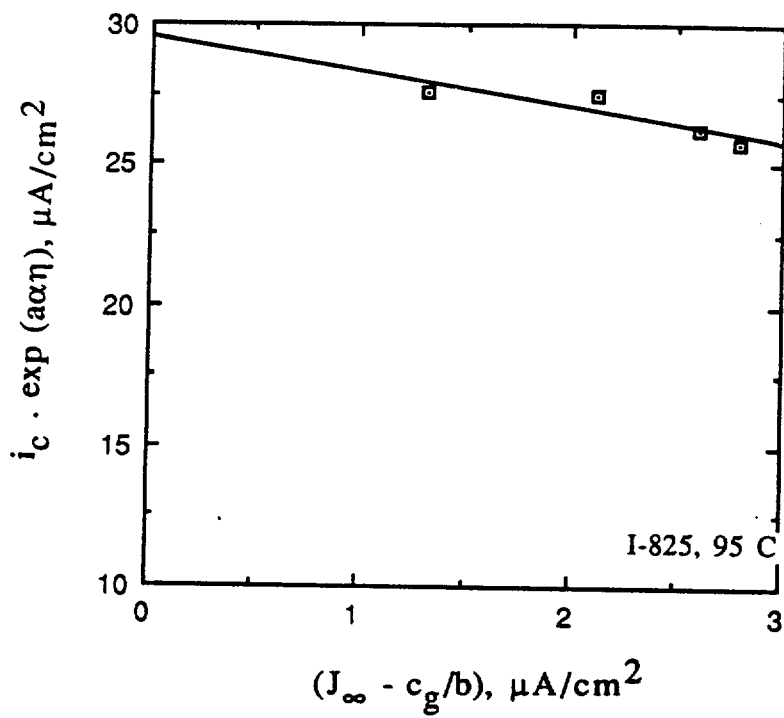


Figure 24: IPZ plot to evaluate surface coverage (I825 at 95°C)

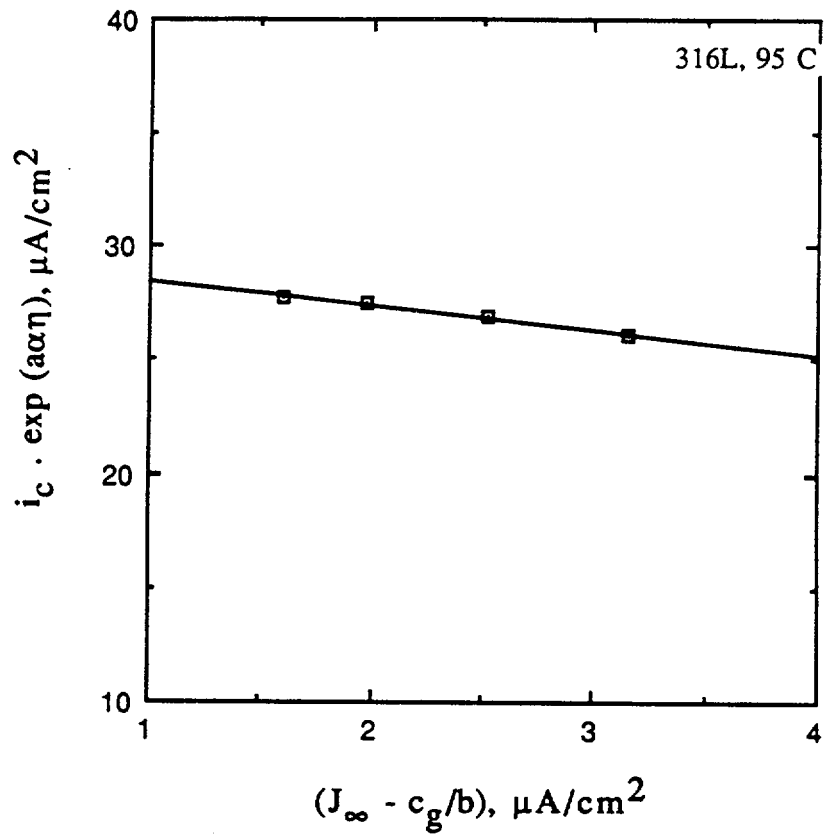


Figure 25: IPZ plot to evaluate surface coverage (316L at 95°C)

Material	D_H cm ² /s	α	i_0 μ A/cm ²	θ_H ($i_C=1$ mA/cm ²)	k_{abs}
C 22	$9 \cdot 10^{-10}$	0.43	61.1	0.053	0.982
I-825	$5.1 \cdot 10^{-10}$	0.41	49.1	0.073	0.991
316L	$3 \cdot 10^{-10}$	0.41	29.5	0.113	1.001

Table 5: Summary of I-P-Z analysis of permeation data

Material	k _{abs}	$\theta_H = f(i_c)$ ($i_c, \mu A/cm^2$)		
		200	400	800
C 22	0.982	0.013	0.028	0.044
I-825	0.991	0.029	0.039	0.062
316L	1.001	0.058	0.071	0.101

Table 6: Surface coverage of hydrogen (θ_H) function of charging current density

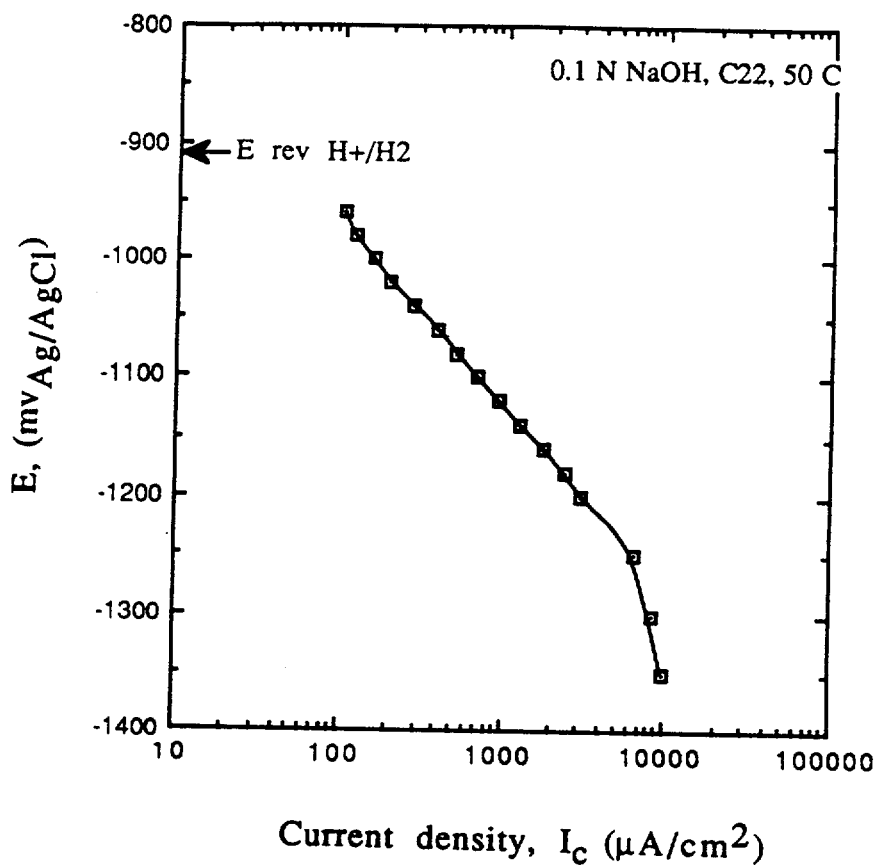


Figure 26: Cathodic polarization plot of C22 in 0.1N NaOH at 50°C

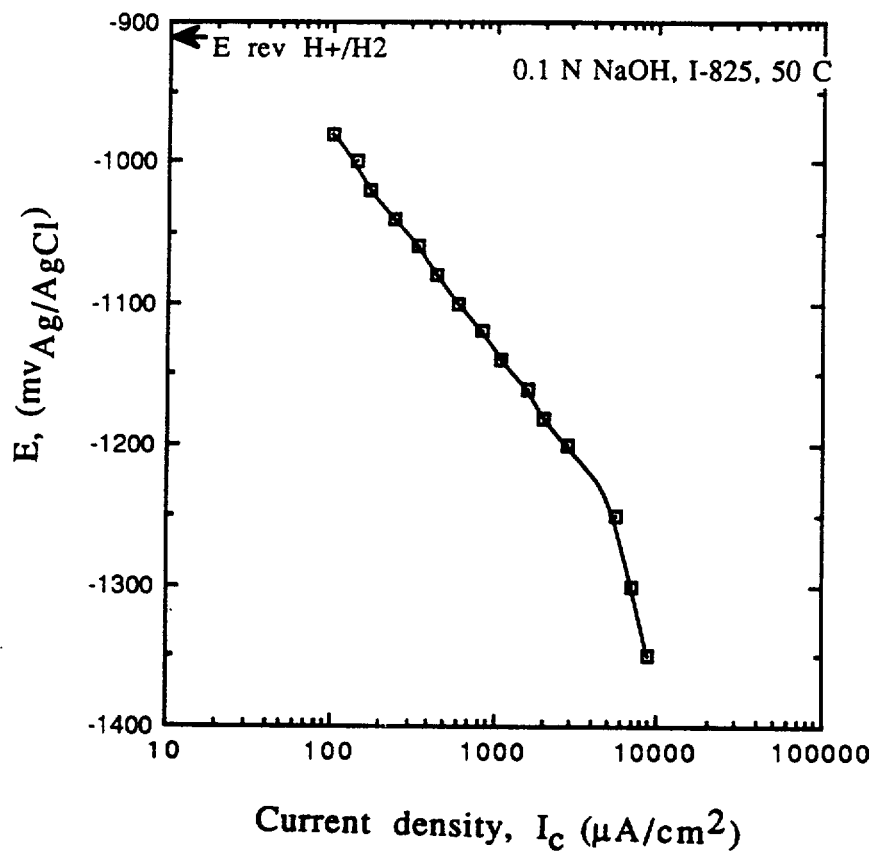


Figure 27: Cathodic polarization plot of I825 in 0.1N NaOH at 50°C

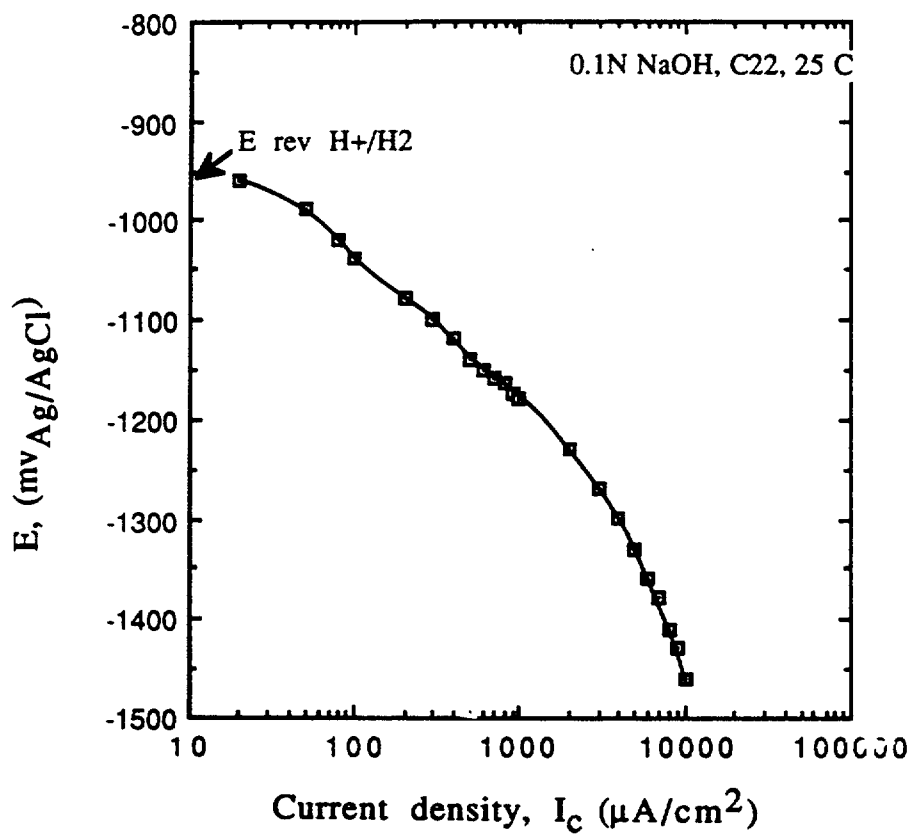


Figure 28: Cathodic polarization plot of C22 in 0.1N NaOH at 25°C

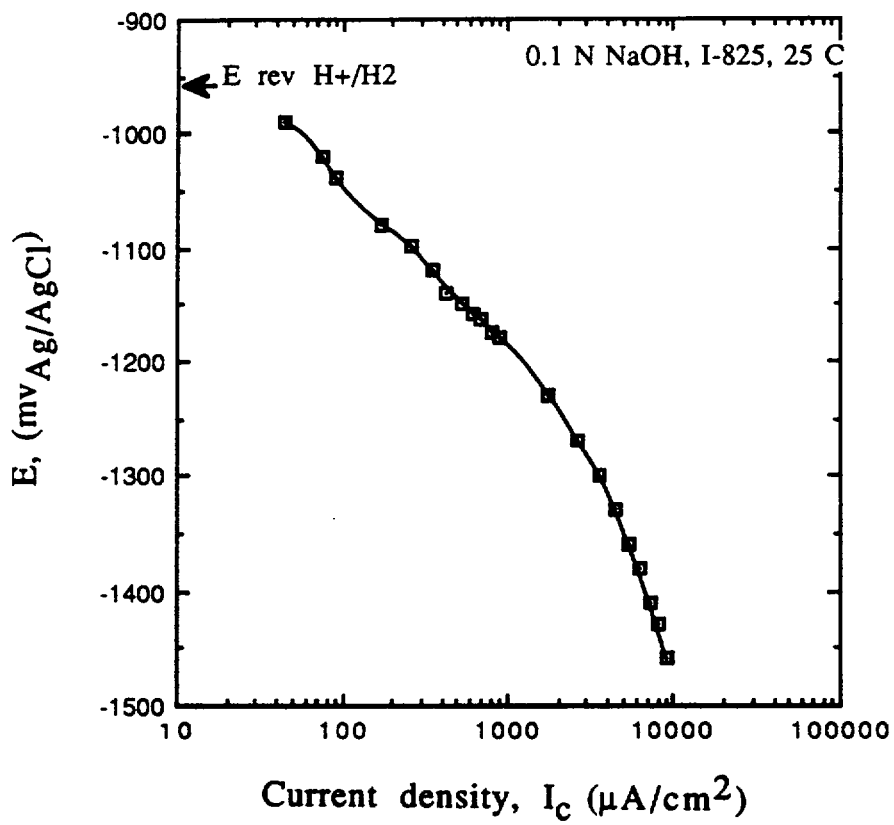


Figure 29: Cathodic polarization plot of I825 in 0.1N NaOH at 25°C

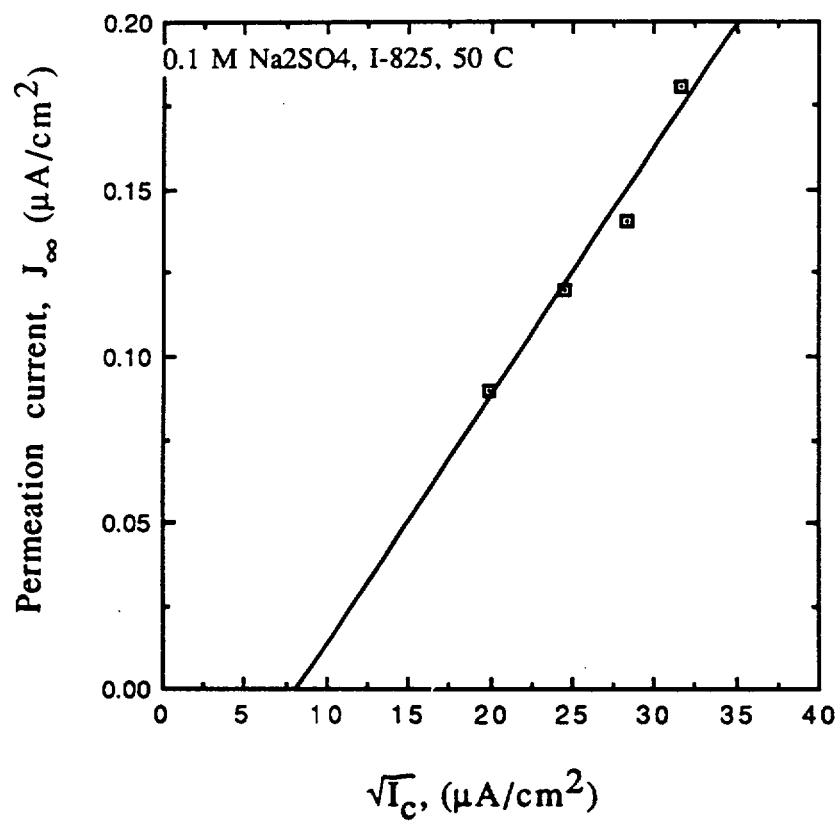


Figure 30: Permeation current-charging current relationship (I825 at 50°C)

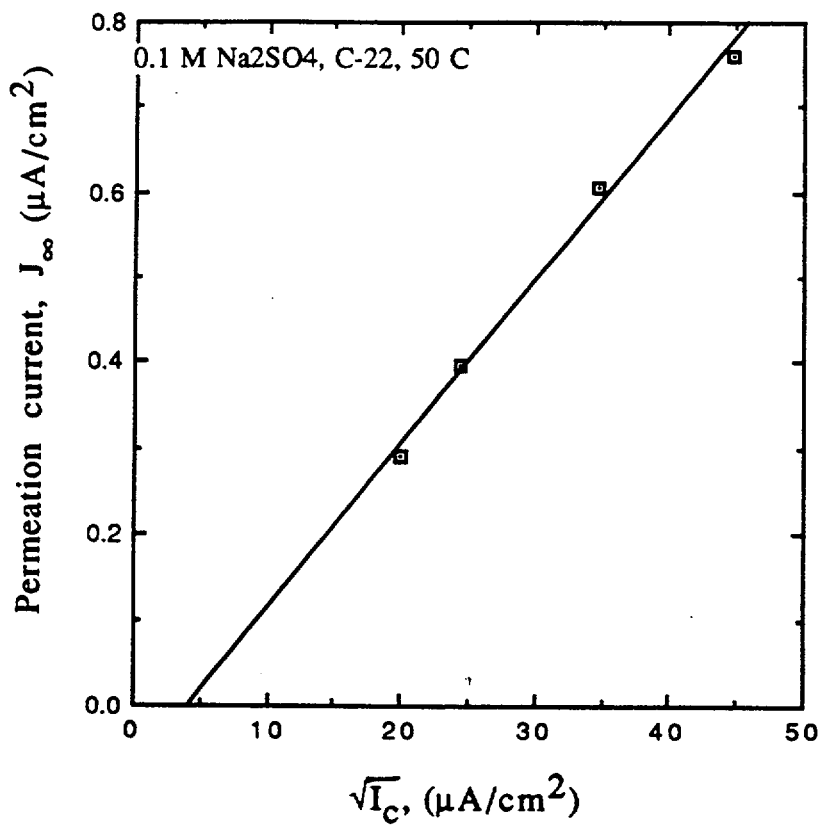


Figure 31: Permeation current-charging current relationship (C22 at 50°C)

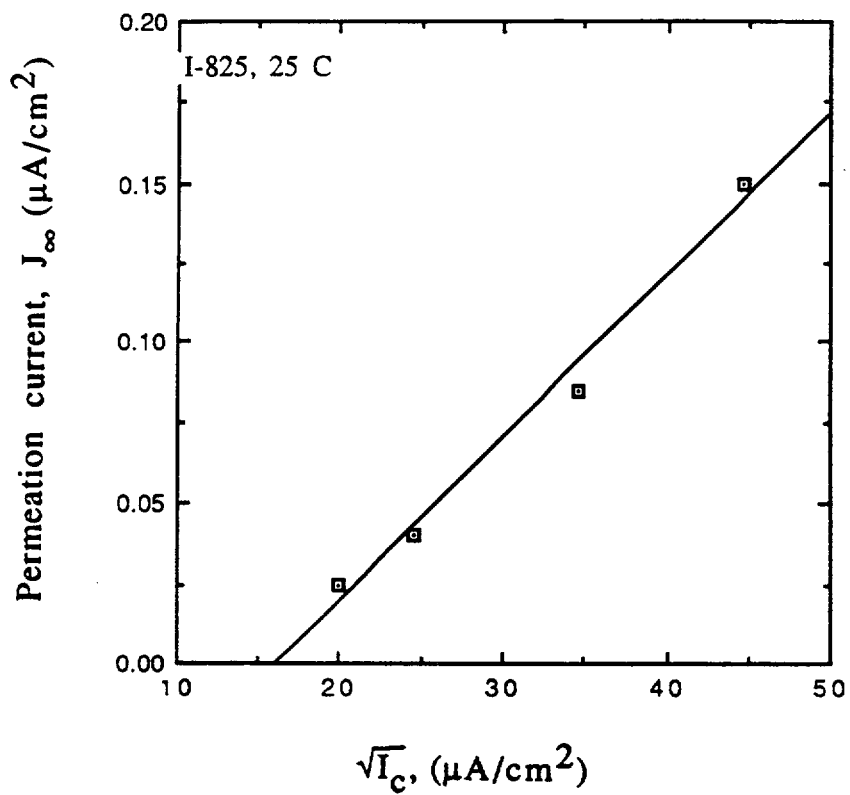


Figure 32: Permeation current-charging current relationship (I825 at 25°C)

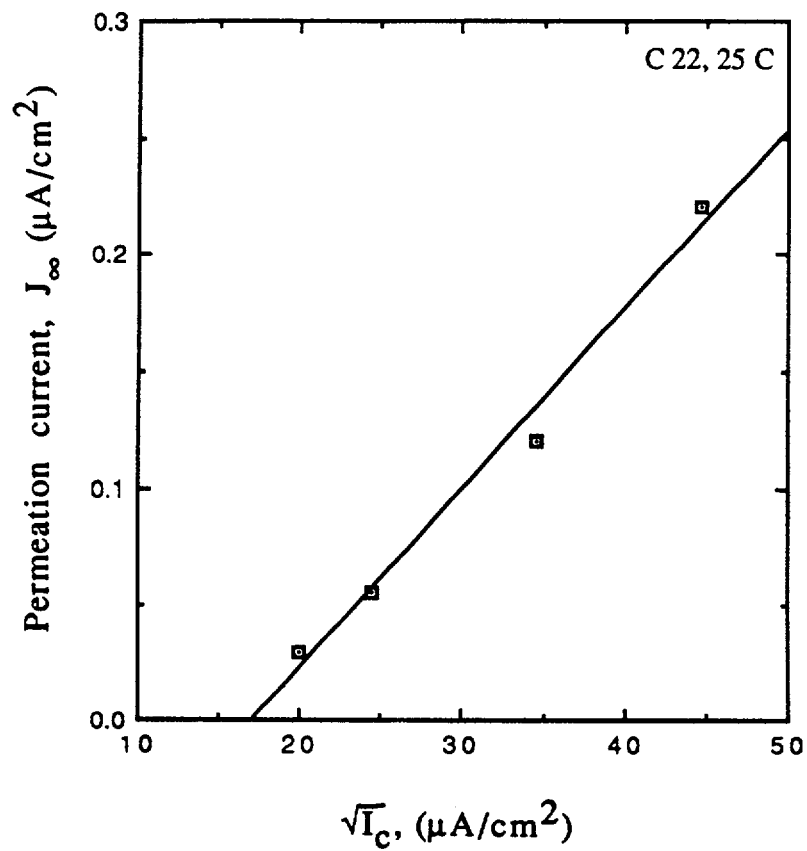


Figure 33: Permeation current-charging current relationship
(C22 at 25°C)

	Material	Temp., °C	ic ($\mu\text{A}/\text{cm}^2$)			
			400	600	1200	2000
Permeation flux, $\mu\text{A}/\text{cm}^2$ ----->	C-22	25	0.03	0.06	0.10	0.22
		50	0.29	0.39	0.61	0.76
		95	1.69	2.23	3.58	4.92
	I-825	50	0.09	0.12	0.20	0.27
		95	0.55	0.7	1.39	1.96

Table 7: Variation of permeation flux with temperature

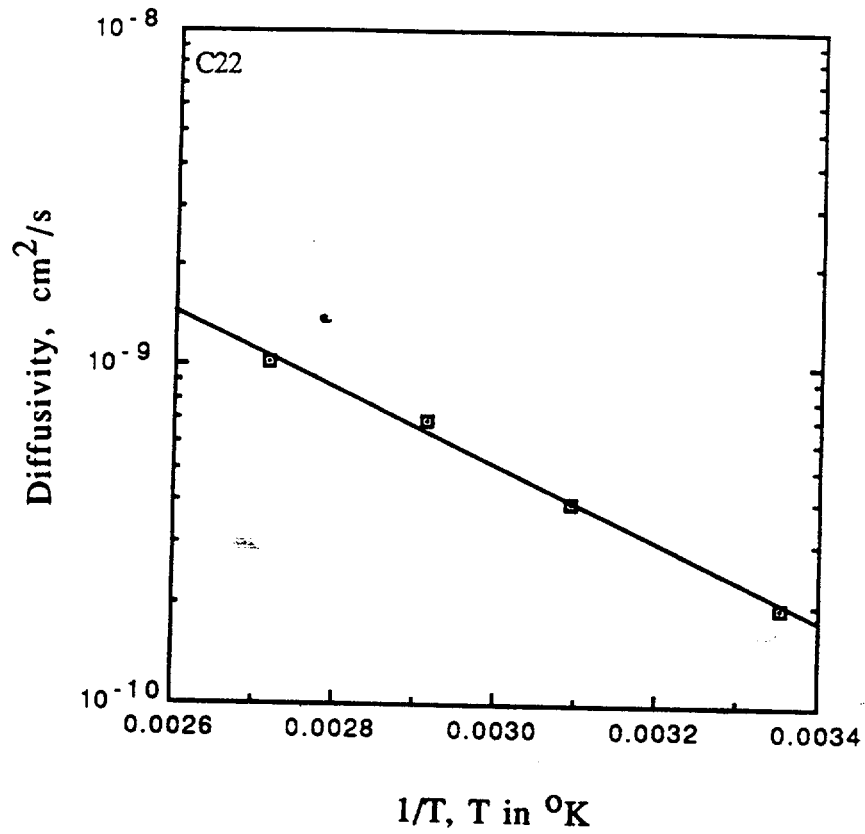


Figure 34: Plot of apparent diffusivity of hydrogen as a function of temperature

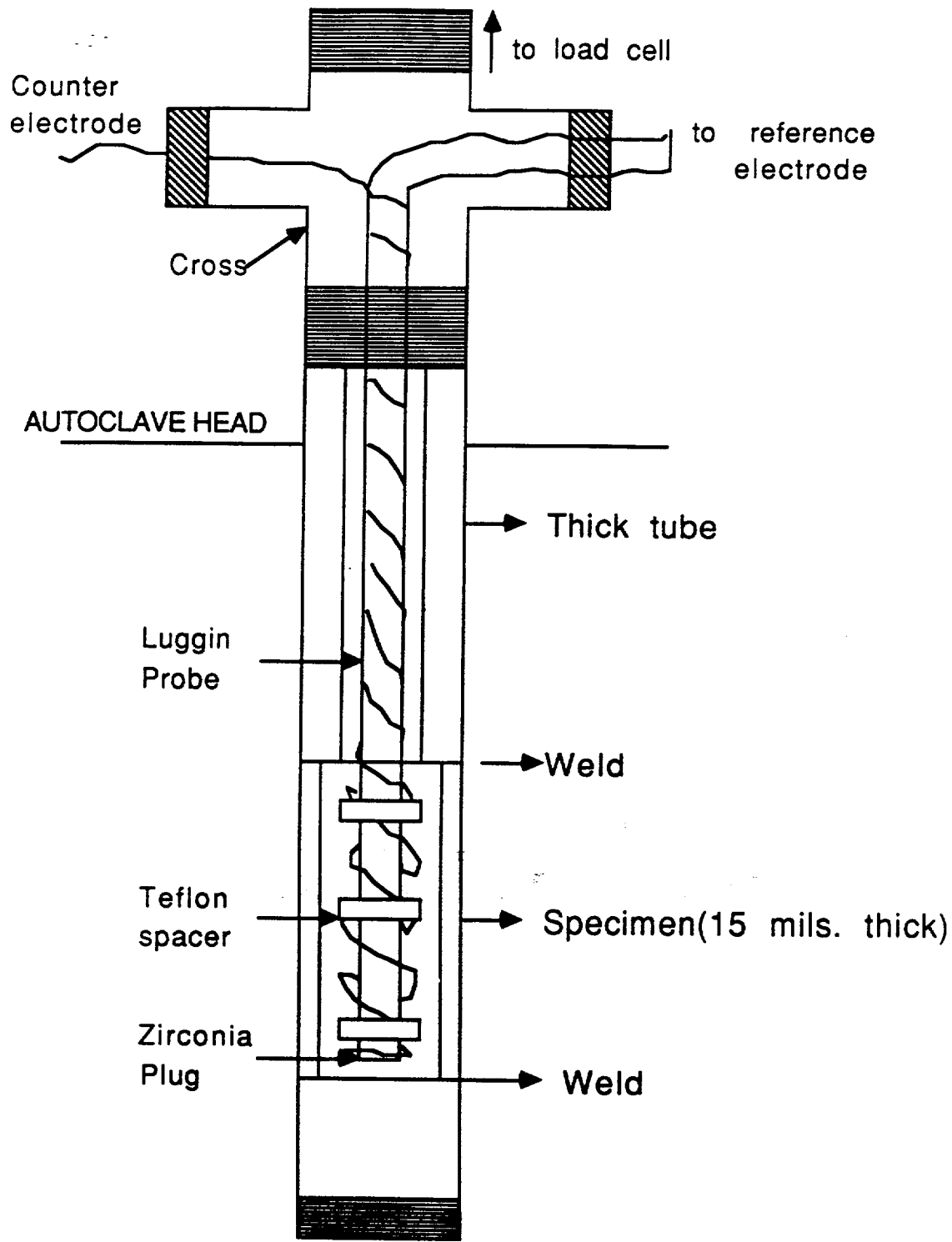


Figure 35: Schematic of location of electrodes in a straining permeation cell

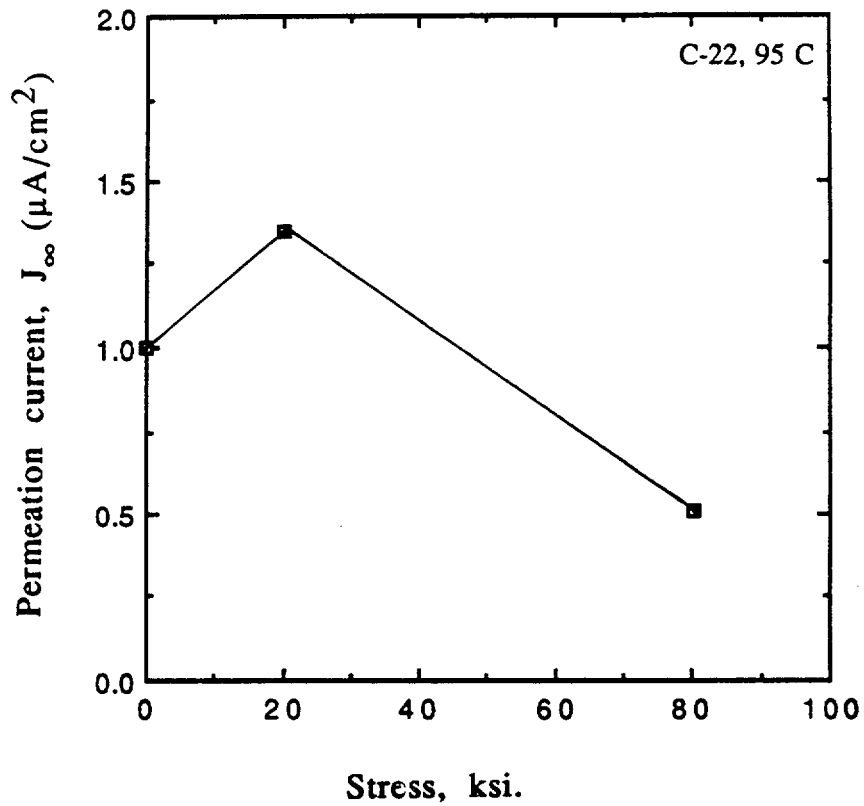


Figure 36: Effect of stress on hydrogen permeation in C22 at 95°C (Charging current density: 2 mA/cm²)

Material	Temp. (° C)	i_c (mA/cm ²)	Time to failure (hours)	Maximum load (ksi.)	%reduction in area
C 22	25	0	165	112.58	74.62
C 22	25	20	118.4	103.6	42.88
C 22	50	20	135.25	105.24	47.54
C 22	85	20	159.5	111.77	64.2
I-825	25	0	99	97.9	71.34
I-825	25	20	95	95.04	67.87
I-825	50	20	95.5	95.45	69.63
I-825	80	20	94	95.7	68.6

Table 8: Summary of slow strain rate test results

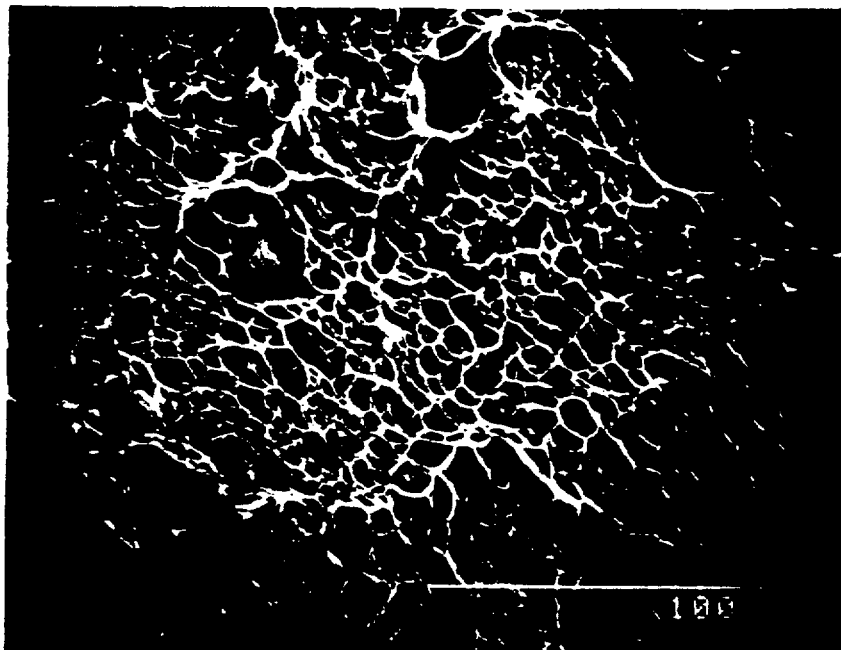


Figure 37: SEM fractograph, C22, without hydrogen charging, 500 X magnification.

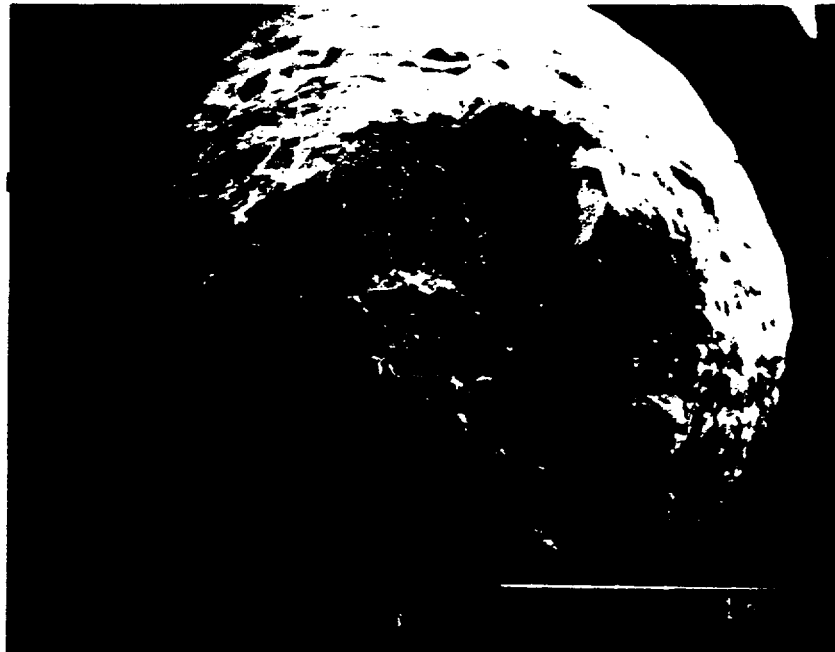


Figure 38: SEM fractograph, C22 without hydrogen charging, 40 X magnification.



Figure 39: Optical micrograph of a C22 SSRT specimen, 25°C ,longitudinal section with hydrogen charging 50X magnification.

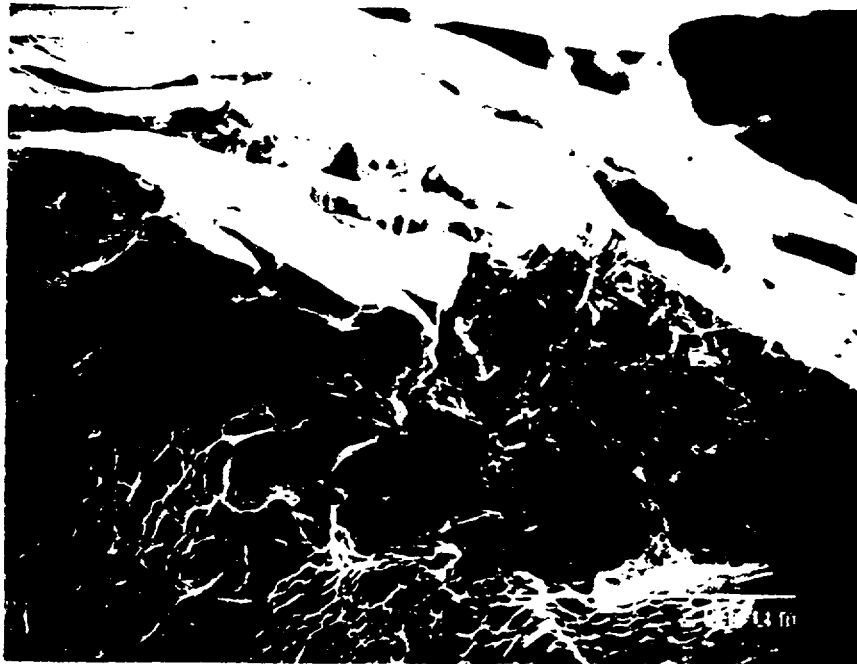


Figure 40: SEM fractograph, C22 with hydrogen charging at 25°C, 200 X (secondary cracks along the gage length)



Figure 41: SEM fractograph, C22 with hydrogen charging at 25°C, 500 X magnification.

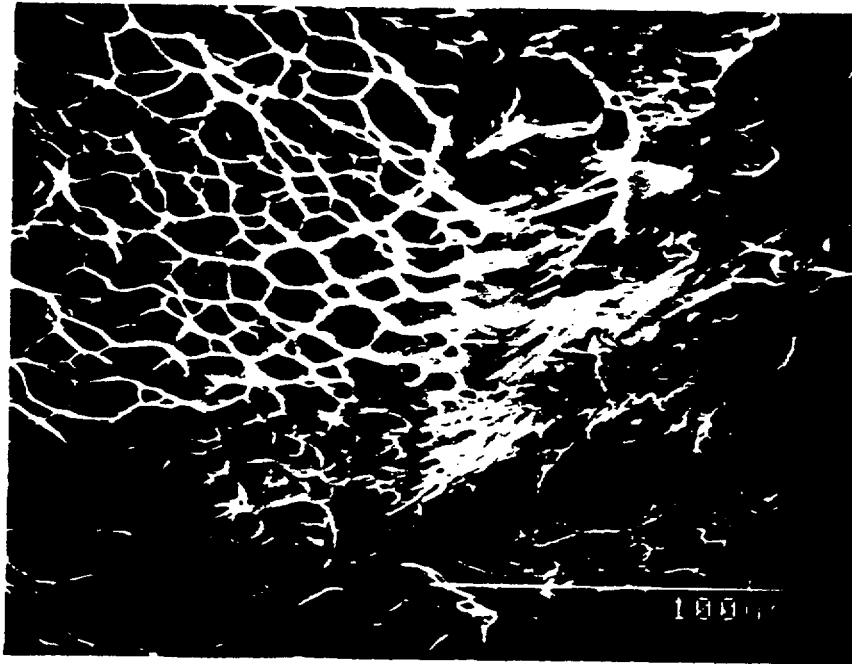


Figure 42: SEM fractograph, C22 with hydrogen charging at 25°C, 500 X magnification, (transition from QC to MVC).

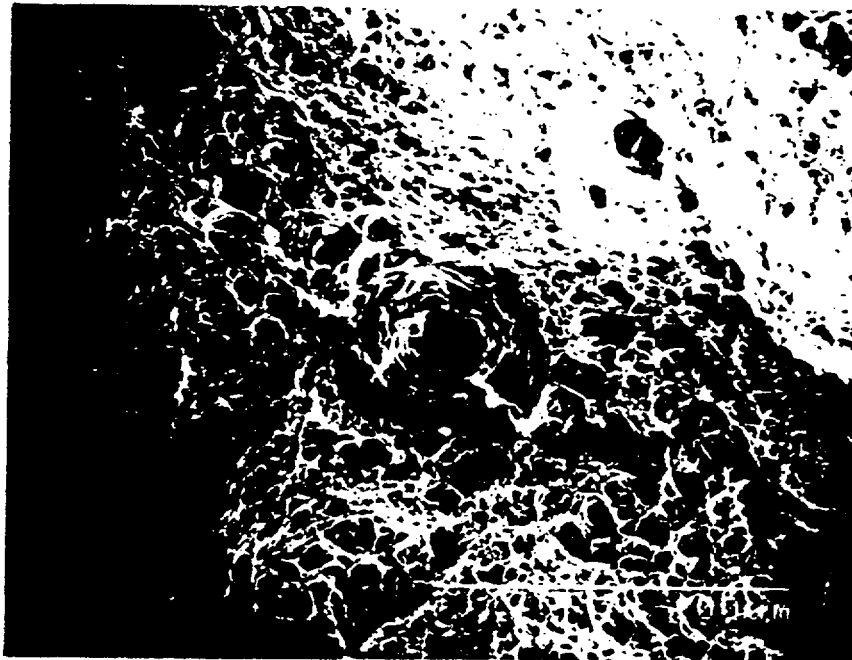


Figure 43: SEM fractograph, I825 with hydrogen charging at 25°C, 500 X magnification.



Figure 44: Optical micrograph of a I825 SSRT specimen, 25°C, longitudinal section, with hydrogen charging, 50 X magnification.

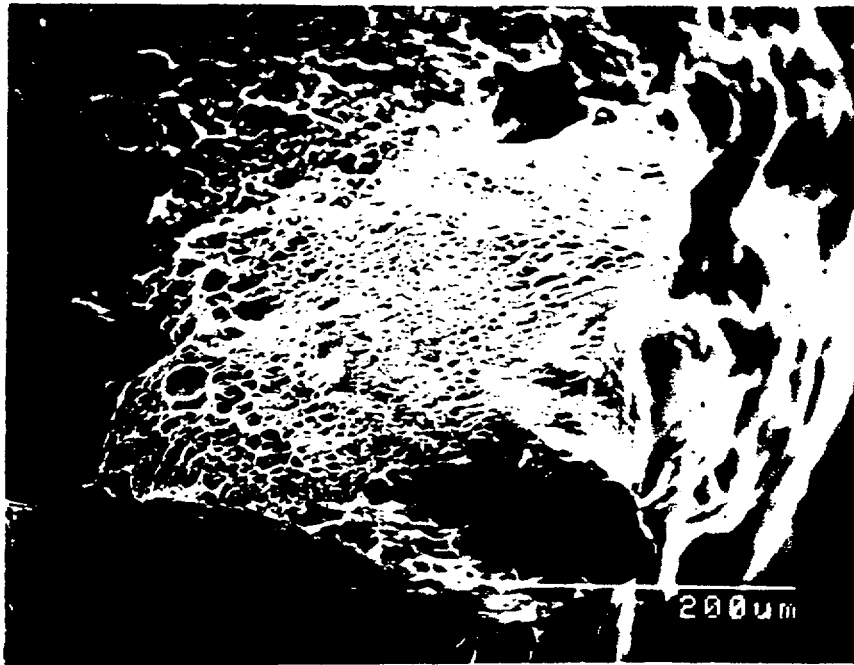


Figure 45: SEM fractograph, C22 with hydrogen charging at 85°C, 200 X magnification.



Figure 46: Optical micrograph of a C22 SSRT specimen, 50°C, longitudinal section with hydrogen charging, 50 X magnification.



Figure 47: Optical micrograph of a I825 SSRT specimen, 50°C, longitudinal section with hydrogen charging, 50 X magnification.

Element	Structure	3 d electrons
Fe	$[\text{Ar}] 3d^6 4s^2$	$\uparrow\downarrow \uparrow \uparrow \uparrow$
Cr	$[\text{Ar}] 3d^5 4s^1$	$\uparrow \uparrow \uparrow \uparrow \uparrow$
Ni	$[\text{Ar}] 3d^8 4s^2$	$\uparrow\downarrow \uparrow\downarrow \uparrow\downarrow \uparrow \uparrow$

Figure 48: Electronic structure of iron, chromium and nickel